Control of two-dimensional ion crystals in a radio-frequency trap for quantum simulation

Dominik Kiesenhofer

Thesis submitted to the
Faculty of Mathematics, Computer Science and Physics
of the
Leopold-Franzens University of Innsbruck
in partial fulfillment
of the requirements for the degree of

Doctor of Philosophy
(Physics)

October 2024

The work for this thesis was carried out under the supervision of

Assoz. Prof. Dr. Christian F. Roos and
o. Univ-Prof. Dr. Rainer Blatt

at the

Institute for Quantum Optics and Quantum Information (IQOQI) Innsbruck
of the Austrian Academy of Sciences and the
Institute for Experimental Physics of the University of Innsbruck.

Quand une bride se ferme, une autre s'ouvre.

Photo by David Jordan, IQOQI Innsbruck

Abstract

Ions confined in radio-frequency (rf) traps are one of the most promising platforms for achieving universal quantum computing beyond classical capabilities. Similarly, some of the most advanced quantum simulation experiments have been conducted with linear strings of about 50 ions. However, scaling up these systems to study more complex models of interacting quantum matter presents both fundamental and technical challenges, including the inability to naturally implement models with more than one dimension.
This work presents a novel apparatus designed for quantum simulation experiments with two-dimensional crystals of $^{40}Ca^{+}$ ions in a rf trap, effectively bypassing these scaling limitations. Nevertheless, two-dimensional crystals in rf traps pose their own challenges, such as inevitable micromotion of ions displaced from the trap's symmetry axis, as well as crystal configuration changes and melting caused by background gas collisions and rf heating. This work demonstrates how these issues are overcome and lays the groundwork for studying two-dimensional spin models with single-particle control in the near future.
Alongside details on the experimental setup, excellent control of two-dimensional crystals consisting of up to approximately 100 ions, is shown both at the classical and quantum level. We achieve excellent stability of planar ion crystals and employ a clustering algorithm to detect distinct crystal configurations, enabling the mitigation of configuration changes by adjusting trap parameters. Furthermore, this approach allows for the automatic detection of such changes during individual experiments, thereby practically eliminating their detrimental effects on measurement outcomes.
Using electromagnetically induced transparency cooling and polarization gradient cooling, fast multimode cooling of crystals in two-dimensional configurations containing up to 105 ions and 22 ions, respectively, is achieved, bringing them close to their motional ground state. This meets another essential requirement for the implementation of long-range entangling interactions.
Since estimating the temperature of large, ground-state-cooled ion crystals is challenging due to complex many-body interactions, a new thermometry method, forming a generalization of the well-known sideband ratio technique for single ions, is tested on individual modes of a planar 19-ion crystal. The results are consistent with numerical simulations and measurements obtained with a single ion and an 8-ion crystal. Finally, as a first step towards quantum simulation of spin lattice models in two dimensions, the last chapter explores the build-up of spin-spin correlations during the application of Ising-type interactions using stimulated Raman transitions.

Kurzdarstellung

Ionen, die in Radiofrequenz(rf)-Fallen gehalten werden, gehören zu den vielversprechendsten Plattformen für die Verwirklichung universeller Quantencomputer jenseits der Fähigkeiten klassischer Rechner. Ebenso wurden einige der fortschrittlichsten Quantensimulationsexperimente mit linearen Ketten von etwa 50 Ionen durchgeführt. Das Hochskalieren dieser Systeme zur Untersuchung komplexerer Modelle wechselwirkender Quantenmaterie stellt jedoch sowohl fundamentale als auch technische Herausforderungen dar, einschließlich dem Unvermögen, Modelle mit mehr als einer Dimension natürlicherweise zu implementieren.
Diese Arbeit stellt einen neuen experimentellen Aufbau vor, der für Quantensimulationsexperimente mit zweidimensionalen $^{40}Ca^{+}$-Ionenkristallen in einer rf-Falle entwickelt wurde und diese Skalierungsprobleme effektiv umgeht. Zweidimensionale Kristalle in rf-Fallen bringen jedoch eigene Herausforderungen mit sich, wie etwa die unvermeidliche Mikrobewegung der Ionen, die abseits der Symmetrieachse der Falle angeordnet sind, sowie Kristallkonfigurationsänderungen und das Schmelzen von Kristallen, die durch Kollisionen mit dem Hintergrundgas und rf-Heizen verursacht werden können. Diese Arbeit zeigt, wie diese Probleme überwunden werden und legt damit den Grundstein für die Untersuchung von zweidimensionalen Spin-Modellen mit Einzelteilchenkontrolle in naher Zukunft. Neben Details zum experimentellen Aufbau wird die Kontrolle von zweidimensionalen Kristallen, die aus bis zu etwa 100 Ionen bestehen, sowohl auf klassischer als auch auf quantenmechanischer Ebene demonstriert. Wir erreichen zudem eine ausgezeichnete Stabilität der planaren Ionenkristalle und setzen einen Cluster-Algorithmus ein, um unterschiedliche Kristallkonfigurationen zu erkennen, was wiederum die Minderung von Konfigurationswechsel durch Anpassung der Fallenparameter ermöglicht. Darüber hinaus erlaubt uns dieser Ansatz, solche Konfigurationswechsel während einzelner Experimente automatisch zu erkennen, wodurch ihr nachteiliger Einfluss auf die Messergebnisse praktisch eliminiert wird.
Durch Kühlen mittles elektromagnetisch induzierter Transparenz (EIT) sowie mittels Polarisationsgradienten-Kühlen (PG) erreichen wir das schnelle multimodale Kühlen von bis zu 105 Ionen (EIT) bzw. 22 Ionen (PG) in zweidimensionalen Konfigurationen nahe an ihren Grundzustand. Damit wird eine weitere wesentliche Voraussetzung für die Implementierung von langreichweitigen Verschränkungswechselwirkungen erfüllt. Da die Bestimmung der Temperatur großer, in den Grundzustand gekühlter Ionenkristalle aufgrund komplexer Vielteilchen-Wechselwirkungen äußerst schwierig ist, testen wir eine neue Thermometriemethode, die eine Verallgemeinerung der bekannten Seitenband-Methode

für einzelne Ionen darstellt, mit einem planaren 19-Ionen-Kristall. Die Ergebnisse stimmen mit Messungen eines einzelnen Ions sowie eines 8-Ionen-Kristalls überein.
Schließlich wird als erster Schritt hin zur Quantensimulation von zweidimensionalen Spin-Gitter-Modellen der Aufbau von Spin-Spin-Korrelationen während der Anwendung Ising-artiger Verschränkungswechselwirkungen mithilfe stimulierter Raman-Übergänge untersucht.

Publications

The work presented in this thesis has led to the following publications:

- D. Kiesenhofer, H. Hainzer, A. Zhdanov, P. C. Holz, M. Bock, T. Ollikainen, and C. F. Roos, "Controlling Two-Dimensional Coulomb Crystals of More Than 100 Ions in a Monolithic Radio-Frequency Trap", PRX Quantum 4, 020317 (2023).
- I. Vybornyi, L. S. Dreissen, D. Kiesenhofer, H. Hainzer, M. Bock, T. Ollikainen, D. Vadlejch, C. F. Roos, T. E. Mehlsäubler, and K. Hammerer, "Sideband Thermometry of Ion Crystals", PRX Quantum 4, 040346 (2023).
- M. Joshi, A. Fabre, C. Maier, T. Brydges, D. Kiesenhofer, H. Hainzer, R. Blatt, and C. Roos, "Polarization-gradient cooling of 1D and 2D ion Coulomb crystals", New Journal of Physics 22, 103013 (2020)

During my PhD work I have also contributed to the following publication, which is not discussed in this thesis:

- H. Hainzer, D. Kiesenhofer, T. Ollikainen, M. Bock, F. Kranzl, M. K. Joshi, G. Yoeli, R. Blatt, T. Gefen, and C. F. Roos, "Correlation Spectroscopy with Multiqubit-Enhanced Phase Estimation", Phys. Rev. X 14, 011033 (2024).

Contents

Acronyms

ac	alternating current
ADC	analog-to-digital converter
AQT	Alpine Quantum Technologies
AOD	acousto-optic deflector
AOM	acousto-optic modulator
AWG	arbitrary waveform generator
BSB	blue sideband
COM	center-of-mass
DAC	digital-to-analog converter
dc	direct current
DDS	direct digital synthesizer
ECDL	external cavity diode laser
EIT	electromagnetically induced transparency
EMCCD	electron-multiplying charge-coupled device
FEM	finite element method
FFT	fast Fourier transform
FWHM	full width at half maximum
GUI	graphical user interface
ICA	independent component analysis
IP	in-plane
IQOQI	Institute for Quantum Optics and Quantum Information
LF	low-frequency
MS	Mølmer-Sørensen
NEG	non-evaporative getter
ODE	ordinary differential equation
OOP	out-of-plane

PCA	principal component analysis
PCF	photonic crystal fiber
PG(C)	polarization-gradient (cooling)
PhD	philosophiae doctor (doctor of philosophy)
PI(D)	proportional-integral(-derivative)
PM	polarization-maintaining
PP	pseudo-potential
PI(D)	proportional-integral(-derivative)
PM	polarization-maintaining
PP	pseudopotential
RAP	rapid adiabatic passage
rf	radio frequency
RGA	residual gas analyzer
RSB	red sideband
SB	sideband
SM	single-mode
SS	stainless steel
SVD	singular value decomposition
TA	tapered amplifier
TTL	transistor-transistor logic
UHV	ultra-high vacuum
VQE	variational quantum eigensolver
VQS	variational quantum simulation
XHV	extreme-high vacuum

Chapter 1

Introduction

Quantum many-body physics is at the core of many fascinating phenomena resulting from the interaction between particles. As such, it offers numerous problems that are of fundamental interest in fields like condensed matter physics, high-energy physics as well as quantum chemistry or quantum biology to mention a few. The interactions between matter at a microscopic level can give rise to quantum correlations, in particular quantum discord and entanglement, which accompany phenomena like quantum magnetism, high-temperature superconductivity and quantum phase transitions. At the same time, these interactions constitute valuable resources in quantum information science and quantum measurements in general. Due to the computational complexity and the unmanageable, exponentially growing state space for larger numbers of particles, most problems involving interacting many-body systems can neither be solved analytically nor by exact numerical simulations. Therefore, various strategies for approximating certain quantities have been pursued to find solutions to such problems. Amongst these approaches are perturbation theories, mean-field theories, lattice gauge theories, density functional theory [1], and more recently tensor networks [2] and neural network quantum states [3] to name a few important ones. For larger particle numbers, however, in most cases these strategies are still computationally unmanageable or they lack the ability to produce accurate results. One way to overcome these issues is to study physical properties directly in a controllable quantum system representing the physical model of interest. This approach is referred to as *quantum simulation*. The idea of using well-controlled quantum systems to solve quantum problems goes back to the early 1980s. It was most famously proposed in 1982 by Richard Feynman [4] after being discussed by Yuri Manin already in 1980 [5]. In the same year, Paul Benioff had established the foundation to represent the computation processes of classical Turing machines by quantum-mechanical Hamiltonian models [6]. Decades of research following these ideas have led to the extensive theory and toolkit that we have in quantum information science today. The concept of the quantum simulator has to be contrasted with the idea of a full-fledged quantum computer as a general-purpose device being able to solve any generic problem in a *digital* way. An analog quantum simulator is a special-purpose device targeted at solving specific quantum mechanical problems by creating a 1:1-correspondence between the model of interest and the precisely controllable

quantum system in the laboratory. This way, the quantities of interest can be observed directly by probing a system of interacting particles.

As per today, it remains unclear when large-scale, fault-tolerant quantum computers will be available, giving rise to the full potential of quantum simulators as an intermediate step. In the present era of noisy intermediate-scale quantum (*NISQ*) devices [7], quantum simulation represents a powerful tool for exploring quantum physics on a scale of hundreds of particles being already far beyond the capabilities of classical computers. At the sacrifice of a certain extent of the fidelity of the applied quantum operations (in contrast to fault-tolerant quantum computers), quantum simulators can provide insights into specific quantum many-body problems at these scales. Probably the most widely studied models using quantum simulators today are Ising-type models describing the quantum magnetism of spin-1/2 systems. The interactions underlying this (toy) model are also the native type of spin-spin interactions of the device presented in this thesis. Moreover, recent hybrid approaches, using variational optimization on a classical computer in combination with a quantum simulator, enable the study of more general classes of physical systems such as models relevant to high-energy physics [8].

Various physical platforms have been suggested to realize quantum simulators as well as quantum computers such as neutral atoms in optical lattices or tweezer arrays, superconducting qubits, photonic waveguide arrays, Rydberg atom arrays, trapped molecules and trapped ions. Without a discussion about the pros and cons of all these platforms, this work focuses on quantum simulation with trapped ions, in particular ions held in radio-frequency (rf) traps. Trapped atomic ions represent precisely controllable, identical particles, which have been employed successfully in quantum computation, quantum sensing and metrology, quantum communication and also quantum simulation. For many decades trapped ions have been used in spectroscopic experiments for the study of atomic physics. Persistent development of new techniques and technologies have enabled excellent control of both the ions' electronic as well as motional degrees of freedom, which led to the realization of the most advanced devices in quantum information science to date. As a result, trapped ions have also escaped the scope of pure academic interest being the basis for countless developments in private industry around the globe. The trapped-ion group in Innsbruck has been part of these developments since the 1990s and contributed to quantum information processing with trapped ions from the earliest days onwards [9].

The first proof-of-principle analog quantum simulation experiments realizing a frustrated spin model with three spins using a string of trapped ions have been reported in 2010 [10] by the group of *C. Monroe*. They were followed by experiments in Penning traps (group of *J. Bollinger*) using large two-dimensional lattices of hundreds of trapped ions to simulate Ising interactions [11, 12]. Until recently, however, experiments in Penning traps were lacking single-particle control due to technical challenges caused by the inherent rotation of the ion crystals. The first proof-of-principle experiments demonstrating the individual addressing of ions in crystals held in Penning traps, which are rotating at frequencies of several tens of kHz, using a single focused laser beam have been presented in Ref. [13].

In Innsbruck, besides experiments using digital quantum simulation [14–16], analog quantum simulation experiments with linear ion crystals have been carried out for more than

a decade now [8, 17, 18]. The more recent works demonstrate the possibilities to study physics beyond quantum magnetism using the same experimental platform [19–21]. In these quantum simulation experiments, the entangling interactions are mediated by global laser fields coupling to the ion crystal's vibrational modes of motion, which are governed by the Coulomb forces between the ions. In addition, coherent single-ion control is implemented via tightly focused laser beams steered by acousto-optical deflectors.

So far, complete quantum control has been demonstrated with linear ion crystals of up to several tens of particles [22]. In order to study physics in a regime, which is truly intractable by classical machines, these numbers need to be scaled up. However, increasing the number of ions in a linear configuration entails mainly two technical problems: First, trapping more ions requires extremely anisotropic potentials [23,24], where lower axial trap frequencies lead to increasing axial heating rates. Second, the manipulation of individual ions with tightly focused laser beams, as it is state-of-the-art, becomes problematic as the crystal's spatial expansion, that needs to be covered, grows with the number of ions. There are other ways to scale up to larger ion numbers, though. One approach followed in this thesis is to trap ions in a two-dimensional crystal configuration, loosening the restrictions on the trap anisotropy and reducing the spatial extent in a single direction.

There are several options to trap ions in a 2d geometry: In Penning traps large planar crystals of hundreds of ions have been trapped successfully [12] while single-ion addressing remains challenging as the crystals rotate at tens to hundreds of kHz around the out-of-plane axis [25]. In rf surface trap arrays, nearly arbitrary planar geometries could be realized by trapping individual ions in separate microtraps, which has been realized only with several ions so far [26–28]. However, for entangling interactions mediated by the ions' motion to occur on timescales much shorter than the coherence time, the ions would need to be sufficiently close, with a separation of at least on the order of tens of micrometers. This, in turn, requires the ions to be close to the surface of the chip, where electric field noise leads to motional heating limiting the motional coherence necessary to mediate the interaction. Additionally, ion loss resulting from shallow trap depths and the required free optical access, which often necessitates the integration of optics, presents further challenges in these systems that must be overcome. Another recently taken approach combines the concepts of Penning traps and surface rf trap arrays and attempts to scale up trapped-ion systems by trapping single ions in surface Penning trap arrays [29, 30].

This thesis describes a new experimental apparatus for scaling up a trapped-ion system by confining ions in a 2d configuration in the potential of a single rf trap. This strategy has been pursued by several research groups worldwide [31–36] and allows one to exploit the well-established methodology for ions in rf traps and to benefit from entangling interactions with a tunable range (from all-to-all to nearest-neighbor coupling) as well as the ability to control ions individually, which previous experiments with linear ion crystals have been harnessing for more than a decade. Moreover, holding ion crystals in a two-dimensional configuration naturally enables the study of physical models in two dimensions, a matter of fundamental interest and with applications in various fields. While 2d spin models can be implemented straightforwardly by using the same methods as in quantum simulation experiments with ions strings, entering the second dimension in rf traps entails several

challenges:

Challenge 1: Micromotion In a 2d crystal, all ions displaced from the rf null inevitably experience rf-driven micromotion, which leads to a phase-modulation of the laser-ion interaction at the trap drive frequency. It can be overcome by addressing the ions only from directions perpendicular to the micromotion.

Challenge 2: Optical access Optical access from directions perpendicular to the direction of micromotion is required and unobstructed optical access perpendicular to the crystal plane is needed for single-ion addressing and site-resolved imaging.

Challenge 3: Alignment of trap electrodes Misalignment of the trap electrodes with respect to each other could lead to enhanced nonlinear resonances in the potential causing the ejection of ions from the trap [37, 38]. This effect increases in severity the further an ion is displaced from the rf null [39]. Furthermore, electrode misalignment can cause unwanted micromotion, which cannot be compensated.

Challenge 4: rf heating The implications of rf heating on the experiments are not completely clear *a priori*. Energy transfer from the rf trapping field to the ions can have an impairing effect on entangling interactions mediated by the ions' collective modes of motion and could lead to crystal configuration changes (see *Challenge 5*) and melting [40, 41].

Challenge 5: Crystal configuration changes A 2d ion crystal can occur in various lattice configurations. Transitions between them can be caused by hot vibrational modes, rf heating or background gas collisions. Strategies to mitigate such configuration changes during experiments or for post-processing of experimental data are required.

Throughout this thesis all of these challenges are addressed and strategies to overcome them are presented. Furthermore, the preparation of the out-of-plane vibrational spectrum of 2d ion crystals with up to 105 ions close to the motional ground state is achieved by electromagnetically-induced transparency cooling. This not only checks off another prerequisite for quantum simulation experiments but also, for the first time, demonstrates the cooling of such a large number of ions held in a rf trap near the ground state - a two-fold improvement compared to linear strings [22] and an order of magnitude more than 2d crystals in previously reported experiments [42]. In order to assess the phononic excitations of a 2d crystals, an extension of the single-ion sideband thermometry technique is used to measure the mean phonon numbers of individual modes of a 19-ion 2d crystal. The last part of this work presents first experiments using a bichromatic laser field to realize Ising-type interactions in a 91-ion 2d crystal.

In more detail, this work is structured as follows: The second chapter provides an overview of the foundations of ion trapping in rf traps, as well as quantum optics and quantum information science, focusing on the interaction of electromagnetic fields with trapped ions. The third chapter describes the experimental setup, which was built from scratch and focuses on the vacuum apparatus, the electronics used for trapping and controlling the experiments, and the optical setups. The fourth chapter presents various experiments aimed at the characterization of the experimental apparatus and demonstrates excellent control of 2d ion crystals with up to 105 ions in terms of trapping and coherent properties.

Chapter five presents successful ground-state cooling of 2d crystals with up to 105 ions and thermometry measurements of individual modes of 2d crystals with 19 ions, which is based on a novel approach extending the single-ion sideband thermometry to the case of ion crystals. Finally, in chapter six, stimulated Raman transitions are used to mediate the entangling interactions and experimentally relevant aspects are discussed before the presentation of first experiments demonstrating the build-up of correlations across a 2d ion crystal interacting with a bichromatic laser field. The thesis concludes with a brief discussion and an outlook on future experiments.

Chapter 2

Foundations: Quantum optics and quantum information with trapped ions

The first report of a three-dimensional confinement of a cloud of charged aluminium and iron particles in an rf trap was published in Ref. [43] in 1959. The particles were trapped by a combination of alternating and static electric field in the first closed form of W. Paul's and M. Raether's electric mass filter [44]. Such an rf trap enabling stationary confinement in three dimensions is called a *Paul trap* and it was the starting point of trapping charged particles in *linear* Paul traps. A linear Paul trap is a specific type of rf trap, consisting of linearly extended rf electrodes generating a two-dimensional quadrupole potential along the trap axis. It is the most widely used geometry of a rf trap and the foundation of most ion trapping experiments today. Almost 30 years after the first operation of a Paul trap, in experiments under ultra-high vacuum, the first ions in crystalline form - a *Coulomb crystal* of Mg^+ and Hg^+ ions - were trapped and studied both experimentally and theoretically using numerical simulations [45, 46]. Further numerical studies of phase transitions between the amorphous and the crystalline phase of ions in a rf trap were pursued, first for 1d systems (linear strings of ions) [47] and later extended two 2d crystals [24]. In the decades following the first studies that demonstrated the control of trapped particles at both classical and spectroscopic levels, rf traps have been employed in atomic physics to investigate the properties of individual ions and ion crystals. Beyond that, over the years more emphasis was placed on the exploitation of this rich experimental platform for applications in quantum information science, where all the gained knowledge and techniques for the control of ions can be applied. A first proposal of a logic quantum gate by Cirac and Zoller in 1993 [48] tailored to trapped-ion experiments was only the beginning of what turned out to be one of the most promising and advanced frameworks for quantum computation today. In this chapter, beginning with Sec. 2.1, first the principles of operation of a linear Paul trap are explained, followed by a theoretical description of the ion motion in a rf trap and a discourse of methods for numerically calculating the classical motion of multiple trapped ions. Subsequently, in Sec. 2.4, the ions' motion is treated at a quantum

mechanical level as particles in a quantum harmonic oscillator. As we will see thereafter, the motion of the ions plays an essential role in most applications of trapped-ion systems associated with quantum information processing, quantum simulation, quantum metrology and other related fields. In Sec. 2.2, the basic concepts of quantum information science are presented followed by a review and a discussion of laser-atom interactions in Sec. 2.5. These interactions are fundamental to many of the measurements presented in this work and to many future measurements intended to be carried out in the presented apparatus. Since this work is dedicated to experiments with 2d ion crystals, the fundamentals presented here are either directly applicable to 2d crystals or are discussed separately in this context.

2.1 Trapping ions in a linear Paul trap

2.1.1 Ion motion in the time-dependent potential

Single ion

For a single ion in a rf trap with position (x, y, z) with respect to the trap center, the trapping potential V_{trap} can be divided into a dynamic rf part V_{dyn} and a static part V_{stat}

$$\begin{aligned} V_{\text{dyn}} &= \frac{U_{\text{rf}} \cos(\Omega_{\text{rf}} t)}{2} \left(\alpha_x x^2 + \alpha_y y^2 + \alpha_z z^2\right), \\ V_{\text{stat}} &= \frac{U_{\text{dc}}}{2} \left(\beta_x x^2 + \beta_y y^2 + \beta_z z^2\right), \end{aligned} \tag{2.1}$$

with the geometric factors[1] α_i and β_i and the rf and dc voltages U_{rf} and U_{dc} applied to the rf and dc electrodes, respectively. The Laplace equation $\Delta V = 0$ leads to the condition

$$\sum_i \alpha_i = \sum_i \beta_i = 0 \,, \tag{2.2}$$

which can be obeyed by various trap geometries. However, there are two prominent examples that are most commonly discussed in the literature (e.g. see Ref. [49]) and used in experiments: the hyperbolic trap and the linear Paul trap. The hyperbolic trap creates a dynamic rf confinement in all three directions whereas the linear Paul trap creates rf confinement in form of a two-dimensional quadrupole potential in x and y and a static confinement in the z-direction.

In this work, the setup of an apparatus based on a novel linear Paul trap is presented. For a better understanding of the underlying principles, we focus on the ideal linear Paul trap. A schematic of the geometry of a "classic" linear Paul trap is shown in Fig. 2.1. The trap consists of a pair of elongated (in the ideal case hyperbolic) rf electrodes, a pair of dc/ground electrodes orthogonal to the rf electrodes and two dc *endcap* electrodes arranged along the axial direction. Assuming perfectly aligned, infinitely long rf and ground electrodes, the resulting time-dependent quadrupole potential induces confining

[1] Note that here the geometric factors contain terms $1/r^2_{(\text{rf,dc})}$ with the minimum distances r_i from the trap center to the electrodes.

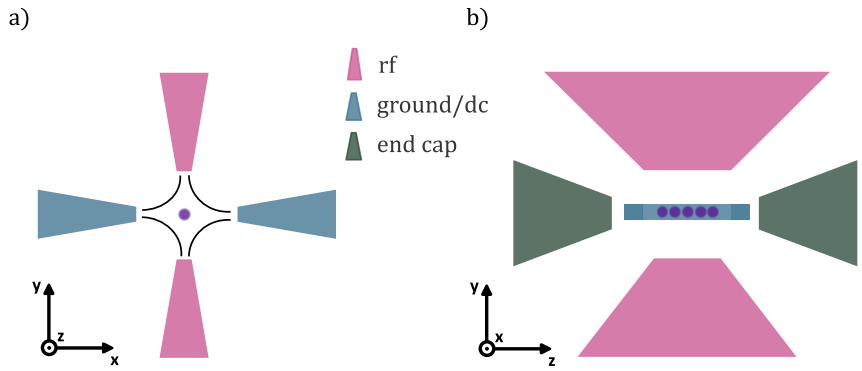

Figure 2.1: Schematic of a linear Paul trap. (a) Axial view without endcap electrodes. A single trapped ion is shown as a purple spot in the center. The electric field lines are indicated by the black lines. (b) Side view. A linear crystal of trapped ions is aligned with the trap axis (z).

forces in the $x-y$ plane and exhibits no curvature in axial (z) direction, which constitutes the trap's symmetry axis. The endcap electrodes generate a confining harmonic potential in z-direction and an anticonfining potential in the two radial directions (x and y). The relations for the geometric factors α_i and β_i for such a geometry are concluded from Eqs. (2.1) and (2.2) as

$$\begin{aligned} &\alpha_x = -\alpha_y, \;\; \alpha_z = 0, \\ &-(\beta_x + \beta_y) = \beta_z > 0 \; . \end{aligned} \tag{2.3}$$

We can now define the dimensionless parameters

$$\begin{aligned} a_{x,y} &= \frac{4QU_{\mathrm{dc}}\tilde{\beta}_{\mathrm{x,y}}}{m\Omega_{\mathrm{rf}}^2 r_{\mathrm{dc}}^2} = -\frac{1}{2}a_z, \\ q_x &= -q_y = \frac{2QV_{\mathrm{rf}}\tilde{\alpha}_x}{m\Omega_{\mathrm{rf}}^2 r_{\mathrm{rf}}^2}, \end{aligned} \tag{2.4}$$

which are typically referred to as *stability parameters* or *Mathieu q and a parameters*. Here, the geometric factors $\beta_i = \tilde{\beta}_i/\tilde{r}_{\mathrm{dc}}^2$ and $\alpha_i = \tilde{\alpha}_i/\tilde{r}_{\mathrm{rf}}^2$ are rescaled with the characteristic distances $\tilde{r}_{\mathrm{rf}}$ and $\tilde{r}_{\mathrm{dc}}$, which, for an ideal linear Paul trap, correspond to the distance from the trap axis to the rf electrodes and the distance from the trap center to the end cap electrodes, respectively. For a single ion, the e.o.m. can be transformed to the canonical form of the Mathieu equation

$$\frac{\mathrm{d}^2 r_k}{\mathrm{d}\zeta^2} + (a_k - 2q_k\cos(2\zeta))\, r_k = 0 \tag{2.5}$$

where $\zeta = \frac{1}{2}\Omega_{\mathrm{rf}}t$.

Stable solutions to these equations, which confine a trapped ion in all three spatial dimensions, can be expressed analytically [49, 50] (cf. Sec. 2.1.3 ff.). In the limit of $a_i \ll q_i \ll 1$

the equations of motion can be approximated by

$$r_k(t) = r_{0,k}\cos(\omega_k t + \phi_k)\left(1 + \frac{q_k}{2}\cos(\Omega_{\mathrm{rf}} t)\right) \text{ for } i \in \{x, y, z\}, \tag{2.6}$$

where ω_k is given by

$$\omega_k = \beta_k \frac{\Omega_{\mathrm{rf}}}{2} \quad \text{with} \quad \beta_k = \sqrt{a_k + \frac{q_k^2}{2}}\ . \tag{2.7}$$

This motion can be regarded as a composition of a harmonic oscillation at frequency ω_k and amplitude $r_{0,k}$, the *secular* motion, and a faster oscillatory modulation of the motion at frequency Ω_{rf}, called *micromotion*. The micromotion amplitude is proportional to the stability parameter q_i and the ion's distance from the trap symmetry axis (z-axis). Micromotion occurring at the equilibrium position of an ion, which might not be coincident with the potential minimum (rf-zero line), is termed *excess* micromotion. A linear chain of ions can be aligned with the rf null in order to mitigate the micromotion and thus adverse effects on the laser-ion interaction. In contrast to linear strings, a number of ions in a two-dimensional configuration is inevitably displaced from the (one-dimensional) rf null and therefore experiences micromotion that cannot be compensated. The discussion in this work is restricted to effects stemming from such excess micromotion, which will simply be denoted as *micromotion*. Residual *intrinsic* micromotion, the description of which goes beyond this simple approximation, however, is unavoidable due to the periodic displacement caused by the secular motion [51, 52]. After laser-cooling the ions to low temperatures, this modulation of the ion trajectory becomes very small and is thus negligible for most experiments. Furthermore, non-compensatable micromotion can stem from imperfections in the trap potential or a phase difference in the rf voltages applied to different electrodes [53]. However, these cases are not treated herein.

Ion crystal

For a multi-ion crystal, we now have to consider the Coulomb interaction between the ions to describe their motion accurately. We will switch to a more general notation for the expression of the potential taking the interaction of N ions into account:

$$V = V_{\mathrm{trap}} + V_{\mathrm{coul}} = \sum_{\mu=1}^{3}\sum_{i=1}^{N}\frac{\Omega_{\mathrm{rf}}}{4}(a_\mu + q_\mu\cos(\Omega_{\mathrm{rf}} t))r_{i,\mu}^2 - \frac{Z^2e^2}{8\pi\epsilon_0}\sum_{\substack{i,j=1\\ i\neq j}}^{N}\left(\sum_{\mu=1}^{3}(r_{i,\mu} - r_{j,\mu})^2\right)^{-\frac{1}{2}} \tag{2.8}$$

with $\mu \in x, y, z$. The Lagrangian for a multi-ion system including the rf part of the potential is thus given by

$$\begin{aligned} L = T - V = &\sum_{\mu=1}^{3}\sum_{i=1}^{N}\frac{m}{2}\dot{r}_{i,\mu}^2 - \sum_{\mu=1}^{3}\sum_{i=1}^{N}\frac{\Omega_{\mathrm{rf}}}{4}(a_\mu + q_\mu\cos(\Omega_{\mathrm{rf}} t))r_{i,\mu}^2 \\ &- \frac{Z^2e^2}{8\pi\epsilon_0}\sum_{\substack{i,j=1\\ i\neq j}}^{N}\left(\sum_{\mu=1}^{3}(r_{i,\mu} - r_{j,\mu})^2\right)^{-\frac{1}{2}}\ . \end{aligned} \tag{2.9}$$

Evaluating the Euler-Lagrange equation

$$\frac{\mathrm{d}}{\mathrm{d}\tau}\frac{\partial \mathcal{L}}{\partial \dot{r}_{i,\mu}} = \frac{\partial \mathcal{L}}{\partial r_{i,\mu}} \tag{2.10}$$

for Eq. (2.9) leads to the equations of motion for an ion crystal in the rf potential

$$\frac{\mathrm{d}^2 r_{i,\mu}}{\mathrm{d}\zeta^2} + \left(a_\mu - 2q_\mu \cos\left(2\zeta\right)\right) r_{i,\mu} + \sum_{\substack{j=1 \\ j\neq i}}^{N} \frac{r_{j,\mu} - r_{i,\mu}}{\left(\sum_\mu (r_{j,\mu} - r_{i,\mu})^2\right)^{\frac{3}{2}}} = 0 \tag{2.11}$$

with $\zeta = \Omega_{\mathrm{rf}} t/2$. These equations are a set of $3N$ coupled and non-linear second order differential equations, which are in general very hard or impossible to solve analytically and expensive to solve numerically, in particular for larger ion numbers. In the following sections we will discuss methods for approximating and solving the equations of motion of an ion crystal to obtain the motional mode frequencies and mode vectors.

2.1.2 Pseudopotential theory

At low temperatures, i.e. for small excursions around the equilibrium position, the rf term of the potential energy can be neglected to solve the equations of motion of an ion crystal. This procedure is often referred to as *secular* or *pseudopotential* approximation. The time-dependency of the coefficients $2q_\mu \cos(2\zeta)$ stemming from the rf nature of the potential is neglected and the ions are treated as oscillating in a purely harmonic and time-independent potential taking only the secular motion into account.

Equilibrium positions

To obtain the normal mode frequencies and mode vectors of the ions in a crystal, in a first step the potential's secular part is used to calculate their equilibrium positions. They are determined by the balance between the confining forces of the trap potential and the repulsive Coulomb forces between the ions. Within the secular approximation the potential energy of a trapped ion crystal, given here in a single dimension, is expressed as

$$V = \sum_{i=1}^{N} \frac{1}{2} M\omega^2 x_i^2(t) + \sum_{i=1}^{N} \sum_{\substack{j=1 \\ i\neq j}}^{N} \frac{Z^2 e^2}{8\pi\epsilon_0} \frac{1}{|x_i(t) - x_j(t)|}], \tag{2.12}$$

where M is the isotope mass, ω is the secular trap frequency, e is the electron charge, Z is the number of charges per ion and ϵ_0 is the vacuum permittivity. For a cold ion crystal, the position of the ith ion can be approximated by an oscillation around their equilibrium position $x_i^{(0)}$ as

$$x_i(t) = x_i^{(0)} + q_i(t), \tag{2.13}$$

where $q_i(t)$ is only a small displacement. The equilibrium positions can then be found by solving

$$\left[\frac{\partial V}{\partial x_i}\right]_{x_i = x_i^{(0)}} = 0. \tag{2.14}$$

This set of N coupled algebraic equations can be solved analytically for $N \leq 3$, while for larger values of N, a numerical solution is required.

Normal modes of motion

For a single ion the secular trapping frequencies can be approximated by

$$\omega_\mu = \beta_\mu \Omega_{\mathrm{rf}}/2 \quad \text{with} \quad \beta_\mu \approx \sqrt{a_\mu + \frac{q_\mu^2}{2}} \; . \tag{2.15}$$

The approximation of the ions' motion in a crystal, on the other hand, is more complex as the ions are coupled by their mutual Coulomb interactions. Using the pseudopotential approximation, the equations of motion can be linearized and consequently decouple into radial and axial modes in case of a linear string [54] or into in-plane and out-of-plane (OOP) modes of motion in a planar ion crystal, where the ions' displacement is restricted to the corresponding axes or planes.

Following Refs. [54] and [55], the coupled equations of motion can be described by the Lagrangian

$$\begin{aligned} L = T - V = & \frac{m}{2} \sum_{\mu=1}^{3} \sum_{i=1}^{N} \left(\dot{q}_{\mu,i}^2 - \omega_\mu^2 \left(x_{i,\mu}^{(0)} + q_{i,\mu} \right)^2 \right) \\ & - \frac{Z^2 e^2}{8\pi\epsilon_0} \sum_{\substack{i,j=1 \\ i \neq j}}^{N} \left(\sum_{\mu=1}^{3} \left(\left(x_{i,\mu}^{(0)} + q_{i,\mu} \right) - \left(x_{j,\mu}^{(0)} + q_{j,\mu} \right) \right)^2 \right)^{-\frac{1}{2}} , \end{aligned} \tag{2.16}$$

where $\mu \in (1,2,3)$ corresponds to the coordinates (x,y,z). A Taylor series expansion around the equilibrium positions yields

$$\begin{aligned} L = & \frac{m}{2} \sum_{\mu=1}^{3} \sum_{i=1}^{N} \left(\dot{q}_{\mu,i}^2 \right) - V_0 - \sum_{\mu=1}^{3} \sum_{i=1}^{N} \left[\frac{\partial V}{\partial x_{i,\mu}} \right]_{q_i=0} q_{i,\mu} \\ & - \sum_{\mu,\nu=1}^{3} \sum_{\substack{i,j=1 \\ i \neq j}}^{N} \left[\frac{\partial^2 V}{\partial x_{i,\mu} \partial x_{j,\nu}} \right]_{q_i=q_j=0} q_{i,\mu} q_{j,\nu} + \mathcal{O}(q_{\mu,i}^3) \; , \end{aligned} \tag{2.17}$$

while taking only up to second order terms in $q_{i,\mu}$ into account. Calculating the partial derivatives explicitly yields

$$\left. \frac{\partial V}{\partial x_{i,\mu}} \right|_{x_{i,\mu}^{(0)}} = \beta_\mu^2 x_{i,\mu}^{(0)} + \sum_{\substack{i=1 \\ i \neq j}}^{N} \frac{x_{j,\mu}^{(0)} - x_{i,\mu}^{(0)}}{|x_{i,\mu} - x_{j,\mu}|^3} \tag{2.18}$$

$$\left. \frac{\partial^2 V}{\partial x_{i,\mu} \partial x_{j,\nu}} \right|_{x_{i,\mu}^{(0)}} = \delta_{ij} \delta_{\mu\nu} \beta_\mu^2 + \sum_{\substack{k=1 \\ k \neq i}} \frac{\delta_{kj} - \delta_{ij}}{|x_{i,\mu} - x_{k,\mu}|^3} \left(\delta_{\mu\nu} - 3 \frac{(x_{i,\mu}^{(0)} - x_{k,\mu}^{(0)})(x_{i,\nu}^{(0)} - x_{k,\nu}^{(0)})}{|x_{i,\mu} - x_{k,\mu}|^3} \right) \; . \tag{2.19}$$

The constant term V_0 is not contributing to the dynamics of the system and can be neglected. Furthermore, for ions in the crystalline phase, the first derivative Eq. (2.18) is zero (cf. condition for equilibrium positions Eq. (2.14)) resulting in a set of linear, coupled equations of motion

$$\ddot{x}_{i,\mu} = -\sum_{j=1}^{N}\sum_{\nu=1}^{3} \left.\frac{\partial^2 V}{\partial x_{i,\mu}\partial x_{j,\nu}}\right|_{x_{i,\mu}^{(0)}} x_{j,\nu} \ . \tag{2.20}$$

To obtain the normal modes of motion the Hessian matrix $H^{(1)} \equiv \left.\frac{\partial^2 V}{\partial x_{i,\mu}\partial x_{j,\nu}}\right|_{x_{i,\mu}^{(0)}}$ of size $(3N \times 3N)$ is diagonalized as $H^{(1)} = PDP^T$, with D being a diagonal matrix containing the $3N$ normal mode (angular) frequencies and P being an orthogonal matrix containing the $3N$ mode vectors $b_i^{(p)}$ of the pth mode:

$$D = \mathrm{diag}(\omega_1^2, \ \ldots \ , \omega_{3N}^2) \ \text{ and } \ P = \left[b^{(1)} \ldots \ b^{(3N)}\right] \ . \tag{2.21}$$

The matrix $H^{(1)}$ is a real, symmetric, and positive definite matrix and therefore its eigenvalues $\mu_p = \omega_p^2$ must be real and non-negative. The eigenvectors $b_i^{(p)}$ (mode vectors) form an orthonormal basis set expressed by

$$\sum_{i,\mu} b_{i,\mu}^{(p)} b_{i,\mu}^{(q)} = \delta_{pq}, \ \ \sum_{i,j}\sum_{\mu,\nu} b_{i,\mu}^{(p)} b_{j,\nu}^{(p)} = \delta_{ij}\delta_{\mu\nu}, \tag{2.22}$$

and reveal the mode structure, i.e. the weights of the individual ions contributing to a particular mode with respect to a specified direction. Using the mode vectors, the normal modes can be represented by collective coordinates

$$Q_p(t) = \sum_{i,\mu} b_{i,\mu}^{(p)} q_{i,\mu}(t) \ \text{, where } 1 \le p \le N \ . \tag{2.23}$$

With these new coordinates, the Lagrangian takes on the form

$$L = \frac{m}{2}\sum_{p=1}^{3N}\left(\dot{Q}_p^2 - \omega_p^2 Q_p^2\right) \tag{2.24}$$

and the equations of motion represent a set of uncoupled ODEs

$$\ddot{Q}_p + \omega_p^2 Q_p = 0 \ . \tag{2.25}$$

Within this approximation, the normal modes are completely independent of each other and the collective motion of the ions in a crystal can be regarded as a linear combination of the $3N$ normal modes.

It is worth noting that there are three modes, where all ions oscillate synchronously with equal amplitude along one of the three principal axes ($\hat{e}_\lambda$). These modes are the so-called center-of-mass (COM) modes as they are the only modes, where the crystal's center of mass is moving. The COM modes are the equivalent of the secular frequencies of a single trapped ion in a harmonic potential. For the three COM modes, there is a simple expression for the mode vectors:

$$b_{i,\mu}^{COM_\lambda} = \frac{1}{\sqrt{N}}\hat{e}_\lambda \ . \tag{2.26}$$

Within the secular approximation, deviations from the true motional frequencies can occur and methods considering the time dependency of the full rf potential might be more suitable. One of these methods, the Floquet-Lyapunov approach [56, 57], is discussed in Appendix A, which solves a set of coupled Mathieu equations taking the full rf dynamics into account (see Sec. 2.1.4).

Mode cross coupling

Third-order and higher terms in q_μ containing non-linearities, which have been neglected in Eq. (2.17), represent a cross-coupling between modes of motion, in case of a 2d crystal between modes in the in-plane (axial) and out-of-plane (radial) directions, due to Coulomb interaction between the ions. A third order term can lead to motional decoherence by *three-mode mixing*, an energy transfer between three modes of motion if a resonance condition $\omega_k = |\omega_m \pm \omega_l|$ is met, e.g. by annihilation of a phonon of a mode of higher frequency and creation of two phonons of lower frequency modes or *vice versa*. In our experiment, we have not observed any harmful effects, which we would attribute to mode-mode coupling; however, this may be subject to further investigations in the future. For the interested reader, a discussion on three-mode mixing in linear trapped-ion crystals due to this third-order term can be found in Ref. [55], where a value for the minimum trap anisotropy is derived in order to meet Fermi's golden rule. Electric field imperfections as another source of heating and decoherence due to three-mode mixing are treated in Sec. 4.1.8 of Ref. [58].

2.1.3 Periodic crystal solution - Micromotion amplitude

In Sec. 2.1.2 we have derived the equations of motion for an ion crystal in a rf trap (Eq. (2.11)). A stable solution to these equations is a π-periodic solution, with its periodicity given by the trap drive frequency Ω_{rf}. This allows for an analytical derivation of the micromotion amplitude, the steps of which we will briefly discuss based on Ref. [56].

The Fourier series of a periodic solution in dimensionless units is given by

$$r_{i,\mu}^{\pi}(\tau) = \sum_{n=-\infty}^{+\infty} B_{2n,i,\mu} e^{i2n\tau} \tag{2.27}$$

Inserting this solution into Eq. (2.11) yields a recursive relation for the coefficients $B_{2n,i,\mu}$. The Coulomb term in this relation is expanded (Taylor and Fourier) around $B_{0,i} - B_{0,j}$,

keeping only the leading order. By using $B_{2n,i,\mu} = B_{-2n,i,\mu}$ and neglecting higher order terms in q_μ (i.e. $B_{2n,i,\mu} = B_{-2n,i,\mu} \approx 0$ for $n > 1$) corresponding to higher harmonics of the rf drive frequency Ω_{rf}, it can be shown that $B_{2,i,\mu} = -\frac{q_\mu}{4} B_{0,i,\mu}$, and the periodic crystal solution can be simplified to

$$r^{\pi}_{i,\mu}(\tau) \approx B_{0,i,\mu} - \frac{q_\mu}{2} B_{0,i,\mu} \cos(2\tau). \tag{2.28}$$

Equation (2.28) describes the ions' micromotion with an amplitude of $\frac{q_\mu}{2} B_{0,i,\mu}$ around their equilibrium positions $B_{0,i,\mu}$ representing the average ion locations. The micromotion amplitude scales with the distance $B_{0,i,\mu}$ from the trap center. In an ideal linear Paul trap, to first order the micromotion in axial direction is 0 due to $q_z = 0$. In the case of the trap geometry described in this thesis, the first order micromotion occurs exclusively in vertical (y) direction and the micromotion amplitude increases with the distance from the rf null, ideally coincident with the ion crystal's center. For a more detailed discussion about micromotion in our setup, please refer to Sec. 4.3.

2.1.4 Linearization about the periodic crystal - Mathieu equation

In this section, following Refs. [56, 59], we outline the path from an ion crystal's total potential given in Eq. (2.8) to the well-known Mathieu equations, which form a set of coupled differential equations representing the equations of motion in the time-dependent rf potential. As a first step, we perform a linearization of the problem by expanding the trapping potential V (Eq. (2.8)) around the stable crystal solution (Eq. (2.28)). The Coulomb term of the total potential is expanded around $r^{\pi}_{i_\mu}(\zeta)$

$$V_{coul} = \sum_{i=1,\mu}^{N} K^{(0)}_{i,\mu}(\tau) u_{i,\mu} + \frac{1}{2} \sum_{i=1,\mu}^{N} \sum_{j=1,\mu}^{N} K^{(1)}_{i,\mu,j,\nu}(\tau) + \mathcal{O}(u^3_{i,\mu}), \tag{2.29}$$

where

$$K^{(0)}_{i,\mu}(\tau) \equiv \left.\frac{\partial V_{\mathrm{coul}}}{\partial r_{i,\mu}}\right|_{r^{\pi}_{i_\mu}(\zeta)} \quad \text{and} \quad K^{(1)}_{i,\mu,j,\nu}(\tau) \equiv \left.\frac{\partial^2 V_{\mathrm{coul}}}{\partial r_{i,\mu} \partial r_{j,\mu}}\right|_{r^{\pi}_{i_\mu}(\zeta)} . \tag{2.30}$$

Discarding higher order terms yield a set of linearized coupled equations of motion:

$$\ddot{r}_{i,\mu} + (a_\mu - 2q_\mu \cos(2\tau) r_{i,\mu} + \epsilon \sum_{j,\nu} K^{\mu,\nu}_{i,j}(\tau) r_{j,\nu} = 0 \ . \tag{2.31}$$

These equations are linearly coupled in the ion coordinates with π-periodic coefficients $K^{\mu,\nu}_{i,j}(\tau)$ in the interaction term, which is of the same order as the diagonal part. We thus expand the coefficient matrix $K^{\mu,\nu}_{i,j}(\tau)$ into its Fourier series

$$K^{\mu,\nu}_{i,j}(\tau) = (K_0)^{\mu,\nu}_{i,j} - 2(K_2)^{\mu,\nu}_{i,j} \cos(2\tau) - \ldots, \tag{2.32}$$

of which we will hereafter only use the two leading terms. With the definitions

$$A^{\mu,\nu}_{i,j} = \delta_{i,j}\delta\mu,\nu a_\mu + \epsilon (K_0)^{\mu,\nu}_{i,j} \quad \text{and} \quad Q^{\mu,\nu}_{i,j} = \delta_{i,j}\delta\mu,\nu q_\mu + \epsilon (K_2)^{\mu,\nu}_{i,j}, \tag{2.33}$$

and using dynamical variables with replaced indices $u_m \equiv r_{i,\mu}$, we can rewrite the equations of motion in vector notation in a simple form as

$$\ddot{\vec{u}} + [A - 2Q\cos(2\tau)]\,\vec{u} = 0. \tag{2.34}$$

Equation (2.34) represents linearized coupled perturbations about the π-periodic solution found in Sec. 2.1.3. It is a set of coupled Mathieu equations, the solution of which are discussed in Appendix A using Floquet-Lyapunov theory [56, 59] to obtain coordinates of decoupled linear oscillators (as in the case of normal modes using pseudopotential theory). In contrast to the secular approximation, the interaction between the ions during their motion along the periodic trajectory in the full time-dependent potential is taken into account in the expansion. Higher harmonics in the Fourier expansion (Eq. (2.32)) can be included to increase the accuracy of results.

2.1.5 Trapping 2d ion crystals

In the following section, a few general considerations regarding the trapping of 2d ion crystals are discussed. A more comprehensive analysis can be found in Refs. [60, 61]).

Trapping condition

In a highly anisotropic potential with strong confinement in the two radial directions, where $\omega_{\mathrm{rad},1} \approx \omega_{\mathrm{rad},2}$, and weak confinement in axial direction, where $\omega_{\mathrm{ax}} \ll \omega_{\mathrm{rad},\{1,2\}}$, ions can be trapped and cooled into a linear configuration aligned with the rf-zero line, ideally experiencing no micromotion. Trapping a two-dimensional crystal, on the other hand, requires a potential with one strongly confining direction orthogonal to the desired crystal plane and associated with the trap oscillation frequency ω_{s}, and two weakly confining directions with ω_{w1} and ω_{w2} ($\omega_{\mathrm{w1}} \approx \omega_{\mathrm{w2}}$) spanning the crystal plane. In Ref. [24], a condition for the formation of planar crystals is analytically derived, which, for $\omega_{\mathrm{w}} = \omega_{\mathrm{w1}} = \omega_{\mathrm{w2}}$, is given by

$$\frac{\omega_{\mathrm{s}}}{\omega_{\mathrm{w}}} > 1.23 N^{\frac{1}{4}}\ , \tag{2.35}$$

where N is the number of ions. To trap an increasing number of ions in a 2d configuration, a higher ratio between the confinement in the strong and the weak directions is required to counteract the repulsive forces between the ions. The literature presents also other scalings [23, 62–64] predicting structural phase transitions as a power-law for the number of ions $\beta_{\mathrm{crit}}(N) \propto N^{-\alpha}$ describing critical values of the trap anisotropy $\beta = (\omega_{\mathrm{ax}}/\omega_{\mathrm{rad}})^2$. These scalings, however, are similar for numbers of several tens of ions [65]. In this work, the scaling behavior is not investigated (apart from qualitative observations) and has a minor practical relevance as the two-dimensional crystals are trapped in a stable regime away from the critical point and the planarity of the crystals is verified in measurements of the micromotion across the crystal (Sec. 4.3.2).

Trap anisotropy

An anisotropic harmonic potential for trapping planar crystals in the yz-plane can be written in its quadratic form as

$$V = \frac{1}{2}\begin{pmatrix} z - z_0, & y - y_0 \end{pmatrix} A \begin{pmatrix} z - z_0 \\ y - y_0 \end{pmatrix}, \tag{2.36}$$

where $A = \begin{pmatrix} \alpha & \gamma \\ \gamma & \beta \end{pmatrix}$ is a symmetric matrix, which can be regarded as the potential's *curvature tensor*. The eigenvalues of A are proportional to the squared secular oscillation frequencies in the crystal plane ω_y^2 and ω_z^2. In turn, Eq. (2.36) can be used to determine the potential anisotropy $\xi = \omega_y/\omega_z$ by analyzing a crystal image with respect to the ion positions and calculating V from the Coulomb force components in the two directions spanning the crystal plane. Compared to spectroscopic measurements, this approach enables a much faster detection of changes in the potential curvature, e.g. caused by a modification of trap voltages.

Crystal shape - Aspect ratio and anisotropy

In an anisotropic harmonic potential with potential anisotropy $\xi = \omega_y/\omega_z$ a two-dimensional crystal takes on an elliptical shape. The ellipticity can be quantified by the crystal's aspect ratio $\zeta = a_2/a_1$, given by the ratio of the semi-major axis length a_1 and the semi-minor axis length a_2. Knowledge of ζ enables a good initial guess of the equilibrium ion positions and can be helpful for numerically simulating the ion positions in a 2d crystal. A simple relation yielding ζ from the trap oscillation frequencies does not exist. For sufficiently large ion numbers, however, we can determine the aspect ratio using a charge fluid model and calculating its shape from potential theory [66]. This relates ζ to ξ by

$$\zeta^2 \frac{K - E}{E - \zeta^2 K} = \xi^{-2}, \tag{2.37}$$

where $K = K(\sqrt{1-\zeta^2})$ and $E = E(\sqrt{1-\zeta^2})$ are complete elliptic functions of the first and second kinds [67].

In practice, the aspect ratio can be measured by calculating the covariance matrix C of the ion positions (y_i, z_i) obtained from recorded fluorescence images of the ion crystal. The aspect ratio is determined via diagonalization of C yielding $\zeta = \sqrt{\lambda_2/\lambda_1}$, where λ_1 and λ_2 are the two eigenvalues of C and $\lambda_1 \geq \lambda_2$.

2.2 Basic concepts in quantum information

In this section, foundations of quantum information theory and the essential quantum "lingo" are introduced. After a review of some of the basics in quantum theory and its representation, the universal quantum computer and its working principle are discussed before diving into quantum simulation with trapped $^{40}Ca^{+}$ ions in the subsequent sections.

2.2.1 Quantum bit

In classical computer technology, information is stored in the form of *bits*. A classic bit can be either in state "0" or state "1". It can, for example, be encoded as dc voltage levels for information processing or in the magnetic state of the surface in a hard drive or a magnetic tape for storage. In quantum information science, the smallest unit of information, analogous to a classical bit, is a *quantum bit* or short *qubit*. It represents a quantum-mechanical two-level system and can, as in the case of classical bits, be encoded in various physical platforms such as the polarization of photons, individual charges in superconducting devices or the electronic states of trapped atoms and ions to name a few. In the following, the two quantum states will be denoted as $|\uparrow\rangle$ and $|\downarrow\rangle$ or equivalently as $|0\rangle$ and $|1\rangle$. In contrast to a classical bit, which is always in either one of the two possible states, a qubit can be in a coherent superposition of the two states

$$|\psi\rangle = c_{\uparrow}\,|\uparrow\rangle + c_{\downarrow}\,|\downarrow\rangle\,, \tag{2.38}$$

representing a linear combination of the two basis states with arbitrary complex coefficients $c_{\uparrow}$ and $c_{\downarrow}$ normalized by $|c_{\uparrow}|^2 + |c_{\downarrow}|^2 = 1$. A superposition state is a fundamental concept in quantum mechanics, where a quantum object cannot only be in a single state but in multiple states simultaneously. In case of a single qubit, it can be in $|\uparrow\rangle$ and $|\downarrow\rangle$ at the same time. However, in a single-shot experiment of a qubit state one will obtain only one of the two states as a measurement outcome, which is referred to as a *projective* measurement. In order to reconstruct the superposition state, the experiment has to be repeated to sample the contributions of the two basis states, where the relative probability of their occurrences is governed by the square of the coefficients $p_{\uparrow} = |c_{\uparrow}|^2$ and $p_{\downarrow} = |c_{\downarrow}|^2$. The fact that the state has to be reconstructed from repeated measurements indicates that an infinite number of measurements would be necessary to determine the expectation value exactly. The finite number of samples of such a Bernoulli distribution leads to a measurement uncertainty that essentially follows that of a binomial distribution [68]. It is referred to as *quantum projection noise*, as *shot noise* or as the *standard quantum limit*. In its simplest form it is given by

$$\Delta p = \sqrt{\frac{p(1-p)}{N}}\,, \tag{2.39}$$

which essentially represents the standard error of the mean of a binomial distribution. It describes the uncertainty of a measurement using a population of uncorrelated qubits. Using entangled states of multiple qubits, the standard quantum limit can be undermined pushing the measurement uncertainty down to the Heisenberg quantum limit [69–71, and others].

Computational state space

The number of possible quantum states for an N-qubit system is given by the total N-qubit Hilbert space $\mathcal{H}_N$ as a tensor product of the individual Hilbert spaces $\mathcal{H}_i$:

$$\mathcal{H}_N = \mathcal{H}_i^{\otimes N} = \bigotimes_{i=1}^{N} \mathcal{H}_i = \mathcal{H}_N \otimes \mathcal{H}_{N-1} \cdots \otimes \mathcal{H}_1 \ . \tag{2.40}$$

The computational state space thus increases exponentially as 2^N with the number of qubits N.

2.2.2 Entanglement

Entanglement is another core concept of quantum mechanics and an inherent tool to the "quantum version" of computation. It is essential for the implementation of quantum gates and algorithms in quantum information processing, quantum simulation and also quantum communication and cryptography. Particles are entangled, if the quantum states of the individual particles cannot be described independently. In contrast to a pure state, an entangled quantum state cannot be decomposed into a product state

$$|\psi_N\rangle = |\psi_n\rangle \otimes |\psi_{n-1}\rangle \otimes \ldots \otimes |\psi_2\rangle \otimes |\psi_1\rangle \tag{2.41}$$

of the basis states $|\psi_n\rangle$ of its constituents. A *maximally* entangled state is a state, for which all reduced density matrices are mixed, i.e. $\mathrm{tr}\,(\rho_i) < 1$ (see Sec. 2.2.4). The most famous and simplest maximally entangled states are the four *Bell states* of a 2-qubit system

$$|\Phi^{\pm}\rangle = \frac{1}{\sqrt{2}}\left(|00\rangle \pm |11\rangle\right), \quad |\Psi^{\pm}\rangle = \frac{1}{\sqrt{2}}\left(|01\rangle \pm |10\rangle\right), \tag{2.42}$$

where the first and second entry in the *ket* vector correspond to the first and second particle. The Bell states form an orthonormal basis of its 4-dimensional Hilbert space. The outcome of a projective measurement on one of the two qubits of a Bell state determines the measurement outcome of the other qubit. This quantum correlation is the manifestation of the particles' entanglement. Another famous example of a maximally entangled state with applications in quantum metrology is the *Greenberger-Horne-Zeillinger* state [72], which in its N-dimensional form for qubits is given by

$$|\psi_{\mathrm{GHZ}}\rangle = \frac{1}{\sqrt{2}}\left(|0\rangle^{\otimes_N} + |1\rangle^{\otimes_N}\right) = \frac{1}{\sqrt{2}}\left(|0...0\rangle + |1...1\rangle\right) \ . \tag{2.43}$$

Further prominent classes of entangled states include the *Dicke* and the W states, which are mentioned only briefly here. Another form of quantum correlations, which occur in context of mixed states, is known as *quantum discord* [73–75]. The treatment of quantum discord goes beyond the scope of this thesis. However, a discussion can be found in Ref. [61] along with correlation spectroscopy experiments with many qubits, carried out in the here presented apparatus, in the presence of correlated magnetic-field noise resulting in quantum discord [76].

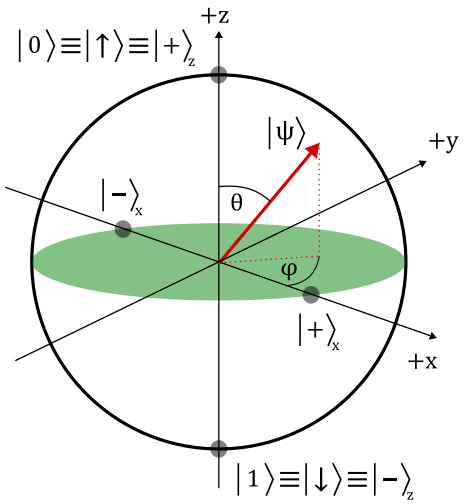

Figure 2.2: The Bloch sphere. A two-dimensional complex vector of a pure qubit state is represented on the surface of a unit sphere using spherical coordinates with the angles θ and ϕ according to Eq. (2.44). The states of the commonly used basis sets $\{|\uparrow\rangle,|\downarrow\rangle\}$ and $\{|-\rangle_x,|+\rangle_x\}$ (introduced in Sec. 2.2.5) are indicated as points on opposite sides of the sphere along with the Bloch vector of an exemplary qubit state $|\psi\rangle$. The *equatorial plane* is shown in green.

2.2.3 The Bloch sphere

The most common way to represent the state of a quantum mechanical two-level system is the *Bloch sphere*. It is a unit-2-sphere, whose north pole and south pole are defined as the states $|\uparrow\rangle = |0\rangle$ and $|\downarrow\rangle = |1\rangle$, respectively[2]. Every qubit state can be represented by a vector on or within this sphere, the so-called Bloch vector. The points on the surface are associated with the pure states of a qubit system. The points inside the Bloch sphere represent all mixed states, whose Bloch vector length is less than 1. A pure state can be written as

$$|\psi\rangle = \cos\left(\frac{\theta}{2}\right)|0\rangle + e^{i\varphi}\sin\left(\frac{\theta}{2}\right)|1\rangle\,, \tag{2.44}$$

where the two angles θ and φ can be interpreted as spherical coordinates of the Bloch sphere, which is shown in Fig. 2.2. A mixed state cannot be written in the same form as in Eq. (2.44) but it can be represented by a density matrix, the formalism of which is introduced in the next section.

2.2.4 Mixed states and the density matrix formalism

A mixed state is a state that can neither be described by a single state vector nor a simple product of pure states. It can represent either a form of a statistical ensemble of states[3] when the statistical mixture is not known, e.g. a thermalized state, or an entangled system.

[2]This aligns with the most common convention but could as well be defined conversely.
[3]Note that this is fundamentally different from a superposition of states.

In general, a quantum state can be described by a positive semi-definite, hermitian and normalized operator named *density operator*, whose representation is given by the *density matrix* ρ. The terms *operator* and *matrix*, however, are commonly used interchangeably in this context. Its properties are summarized by the following expressions:

$$\begin{aligned} \rho^\dagger &= \rho \\ \mathrm{tr}(\rho) &= 1 \\ \rho &\geq 0 \ . \end{aligned} \tag{2.45}$$

As ρ is a positive semi-definite operator, its eigenvalues λ_i are non-negative real values with $\sum_i \lambda_i = 1$. The density matrix is defined as

$$\rho = \sum_i p_i \left|\psi_i\right\rangle \left\langle\psi_i\right| , \tag{2.46}$$

where the states $|\psi_i\rangle$ form an orthonormal basis of the Hilbert space of the N-qubit system and the p_i are non-negative real values, which add up to 1. For an ensemble of pure states the coefficients p_i could be interpreted as the probability of finding a certain pure state upon a projective measurement.

The density matrix representation, as a general formalism, can describe not only mixed states but also pure states. For a pure state, ρ exhibits the following properties:

$$\begin{aligned} \rho &= \left|\psi\right\rangle \left\langle\psi\right| \\ \rho^2 &= \rho \\ \mathrm{tr}(\rho^2) &= P(\rho^2) = 1 \ . \end{aligned} \tag{2.47}$$

The density matrix can be written as an outer product of a pure state vector $|\psi\rangle$ with itself. The trace of the squared density matrix $\mathrm{tr}\,(\rho^2)$ is called *purity* of the system and is 1 only for a pure state. In general, it can take values on $P \in [\frac{1}{2^N}, 1]$, where $P = \frac{1}{2^N}$ corresponds to a fully mixed state.

To clarify the difference between a statistical mixture of states and a superposition, let us look at the example of a system, which is prepared to be in state $|\psi_1\rangle = \begin{pmatrix} 1 \\ 0 \end{pmatrix}$ and $|\psi_2\rangle = \begin{pmatrix} 0 \\ 1 \end{pmatrix}$ with equal probability. The resulting mixed state is a statistical mixture of the two states represented by

$$\rho = \frac{1}{2}\begin{pmatrix} 1 & 0 \\ 0 & 0 \end{pmatrix} + \frac{1}{2}\begin{pmatrix} 0 & 0 \\ 0 & 1 \end{pmatrix} = \begin{pmatrix} 1 & 0 \\ 0 & 1 \end{pmatrix} . \tag{2.48}$$

On the other hand, the density matrix for a superposition of the two states $|\psi\rangle = \frac{1}{\sqrt{2}}(|\psi_1\rangle + |\psi_2\rangle)$ is given by

$$\rho = \left|\psi\right\rangle \left\langle\psi\right| = \frac{1}{2}\begin{pmatrix} 1 & 1 \\ 1 & 1 \end{pmatrix} , \tag{2.49}$$

representing a pure state.

The expectation value of an observable A of a quantum state $|\psi\rangle$ is given by

$$\langle A\rangle = \langle\psi| A |\psi\rangle , \tag{2.50}$$

which, in the density matrix formalism, is replaced by

$$\langle A\rangle = \mathrm{tr}(\rho A) . \tag{2.51}$$

From Eqs. (2.46) and (2.47), we can see that a mixed state can be written as a convex sum of pure state density matrices weighted by the probabilities p_i. The expectation value of a mixed state can then be regarded as the sum of expectation values of the constituent pure states weighted by the probabilities p_i:

$$\langle A\rangle = \sum_i p_i \,\mathrm{tr}(\rho A) . \tag{2.52}$$

Partial trace of a multi-particle system

Working with multi-particle systems in quantum information science, it is sometimes useful to look at the properties of only a subsystem of the composite state. This can be done by taking the partial trace of a subsystem. A multi-particle system is given by the tensor product of the constituent parts, e.g. for a two-particle system with particles A and B by

$$\rho_{AB} = \rho_A \otimes \rho_B, \tag{2.53}$$

analogous to the construction of its Hilbert space via Eq. (2.40). The partial trace of the subsystem A is then given by

$$\mathrm{tr}_A(\rho_{AB}) = \sum_i \left(\langle i|_A \otimes \mathbb{1}_B\right) \rho_{AB} \left(|i\rangle_A \otimes \mathbb{1}_B\right) = \rho_B, \tag{2.54}$$

where $|i\rangle_A$ is an orthonormal basis of the Hilbert space of subsystem A and $\mathbb{1}_B$ is the identity matrix acting only on subsystem B. This way, the subsystem A can be *traced out* enabling the study of properties of the subsystem B.

2.2.5 Pauli representation

A common way of representing a quantum state involves the Pauli operators and its eigenstates. The Pauli matrices are given by

$$\sigma_0 = \begin{pmatrix} 1 & 0 \\ 0 & 1 \end{pmatrix}, \ \sigma_x = \sigma_1 = \begin{pmatrix} 0 & 1 \\ 1 & 0 \end{pmatrix}, \ \sigma_y = \sigma_2 = \begin{pmatrix} 0 & i \\ -i & 0 \end{pmatrix}, \ \sigma_z = \sigma_3 = \begin{pmatrix} 1 & 0 \\ 0 & -1 \end{pmatrix}, \tag{2.55}$$

where the identity matrix $\mathbb{1}$ is denoted as σ_0. The 2×2-dimensional Pauli matrices are Hermitian and, together with the identity matrix, form a basis of the qubit's complex two-dimensional Hilbert space on $\mathbb{C}^2$. Every other Hermitian matrix can thus be decomposed into a linear combination of the Pauli matrices. The two-level system of a qubit, e.g. given

by two well-defined electronic energy levels in a trapped ion, is well described by the Pauli operators, analogous to a spin-1/2 system with the two qubit states being defined as spin-up and spin-down states. A qubit is therefore also referred to as a *pseudospin* - in particular in the context of quantum simulation. The Pauli matrices in the anti-Hermitian form of $\{\frac{i\sigma_m}{2}\}$ form a basis of the Lie algebra $\mathfrak{su}(2)$ and the exponentials of the linear combinations $e^{i\sum_m \alpha_m \sigma_m}$ are generators of the special unitary group SU(2) describing spin-1/2 systems.

In the Pauli basis the two qubit states are defined as

$$|0\rangle = |\uparrow\rangle = |+\rangle_z = \begin{pmatrix} 1 \\ 0 \end{pmatrix} \text{ and } |1\rangle = |\downarrow\rangle = |-\rangle_z = \begin{pmatrix} 0 \\ 1 \end{pmatrix} , \tag{2.56}$$

which are eigenvalues of the Pauli-z operator. In this case the z-axis is thereby determined as the quantization axis. The eigenvectors of σ_x and σ_y correspond to vectors along the two orthogonal directions w.r.t. the z-axis and are denoted as

$$\begin{aligned} |+\rangle_x &= \frac{1}{\sqrt{2}}(|+\rangle_z + |-\rangle_z), \; |-\rangle_x = \frac{1}{\sqrt{2}}(|+\rangle_z - |-\rangle_z), \\ |+\rangle_y &= \frac{1}{\sqrt{2}}(|+\rangle_z + i\,|-\rangle_z), \; |+\rangle_y = \frac{1}{\sqrt{2}}(|+\rangle_z - i\,|-\rangle_z) \; . \end{aligned} \tag{2.57}$$

In the Pauli representation the Bloch vector r_B is simply given by the vector of expectation values for each Pauli operator $a = (\langle\sigma_x\rangle, \langle\sigma_z\rangle, \langle\sigma_z\rangle)$.

2.2.6 Quantum state tomography

In order to apply the density matrix formalism in practice, we also need to define a set of operators forming an orthonormal basis of the Hilbert space to construct a density matrix as in Eq. (2.46). Most commonly, the states are defined in the Pauli basis with the Pauli operators σ_i, such that the density matrix of a single qubit can be written as

$$\rho = \frac{1}{2}\left(\mathbb{1} + \vec{n}.\vec{\sigma}\right), \text{ where } \; \vec{n} = \begin{pmatrix} \langle\sigma_x\rangle \\ \langle\sigma_y\rangle \\ \langle\sigma_z\rangle \end{pmatrix} \text{ and } \vec{\sigma} = \begin{pmatrix} \sigma_x \\ \sigma_y \\ \sigma_z \end{pmatrix} , \tag{2.58}$$

From this equation, we can see that the reconstruction of a single qubit state requires the measurement of the expectation values $\langle\sigma_i\rangle$ of all three Pauli operators. This approach can be extended to multi-qubit systems, for which we find a new orthonormal set of measurement projectors as $\langle\sigma_i^{\otimes N}\rangle$. As an example: For a two-qubit system, the operators for a measurement of $\langle\sigma_z^{(1)}\rangle\langle\sigma_z^{(2)}\rangle$ are $|00\rangle\langle 00|, |01\rangle\langle 01|, |10\rangle\langle 10|, |11\rangle\langle 11|$ with the corresponding observables $\langle\mathbb{1}\mathbb{1}\rangle, \langle\mathbb{1}\sigma_z\rangle, \langle\sigma_z\mathbb{1}\rangle, \langle\sigma_z\sigma_z\rangle$. Together with measurements of $\langle\sigma_x^{(1)}\rangle\langle\sigma_x^{(2)}\rangle$ and $\langle\sigma_y^{(1)}\rangle\langle\sigma_y^{(2)}\rangle$, a complete set of 3^N measurements is performed. This is the principle of quantum state tomography. A more detailed discussion about the quantification of quantum states and processes can for instance be found in Ref. [77]. Although a full tomography is still considered the gold standard of quantum state measurements, there is a large interest in alternative methods, in particular for the reconstruction of large entangled states since the number of required measurements is scaling unfavorably with

the number of qubits ($\propto 3^N$). For future experiments, which will be carried out with the apparatus presented in this theses, this will be of particular importance as it aims at quantum simulation with large qubit numbers on the order of hundreds of ions.

2.2.7 The universal quantum computer

The exploitation of quantum-mechanical phenomena like superposition and entanglement within the framework of an exponentially growing computational state space makes a quantum computer potentially extremely powerful and efficient compared with classical computers. In particular, it can be a superior architecture to solve specific tasks like searching unsorted databases (Grover's quantum search algorithm [78]), factoring prime numbers (Shor's algorithm [79]) or solving quantum many-body problems. These are some of the most prominent examples of applications. However, there are many other tasks, which a quantum computer could be beneficial for, the discussion of which would go beyond the scope of this work.

The requirements to realize a *universal* quantum computer are famously stated in Ref. [80], where DiVincenzo defines the following five criteria:

1. A scalable physical system with well-characterized qubit
2. The ability to initialize the qubit state to a simple fiducial state
3. Long relevant coherence times (in relation to the quantum gate times)
4. A universal set of quantum gates
5. A qubit-specific measurement capability

All criteria can be met by a $^{40}Ca^{+}$-based trapped-ion apparatus, which is described in more detail for this particular platform in Ref. [81]. Apart from the requirement of a universal set of gates, which is discussed subsequently, the DiVincenzo criteria also apply to a quantum simulation apparatus.

2.2.8 Quantum gates

As stated by DiVincenzo, a quantum computer requires a universal set of quantum gates. In a classical computer, information is processed in electronic circuits which implement logic gates using transistors. The classical states of a bit, 0 and 1, are encoded in low and high DC voltage levels. The logic gates are changing the input values of a bit according to a truth table and return an output value. Examples for such gates are the AND, OR, XOR gates and its negated versions NAND, NOR and XNOR as well as the NOT gate. These logic gates typically act on one or two bits. Multiple gates can be combined to create more complex logical circuits such as flip-flops and latches.

Analagous to the classical gates and circuits, a quantum circuit is composed of quantum (logic) gates, which apply a certain algebra to the input qubit states. Quantum gates operators are represented by $2^N \times 2^N$ unitary matrices acting on N qubits. As in the case of classical gates, however, most quantum gates act only on one or two qubits, which

are the building blocks for more complex circuits effectively acting on a larger number of qubits.

There is a large number of different quantum gates. However, there is a manageable number of gates that are commonly used in the field. A few examples of them are given in the following.

Single-qubit gates

Examples for single-qubit gates are:

Pauli-X (X), Pauli-Y (Y), Pauli-Z (Z): $\{X, Y, Z\} = \sigma_{\{x,y,z\}}$, Hadamard: $\mathrm{H} = \frac{1}{\sqrt{2}}\begin{bmatrix} 1 & 1 \\ 1 & -1 \end{bmatrix}$,
Phase gate: $\mathrm{P} = \begin{bmatrix} 1 & 0 \\ 0 & i \end{bmatrix}$, Phase shift gate : $\mathrm{P}(\phi) = \begin{bmatrix} 1 & 0 \\ 0 & e^{i\phi} \end{bmatrix}$.

In addition to these gates we can define arbitrary single-qubit rotations on the Bloch sphere using rotations about the three basis directions $\{x, y, z\}$:

$$U_{\{x,y,z\}}(\theta) = e^{-iR_{\{x,y,z\}}} = e^{-i\frac{\theta}{2}\sigma_{\{x,y,z\}}} \tag{2.59}$$

Using the rotations about the basis directions, we can represent an effective rotation about an arbitrary axis $\vec{n} = (n_x, n_y, n_z)$ by

$$R_{\vec{n}(\theta)} = e^{-i\frac{\theta}{2}\vec{n}\vec{\sigma}} = \cos\left(\frac{\theta}{2}\right)\mathbb{1} - i\sin\left(\frac{\theta}{2}\right)(n_x\sigma_x + n_y\sigma_y + n_z\sigma_z) \ . \tag{2.60}$$

Furthermore, using Euler's rotation theorem, this rotation can be expressed as concatenated rotations about only two axes of the form

$$R_{\vec{n}(\theta)} = e^{i\phi}R_z(\alpha)R_x(\beta)R_z(\gamma) \ , \tag{2.61}$$

which is a sequence of three rotations about the $z-$ and x-axes by the angles (α, β, γ). The term $e^{i\phi}$ is only changing the global phase of the wave function and can therefore be ignored. The global phase of a state is not an observable and does not change the measurable properties of the system. In order to perform arbitrary rotations in a trapped-ion experiment, one commonly makes use of combining clockwise rotations about the z-axis and rotations about an arbitrary perpendicular axis in the xy-plane defined by the angle ϕ. These rotations can be written as

$$\begin{aligned} U(\theta, \phi) = e^{-i\frac{\theta}{2}\sigma_\phi} &= \begin{pmatrix} \cos\frac{\theta}{2} & -ie^{-i\phi}\sin\frac{\theta}{2} \\ -ie^{i\phi}\sin\frac{\theta}{2} & \cos\frac{\theta}{2} \end{pmatrix} \ , \\ U_z(\theta) = e^{-i\frac{\theta}{2}\sigma_z} &= \begin{pmatrix} e^{-i\frac{\theta}{2}} & 0 \\ 0 & e^{i\frac{\theta}{2}} \end{pmatrix} \ , \end{aligned} \tag{2.62}$$

where $\sigma_\phi = \cos(\phi)\sigma_x + \sin(\phi)\sigma_y$. For a light field interacting with an ion, the angles θ and ϕ are determined by the interaction length (pulse length) and the phase of the laser beam.

Note that in the algebra of SU(2) rotations, a rotation of $\theta = 4\pi$ is required to return to the initial state including the phase. For the global phase of a system, however, this has no practical effect since the global phase drops out in a measurement of the expectation value of an operator A given by $\langle\psi| A |\psi\rangle$. However, at this point it should be emphasized that the relative phases, i.e. phase differences between the individual qubit states, are at the core of quantum information experiments and are of utmost importance for any quantum measurements involving multiple qubits.

Multi-qubit gates

As stated in the previous section a universal set of quantum gates is required to realize a quantum computer. A universal gate set is composed of a finite number of gates, which can reproduce any other unitary operation by a sequence of those gates[4]. In principle, there are infinitely many universal sets and all sets containing a universal gate set as a subset are also universal. For the sake of completeness, although not relevant to the presented work, the most famous two- and three-qubit gates shall be mentioned briefly, which are the controlled-NOT, the Mølmer Sørensen (MS), the SWAP and the iSWAP gate as two-qubit gates and the Toffoli as a 3-qubit gate. Examples for universal gate sets are {CNOT,$R_z(\theta)$, $R_\phi(\theta,\phi)$}, {MS,$R_z(\theta)$,$R_\phi(\theta,\phi)$}, {CNOT,H,S,T} and {Toffoli,H}. Probably the most prominent two-qubit gate and the first one ever realized experimentally in trapped ion systems [9] is the controlled-NOT gate, also known as Cirac-Zoller gate [48], which is given by

$$\mathrm{CNOT} = \begin{bmatrix} 1 & 0 & 0 & 0 \\ 0 & 1 & 0 & 0 \\ 0 & 0 & 0 & 1 \\ 0 & 0 & 1 & 0 \end{bmatrix}.$$

In this work, however, we will focus on a setup targeting quantum simulation of many-body physics. In these experiments, we give up on a universal set of quantum gates and instead focus on global entangling interactions acting on all qubits simultaneously in combination with single-qubit rotations. In Innsbruck's quantum computers, the most used native gate set consists of arbitrary single-qubit rotations combined with two-qubit MS gates realized by a bichromatic laser-ion interaction. In the apparatus presented here, the most relevant operation is an MS-like interaction based on a bichromatic drive used to implement global spin-spin interactions of the form $H \propto \sigma_x\sigma_x$ in a multi-qubit system. These interactions are discussed in more detail in Secs. 2.5.4 ff.

2.3 Quantum simulation

As the computational state space for a quantum-mechanical system under study corresponds to the Hilbert space of the N-particle system, the storage of an arbitrary quantum

[4] It is actually not possible to realize all possible (infinite) unitaries with a finite sequence of the universal gates but it is shown that any quantum operation on a finite number of qubits can be approximated efficiently by such a sequence [82]

state of N particles requires a memory for 2^N complex coefficients. This is already extremely demanding for a few tens of particles and for $N = 100$ exceeds the whole world's storage capacity by far [83]. Now, many systems of interest like larger chemical compounds or bio-molecules, or the bulk of a complex material, consist of many hundreds or thousands of atoms. Thinking about quantum-mechanical calculations of such systems and their time evolution requiring operations with $2^N \times 2^N$ matrices, the complexity of such computations on a classical computer becomes obvious. In practice, exact quantum-mechanical calculations (without the use of approximation techniques) of systems with many tens of particles are already out-of-reach for the world's most powerful computers. Therefore, the idea of "simulating" quantum mechanical problems on a controllable quantum device was born several decades ago. A quantum simulator is a special-purpose device, whose purpose is to emulate a quantum-mechanical system of interest by evolving the quantum simulator's state under the unitary $U = e^{-i/\hbar H_{\mathrm{sim}}}$. The general idea is to find a one-to-one correspondence $H_{\mathrm{th}} \leftrightarrow H_{\mathrm{sim}}$ between the Hamiltonian of interest H_{th} and the Hamiltonian implemented in the quantum simulator H_{sim}. The approach of mapping a quantum system of interest onto a controllable quantum device to study its dynamics goes back to Richard Feynman in the early 1980s [4], who was one of the first persons to propose the idea of a quantum computer. He famously suggested to use a computer built of elements obeying the laws of quantum mechanics to simulate a quantum mechanical problem. This is still the core concept of quantum simulation today, in particular of analog quantum simulation. In contrast to analog quantum simulation, *digital* quantum simulation is related more closely to the concept of quantum computation whereas *variational* quantum simulation is a recently established approach referring to hybrid quantum-classical algorithms incorporating classical optimization based on variational principles. Along with a schematic illustration in Fig. 2.3, these three variants of quantum simulation are described briefly in the following paragraphs. Comprehensive reviews discussing quantum simulation using trapped ions as well as other platforms can be found in [84–86].

Analog quantum simulation

In contrast to to a universal quantum computer, an analog quantum simulator does not use a circuit of "logic" quantum gates to solve a problem. In analog quantum simulation, the implemented gate itself - typically an interaction acting globally on the multi-particle quantum system - corresponds to the Hamiltonian one would like to study. The many-body Hamiltonian under investigation is imprinted onto the interacting particles in the quantum simulator. Precise control over the experimental parameters, e.g. the laser parameters (detuning, power, phase, etc.) in case of a trapped-ion machine, allows for engineering the interaction to approximate the Hamiltonian of interest. A standard experimental sequence typically consists of the initial state preparation, the time evolution of the (entangling) interactions emulating the model of interest, and a final measurement of the quantum state. The class of problems, that a quantum simulator can solve, is typically very limited. In trapped-ion devices, the native interactions are Ising-type interactions, which are realized by global Mølmer-Sørensen-like gates, enabling the study of quantum spin models. For the simulation of other classes of Hamiltonians, digital or variational quantum simulation can be employed (see following paragraphs).

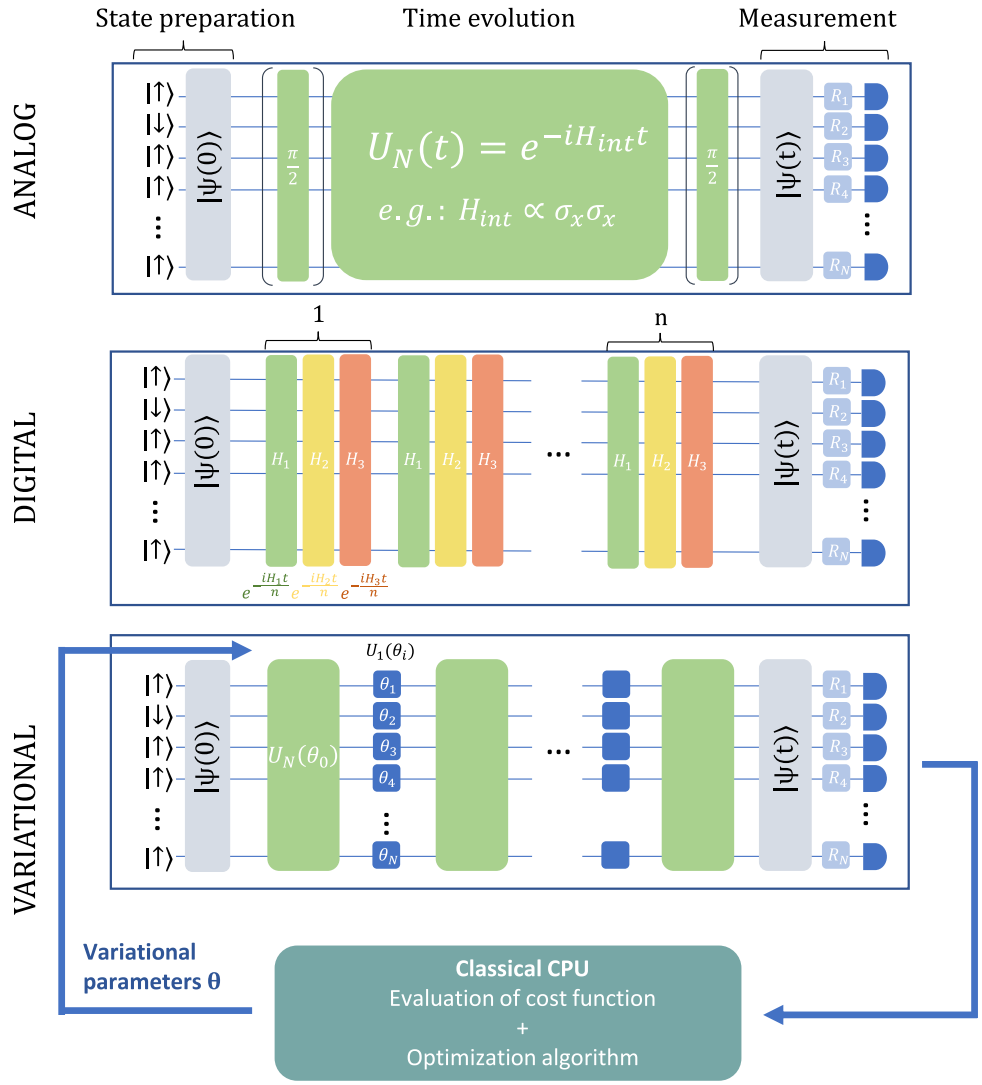

Figure 2.3: Basic schemes of analog, digital and variational quantum simulation. After encoding an N-qubit quantum state to a physical set of qubits (state preparation), the actual quantum circuit (time evolution) is applied. At the end of the circuit, the quantum state is read out via a qubit-resolved measurement. (a) In analog quantum simulation, the initial state is typically evolving freely under an interaction Hamiltonian for a defined time t creating a 1:1-correspondence between the model of interest and the interaction Hamiltonian H_{int} applied to the physical system. (b) In a digital quantum simulation, the Hamiltonian of interest is decomposed into a sum of local Hamiltonians ($H = \sum_i H_i$). Via *Trotterization* the time evolution is expanded into n time steps, where the local operations H_i are applied for the time t/n. These local operations are realized by a universal set of single- and multi-qubit gates. (c) In the variational approach, a classical CPU serves to solve an optimization problem by exploring the parameter space with the help of a quantum processor. In the quantum simulator the initial state is prepared according to a set of parameters θ_i, which are fed back from the optimization algorithm. The new state evolves under a Hamiltonian of interest, e.g. to find the ground-state of the system, and is then evaluated anew by the classical machine.

In the last 15 years, great efforts have been made to promote the field of analog quantum simulation. The most advanced experiments have been realized in Rydberg atom arrays with several tens to up to 200 atoms [87,88], in arrays of hundreds of neutral atoms trapped in optical lattices [89,90] as well as in trapped-ion systems with hundreds of ions in Penning traps (so far lacking control of individual ions) [11,91] and with a few tens to up to about 50 ions in rf traps [19, 22, 92, 93]. As a full-fledged general-purpose quantum computer would be able to solve and simulate all flavors of quantum-mechanical models, analog quantum simulation might seem to be a redundant tool to study very specific problems only. This holds true in a scenario where matured quantum computers are readily available, which is not the case yet. Nowadays, we are entering the so-called *NISQ era*, where *NISQ* stands for *noisy intermediate-scale quantum*, a term introduced by John Preskill in 2018 [7]. It describes the intermediate phase before the age of fault-tolerant large-scale quantum computing[5], but during which high-fidelity control of fifty to hundreds of qubits is feasible - a number, which is already useful for solving certain problems beyond the reach of classical supercomputers. As of today, quantum simulators with such a large number of qubits do not feature the highest fidelities in their quantum operations and, thus, cannot compete with devices developed specifically for high-fidelity quantum information processing with a small number of qubits. However, by sacrificing the gate fidelity to a certain degree, the employment of 50-100 qubits enables the exploration of many interesting systems that are classically intractable, including spin crystals or quantum chemistry simulations. The systems of interest, however, should be robust to small sources of error. Therefore, analog quantum simulators are primarily well-suited for the investigation of so-called *universal properties*, that are less susceptible to small imperfections.

Digital quantum simulation

A digital quantum simulator is an actual gate-based universal quantum computer, which can be used not only for general-purpose quantum information processing but also to simulate any kind of physical system. In digital quantum simulation experiments a Hamiltonian of interest H_{sys} is simulated by a sequence of suitable quantum gates. To translate the system of interest into a sequence of gates, we write the Hamiltonian as a sum of local Hamiltonians $H_{\mathrm{sys}} = \sum_i H_i$ acting only locally on a subset of qubits. For commuting local operations $[H_i, H_j] = 0$, the unitary time evolution operator of the total system Hamiltonian can be given as a product of local unitaries H_i

$$U(t) = e^{-i/\hbar H_{\mathrm{sys}} t} = e^{-i/\hbar \sum_i H_i t} = \prod_i e^{-i/\hbar H_i t} \ . \tag{2.63}$$

In this case the system Hamiltonian can be implemented exactly by a sequence of local gates acting on single or multiple qubits. In the general case, the Hamiltonian of interest cannot be composed of commutating local Hamiltonians only. However, the system Hamil-

[5] As of the present date, the timeline for achieving fault-tolerant large-scale quantum computing remains completely uncertain.

tonian of interest H_{sys} can be approximated using the *Trotter* expansion (*Trotterization*)

$$U(t) = e^{-i/\hbar H_{\text{sys}} t} = e^{-i/\hbar \sum_i H_i t} = \lim_{n\to\infty} \left[\prod_i e^{-i/\hbar H_i t/n} \right]^n , \tag{2.64}$$

where $n \in \mathbb{N}$ is the number of steps in the time evolution. Each time step consists of a sequence of local gates. Since the commutation relation does not hold for local gates, the total time evolution is divided into subsets of sequences applied for a time t/n. These subsets are called Trotter steps and for infinitely small time steps ($n \to \infty$), expression (2.64) is exact. Conversely: The coarser the time steps, the bigger the error. In order to simulate a complex system with a large number of qubits, a large number of Trotter steps and, thus, a large number of gates, is required to approximate it well, which in turn necessitates a high fidelity of the applied gate operations to avoid error accumulation during long sequences. This leads to the conclusion that digital quantum simulation of large systems requires fault-tolerant quantum computation in the first place pointing to analog and variational quantum simulation as the potentially more promising candidates for scientific gain in quantum simulation for the upcoming years of the NISQ era.

Variational quantum simulation

Variational quantum simulation (VQS) is a recent development in the field of quantum simulation. It is based on the idea of having a hybrid quantum-classical loop between a quantum (co-)processor and a classical computer to solve an optimization problem given a certain cost function. Such a hybrid quantum-classical machine is often termed *variational quantum eigensolver* (VQE). This approach was first introduced using an integrated photonics circuit in Ref. [94] and further developed in Ref. [95]. In these and subsequent experiments it was primarily used to solve problems in quantum chemistry, such as finding ground-state energies [94] and determining the transition frequencies of molecules [96]. Using a trapped-ion quantum simulator, VQS was established as an alternative approach to digital and analog simulation in Ref. [8], where it was employed to determine the ground state of a lattice Schwinger model, a model used in high-energy physics. In such a variational quantum simulation, the Hamiltonian of the spin lattice model does not have to be physically realized in the laboratory system but it exists only as a measurement prescription in the form chains of Pauli operators, which are applied in the "quantum part" of these hybrid experiments. This is crucial as it opens up the possibility to study models that would otherwise be out of reach in analog or digital quantum simulation. The general idea of such a hybrid scheme is outlined as follows: Using an *ansatz* set of quantum states, a state $\langle\psi(\boldsymbol{\theta})|$ is prepared in the quantum simulator. The expectation value of the Hamiltonian under study $\langle\psi(\boldsymbol{\theta})| H_{\text{sys}} |\psi(\boldsymbol{\theta})\rangle$, representing the cost function, is then measured and parsed to the classical computer. In a classical optimization algorithm (e.g. a *dividing rectangles* (DIRECT) algorithm in Ref. [8]) new parameters are chosen with the goal of minimizing the cost function. The parameters are fed back to the quantum simulator, which prepares the new state and measures the cost function again. This loop is repeated until the value of the cost function converges. In this way the costly operation of finding the expectation value of a potentially highly entangled state is performed by the

quantum machine whereas the fast and efficient (gradient-free) optimization algorithm is carried out by the classical computer.

2.4 Quantized motion

2.4.1 Quantum harmonic oscillator

In Sec. 2.1.2 the trapping potential is approximated by a harmonic (pseudo)potential allowing to describe the ions as coupled harmonic oscillators. In a quantum mechanical treatment of the harmonic oscillator, the classical position and momentum coordinates x_i and p_i are replaced by their quantum mechanical operators $\hat{x}_i$ and $\hat{p}_i = -i\hbar\frac{\partial}{\partial x_i}$. These operators obey the canonical commutation relations

$$\begin{aligned} [\hat{x}_i, \hat{p}_j] &= i\hbar\delta_{i,j}, \\ [\hat{x}_i, \hat{x}_j] &= 0, \\ [\hat{p}_i, \hat{p}_j] &= 0. \end{aligned} \tag{2.65}$$

The Hamiltonian describing a single particle of charge q in a quantum harmonic oscillator is given by

$$H = \sum_{i=1}^{3} \frac{\hat{p}_i^2}{2m} + \frac{1}{2}m\omega^2\hat{x}_i^2, \tag{2.66}$$

where m is the mass of the particle and ω is the angular oscillation frequency. We further introduce *ladder* operators, also referred to as raising (creation) operator $a^\dagger$ and lowering (destruction) operator a, as

$$\begin{aligned} a^\dagger &= \sqrt{\frac{m\omega}{2\hbar}}\left(\hat{x} - \frac{i}{m\omega}\hat{p}\right), \\ a &= \sqrt{\frac{m\omega}{2\hbar}}\left(\hat{x} + \frac{i}{m\omega}\hat{p}\right). \end{aligned} \tag{2.67}$$

Using the ladder operators, the position and momentum operators can be expressed as

$$\begin{aligned} \hat{x}_i &= \sqrt{\frac{\hbar}{2m\omega}}\left(a^\dagger + a\right) \quad \text{and} \\ \hat{p}_i &= i\sqrt{\frac{\hbar m\omega}{2}}\left(a^\dagger - a\right), \end{aligned} \tag{2.68}$$

leading to the fermionic commutation relations

$$\left[a, a^\dagger\right] = 1 \text{ and } \left[a^\dagger, a^\dagger\right] = \left[a, a\right] = 0. \tag{2.69}$$

With the number operator

$$\hat{N} = a^\dagger a, \tag{2.70}$$

we are able to rewrite the Hamiltonian in the following form:

$$H = \hbar\omega \left(\hat{N} + \frac{1}{2} \right). \tag{2.71}$$

In this picture, we can now define the number states $|n\rangle$ being energy eigenstates of H corresponding to a number of n excitations in the systems. The origin of the terminology "ladder" (or "creation", "annihilation" etc.) operator as well as "number" operator will be revealed as we examine their action on the eigenstates. The ladder operators add one excitation to or remove one excitation from the system,

$$\begin{aligned} a^\dagger |n\rangle &= \sqrt{n+1}\, |n+1\rangle \\ a\, |n\rangle &= \sqrt{n}\, |n-1\rangle \\ a\, |0\rangle &= 0, \end{aligned} \tag{2.72}$$

whereas the number operator restores the number of excitations

$$\hat{N} |n\rangle = n\, |n\rangle . \tag{2.73}$$

This representation is called *Fock*[6] or *occupation number representation* and offers intuitive insights, in particular in the context of field theories. It is considered the most particle-like quantum mechanical representation whereas *coherent states*[7] are considered the most "classical" states as they resemble the oscillatory behavior of a classical harmonic oscillator.

2.4.2 Coherent states and the driven quantum harmonic oscillator

In the treatment of a quantum harmonic oscillator, it can be beneficial to switch to a description in phase space, which is represented by coherent states. The canonical form of a coherent state in the Fock basis is given by

$$|\alpha\rangle = \sum_n e^{-|\alpha|^2/2} \frac{\alpha^n}{\sqrt{n!}} |n\rangle \ , \tag{2.74}$$

which is defined as an eigenstate of the annihilation operator

$$a\, |\alpha\rangle = \alpha\, |\alpha\rangle \ , \tag{2.75}$$

and, therefore, α is in general a complex number due to the non-hermiticity of the annihilation operator a. Note that the creation operator $a^\dagger$ has no eigenstate in *ket*-form while the annihilation operator a does not have a eigentstate in *bra*-form. However, we can write down the action of $a^\dagger$ on the *bra* of a coherent state as $\langle\alpha|\, a^\dagger = \alpha^* \langle\alpha|$. For a given coherent state, one can also infer the distribution of Fock states, where the probability to find a certain Fock state $|n\rangle$ in a coherent state $|\alpha\rangle$ is given by a Poisson distribution

$$p_\alpha(n) = \frac{\alpha^{2n}}{n!} e^{-|\alpha|^2} \ , \tag{2.76}$$

[6] Fock states are named after Russian physicist Wladimir Alexandrowitsch Fock.

[7] Coherent states are also denoted as *Glauber* states as they were introduced by Roy J. Glauber in 1963 [97].

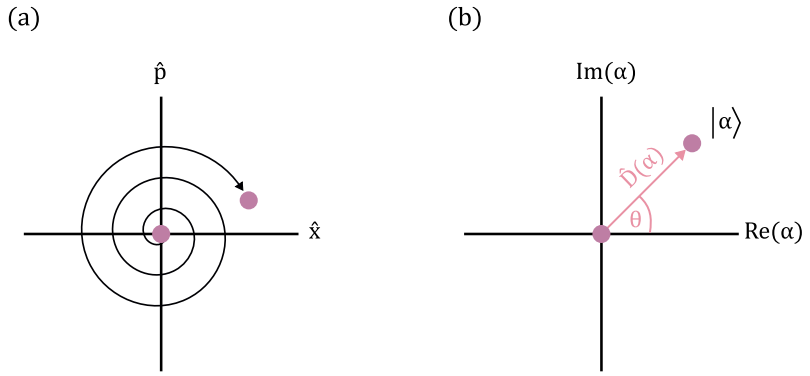

Figure 2.4: Phase space representation of the trajectory of a resonantly driven harmonic oscillator. (a) Initially at rest, the state is rotating while the amplitude of the motion is continuously increasing over time. (b) Phase space-representation in the co-rotating frame, where the spiraling motion corresponds to a linear displacement. The operator $D(\alpha)$ displaces the initial motional ground state $|0\rangle$ to a coherent state $|\alpha\rangle$ along a straight line. The angle is given by the phase difference $\theta = \phi_d$ between the harmonic oscillator and the driving force.

with a mean phonon number $\bar{n} = |\alpha|^2$ and a variance $\sigma^2 = |\alpha|^2$.

When a quantum harmonic oscillator is driven by an external periodic force of the form

$$F_d(t) = A_d \sin(\omega_d t + \phi_d) = \frac{A_d}{2i}\left[e^{i(\omega_d t+\phi_d)} - e^{-i(\omega_d t+\phi_d)}\right] \tag{2.77}$$

with amplitude A_d, frequency ω_d and phase ϕ_d, the Hamiltonian extends to $H = H_{\mathrm{QHO}} + H_d(t)$. In the interaction picture, a rotating frame approximation can be applied [8], which simplifies the Hamiltonian to

$$H_{\mathrm{I}} = A_d \frac{x_0}{2i}\left(a e^{i\Phi_d} + a^\dagger e^{i\Phi_d}\right) \ . \tag{2.78}$$

The unitary time evolution of the given Hamiltonian is better expressed by the displacement operator

$$D(\alpha) = e^{\alpha a^\dagger - \alpha^* a} \ , \tag{2.79}$$

where $\alpha = \frac{A_d x_0 t}{2\hbar}$ is a dimensionless amplitude representing the distance from the origin in a co-rotating frame. The displacement operator creates a coherent state when applied to the vacuum state $|0\rangle$

$$D(\alpha)\,|0\rangle = |\alpha\rangle \ , \tag{2.80}$$

"displacing" the state by the amount of α. In phase space a coherent state can be represented by $\alpha = |\alpha|e^{i\theta}$ with the amplitude $|\alpha|$ and the phase θ of the state $|\alpha\rangle$, which is illustrated in Fig. 2.4.

[8] A more detailed derivation can be found Ref. [65].

2.5 Laser-atom interactions

In the first sections of this chapter, the principles of trapping ions in a (linear) Paul trap were discussed. In Secs. 2.2 ff. the basics of quantum information theory were introduced whereas in Sec. 2.4 the ion motion was described on a quantum mechanical level. In this section all these concepts will be combined reviewing the quantum mechanical description of the interaction between a trapped particle, treated as a two-level system, and a coherent electromagnetic field. The "laser-atom"[9] interaction is the basis of the coherent operations used in quantum information science with trapped atoms. It enables quantum control over both the internal (electronic) and motional degrees of freedom, not only for a single particle but also for ion crystals, by coupling the internal states across the crystal through the ions' collective motion. The quantum harmonic oscillator modes are used to mediate the coupling via Coulomb interactions. This way, entanglement between ions can be created and used as a fundamental resource in quantum simulation to create *spin-dependent forces* (spin-spin interactions). The subsequent sections are following the progression of some of my predecessors in quantum simulation experiments in Innsbruck given in Refs. [65,81,98] as well as Ref. [49].

2.5.1 Interaction with a two-level system

In the following, we will review the interaction of a monochromatic, coherent electromagnetic field with a localized atom. The interaction Hamiltonian is split into two parts $H_\mathrm{I} = H_a + H_L$ consisting of the Hamiltonian of the bare atom H_a and of the light field H_L. The Hamiltonian describing a bare two-level system is given by

$$H_\mathrm{a} = \frac{\hbar\omega_0}{2}\sigma_z, \tag{2.81}$$

where ω_0 is the atomic transition frequency and σ_z is the Pauli operator with the eigenstates $\begin{pmatrix}0\\1\end{pmatrix} = |\downarrow\rangle = |-\rangle_z = |g\rangle$ and $\begin{pmatrix}1\\0\end{pmatrix} = |\uparrow\rangle = |+\rangle_z = |e\rangle$, referred to as the ground state and the excited state, respectively. The two states are separated by $\hbar\omega_0$ in energy. Now we let the atom interact with a light field of the form $E = E_0\cos(\omega_\mathrm{L}t + \phi_\mathrm{L})$, which can be described by the Hamiltonian

$$H_\mathrm{L} = \hbar\Omega\sigma_x\cos(\omega_\mathrm{L}t + \phi_\mathrm{L}), \tag{2.82}$$

where we express the coupling strength by the Rabi frequency $\Omega \propto E_0$, which for a dipole transition is given by [54]

$$\Omega = \left|\frac{eE_0}{\hbar}\langle 1|\,\hat{\boldsymbol{r}}\cdot\hat{\mathbf{k}}\,|2\rangle\right|, \tag{2.83}$$

where $\hat{\mathbf{r}}$ is the electron's position operator and $|1\rangle$ and $|2\rangle$ the two involved states. Geometrical considerations regarding the coupling strength can be found in Sec. 3.4.3. of

[9] The term *laser-atom interaction* also applies to interactions between atoms and electromagnetic fields in the radio-frequency range.

Ref. [99] for the quadrupole transition in $^{40}Ca^{+}$. Using the rotating wave approximation (RWA), the full Hamiltonian of the bare atom and the light field is given by

$$H_{\mathrm{I}} = \hbar\frac{\Omega}{2}\left[\sigma_x \cos(\Delta t + \phi_{\mathrm{L}}) + \sigma_y \sin(\Delta t + \phi_{\mathrm{L}})\right], \tag{2.84}$$

where we transformed $H_{\mathrm{I}} = H_{\mathrm{a}} + H_{\mathrm{L}}$ into the interaction picture with $U = e^{-iH_{\mathrm{a}}t/\hbar}$ and introduced $\Delta = \omega_{\mathrm{L}} - \omega_0$ as the detuning of the laser frequency from the bare atomic transition frequency. In the RWA, we neglect all terms rotating at the sum frequency $\omega_+ = \omega_{\mathrm{L}} + \omega_0$ as these oscillations average out on time scales that are large compared to the time scale defined by the atomic transition frequency, i.e. $\Delta = |\omega_{\mathrm{L}} - \omega_0| \ll |\omega_0 + \omega_{\mathrm{L}}|$. With the electronic raising and lowering operators

$$\sigma_{\pm} = \frac{1}{2}(\sigma_x \pm i\sigma_y) \ , \tag{2.85}$$

the interaction Hamiltonian (2.84) can be rewritten as

$$H_{\mathrm{I}} = \hbar\frac{\Omega}{2}\left[e^{-i(\Delta t+\phi_{\mathrm{L}})}\sigma_+ + e^{+i(\Delta t+\phi_{\mathrm{L}})}\sigma_-\right] \ . \tag{2.86}$$

In the following, we are distinguishing two cases: the interaction with (a) a resonant and (b) a non-resonant light field. For doing so, we will switch to yet another representation using $H_0 = \frac{\hbar\omega_{\mathrm{L}}}{2}\sigma_z$ instead of (2.81) as the first part of the interaction Hamiltonian H_{I}. With this definition, Eq. (2.86) can be restated as a time-independent interaction Hamiltonian

$$H_{\mathrm{I}} = \hbar(-\frac{\Delta}{2}\sigma_z + \frac{\Omega}{2}\sigma_x) \ . \tag{2.87}$$

This seemingly counterintuitive picture, where the phase reference is given by the frequency ω_L, which can differ from the bare atomic transition frequency ω_0, in turn provides more intuitive insights in the following discussion of the two cases of resonant and non-resonant interactions.

(a) Resonant light field, $\Delta = 0$

A resonant laser coherently drives population between the $|\downarrow\rangle$ and the $|\uparrow\rangle$ state. The corresponding unitary operator is explicitly given as

$$H_{\mathrm{I}} = e^{-i\frac{H_{\mathrm{I}}t}{\hbar}} = \begin{pmatrix} \cos\left(\frac{\Omega t}{2}\right) & -ie^{i\phi_{\mathrm{L}}}\sin\left(\frac{\Omega t}{2}\right) \\ -ie^{i\phi_{\mathrm{L}}}\sin\left(\frac{\Omega t}{2}\right) & \cos\left(\frac{\Omega t}{2}\right) \end{pmatrix} \ . \tag{2.88}$$

On the Bloch sphere, this unitary operation represents a rotation about an arbitrary axis in the equatorial plane (xy-plane), which is defined by the phase ϕ, with a polar angle of $\theta = \Omega t$. Such a single-qubit rotation can also be written as

$$R(\theta, \phi) = e^{-i\theta(S_x\cos\phi + S_y\sin\phi)} \ , \tag{2.89}$$

where $S_{x,y} = \frac{\sigma_{x,y}}{2}$ denote the Pauli spin operators. The coupling strength, i.e. the intensity of the electromagnetic field, as well as the interaction time define the population transfer

probability from the state $|\downarrow\rangle$ to the state $|\uparrow\rangle$ or *vice versa*. A phase of $\phi = 0$ corresponds to a rotation $R_x(\theta)$ about the x-axis whereas $\phi = \pi/2$ corresponds to a rotation $R_y(\theta)$ about the y-axis. Continuous coherent excitation results in oscillations between the ground and the excited state at the Rabi frequency Ω that are called *Rabi oscillations* or *Rabi flops*.

(b) Non-resonant light field, $\Delta \neq 0$, $\Delta \gg \Omega$

The non-resonant excitation of a two-level system leads to the ac-Stark shift of its energy levels, also known as Autler-Townes effect. The Hamiltonian (2.87) is thus also referred to as ac-Stark Hamiltonian H_{AC}. Its eigenvalues are $\lambda_\pm = \pm\frac{\hbar}{2}\sqrt{\Delta^2 + \Omega^2}$ and the shift of the energy levels is given by $\delta = \lambda_\pm - \lambda_\pm|_{(\Omega=0)}$. Since the shifts of the two states occur in opposite direction, the resulting overall shift of the atomic transition frequency is twice as big:

$$\delta_{\mathrm{ac}} = -\frac{\Omega^2}{2\Delta} \ . \tag{2.90}$$

Note that this expression holds under the assumption that Δ is considerably bigger than Ω. The sign of the detuning Δ, i.e. red or blue detuning with respect to the bare transition, determines the sign of the frequency shift δ of the individual states. For $\Delta \gg \Omega$, the effective Hamiltonian is proportional to σ_z and effectively represents a rotation about the z-axis given by the unitary operation

$$R_z = Z(\theta) = e^{-i\theta S_z} = e^{-i\delta_{\mathrm{ac}}\hat{\sigma}_z/2t} \ , \tag{2.91}$$

where S_z is the Pauli spin operator and the rotation angle is $\theta = \delta_{\mathrm{ac}}t = \frac{\Omega^2}{2\Delta}t$. Starting from the ground state $|0\rangle$, the probability P_1 to find an ion in the excited state $|1\rangle$ can be calculated as

$$P_1(t) = |\langle\psi(t)\rangle\, \psi(0)|^2 = \frac{\Omega^2}{\Omega_{\mathrm{eff}}} \cos^2(\Omega_{\mathrm{eff}}t/2) \ , \tag{2.92}$$

where $\Omega_{\mathrm{eff}} = \sqrt{\Omega^2 + \Delta^2}$ is the effective Rabi frequency. Ω_{eff} increases with larger detuning while the amplitude (contrast) of the coherent oscillation decreases.

Definition of the Rabi frequency

Consistent with Eqs. (2.84)–(2.87), in this work the Rabi frequency frequency is defined as the frequency at which the population oscillates between the ground state and the excited state - in contrast to another definition used in literature, where Ω is defined as the frequency at which the wave function returns to its original state. The latter definition infers that a rotation of 4π is required to yield the original state as a rotation of only 2π leads to a factor of -1, which is consistent with the SU(2) algebra.

2.5.2 Spin-motion coupling of a trapped ion

To describe a trapped ion interacting with a laser beam, we now additionally consider the quantized oscillatory motion in the harmonic trapping potential with the oscillation

frequency ω_s. Still assuming a pure electronic two-level system, the total Hamiltonian can be written as a sum of three parts:

$$\begin{aligned} H &= H_\mathrm{a} + H_\mathrm{m} + H_\mathrm{int} \\ &\text{with} \\ H_\mathrm{a} &= \frac{\omega_0}{2}\sigma_z, \\ H_\mathrm{m} &= \hbar\omega_s a^\dagger a, \\ H_\mathrm{int} &= \hbar\Omega(\sigma_+ + \sigma_-)\cos(k\hat{x} - \omega_\mathrm{L} t - \phi), \end{aligned} \tag{2.93}$$

where H_a describes the bare two-level system, i.e. the internal state of the atom, H_m the motion in the harmonic potential and H_int the atom-light interaction. Using $U = e^{i/\hbar H_0 t}$, where $H_0 = H_\mathrm{a} + H_\mathrm{m}$, after applying the rotating-wave approximation neglecting oscillating terms at optical frequencies, we can express the interaction Hamiltonian in the interaction picture as[10]

$$H_\mathrm{I} = U^\dagger H U = \hbar\frac{\Omega}{2}(\sigma_+ e^{-i(\Delta t+\phi)} e^{i\eta(ae^{-i\omega_s t} + a^\dagger e^{i\omega_s t})} + \sigma_- e^{i(\Delta t+\phi)} e^{-i\eta(ae^{-i\omega_s t} + a^\dagger e^{i\omega_s t})}) \ , \tag{2.94}$$

introducing the Lamb-Dicke parameter $\eta = kx_0\cos(\theta_k) = k\sqrt{\frac{\hbar}{2m\omega_s}}\cos(\theta_k)$, where x_0 denotes the spatial expansion of the ground state and θ_k denotes the angle between the laser k-vector and the direction of the ion's motion. Next, we apply the *Lamb-Dicke* approximation to simplify expression (2.94) by assuming that the spatial extent of the motional wave packet is small compared to the wavelength of the laser interacting with the ion, i.e. $x_0 \ll \omega_\mathrm{L}$:

$$e^{i\eta(ae^{-i\omega_s t} + a^\dagger e^{i\omega_s t})} = \mathbb{1} + i\eta(ae^{-i\omega_s t} + a^\dagger e^{i\omega_s t}) + \mathcal{O}(\eta^2). \tag{2.95}$$

The assumption above holds for $\eta^2(2\bar{n}+1) \ll 1$, defining the *Lamb-Dicke regime*, which requires a sufficiently small motional quantum number $\bar{n}$, that is typically achieved already after Doppler cooling. This condition essentially ensures a small coupling between the ion's internal and motional state. A Lamb-Dicke parameter of $\eta < 1$ means that the energy spacing of the harmonic oscillator states is larger than the recoil energy of the ion leading to a suppression of changes in the ion's motional state[11].The interaction Hamiltonian in the Lamb-Dicke approximation takes on the form

$$H_\mathrm{I} = \hbar\frac{\Omega}{2}\left(\sigma_+ e^{-i(\Delta t+\phi)}\left[1 + i\eta(ae^{-i\omega_s t} + a^\dagger e^{i\omega_s t})\right] + h.c.\right) + \mathcal{O}(\eta^2) \ . \tag{2.96}$$

For coherent control of an ion's motional state, we now assume the operation in the *resolved sideband limit*, in which the carrier Rabi frequency is small compared to the ion's

[10] We further use $k\hat{x} = \eta(a + a^\dagger)$ and $e^{i\frac{\theta}{2}\sigma_z}\sigma_\pm e^{-i\frac{\theta}{2}\sigma_z} = e^{\pm i\theta}\sigma_\pm$. In addition, a Taylor expansion of $e^{i\eta(a+a^\dagger)}$ as well as less evident relations for the ladder operators are used to arrive at Eq. (2.94).

[11] Note that $\eta < 1$ is a necessary but not sufficient condition for the Lamb-Dicke regime.

oscillation frequency $\Omega \ll \omega_s$ ensuring well resolved motional sidebands. This condition allows the application of another rotating wave approximation to neglect terms oscillating at frequencies on the order of the ion's oscillation frequency ω_s and higher. By setting the detuning of the laser beam to either $\Delta = 0$ or $\Delta = \pm\omega_s$ we can define three different cases forming the basis of many quantum operations in experiments with trapped ions:

Carrier transition, $\Delta = 0$. The laser is resonant with the bare electronic transition and acts only on the internal state while leaving the motional state unchanged. This results in transitions of the kind $|\downarrow, n\rangle \leftrightarrow |\uparrow, n\rangle$ with $n = 0, 1, 2, ...$ The interaction is described by the Hamiltonian

$$H_{\text{car}} = \hbar\frac{\Omega}{2}\left(\sigma_+ e^{-i\phi} + \sigma_- e^{i\phi}\right) . \tag{2.97}$$

Red sideband (RSB) transition, $\Delta = -\omega_s$. The light field couples the electronic ground state to the excited state while decreasing the motional quantum number by 1 when exciting the ion to the upper state by a π-pulse. The Hamiltonian is given by

$$H_{\text{RSB}} = i\hbar\frac{\eta\Omega}{2}\left(\sigma_+ a e^{-i\phi} - \sigma_- a^\dagger e^{i\phi}\right) . \tag{2.98}$$

Red sideband transitions are expressed by transitions of the form $|\downarrow, n\rangle \leftrightarrow |\uparrow, n-1\rangle$[12]. The laser couples the quantum states pairwise on these transitions with an effective coupling strength of $\Omega_{n-1,n} = \eta\Omega\sqrt{n}$ that depends on the vibrational occupation number n (cf. Eq. (5.14)(a) in Sec. 5.3). In combination with a third level used for repumping the ion's internal state to $|\downarrow\rangle$, this transition can be used for *resolved-sideband cooling*: The ion's vibrational quantum number is reduced during the excitation on the red sideband and is unlikely to be changed in the dissipative repumping process allowing for the reduction of the phonon number by one in each cycle.

Blue sideband (BSB) transition, $\Delta = +\omega_s$. Analogous to the RSB transition, the light field resonant with the BSB transition couples the electronic ground state to the excited state while increasing the motional quantum number by 1 in transitions of the form $|\downarrow, n\rangle \leftrightarrow |\uparrow, n+1\rangle$[13]. The Hamiltonian for the blue sideband transition is given by

$$H_{\text{BSB}} = i\hbar\frac{\eta\Omega}{2}\left(\sigma_+ a e^{-i\phi} - \sigma_- a^\dagger e^{i\phi}\right) . \tag{2.99}$$

Akin in the case of the RSB excitation, the laser couples the quantum states pairwise with a coupling strength $\Omega_{n+1,n} = \eta\Omega\sqrt{n+1}$ (cf. Eq. (5.14)(a) in Sec. 5.3).

The dependence of the coupling strength on the motional quantum number allows one to infer the Fock state populations by measuring the evolution of the excited state population on the sideband transitions. The sideband transitions can thus be used for temperature measurements applicable to single ions as well as multi-ion crystals, which is treated in more detail in Sec. 5.3. Furthermore, the coupling of the motional and the electronic

[12]The state $|\downarrow, 0\rangle$ remains uncoupled when the laser is resonant with the red sideband transition.

[13]Equivalent to the RSB transition, here the state $|\uparrow, 0\rangle$ remains uncoupled for an excitation resonant with the RSB transition.

state enables the exploitation of the Coulomb interactions between the ions in a crystal to mediate interactions between them via excitation and de-excitation of the ions' collective motion. This is the foundation of most multi-qubit quantum gates applied in trapped-ion experiments and the idea behind the first realization of a two-ion quantum gate, namely the CNOT gate (Cirac-Zoller gate) [48]. More relevant for quantum simulation, spin-dependent forces acting on many qubits can be realized based on the same principles, which will be discussed in the following sections.

2.5.3 Resonant bichromatic interaction

We now consider the interaction of an atom with a *bichromatic* light field exciting an ion simultaneously on the red and the blue sideband with equal coupling strength. This interaction forms the basis for the creation of entanglement between multiple ions, e.g. used in quantum gates such as the Mølmer-Sørensen gate, and serves as the foundation of spin-spin interactions in quantum simulation. The Hamiltonian describing this vital interaction is given by

$$H_{\text{bic}} = \frac{\Omega}{2} i\hbar\eta \left(\sigma_+ a e^{-i\phi_r} - \sigma_- a^\dagger e^{i\phi_r}\right) + \frac{\Omega}{2} i\hbar\eta \left(\sigma_+ a^\dagger e^{-i\phi_b} - \sigma_- a e^{i\phi_b}\right) . \tag{2.100}$$

It can be restated as

$$H_{\text{bic}} = \frac{\Omega}{2} i\hbar\eta \left(\cos(\phi_+)\sigma_x - \sin(\phi_+)\sigma_y\right) \Big(\cos(\phi_-)(a^\dagger + a) + i\sin(\phi_-)(a^\dagger - a)\Big) , \tag{2.101}$$

using the definitions

$$\phi_+ = \frac{\phi_r + \phi_b - \pi}{2} \quad \text{and} \quad \phi_- = \frac{\phi_r - \phi_b}{2} . \tag{2.102}$$

The Hamiltonian (2.101) describes not only a pairwise coupling of the states $|\downarrow, n\rangle \leftrightarrow |\uparrow, n+1\rangle$ as well as $|\uparrow, n\rangle \leftrightarrow |\downarrow, n+1\rangle$ but also a coupling of all states

$$|\downarrow, 0\rangle \leftrightarrow |\uparrow, 1\rangle \leftrightarrow |\downarrow, 2\rangle \leftrightarrow |\uparrow, 3\rangle \leftrightarrow \ldots \text{ and}$$
$$|\uparrow, 0\rangle \leftrightarrow |\downarrow, 1\rangle \leftrightarrow |\uparrow, 2\rangle \leftrightarrow |\downarrow, 3\rangle \leftrightarrow \ldots$$

It represents a spin-dependent force acting on an ion as it couples the spin projection operator $\sigma_\pm$ to the ladder operators of the harmonic oscillator. If the qubit is in an eigenstate of $\sigma_\pm$, i.e. $|\pm\rangle$, the Hamiltonian displaces the state in phase space by $\alpha = -i\frac{\Omega}{2}\eta t$ (cf. Sec. 2.4.2) without altering the qubit state. The bichromatic interaction displaces the two electronic eigenstates $|+\rangle$ and $|-\rangle$ into opposite directions (Fig. 2.5(a)). Applying the resonant bichromatic interaction to an equal superposition of both eigenstates $|\downarrow\rangle = \frac{1}{\sqrt{2}}(|+\rangle - |-\rangle)$ in the motional ground state $|0\rangle$, leads to the creation of a so-called motional Schrödinger cat state, a superposition of the coherent states $|\pm\alpha\rangle$ maximally entangled with the internal qubit states $|\pm\rangle$. Setting $\phi_+ = \phi_- = 0$, the Hamiltonian takes on the form

$$H_{\text{bic}} = \frac{\Omega}{2}\eta\sigma_x(a^\dagger + a)$$

and, acting on $|\psi\rangle = \frac{1}{\sqrt{2}}(|+\rangle - |-\rangle)\,|0\rangle$, yields

$$|\psi(t)\rangle = \frac{1}{\sqrt{2}}\left(|+\rangle_x\,|\alpha\rangle - |-\rangle_x\,|-\alpha\rangle\right). \tag{2.103}$$

This superposition of coherent states $|\pm\alpha\rangle$ has been realized experimentally, i.a. with trapped ions [98,100], and can for instance be used to enhance the measurement sensitivity in spectroscopy [98].

2.5.4 Non-resonant bichromatic interaction - MS interaction

In the following, we will look at the impact of a non-resonant bichromatic interaction applied to two ions simultaneously, assuming a coupling exclusively to the COM mode. The interaction is known as Mølmer-Sørensen (MS) interaction as it was first studied by A. Sørensen and K. Mølmer in [101–103], although it was independently and simultaneously worked out by E. Solano *et al.*, as published in [104]. It is one of the most widely used interactions in trapped-ion quantum computation but also constitutes an essential resource in analog quantum simulation. It allows one to entangle the internal states of two or more ions making use of the joint motion of the ions in the trap without transferring populations to states with altered vibrational quantum numbers. In other words, after the gate cycle the initial motional state is unchanged.

At first, an additional detuning δ_{sb} from the sidebands is introduced such that the total detuning from the bare transition becomes $\Delta_{r,b} = \pm(\omega_s + \delta_{\mathrm{sb}})$. With the detuning δ_{sb}, the phases $\phi_{r,b}$ effectively become time-dependent as $\phi_r = \phi_{r,0} - \delta_{\mathrm{sb}}t$ and $\phi_b = \phi_{b,0} + \delta_{\mathrm{sb}}t$. Consequently, the phases of the bichromatic Hamiltonian (2.101) become

$$\phi_+ = \frac{\phi_r + \phi_b - \pi}{2} = \frac{\phi_{r,0} + \phi_{b,0} - \pi}{2}$$

and

$$\phi_- = \frac{\phi_r - \phi_b}{2} = \frac{\phi_{r,0} - \phi_{b,0}}{2} - \delta_{\mathrm{sb}}t\ . \tag{2.104}$$

For simplicity, we can set $\phi_{r,0} = \phi_{b,0} = \frac{\pi}{2}$ [14] and thus the MS Hamiltonian is given by

$$\begin{aligned} H_{\mathrm{MS}} &= i\hbar\frac{\eta\Omega}{2}\left(\sigma_x^{(1)} + \sigma_x^{(2)}\right)\left(\cos(\delta_{\mathrm{sb}}t)(a^\dagger + a) - i\sin(\delta_{\mathrm{sb}}t)(a^\dagger - a)\right) \\ &= i\hbar\frac{\eta\Omega}{2}\left(\sigma_x^{(1)} + \sigma_x^{(2)}\right)\left(a^\dagger e^{-i\delta_{\mathrm{sb}}t} + a e^{i\delta_{\mathrm{sb}}t}\right) \\ &= i\hbar\frac{\eta\Omega}{2}S_x\left(a^\dagger e^{-i\delta_{\mathrm{sb}}t} + a e^{i\delta_{\mathrm{sb}}t}\right)\ , \end{aligned} \tag{2.105}$$

where $S_x \equiv \sigma_x^{(1)} + \sigma_x^{(2)}$. This interaction Hamiltonian describes an off-resonantly driven harmonic oscillator. The driving force is spin-dependent due to the Pauli spin operator σ_x

[14] One could also choose $\phi_{r,0} = \pi$ and $\phi_{b,0} = 0$, which yields the other motional quadrature component $H_{\mathrm{MS}} = i\hbar\frac{\eta\Omega}{2}\left(\sigma_x^{(1)} + \sigma_x^{(2)}\right)\left(a^\dagger e^{-i\delta_{\mathrm{sb}}t} - a e^{i\delta_{\mathrm{sb}}t}\right)$.

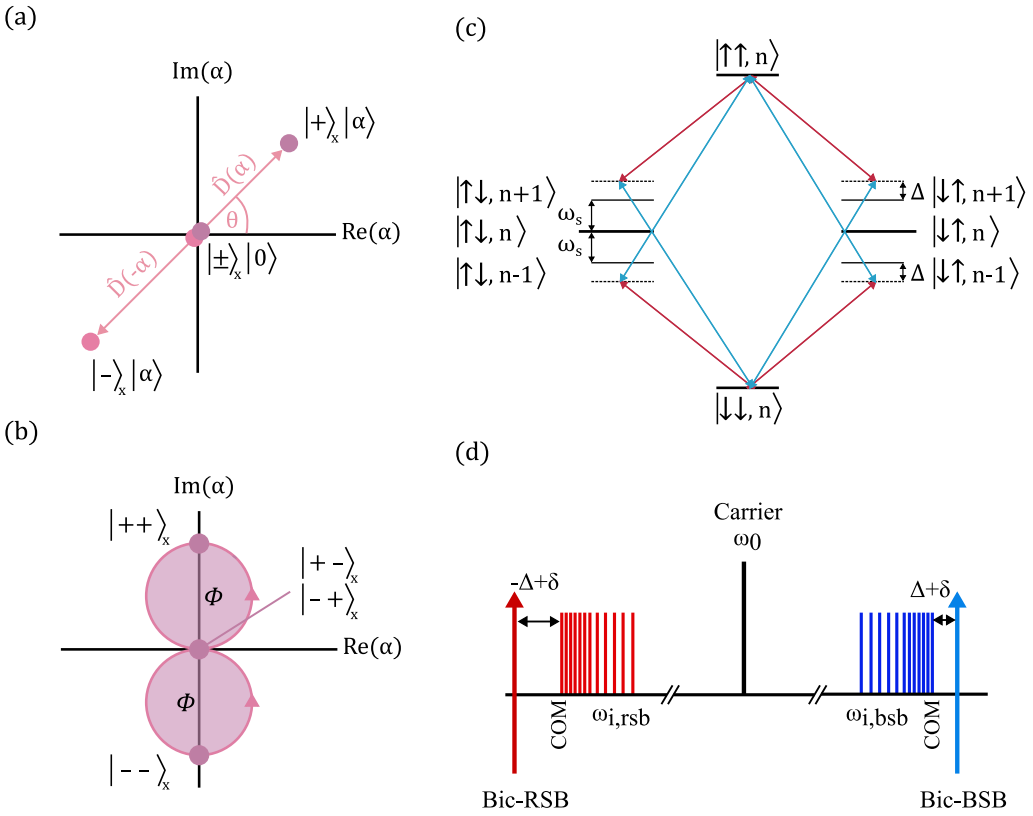

Figure 2.5: Resonant and off-resonant bichromatic interaction. (a) Phase space representation of motional states in the co-rotating frame. (a) A bichromatic field resonant with the particle's motion results in a state-dependent force displacing the two states $|+\rangle_x$ and $|-\rangle_x$ in opposite directions. (b) An off-resonant bichromatic field interacting with a two-particle state displaces the two states $|++\rangle_x$ and $|--\rangle_x$ along circles in the same rotational direction but in opposite initial directions. This picture corresponds to a Mølmer-Sørensen gate. After one rotation, they states pick up the geometric phase Φ. (c) Illustration of the laser detunings and interaction paths for an MS interaction. Constructive interference of the four different paths couple the two states $|\downarrow\downarrow\rangle$ and $|\uparrow\uparrow\rangle$. (d) Bichromatic laser detunings as used to implement a global Ising-type interaction in quantum simulation experiments with multiple qubits. The red and blue motional sidebands are indicated by the red and blue lines as well as the two tones of the bichromatic light field. In addition to the symmetric detuning Δ from the COM mode, a centerline detuning δ leads to an off-resonant B-field term in Eq. (2.117) and for larger values to the XY-type interaction given in Eq. (2.118).

acting on a and $a^\dagger$. Instead of displacing the state linearly in phase space, as in the case of the resonant interaction, the off-resonant drive displaces the atomic wave function in a circular motion (see Fig. 2.5(b)). The wave function periodically returns to its original state after the interaction time $t = \frac{2\pi}{|\delta_{\mathrm{sb}}|}$. However, after closing the loop in phase space it picks up a phase Φ, which is proportional to the trajectory-enclosed area and referred to as the *geometrical* phase or *Berry* phase [105]. The detunings and interaction paths are schematically shown in Fig. 2.5(c).

The time propagator for the MS interaction is given by

$$\begin{aligned} U(t) &= \hat{D}(\alpha(t)S_x)e^{i\Phi(t)S_x^2} \\ \text{with} \quad \alpha(t) &= i\left(\frac{\eta\Omega}{2\delta_{\mathrm{sb}}}\right)\left(e^{-i\delta_{\mathrm{sb}}t} - 1\right) \\ \text{and} \quad \Phi(t) &= \left(\frac{\eta\Omega}{2\delta_{\mathrm{sb}}}\right)^2 (\sin\delta_{\mathrm{sb}}t - \delta_{\mathrm{sb}}t) \ . \end{aligned} \tag{2.106}$$

After time $\tau = \frac{2\pi N}{|\delta_{\mathrm{sb}}|}$ the displacement operator becomes 1 and the motional state returns to its initial state. The Hamiltonian can then be seen as an effective spin-spin interaction of the kind $H_{\mathrm{eff}} \propto \sigma_x^{(1)} \otimes \sigma_x^{(2)}$. For the MS entangling gate, we choose a Rabi frequency of $\Omega = \frac{|\delta_{\mathrm{sb}}|}{2\eta}$ to create a maximally entangled state as well as $\tau_{\mathrm{gate}} = \frac{2\pi}{|\delta_{\mathrm{sb}}|}$, which results in the Hamiltonian

$$H_{\mathrm{MSgate}} = \hbar\frac{\pi}{4}\,\mathrm{sign}(\delta_{\mathrm{sb}})\sigma_x^{(1)}\sigma_x^{(2)} \ , \tag{2.107}$$

and the corresponding time propagator

$$U_{\mathrm{MSgate}} = e^{-i\hbar\frac{\pi}{4}\,\mathrm{sign}(\delta_{\mathrm{sb}})\sigma_x^{(1)}\sigma_x^{(2)}} \ . \tag{2.108}$$

As for a gate applied to $N > 2$ ions, this approach can be extended by using the N-qubit spin operator $S_x^N = \sum_{i=1}^N \sigma_x^{(i)}$ leading to mutual spin-spin interactions between all spin pairs. As long as the COM mode is used to mediate the interaction, the coupling strength between all pairs of spins is equal. Since the MS Hamiltonian solely contains operators acting on the internal state of the ions, within this treatment of the ideal two-level systems, the MS gate is independent of the motional state of the ions. This contrasts other gates such as the CNOT, which requires the ions to be in the motional ground state at the beginning of the operation. However, during an MS interaction, imperfect ground-state cooling or motional heating leads to increasing dephasing rates and therefore the ions are usually ground-state cooled in experiments and the heating during the interaction should be minimized [21].

As a side note: An N-qubit MS gate applied to an N-ion crystal in a product state $|\downarrow\rangle^{\otimes N}$ can create a GHZ state $|\Psi_{\mathrm{GHZ}}\rangle = \frac{1}{\sqrt{2}}(|\downarrow \ldots \downarrow\rangle + |\uparrow \ldots \uparrow\rangle = \frac{1}{\sqrt{2}}(|\downarrow\rangle^{\otimes N} + |\uparrow\rangle^{\otimes N}$ [106].

2.5.5 Effective spin-spin interactions with tunable interaction range

Up to here, we considered exclusively the coupling to the COM mode of an ion crystal. We will now further detune the bichromatic light fields from the vibrational sidebands and

investigate the coupling to multiple vibrational modes. By increasing the detuning such that the coupling to the sidebands is much weaker than the detuning from the motional modes of interest ($\eta\Omega \ll \delta_{\mathrm{sb}}$), the motional state is hardly changed by the interaction. In this weak coupling regime, the interactions between spin pairs are mediated by multiple vibrational modes and the coupling strengths can be written as a sum of the couplings to the individual modes. In order to write down the Hamiltonian describing this scenario, the Lamb-Dicke factors $\eta_{m,i}$ of each ion i and each mode m have to be taken into account. The Hamiltonian describing the spin-spin interactions takes the form

$$H_{\text{spin-spin}} = \frac{1}{2}\sum_{i,j}\sum_{m}\eta_{i,m}\eta_{j,m}\Omega^2\frac{\omega_m}{\Delta^2-\omega_m^2}\sigma_x^{(i)}\sigma_x^{(j)} \ . \tag{2.109}$$

We can rewrite the Lamb-Dicke factors with the help of the normalized eigenvectors $\mathbf{b}_m$ of the vibrational modes of the ion crystal as $\eta_{i,m}\eta_{j,m} = \frac{\hbar k^2}{2m\omega_m}b_{i,m}b_{j,m}$ [54] and express Eq. (2.109) as

$$H_{\text{spin-spin}} = \sum_{i,j}J_{ij}\sigma_x^{(i)}\sigma_x^{(j)} \ , \tag{2.110}$$

where the spin-spin coupling coefficients are given by

$$J_{ij} = \frac{\Omega^2}{2}\frac{\hbar k^2}{2m}\sum_{m}\frac{b_{i,m}b_{j,m}}{\Delta^2-\omega_m^2} \ . \tag{2.111}$$

The coupling matrix J_{ij} can be approximated by a power law decay [107]

$$J_{ij} \propto \frac{1}{|i-j|^{\alpha}} \ , \tag{2.112}$$

with the ion-ion distance[15] $r_{ij} = |\vec{r}_i - \vec{r}_j| = |i-j|$ and the exponent $0 < \alpha < 3$ tunable from infinite-range interactions ($\alpha = 0$) to short-range interactions ($\alpha = 3$) by choice of the sideband detuning δ_{sb}. For $\delta_{\mathrm{sb}} = 0$ the electromagnetic field is on resonance with the COM mode and leads to an infinite-range all-to-all coupling whereas for an increasing detuning $\delta_{\mathrm{sb}} > 0$, the coupling to other motional modes increases relative to the COM mode. In the limit of a large detuning all modes couple approximately equally, which results in a dipolar-like short-range interaction. The power-law approximation in Eq. (2.112) is usually a reasonable fit, although the underlying behaviour for larger crystals may be more subtle. A deeper investigation into this topic can be found in [108].

The Hamiltonian (2.110) effectively represents an Ising model without the magnetic field term. In the next section we will explore the construction of an Ising model including a transverse B-field term, finally leading to an XY Heisenberg model.

2.5.6 Transverse field Ising model and XY model

The missing ingredient to realize an interaction with a transverse magnetic-field term, is an additional asymmetric detuning δ of the two frequency components constituting

[15] The notation $|i-j|$ used for the ion-ion distance might be unconventional and ambiguous but is widely used in the field, so I defer to this notation.

the bichromatic light field with respect to the carrier. It is referred to as *centerline detuning*. The total detunings of the two bichromatic tones will be $\Delta_\pm = \pm(\omega_s + \Delta) + \delta$, where the centerline detuning shifts both components in the same direction such that they are asymmetric about the carrier (Fig. 2.5(d)). In addition, we will see that the Ising Hamiltonian transforms into an XY model by increasing the centerline detuning but first we briefly outline the necessary steps to arrive at the desired spin-spin interaction Hamiltonian.

We again start from the two bichromatic components and choose $\phi_+ = \phi_- = 0$, such that

$$H_{\text{bic,cl}} = \hbar\eta\frac{\Omega}{2}\left(ae^{i\Delta t} + a^\dagger e^{-i\Delta t}\right)\left(\sigma^+ e^{-i\delta t} + \sigma^- e^{i\delta t}\right) . \tag{2.113}$$

Next, a Magnus expansion is applied to the time propagator of the Hamiltonian to approximate its time evolution [109, 110]. In the following, the first two orders will be taken into account:

$$U_{\text{I}}(t) = \exp\left\{-\frac{i}{\hbar}\left(\int_0^t dt' H_{\text{I}}(t') - \frac{i}{2\hbar}\int_0^t dt' \int_0^{t'} dt''[H_{\text{I}}(t'), H_{\text{I}}(t'')] + ...\right)\right\} . \tag{2.114}$$

Thorough calculations of the first two orders to derive effective Hamiltonians can be found, e.g. in [65, 109]. Following Ref. [65], in the regime of $\Delta \gg \eta\Omega$, where the detuning is large compared to the coupling strength, the first order term introduces only a global phase and can therefore be neglected. The second order term is simplified by adiabatic elimination of all fast-oscillating terms containing Δ or $\Delta \pm \delta$, and after applying a Taylor expansion in $\frac{\delta}{\Delta}$ we arrive at

$$\begin{aligned} H_{\text{I}}^{(\text{eff})} = \left(\frac{\eta\Omega}{2}\right)^2 \Bigg\{ & \sum_i (2\bar{n}+1)\frac{\delta}{\Delta^2}\sigma_i^z + \\ & + \sum_{i,j}\left(\frac{1}{\Delta} + \frac{\delta^2}{\Delta^3}\right)\left(\sigma_i^+\sigma_j^+ e^{-2i\delta t} + \sigma_i^+\sigma_j^- + \sigma_i^-\sigma_j^+ + \sigma_i^-\sigma_j^- e^{2i\delta t}\right)\Bigg\} . \end{aligned} \tag{2.115}$$

We distinguish between three relevant regimes:

Regime 1: $\boldsymbol{\delta = 0}$

This case is already treated above in Sec. 2.5.5 and yields the pure Ising Hamiltonian (2.110) without a magnetic-field term:

$$H_{\text{spin-spin}} = \sum_{i,j} J_{ij}\sigma_x^{(i)}\sigma_x^{(j)} . \tag{2.116}$$

Regime 2: $\boldsymbol{\delta \approx J}$

Using $H_{\text{I}}^{(\text{eff})} = (H_{\text{I}}^{(\text{eff})} - H_0) + H_0$, the Hamiltonian $H_{\text{I}}^{(\text{eff})}$ can be transformed into a time-independent form by moving to an interaction picture with respect to $H_0 = -\frac{\delta}{2}\sum_i \sigma_i^z$ [65],

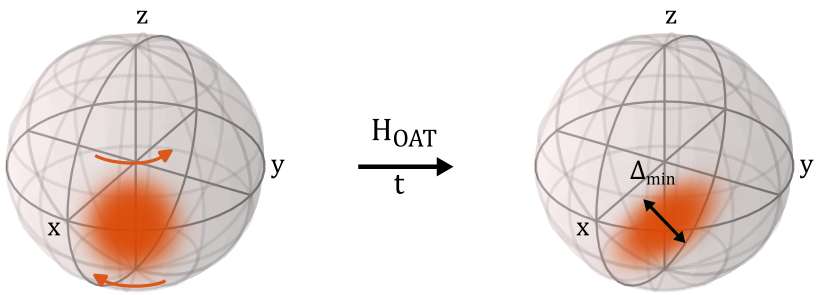

Figure 2.6: Illustration of the collective spin Bloch sphere showing the action of the one-axis twisting Hamiltonian applied to a coherent spin state. The symmetric (Gaussian) distribution of the collective spin's measurement uncertainty is squeezed along one direction represented by a twisting action on the Bloch sphere. The direction of minimum variance $\Delta_{\min} \equiv \langle \Delta(\hat{S}_{\mathbf{n}_\perp})^2 \rangle$ is indicated for the squeezed spin state. In experiments with trapped ions, the OAT model can be approximated by the XY-Hamiltonian (see main text).

which finally yields the transverse-field Ising Hamiltonian

$$H_{\text{Ising}} = H_{\text{I}} + H_B = -\sum_{i,j}^{N} J_{i,j}\sigma_x^{(i)}\sigma_x^{(j)} - \sum_{i}^{N} B\sigma_z^{(i)} \ , \tag{2.117}$$

with a tunable transverse magnetic field $B = \frac{\delta}{2}$.

Regime 3: $\delta \gg J$

For a large centerline detuning δ, a RWA can be applied with respect to terms oscillating rapidly at $e^{\pm 2i\delta t}$, leading to the XY-model Hamiltonian[16]

$$H_{\text{XY}} = \hbar J \sum_{i,j} \sigma_i^+\sigma_j^- + \sigma_i^-\sigma_j^+ \ . \tag{2.118}$$

2.5.7 Spin squeezed states and the one-axis twisting model

For quantum metrological applications, so-called *spin squeezed states* [69] are widely discussed and investigated as states with reduced noise distribution in one direction compared to an uncorrelated coherent spin state. Such non-Gaussian[17] states can provide a metrological gain and are therefore of great interest regarding a range of applications. A global

[16] $H_{\text{XY}} \propto \boldsymbol{\sigma_i}\boldsymbol{\sigma_j} - \sigma_i^z\sigma_j^z = 2(\sigma_i^+\sigma_j^-) + \text{h.c.}$

[17] Non-Gaussian in terms of the measurement variance.

interaction in the form of the *one-axis twisting* (OAT) model [111]

$$H_{\mathrm{OAT}} = \frac{\chi}{2}\sum_{i<j}^{N}\sigma_i^z\sigma_i^z \tag{2.119}$$

creates such a spin squeezed state starting from an initially uncorrelated coherent spin state with all spins polarized along $+x$: $|+\boldsymbol{X}\rangle = \otimes_{i=1}^{N}|+\rangle_i = \otimes_{i=1}^{N}1/\sqrt{2}(|\uparrow\rangle + |\downarrow\rangle$. The interaction (2.119) shears the classical noise distribution of the collective spin, reducing the measurement uncertainty in one direction while increasing it in another direction. The shearing is schematically depicted in Fig. 2.6.

While it is not easy to implement the OAT model in a trapped-ion experiment directly, its similarity to the models discussed in the previous sections, which are in fact accessible in the lab, is evident. For a sufficiently long interaction range the OAT model can be approximated by the power-law Ising model, where $\chi \approx \bar{J} = \frac{\sum_{i<j}J_{ij}}{N(N-1)/2}$ with $\bar{J}$ being the average coupling between spin pairs. Introducing a strong transverse field term to the Ising Hamiltonian, the effective interaction can be approximated by the XY model (Eq. (2.118)), which stabilizes the collective behavior during the interaction as it favors the alignment of the spins [71].

An important figure of merit for spin squeezed states is the *Wineland* squeezing parameter

$$\xi^2 = \frac{N\langle\Delta(\hat{S}_{\mathbf{n}_\perp})^2\rangle}{\left|\langle\hat{\boldsymbol{S}}\rangle\right|^2}\ , \tag{2.120}$$

with the minimum variance $\langle\Delta(\hat{S}_{\mathbf{n}_\perp})^2\rangle \equiv \langle(\hat{S}_{\mathbf{n}_\perp} - \langle\hat{S}_{\mathbf{n}_\perp}\rangle)^2\rangle$ in a direction $\mathbf{n}_\perp$ orthogonal to the mean collective spin vector $\langle\hat{\boldsymbol{S}}\rangle$ and the vector length $\left|\langle\hat{\boldsymbol{S}}\rangle\right|$. It is a measure for the metrological gain in phase sensitivity compared to an uncorrelated coherent spin state and it is an indicator of entanglement (or correlated states) for $\xi^2 < 1$. For the ideal OAT model, the Wineland squeezing parameter scales with the number of ions as $N^{-2/3}$, which is fulfilled for the power-law Ising model when $\alpha < 2D/3$, where D is the dimensionality of the system [71]. For long evaluation times, the interaction can generate other non-Gaussian states like so-called *q-headed cat states*, requiring other methods, such as the quantum Fisher information, to characterize their metrological advantage [71, 112].

2.6 The $^{40}Ca^{+}$ ion as a qubit

Apart from experiments devoted to highly charged ions, in most quantum information experiments, singly charged ions with a single residual valence electron are used to benefit from the hydrogen-like energy scheme. Hence, many of the employed species belong to the alkaline earth metals. The most commonly used ones are Ytterbium ($^{171}Yb^{+}$[18]), Beryllium ($^{9}Be^{+}$), (Barium ($^{137}Ba^{+}$ and $^{133}Ba^{+}$), Magnesium ($^{25}Mg^{+}$), Strontium ($^{87}Sr^{+}$) and Calcium ($^{40}Ca^{+}$). In general, the trapped ion should have various transitions that are

[18] Due to the nuclear spin ($I = 1/2$) and the hyperfine qubit's lower susceptibility to magnetic-field fluctuations compared to $^{40}Ca^{+}$ $^{171}Yb^{+}$ is a popular choice in many quantum information experiments.

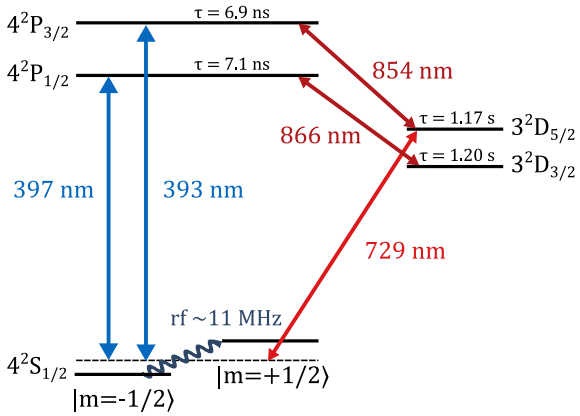

Figure 2.7: Relevant energy levels and transitions used in $^{40}Ca^+$ ions.

accessible in the optical or rf regime and which can be used for different tasks. Qubits can be encoded in either long-lived states accessed via optical transitions or in the sublevels of a Zeeman qubit or hyperfine qubit in the presence of a nuclear spin. However, there is (not yet) a *Goldilocks* qubit that satisfies all experimental requirements. All ion species come with advantages and disadvantages. A recent proposal of the so-called *omg* (optical, metastable, ground-state) architecture [113] discusses the optimization of the requirements of state preparation and cooling, gates, and storage in a single species by using interconvertible qubits encoded in an optical transition, in two metastable states (rf) and two sub-states of the ground-state (rf), all of which can be used for specific tasks, e.g. making use of sympathetic cooling during the execution of a quantum algorithm. This approach is combining the functionality of a single-species register and dual-species architectures, the ladder of which suffers from both fundamental and technical challenges.

The experiments presented in this thesis are performed using $^{40}Ca^+$ ions and build on the extensive experience in quantum information science with trapped $^{40}Ca^+$ ions in Innsbruck. With no nuclear spin, the $^{40}Ca^+$ ion exhibits a relatively simple, hydrogen-like energy level scheme, as depicted schematically in Fig. 2.7, exhibiting transition frequencies ranging from the near-UV to near-IR. The transitions are well-suited for manipulation using commercially available and mature laser technology. The degeneracy of the sublevels of states is lifted by applying an external magnetic field. A B-field of about 4 Gauss is commonly used in experiments with $^{40}Ca^+$ ions, creating a splitting of about 11 MHz between the two Zeeman levels in the $4^2S_{1/2}$ ground-state manifold. The resulting ground-state splitting lies within the natural line width of the $4^2S_{1/2} \leftrightarrow 4^2P_{1/2}$ transition of $\gamma \approx 2\pi \times 21.57$ MHz [114], which is used for Doppler cooling. At the same time it is significantly larger than the typical trap oscillation frequencies of a few MHz allowing sideband-resolved manipulation of the ions. The *clock transition* in the $^{40}Ca^+$ ion is given by a quadrupole transition between the $4^2S_{1/2}$ and the $3^2D_{5/2}$ manifold with a lifetime of about 1.17 seconds (~1 Hz linewidth) [115]. A qubit in the $^{40}Ca^+$ ion can be encoded either as an optical qubit in one of the two $|4^2S_{1/2}\rangle$ Zeeman levels in combination with one of the five $3^2D_{5/2}$ Zeeman levels, e.g. $|4^2S_{1/2}, m_s = -1/2\rangle = |1\rangle = |\downarrow\rangle$ and $|3^2D_{5/2}, m_s = -5/2\rangle = |0\rangle = |\uparrow\rangle$, or in the two Zeeman states of the $4^2S_{1/2}$ manifold,

explicitly the $|4^2\mathrm{S}_{1/2}, m_\mathrm{s} = -1/2\rangle = |1\rangle = |\downarrow\rangle$ state and the $|4^2\mathrm{S}_{1/2}, m_\mathrm{s} = +1/2\rangle = |0\rangle = |\uparrow\rangle$ state. The ladder is usually referred to as *Zeeman qubit* or *ground-state qubit*. The optical qubit transition can be manipulated with light at 729 nm whereas the ground-state qubit can be driven either directly using a (global) rf field at about 11.5 MHz, or off-resonantly using a stimulated Raman transition coupling the two Zeeman levels via a virtual level (in this work at about 396 nm).

The ions are Doppler cooled as well as ground-state cooled via electromagnetically induced transparency (EIT) cooling using light at 397 nm[19]. Light at 866 nm is employed to repump the population from the metastable $3^2\mathrm{P}_{3/2}$ state back to the $3^2\mathrm{P}_{1/2}$ state during laser cooling. For the ground-state preparation via optical pumping, a 854-nm laser is used in conjunction with a 729-nm-laser to drive the $3^2\mathrm{D}_{5/2} \leftrightarrow 4^2\mathrm{P}_{3/2}$ transition. A 422-nm laser serves for the isotope-selective loading of $^{40}\mathrm{Ca}^+$ ions, exciting the neutral Ca atoms on the $4\mathrm{s}^2\ {}^1\mathrm{S}_0 \leftrightarrow 4\mathrm{s}4\mathrm{p}\ {}^1\mathrm{P}_1$ transition before ionizing them in a second step using a laser at 375 nm. For a more detailed description of the used transitions and employed laser setups, refer to Sec. 3.6.

[19]Note that sideband cooling with 729-nm light can be used as a ground-state cooling technique but this becomes impractical for larger ion crystals as individual modes are cooled sequentially.

Chapter 3

Experimental setup

This work is building upon the well-proven methodology and cutting-edge technology in trapped-ion experiments and extending it to experiments with two-dimensional crystals. The experimental setup described in this chapter was built completely from scratch. While implementing state-of-the-art technology in all areas, several components were newly designed and developed. A novel monolithic three-layer rf trap was designed, enabling the storage of 2d ion crystals with unobstructed optical access perpendicular to the crystal plane and micromotion-free access from multiple directions. The vacuum setup, based on a compact hydrogen-annealed stainless-steel chamber, was designed to allow for optical access from all relevant directions and materials were chosen carefully to achieve low outgassing. Furthermore, state-of-the-art laser technology, electronics as well as experiment control hardware and software are employed to compose a compact, stable and remotely controllable setup. For fast and reliable loading of crystals with a deterministic number of $^{40}Ca^{+}$ ions, we refrain from using a resistively heated Calcium oven and instead opt for pulsed laser ablation. A redesigned home-built PI circuit for stabilization of the trap rf power is used to suppress fluctuations in trap oscillation frequencies. EIT cooling is employed to simultaneously cool multiple motional modes, which is essential when working with larger numbers of ions. Coupling the Zeeman ground-state qubit via a stimulated Raman transition at about 396 nm enables stronger entangling interactions compared to interactions implemented on the optical qubit as done in previous quantum simulation experiments in Innsbruck. Since conventional methods for quantum-state discrimination applied in experiments with linear strings of ions are not straightforwardly applicable to experiments with 2d crystals, a new algorithm for quantum-state readout, suitable for linear and planar crystal configurations of arbitrary shape, was implemented. The experiment control system is based on the Sinara hardware platform in combination with a control software tailored to the requirements in the presented experiments.

All these constituent parts are described in more detail throughout this chapter. In Sec. 3.1 the trap design and geometry is discussed. The vacuum apparatus including all mechanical and in-vacuum parts is presented in great detail in Sec. 3.2, where the initial subsection is dedicated to a discussion about cryogenic setups. The setup for the generation of the quantization field and for the compensation of magnetic-field gradients is discussed in

Sec. 3.3. Details on the trap rf and dc electronics are presented in Sec. 3.4. Sec. 3.5 describes the experiment control hardware and software components concluding with a subsection about the employed algorithm for quantum-state readout. Descriptions of all optical setups are given in Sec. 3.6 followed by a final discussion of the setup to drive the ground-state qubit via an rf coil in Sec. 3.7.

3.1 Ion trap

In this section, a discussion of different trapping geometries for 2d crystals in a rf trap (Sec. 3.1.1) is followed by a description of the new trap design and its operating parameters (Sec. 3.1.2). For a more detailed discussion of the design, simulations, and testing of the trap, please refer to the PhD thesis of Helene Hainzer [61].

3.1.1 Trapping geometries for 2d crystals

In a standard linear Paul trap consisting of a pair of rf electrodes, a pair of dc electrodes orthogonal to them, and two endcap electrodes, there are essentially two ways of trapping planar ion crystals:

Geometry 1: A 2d crystal can be trapped in the plane spanned by the two radial directions by applying dc voltages to the endcap electrodes, ensuring that the confinement in the axial direction is much stronger than the confinement in the two radial directions provided by the rf field (Fig. 3.1(a)).

Geometry 2: A crystals can be squeezed into a plane spanned by one radial direction and the axial direction by applying dc voltages on the dc electrodes strongly confining the ions in the direction orthogonal to the dc electrodes. (Fig. 3.1(b)).

Trapping 2d crystals using the first geometry has been realized by several groups worldwide [31, 33, 34], where the crystals are sometimes referred to as *radial* crystals. The second geometry is the geometry chosen for the experimental setup described in this work but it has been pursued also by other groups, e.g. the groups of Kihwan Kim [34] and Luming Duan [36]. Regarding the requirements for rf-power stability, radial crystals are preferable as shown in Appendix A of Ref. [60]. However, with regard to the adverse influence of micromotion on the laser-ion interaction, the second orientation is clearly advantageous because, to first order, micromotion occurs only in a single radial direction (between the two rf electrodes, see Fig. 3.1(b) and (c)). This geometry offers an entire plane orthogonal to the crystal plane, allowing for micromotion-free addressing of the ions with laser beams. In contrast, using geometry 1 leads to micromotion occurring in all radial directions within the crystal plane, leaving only a single direction orthogonal to the plane unaffected by micromotion.

3.1.2 A novel monolithic rf trap for 2d crystals

Trap design

For the experimental setup described in this thesis, the second trapping geometry (Fig. 3.1(b))

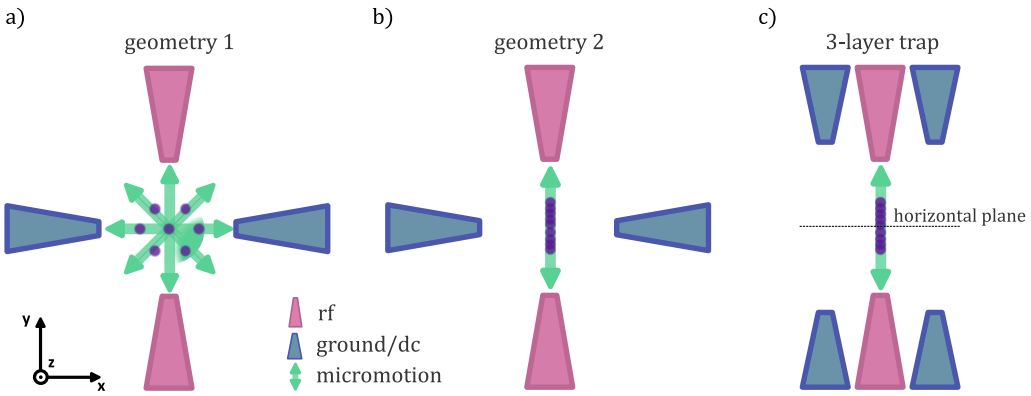

Figure 3.1: Geometries for storage of 2d crystals. (a) The crystal plane coincides with the radial plane of the linear Paul trap. Such a "radial" trapping geometry entails micromotion of the ions along their radial directions. (b) The crystal plane is spanned by the axial and a radial direction (here: between the two rf electrodes). Micromotion occurs only along the direction between the rf electrodes (y-direction). (c) A three-layer trap design allows for free optical access perpendicular to the crystal plane when trapping ions using geometry 2 shown in (b).

is chosen. The crystal plane is spanned by the axial direction (z) and the vertical radial direction (y). Hence, to first order, micromotion occurs only in y-direction providing micromotion-free access within the entire xz-plane, also referred to as the *horizontal* plane. In order to achieve free optical access perpendicular to the crystal plane, the trap design is based on a three-layer trap design [116] as shown in Fig. 3.1(c). The two rf electrodes are placed on the top and bottom of the middle layer. The dc electrodes, representing the orthogonal blades and endcap electrodes in a standard linear Paul trap, are located at the top and bottom with respect to the trap center and constitute the outer layers of the three-layer trap. These electrodes are segmented such that a total of 8 dc segments on the two outer layers, herein referred to as *endcap electrodes*, create the axial confinement. The 4 dc middle segments on the outer layers enable additional confinement in x-direction to create the anisotropy necessary for trapping 2d crystals in the yz-plane. The actual realization of the three-layer design is shown in Fig. 3.2.

Small alignment imperfections of the electrodes could prevent stable trapping of planar crystals (cf. challenge 3 in chapter 1). Therefore, the trap is realized as a monolithic design, accommodating all three layers on a single chip. The monolithic design ensures a precise arrangement of the electrodes with respect to each other and thereby bypasses the hand-assembly of the trap. The electrodes are separated by trenches with undercuts extending underneath the surface of the chip [117, 118], which is shown in the left zoom in Fig. 3.2. The trenches are 50 μm wide and ensure electrical isolation after metallization of the trap surface. Additional layers, hosting ground electrodes, are added between the rf and dc electrodes. They are introduced to shield axial rf-field components due to the trenches between the individual segments that could otherwise result in unwanted micromotion. The dc and ground electrodes are recessed in y-direction with respect to the rf electrode

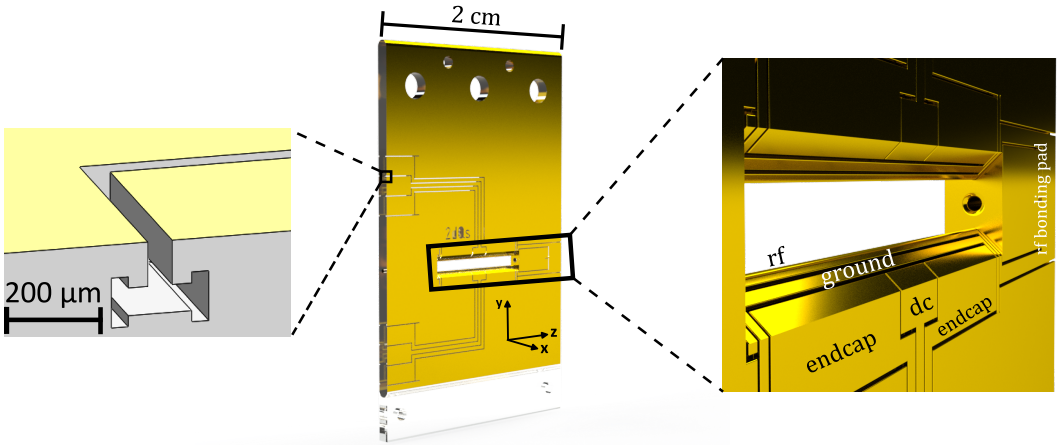

Figure 3.2: 3d rendering of the trap chip. The left part illustrates the trench geometry used to electrically isolate two electrodes. The right zoom onto the trap chip's center reveals the three-dimensional arrangement of the electrodes.

to allow optical access from an angle of 45° from the top and bottom.

The trap chip has a size of 31.5 × 20 mm and a substrate thickness of 1 mm. In addition to optical access from the front and back, lateral holes with a diameter of about 300 μm allow for access along axial direction from both sides. The rather macroscopic electrode-ion distance of 400 μm ensures a low level of heating due to Johnson noise and blackbody radiation, and avoids "anomalous" heating [119]. The rf electrodes are 9.3 mm long [1], the middle segments are 1.5 mm long and the endcap segments are 3.45 mm long. The length of the middle segment is chosen such that a tilting of the crystal by application of asymmetric voltages on the outer dc segments can be performed efficiently with reasonably low voltages. Wirebonding pads are placed on both sides of the chip to electrically connect the trap to the dedicated dc and rf interposer boards. Three through holes in the top area of the chip allow for mounting the trap with M2 screws. Additional smaller holes on the top and bottom are introduced to facilitate the fixation for transport.

The trap was microfabricated and gold-coated by Translume[2]. The trap chip is based on a fused-silica substrate and was processed via subtractive laser-induced etching, which has been used recently for the fabrication of several other ion traps [117, 120–122]. In the first step of the fabrication process, the designed structures are written into the substrate by a fs-pulsed laser modifying the chemical properties of the glass locally. In the second step the substrate is immersed in a bath of hydrofluoric acid predominantly etching the previously illuminated areas. This way, the desired electrode structures can be manufactured with sub-μm precision, which enables the creation of the trenches isolating the electrodes and further guarantees the precise alignment of the electrodes. In the last step the trap was coated via thick-film sputtering with ∼30 nm of titanium as adhesion layer and ∼3 μm of

[1] The central slot has a width of 9.4 mm.
[2] Translume Inc., Ann Arbor, MI 48108, USA

gold[3]. To prevent electrical shorts, the trap was coated in several consecutive sputtering steps. During the intervals between these steps, the trap was allowed to cool down, mitigating the indiscriminate deposition of gold atoms due to thermal processes on the surface. Photos of the gold-coated trap inside the vacuum chamber are shown in Fig. 3.5.

Trap parameters

Electrical tests of the trap revealed that the maximum voltage applicable to the rf electrodes is about 1 kV peak-to-peak to avoid the risk of electrical shorts. This represents the voltage, at which the trap is typically operated. The targeted secular oscillation frequency in the strongly confining direction is about 2 MHz[4]. To keep micromotion and rf heating at a low level, a low q parameter is beneficial. The electrode-ion distance, the q parameter, the maximum voltage and the targeted secular frequency together provide a constraint for the choice of the rf drive frequency, which forms the basis for the design of the helical resonator. In the presented experiments, the trap is operated at $\Omega_{\mathrm{rf}} = 2\pi \times 43.22$ MHz, which ensures $q \lesssim 0.1$. In typical experiments the ion crystals are trapped in a potential with secular oscillation frequencies ω_{s} of about $2\pi \times 2.2$ MHz in the out-of-plane direction and a few hundred kHz in the two weakly confining directions. Finite element simulations of the potential in the radial plane suggest a trap depth of about 4 eV. The principal axes of the trap potential are well aligned with the trap's geometrical axes x, y, and z. Therefore, in this work the secular frequencies in strong and weak directions ω_{s}, ω_{w1} and ω_{w2} are synonymously denoted as ω_x, ω_y, and ω_z, respectively. The x-axis is the direction perpendicular to the ion crystal plane and is referred to as *out-of-plane* direction.

3.2 Vacuum apparatus

When working with a large number of ions, a good vacuum quality is a crucial element of an experiment to mitigate detrimental background gas collisions and the formation of molecular (dark) ions. Careful choice of the used materials, cautious handling of all components and suitable cleaning protocols are essential for the successful realization of lowest pressures in a UHV/XHV system. The following subsections provide details on the considerations guiding the selection of materials and methods, along with a description of the employed components.

3.2.1 Considerations for a cryogenic setup

One possible way of reaching ultra-low pressures in the experiment is the embedding of the ion trap in a cryogenic environment. In the first phase of my PhD work, I conducted an extensive research to obtain an overview of cryogenic systems on the market as well as systems already in use by other research groups. In the end, we regarded the unknowns of the commercially available cryogenic setups as too risky for this project and instead focused on the design of a room temperature setup. Recent advancements in the cryogenic sector,

[3]The specified thickness of the gold layer is based on the manufacturer's estimation and has not been measured.

[4]Originally, this value was intended to be higher ($\omega_{\mathrm{s}} \approx 4$ MHz) but electrical tests indicated a lower limit of the maximally applicable voltage, which is now 1 kV instead of the originally targeted 2 kV peak-to-peak.

may have changed the situation in the meantime. However, the most relevant aspects regarding the use of cryogenic setups for trapped-ion quantum information experiments will be discussed in the following.

For experiments aiming at quantum simulation experiments, there are two main concerns: First, vibrations can be transmitted from the compressor and the cold head to the cold stage, where the ion trap is located. Fluctuations in the optical path length due to vibrations lead to a phase-modulation of the laser in the ions' rest frame. However, for coherent manipulation of a qubit, the phase of the light field with respect to the ions has to be well-defined and coherent. Therefore, it is desirable to mitigate vibrations to a level of about less than 1 % of the operating wavelength, i.e. $\lesssim 4$ nm for coherent stimulated Raman transitions at 395 nm. At the beginning of this project in 2018, comparable values have not been achieved reliably in other setups and at no manufacturer could provide data to guarantee such a low level of vibrations. Second, magnetic-field fluctuations caused by moving ferromagnetic parts in the cryocooler potentially lead to adverse effects on the quantum coherence of magnetic-field sensitive qubits. Akin to the level of vibrations, the magnetic fields caused by the cryogenic systems are of unknown magnitude and the manufacturers could not provide any data. The uncertainties in terms of vibrations and magnetic-field fluctuations led us to refrain from the realization of a cryogenic setup.

A third requirement for a cryogenic setup would be the suitability for a vacuum bake-out to maintain a true UHV system. While this is not a strict requirement to reach UHV/XHV pressures, we consider it a valuable feature to reduce contaminants and, therefore, the risk of failure as much as possible. Further aspects to take into consideration are the required cooling capacity, the general handling of the apparatus to ensure a fast duty cycle (e.g. for trap testing), and the acquisition costs as well as the running costs (e.g., for helium supply in case of a flow cryostat).

Dilution refrigerators using mixtures of ^{3}He/^{4}He to cool to mK-temperatures are very expensive devices but do not add value to ion-trapping experiments since a 4K system is sufficient to freeze out residual background gas[5] via physisorption on the cryogenic surfaces of the vacuum vessel. Therefore, a key decision is to make between a closed-cycle cryocooler and an open (wet) system such as a flow or bath cryostat. In contrast to a flow cryostat, a bath cryostat requires a big tank of liquid Helium providing constant cooling without the possibility to control the coolant consumption. The purchase costs for a bath cryostat are substantially higher than for a flow cryostat. Both wet systems require a replenishment of liquid coolant that is associated with increased running costs and the need for a reliable source of liquid helium. Experiences in the ion-trapping group in Innsbruck show that this can be challenging. Hence, for this project, a closed-cycle system would have been the preferred option.

There are mainly two types of closed-cycle systems available: pulse-tube (PT) and Gifford-McMahon (GM) cryocoolers. One main advantage of the PT cooler is the absence of moving pistons in the cold head, potentially reducing vibrations and magnetic-field fluctuations caused by moving ferromagnetic parts. The various commercial cryogenic systems

[5]The boiling point of hydrogen at normal pressures is about 20 K, the melting point about 14 K.

also differ in the implemented method to mechanically decouple the cold tip from the vibrating cold head. Most commercial ultra-low vibration closed-cycle systems use a buffer gas heat exchange for this purpose. However, some companies provide cold tips, that are decoupled from the cold head via flexible bellows of about 1 m length further reducing the level of vibrations. These systems appeared to be among the most promising options, although the cooling power is often limited to ≤ 1 W. Such systems are offered by *Janis, Inc.*[6] and *Cold Edge Technologies*[7].

It should be noted here that several research groups around the world have built cryogenic setups for ion-trapping experiments with a custom-designed vibration isolation, e.g. [123, 124]. However, the development and assembly of such an apparatus is typically associated with a time requirement of several years, which was not considered for the presented experiments.

3.2.2 Vacuum chamber design

A custom vacuum chamber was designed to be as compact as possible while providing optical access from all required directions. Irrespective of the design of the chamber, the choice of material is a key question arising in search of a low-outgassing solution. The most common materials used for vacuum vessels are austenitic stainless steels (SS), such as SS 304 L and SS 316 L(N). In addition to their good mechanical properties and weldability, they are essentially non-magnetic. When only low-outgassing materials are used, the residual gas load inside the vacuum chamber is usually limited by outgassing of hydrogen molecules (H_2) from the stainless steel vessel. Low hydrogen-annealing, a thermal cycling procedure, in which a stainless steel vessel gets baked at temperatures up to 1200 °C, can substantially reduce the outassing rate of hydrogen of a stainless steel vessel. Additionally, residual magnetization, e.g. from welding or material deformation, can be eliminated by heating above the Curie temperature, and material impurities and stress can be reduced.

In contrast to stainless steel, aluminium or titanium offer lower outgassing rates but have several drawbacks to consider: Aluminium is a relatively soft material and, therefore, comes at the risk of damage of threads or knife edges of CF flanges. Although some companies claim the stability of knife-edges after 100 closing cycles and baking up to 180°, the outgassing rate compared with that of a hydrogen-annealed stainless steel vessel, is not convincing considering the increased risk of damage. At the time of designing the presented experimental setup, it was not feasible to get an aluminium chamber as compact as a stainless steel chamber while meeting our requirements. The increase in volume and in-vacuum surface for such a chamber would have counteracted the benefit of using a lower-outgassing material. In Ref. [125] the presented hydrogen outgassing rate of aluminium and titanium compared with low-hydrogen annealed stainless steel is lower by a factor of two and four, respectively. However, given the geometric constraints in the chamber design for aluminium leading to a larger surface area in vacuum, the absolute outgassing rate in such a chamber is suspected to improve only by a significantly lower factor. Titanium, on

[6] Janis Recirculating Gas Cooler RGC4-ST500
[7] Cold Edge Stinger

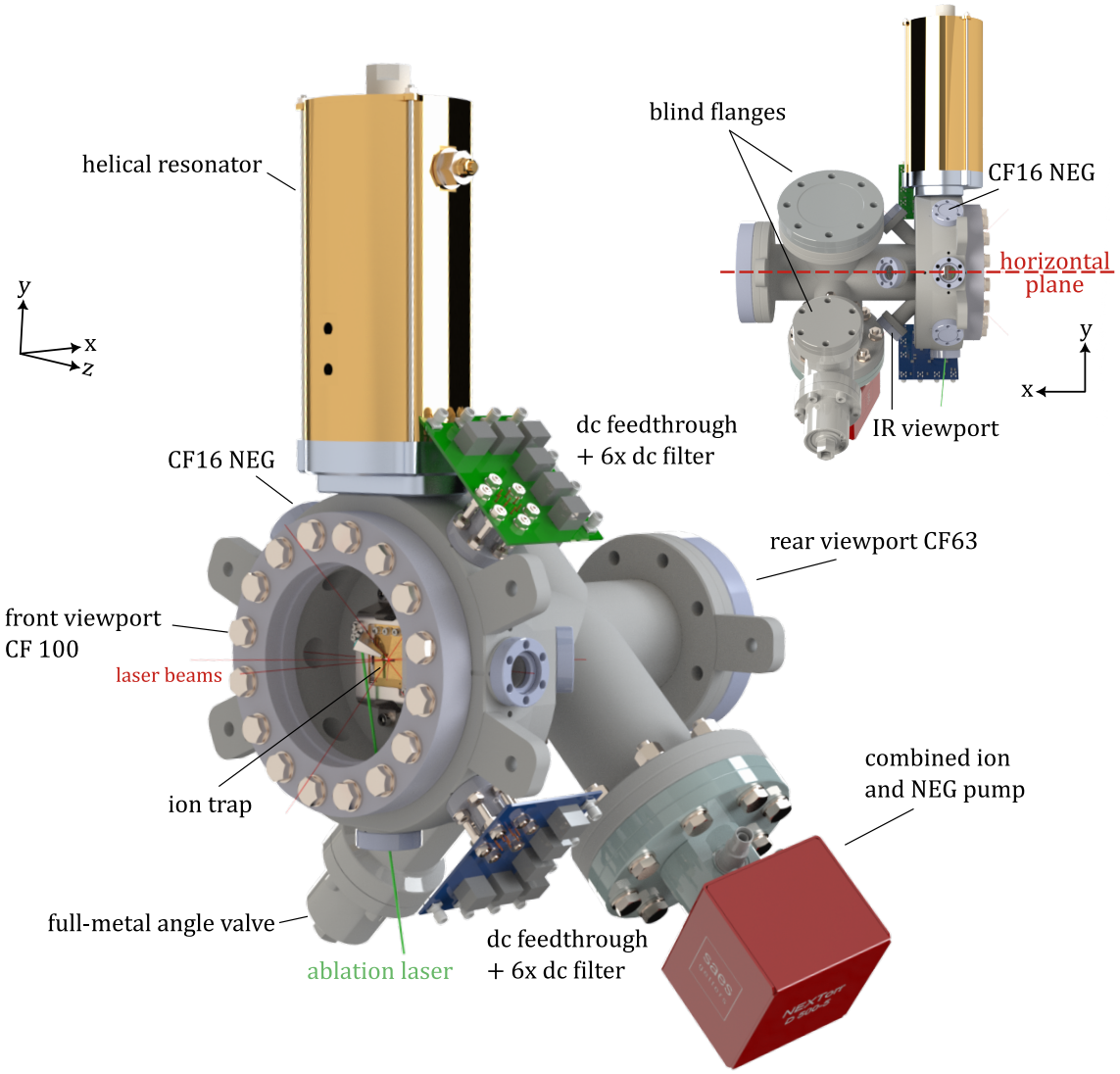

Figure 3.3: 3d rendering of the vacuum apparatus.

the other hand, offers low outgassing and low magnetic permeability while providing high material strength. However, the purchase cost of a titanium chamber would have been an order of magnitude higher than that of a conventional stainless steel chamber. Therefore, SS 316 LN is the material of choice for the presented vacuum chamber.

The custom chamber design was manufactured by Pfeiffer Vacuum [8]. It is made of stainless steel 316 LN and was vacuum fired (low-hydrogen annealed) at 1050 °C for 120 minutes. The inner surface is electro-polished with a surface roughness of Ra $\lesssim 1.2$ μm, where Ra is the mean profile height deviation from the mean line. All other flanges attached to the main corpus of the chamber, i.e. feedthroughs and windows, are also made of SS 316 LN. A rendering of the vacuum chamber is displayed in Fig. 3.3. The design allows for optical access from all relevant directions, i.e. various directions within the horizontal plane as well as 45° access from the top and bottom. The chamber's main corpus is a cylinder with an outer diameter of 172 mm hosting a CF100 viewport in the front and eight CF16 viewports along the side. Four nipples at an angle of 45° are welded into the backside of the main corpus and equipped with CF16 viewports. The design features high optical access including directions at 45° from the front, back, top and bottom. A CF63 cross is welded into the backside of the corpus allowing for efficient pumping and additional optical access from the backside of the trap. A full-metal UHV/XHV valve[9] is used as docking site for a turbomolecular pump and for isolation of the vacuum chamber after the bake-out. A combined NEG-ion pump[10] is mounted to the bottom right CF63 flange of the cross to continuously pump the vacuum chamber after isolation from the turbomolecular pump. A μ-metal shield around the NEG-ion pump shields the magnets necessary for the operation of the ion pump. An additional CF16 NEG[11] attached to the top left flange of the main corpus provides additional pumping relatively close to the trap[12]. A spare CF63 flange on the cross is closed with a low-hydrogen annealed blank flange.

3.2.3 In-vacuum parts

Materials of in-vacuum parts

All screws, nuts and washers used in vacuum are composed of either grade 2 or grade 5 titanium and all screws, nuts and washers attached to the air side of the vacuum apparatus, including the helical resonator, are made of grade A4 (316) stainless steel or titanium to ensure low outgassing and low magnetic permeability. Tapped (vented) screws were used in case of blind holes, e.g. in the back wall of the chamber. The trap holder as well as the holder and aperture for the ablation target, referred to as *the funnel*, are made of grade 4 titanium and were fabricated by wire-cut electrical discharge machining (wire erosion). In order to decrease the surface roughness after the wire erosion procedure (typically $Ra \approx 12 - 20$ μm) and therefore reduce the adsorption of water and subsequent

[8] Pfeiffer Vacuum GmbH, Berliner Strasse 43, 35614 Asslar

[9] VAT 57132-GE02, CF40 all-metal angle valve

[10] SAES NexTorr D500-5; power supply and controller: NIOPS-04

[11] SAES CapaciTorr CF16-MK2-172-2X16-10

[12] Simulations and measurements of the thermal profile of such a CF16 NEG provided by the manufacturer made us confident that the heat load on the CF100 front window and its seal is acceptable.

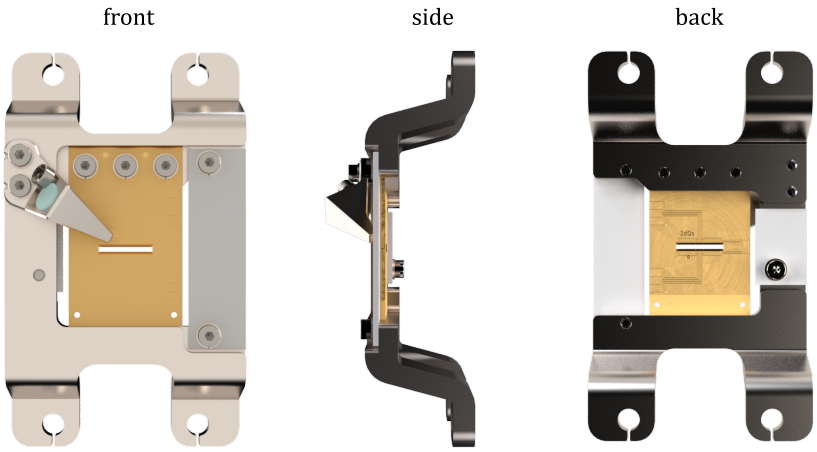

Figure 3.4: 3d drawings of the titanium trap holder hosting the trap chip, the ablation funnel, the dc interposer board (mounted on the front side) and the rf interposer boards (mounted on the back side). The trap's dc electrodes are wirebonded to the double-sided dc interposer board from both sides. The rf electrodes are wirebonded to the small rf interposer board only from the back side of the holder.

outgassing, the trap holder and the funnel were plasma-polished[13].

Trap mount

The trap chip is mounted to the frame by three M2 screws. By using spring-lock washers and by including sufficient tolerances in the mounting holes of the trap, we reduced the risk of damage during a bake-out resulting from a mismatch of the coefficients of thermal expansion between fused silica and titanium. A contact area of $A \approx 6 \times 20$ mm^2 provides considerable thermal anchoring to the titanium frame. The trap holder is mounted onto the rear wall of the main corpus using four vented M4 screws.

Ablation target and funnel

The ablation funnel has a an aperture of 300 μm diameter in the front. The inner gradually conical structure is achieved through multiple bores with decreasing diameters. The ablation target[14] is placed into a recess on top of the funnel and fixated with a Ti M2 screw. It can be targeted by a laser beam entering through a hole with a diameter of 2.2 mm on the bottom side of the funnel. The distance from the target to the trap center is about 15 mm. For alignment, we used a laser pointer illuminating the trap center through the funnel and ensured that the trap center is hit symmetrically by the light cone. Before placing the target inside, the rapidly oxidizing surface of the Ca target was scraped off.

[13] plasotec GmbH, Arthur-Wilke-Straße 2, D-14727 Premnitz, Germany. The company claims a reduction of the surface roughness of maximally about 85 %.

[14] Vacuum Engineering & Materials Co. (VEM), Cylindrical target, 5x3 mm

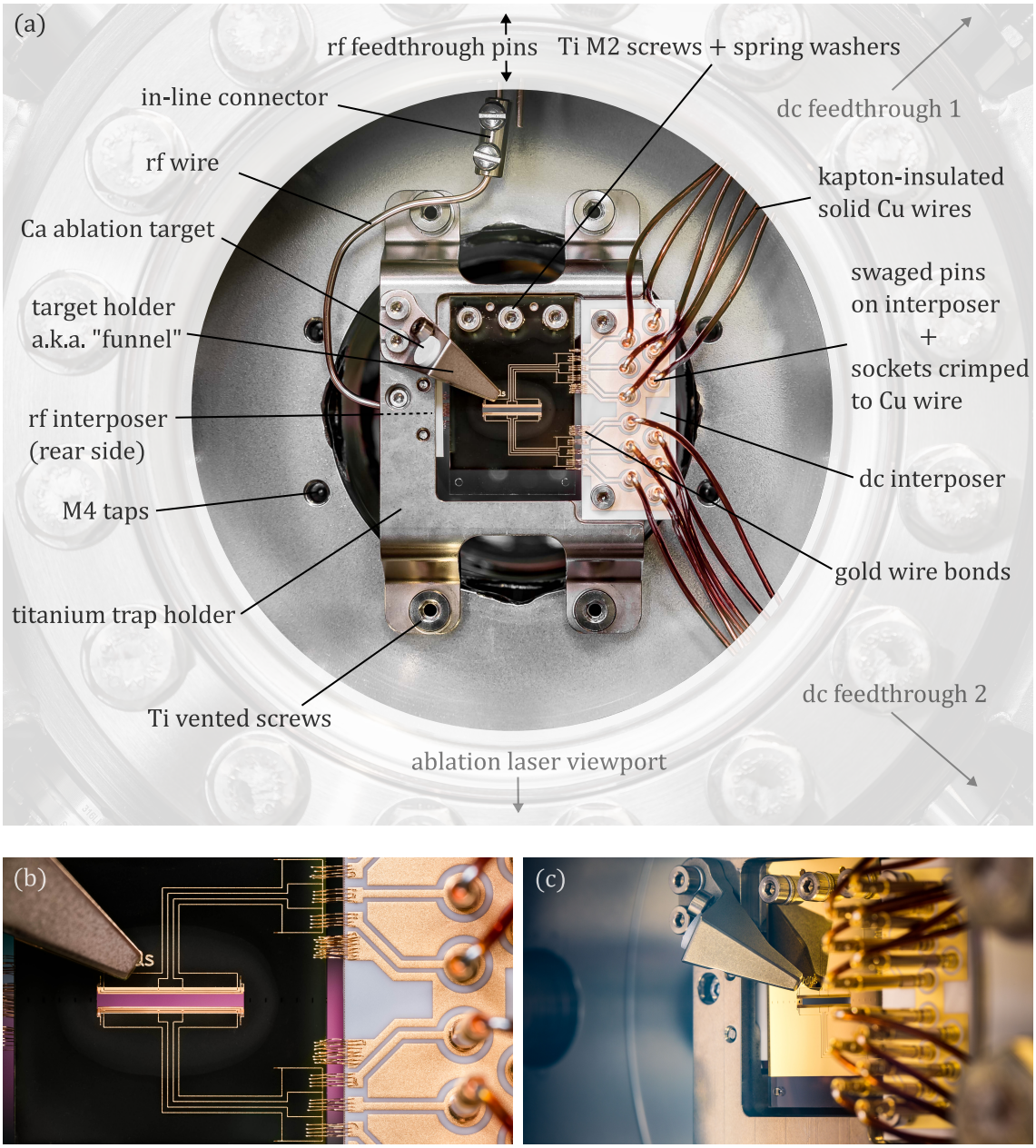

Figure 3.5: Photographs of the ion trap assembly in vacuum. (a) Picture of the assembly seen through the front viewport featuring in-vacuum components. (b) Detailed view of the ion trap showing wirebonds connecting the trap electrodes with the dc interposer board. In the upper left corner the ablation funnel is partly visible. (c) Detailed view from the side as "seen" by a laser beam entering the front viewport at an angle of about 45°. Image credits: David Jordan, IQOQI Innsbruck

Electrical feedthroughs

Two CF16 electrical feedthroughs[15] on the main corpus, each with 8 bare copper pins (AWG 20/0.81 mm diameter) on the air and vacuum side, provide sufficient connections to supply all twelve dc electrodes individually. Another CF16 feedthrough[16] with two bare copper pins (AWG 16/1.29 mm diameter) is mounted on the top flange and is suitable for high voltages up to 6 kV. One of the pins is used to connect the rf electrode. The other one is grounded to the chamber on the air side. The helical resonator is located on top of the rf flange and mounted using dedicated screw holes in the vacuum chamber.

Electrical connections, interposer boards

We completely avoided any solder connection in vacuum to prevent virtual leaks and unwanted residuals of potentially outgassing substances from flux or solder. Instead, we used only crimp, in-line or spring-loaded connectors. Two alumina PCBs, referred to as rf and dc *interposer boards*, are used to interconnect the wires coming from the electrical feedthroughs with the ion trap chip. The gold wirebonding pads and traces are screen-printed on a 96% alumina substrate[17]. The dc interposer board is a double-sided PCB with 6 wirebonding pads on each side. Gold traces connect the wirebonding pads close to the trap chip with the plated through holes on the side away from the trap. These holes accommodate pins[18], which are finally plugged into the corresponding sockets[19] that are crimped onto silver-plated and Kapton-insulated solid copper wires (AWG 20/0.81 mm). On the other side of these wires, spring-loaded sockets[20] are crimped onto the wire and plugged onto the bar copper pins of the vacuum feedthrough. As we reached for a solder-free vacuum apparatus, it turned out to be challenging to mount the gold pins on the interposer. First trials with sinter nano-silver paste were unsuccessful as the connections were found to be highly fragile. Finally, we used a swage assembly tool[21] and a manual arbor press to fasten the hollow cylindrical backside of the pin to the gold-coated dc interposer board. Note that swage assembly is generally not used for ceramic PCB substrates. Due to alumina's brittleness it is a very delicate task and therefore not suited to be applied on a larger scale. To connect the rf feedthrough with the rf interposer board a solid copper wire (AWG 16/1.29 mm) is attached to one of the two pins of the rf feedthrough using an in-line connector [22]. The other end of the solid copper wire was manually flattened and drilled to create a cable lug, which is attached to a gold plated via on top of the rf interposer board using an M1.6 screw and a nut.

Wirebonding

The ion trap is connected to the interposer boards via gold wirebonds[23] with a wire

[15] VACOM CF16LNS-HV1-8-CE-CU081
[16] VACOM CF16LNS-HV6-2-CE-CU13
[17] Elceram, Okružní 1144, 500 03 Hradec Králové, Czech Republic
[18] AccuGlass Products 110008, Gold Pins Male, Type: T2, 20-24 AWG
[19] AccuGlass Products 110009, Gold Sockets Female, Type: T2, 20-24 AWG
[20] Vacom EK-C-CB081, crimp connectors with spring-loaded sockets
[21] Mill-Max 900-00-025-00-415000, Swage Punch & Anvil Kit
[22] Accu-Glass Products, In-Line Connector - 0.059
[23] Wirebonder:F&S Bondtec Bonder 5330; bonding tool: SPT UT45A-C-3540-1.00-CGM

diameter of 50 μm. For low resistance and redundancy of connections, all electrodes are connected with multiple wirebonds, the number of which is limited by space constraints. The dc electrode pads host 4 bonds each, the rf electrode pad hosts 8 bonds. For additional grounding of the trap, multiple wirebonds were placed from both the dc and rf interposer boards' ground to the trap's ground plane.

Viewports

All viewports[24] used for optical access to the trap center are either anti-reflection(AR)-coated for 395, 397, 729, 854, and 866 nm or broadband-coated for the range from 395 to 866 nm on both sides. The CF100 viewport (front) has a substrate thickness of 6.4 mm and is compatible with a spare Silloptics objective[25], which was available in the ion trapping group in Innsbruck. A CF63 viewport grants optical access from the backside of the chamber. In the case of the CF16 viewports, we found that the AR coating on the broadband-coated viewports performs better than the custom AR coating at specific wavelengths, which is why we preferred to use them where possible. Two CF16 viewports are mounted to the left and right side of the main corpus to gain axial access to the trap. Four CF16 viewports are mounted onto the 45°-nipples on the backside of the chamber. The viewport used for the ablation laser beam entering on the bottom of the main corpus is a broadband-coated window ensuring high transmission at 515 nm. The 45°-nipple on the bottom of the chamber is equipped with a Zinc Selenide viewport allowing for transmission of infrared light between 0.6 and 20 μm. It was used to monitor the trap temperature with an infrared camera during electrical tests of the trap. The flanges of all viewports are made of non-magnetic stainless steel 316 LN.

Cleaning and assembly

The vacuum parts as well as tools for the assembly were cleaned according to standard UHV cleaning protocols. If permitted according to the manufacturers' instructions, parts were cleaned with degreaser, acetone, isopropanol and methanol in multiple and repeated steps using an ultrasonic bath. Apart from visible contamination, the vacuum windows were not cleaned since they were delivered UHV ready. In case of stains on the glass surface, we cleaned them with isopropanol and subsequently with methanol according to the manufacturer's cleaning notes.[26] All parts containing copper were not cleaned using acetone but only isopropanol and methanol instead. The oxide layer on the surface of the copper pins of the electrical feedthroughs was manually removed with diluted formic acid[27] before continuing with the cleaning procedure using the ultrasonic bath. The trap chip itself was cleaned by the manufacturer after fabrication and, therefore, not cleaned any further to avoid the introduction of debris into the trenches, which could lead to electrical shorts between electrodes. All vacuum parts were assembled under a laminar flow hood.

[24] MPF Products Inc., 3046 Bramlett Church Rd. Gray Court, SC 29645, DUV grade fused-silica, Corning HFPS,

[25] The Silloptics objective is designed for a substrate thickness of 6 mm.

[26] For more persistent stains acetone can be used first, which should be tested on a clean surface to avoid residual stains and contaminants on in-vacuum parts. This was not necessary in our case.

[27] The feedthroughs were dived into a bath of diluted formic acid ($\sim$ 1 cm deep) for a few minutes. This step was followed by manual etching of the surface using lint-free swabs.

During the assembly of parts inside the vacuum vessel, requiring the exposure of the open vessel to air, it was vented with Argon using the turbomolecular pump.

3.2.4 Bake-out procedure

All metallic in-vacuum parts were air-baked at a temperature of 300 °C for about 24 hours to reduce hydrogen outgassing. All parts attached to the chamber are bakeable up to 200 °C limited by the bake-out temperature of the viewports. After assembly, the vacuum setup was put entirely into a dedicated oven and baked for about eight days at 200 °C while pumping the chamber with a turbomolecular pump[28]. The temperature was ramped up and down automatically with a ramp speed between 0.1 and 0.3 K/min. The whole chamber was wrapped in aluminium foil to provide a more balanced heat distribution and to mitigate stress on the metal-glass interface of the vacuum windows. The vacuum vessel was connected to the turbo pump station by a flexible hose guided through a hole in the oven wall. The parts outside of the oven, such as the bellows connecting the chamber, the tee, the tubes attached to the residual gas analyzer (RGA) and tubes housing a pressure sensor of the turbo pump, were heated via fiberglass-shielded electric heating tapes. The temperature of these parts was monitored using thermoelements at multiple points and ramped up slowly to values well below the maximum temperatures of the individual parts.

During the bake-out, the overall pressure as well as the partial pressures of the most relevant fractions were monitored using an RGA[29]. After baking for several days, the NEGs were put into *conditioning mode*[30], i.e. heated to a moderate temperature of about 200 °C. This facilitates desorption of physisorbed species and reduces outgassing during activation of the NEGs at a later stage. After about 8 days of baking at 200 °C, the pressure had settled and the total pressure was dominated by the partial pressure of hydrogen[31]. The oven temperature was ramped down and at a temperature of about 75 °C displayed by the oven[32], the NexTorr NEG was activated for 1 hour. The CF16 NEG was activated for about 45 minutes with a current of 3.5 A[33]. After the oven had reached room temperature, the ion pump's magnets were installed and the pump was activated subsequently. We kept the valve open for another 10 minutes to eventually pump out outgassing contaminants from the activation of the ion pump. The current of the ion pump displayed on the controller is proportional to the pressure. After cool-down it switched between 0 and 1 nA, the lowest achievable values, limited by leakage currents in the ion pump controller. After a Helium leak test, the valve was closed to isolate the

[28] Pfeiffer Hi Cube 80 Eco

[29] Stanford Research Systems RGA 100

[30] For the NexTorr pump it was activated using the NIOPS controller. For conditioning of the CF16 CapaciTorr NEG, we applied 1.5 A to it.

[31] The pressure was measured close to the turbo pump station. In order to test if it is dominated by the residual pressure of the pump station, the heating tapes were ramped down and the temperature of the oven was ramped down from 200 to 190 °C. The partial pressures, measured by the RGA, did not decrease indicating that they were dominated by the residual pressure in the turbo pump station

[32] The temperature of the chamber was assumed to be substantially higher. The recommended temperature for the activation of the NEGs is 90°C.

[33] The recommended current of 5 A for reaching 450 °C in *nude* configuration can be reduced in case that the NEG is shielded by the chamber walls.

chamber from the turbo pump. Subsequently, we performed another Helium leak test and found that spraying helium directly on one of the 45° CF16 windows caused a temporary increase of the ion pump current from 0 to 5 nA. It is unclear whether this increase can be traced back to a tiny leak or to leakage currents caused by temperature fluctuations in the ion pump due to the helium spray. In spite of these observations, the setup is used in this state and the vacuum quality compares very well to other setups. Experiments indicate low collision rates, e.g. inferred from the analysis of lattice configuration changes. In addition, we observe low rates of chemical reactions forming molecular (dark) ions. Experiments with larger crystals are usually limited by the appearance of additional dark ions after several hours. At this point, the apparatus has been operated for about 4 years.

It is worth noting that we encountered several setbacks during the bake-out procedure: After the first bake-out, the UHV valve, isolating the chamber, was leaking (reason unknown) and had to be exchanged. During the second bake-out, due to a malfunction of an electro-mechanical relais[34], the oven overheated from 200 °C up to about 260 °C within 30 minutes and caused leaks in several windows and damaged the RGA's electron multiplier as a consequence of the sudden increase in pressure. Although care was taken to slowly ramp the temperature up and down, further bake-out runs caused leaks in several CF16 windows until we finally accomplished a low pressure.

3.3 Quantization field and magnetic-field shielding

Low magnetic-field fluctuations are essential for preserving the coherence of the Zeeman ground-state qubit as well as the optical qubit encoded in one of the $S_{1/2}$ states and one state in the $D_{5/2}$ manifold. The quantization axis in the presented apparatus is oriented in the horizontal plane at an angle of 45° with respect to the crystal plane (see Fig. 3.15). It is defined by permanent magnets providing a constant field of about 4.1 Gauss without the need of stable current sources. The resulting Zeeman splitting of the two $S_{1/2}$ states is about 11.5 MHz. We use cylindrical, axially magnetized Samarium Cobalt (Sm_2Co_{17}) magnets with a low temperature coefficient[35]. The magnet holders are placed on top of the breadboard at two opposite sides of the vacuum chamber at a distance of about 250 mm between the two holders. Each holder accommodates 74 slots for individual magnets, arranged in three concentric rings with the radii $r_1 = 20.5$ mm, $r_2 = 27.75$ mm and $r_3 = 35$ mm. This design enables a flexible arrangement of the magnets to provide a homogeneous field in the trap center. A 3d image of one of the two holders is shown in Fig. 3.7(a). We use an equal direction of polarization for all inserted magnets. An asymmetric spatial arrangement of the magnets, shown in Fig. 3.7(b) and (c), is empirically found to minimize the magnetic-field gradient. To this end, the gradient across a large ion crystal is measured via correlation spectroscopy[36], a method presented in detail in

[34] For the bake out, an oven at the IQOQI Innsbruck (ConThermo Wärmeschrank 600 ALV) was used. The oven manufacturer recommends to exchange the relais every year.

[35] BVI Magnet GmbH, Sm_2Co_{17}, material: XGS24LTC, size: 6 x 10 mm (diameter x height), Br = 1T±0.04T, temperature coefficient of remanence: 0.03 %/K

[36] Using N-ion correlation spectroscopy phase differences across the ion crystal can be detected efficiently and precisely in the presence of correlated phase noise.

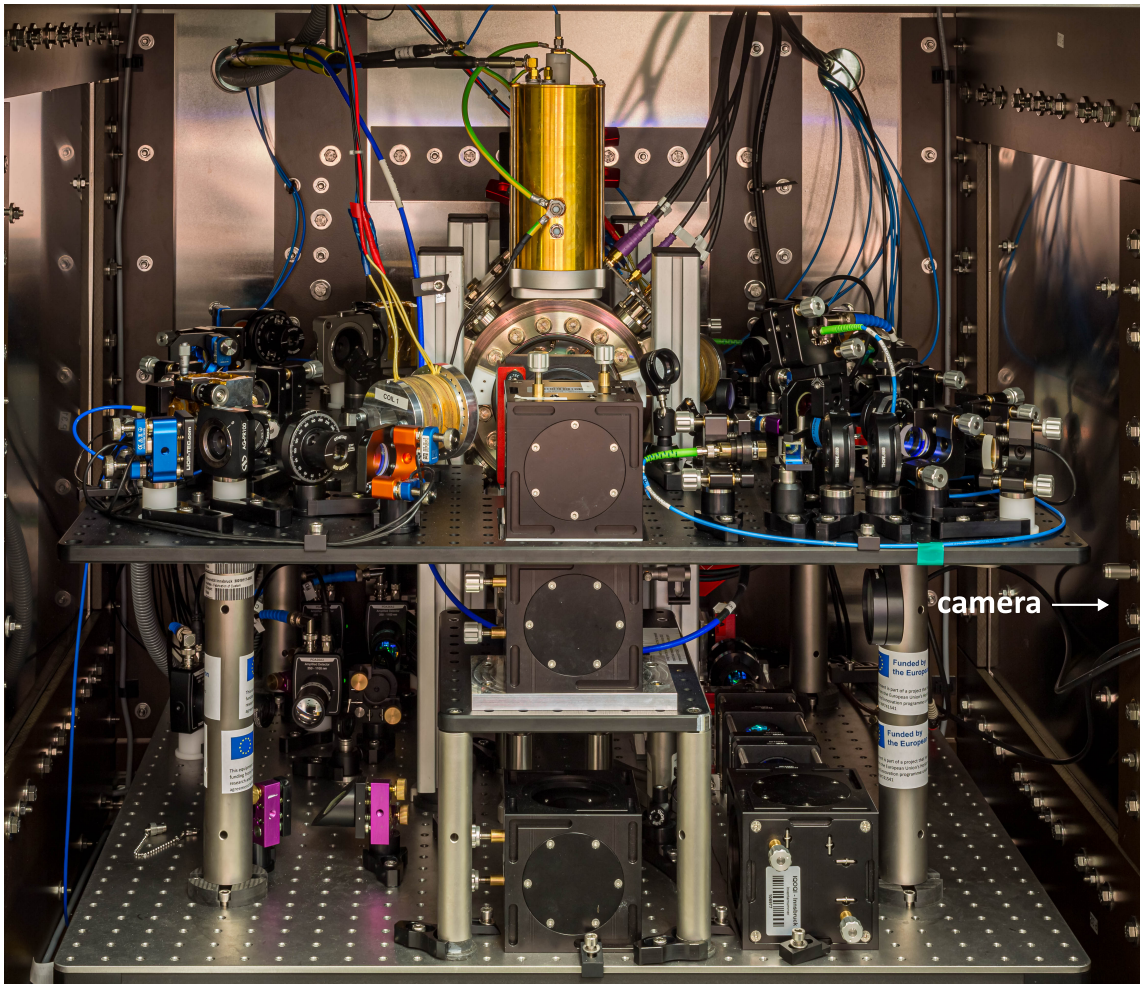

Figure 3.6: Photo of the experimental setup inside the μ-metal shield. The top breadboard around the trap is used for optical setups used to manipulate and guide the laser beams addressing the ions within the horizontal plane. It further hosts the magnet holders and is connected to aluminium profiles (Item) holding the vacuum chamber. The bottom breadboard (70x70 cm) hosts photodiodes used for laser power monitoring and will host the setup for single-ion addressing in the near future. The small breadboard in between the lower and upper layer accommodates the objective as well as a mirror holder (black cube) with a dichroic mirror to guide the collected light to the camera and PMT while transmitting light at 729 nm for single-ion addressing. Image credit: David Jordan IQOQI

Refs. [76] and [61].

A residual field gradient can be compensated with the help of two opposing coils in anti-Helmholtz configuration mounted behind the permanent magnets. To this end, we apply a current of 39 mA to the coils. Additional coils in Helmholtz configuration (behind the gradient compensation coils, see Fig. 3.6) would, in principle, allow for the compensation of ac magnetic-field noise including 50-Hz-noise and its harmonics. This can, for instance, be achieved by using a feed-forward approach as implemented successfully in two other ion-trapping experiments in Innsbruck [126]. However, this has not been required in the presented apparatus.

In order to attenuate external ac and dc magnetic fields, the ion trap setup is enclosed in a multi-layer metal shield from Imedco[37] consisting of two adjoined μ-metal layers of 1 mm thickness each and a thick layer of highly conductive aluminium on the outside. Holes in the shield allow the passage of cables and optical fibers as well as the ions' fluorescence towards the camera. A hinged door enables full access from the front side of the vacuum chamber. Closable apertures in the side walls allow restricted access from all other sides. The shield itself is mounted to the optical table via two plates on the side of the shield. Aluminium blocks are used as a spacer between the optical table and the shield. The breadboard hosting the trap setup is held by five stainless steel posts, which are mounted directly on top the optical table to decouple the trap setup mechanically and electrically from the magnetic shield. Five holes in the bottom of the magnetic shield allow for the passage of these posts. Sorbothane pads on top of the posts decouple the breadboard from vibrations from the table and in addition, electrically isolate the trap setup from it.

The occurrence of a geomagnetic storm[38] was exploited to estimate the attenuation of the installed μ-metal shield in the experiment. To this end, correlation spectroscopy measurements [76] were carried out to track the dc magnetic-field changes seen by the ions over about 500 minutes, which were caused by the enhanced geomagnetic activity in Innsbruck's proximity. The fluctuations seen in the experiment match well with the earth magnetic field changes measured by the *Geomagnetic Observatory Fürstenfeldbruck* (near Munich). A fit of the combination of the north-south and the east-west field components suggests a dc field attenuation factor of 66 with an angle of 38° between the quantization field and the east-west field component.

3.4 Trap electronics

The following sections describe the electronics to supply the trap electrodes with rf and dc voltages. A resonant circuit, described in Sec. 3.4.1 creates high rf voltage at a frequency of about 43 MHz. Using an ion crystal's motional modes to mediate entangling interactions requires stability of the motional mode frequencies. Therefore, an active rf power stabilization circuit is employed, which is described in Sec. 3.4.2. The dc electronics including voltage dividers and the filter design to suppress high frequency noise are discussed in Sec. 3.4.3. In Sec. 3.4.4 the calculation of voltage sets to control the position,

[37] Imedco AG, Industriestrasse West 14, 4614 Hägendorf, Switzerland

[38] In the night from the 01.12.2023 to the 02.12.2023 polar lights were visible by eye in South Germany.

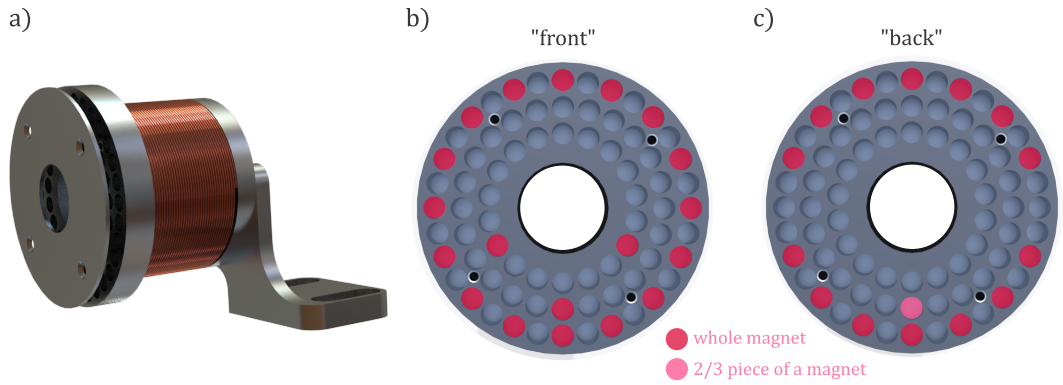

Figure 3.7: (a) 3d image of one of the two permanent magnet holders. The magnets are placed in cylindrical recesses in the holder behind the lid, which is slightly lifted in this image. Holes in the center of the holders provide optical access along the direction of the magnetic field. (b-c) Front view of the two permanent magnet holders (shown without mount) and asymmetric arrangement of magnets as used in the setup. The holder in the front (b) accommodates a total of 19 magnets, with 16 magnets placed in the outer and 3 in the inner ring. The holder facing the backside of the vacuum vessel's main corpus (c) contains 15 magnets in total. 14 magnets are placed in the outer ring. An additional magnet was cut into two pieces with about 2/3 and 1/3 of the original size. The 2/3-piece is placed in the middle ring of the holder.

orientation and shape of planar crystals, e.g. for minimizing micromotion (Sec. 4.3), is described.

3.4.1 rf supply

The rf drive circuit is shown schematically in Fig. 3.9(a). Its core represents an RLC series circuit consisting of Ohmic losses, a helical resonator and the ion trap itself. The rf drive signal is generated by a signal generator[39]. It is pre-amplified by a high-power amplifier[40] with a gain of approximately 43 dB before subsequent amplification by the resonant circuit. The design of the helical resonator follows a guideline given in Ref. [127]. The choice of the resonance frequency is governed by the targeted secular frequency and the aim for a low q parameter of $q \lesssim 0.1$. Our ion trap is operated typically at rf voltages of about 1 kV peak-to-peak with a rf drive frequency of $\Omega_{\mathrm{rf}} \approx 2\pi \times 43.2$ MHz. A resonance frequency of about 43 MHz is obtained by proper choice of the number of windings defining the height of the coil. A rendering of the helical resonator on top of the vacuum chamber is displayed in Fig. 3.8(a) and a top view of the inside of the shield is shown in Fig. 3.8(b). The dimensions of the resonator wire, the winding pitch, the shield were chosen as in previous experiments in Innsbruck. Inside the helical resonator a copper wire with a diameter of 5 mm is wound with a winding pitch of 10 mm forming a coil with a diameter of 40.4 mm and a height of 70 mm. The outer shield is a copper cylinder with an inner diameter of 80 mm

[39] Rohde&Schwarz SMB-100B
[40] Mini-Circuits LZY-22+

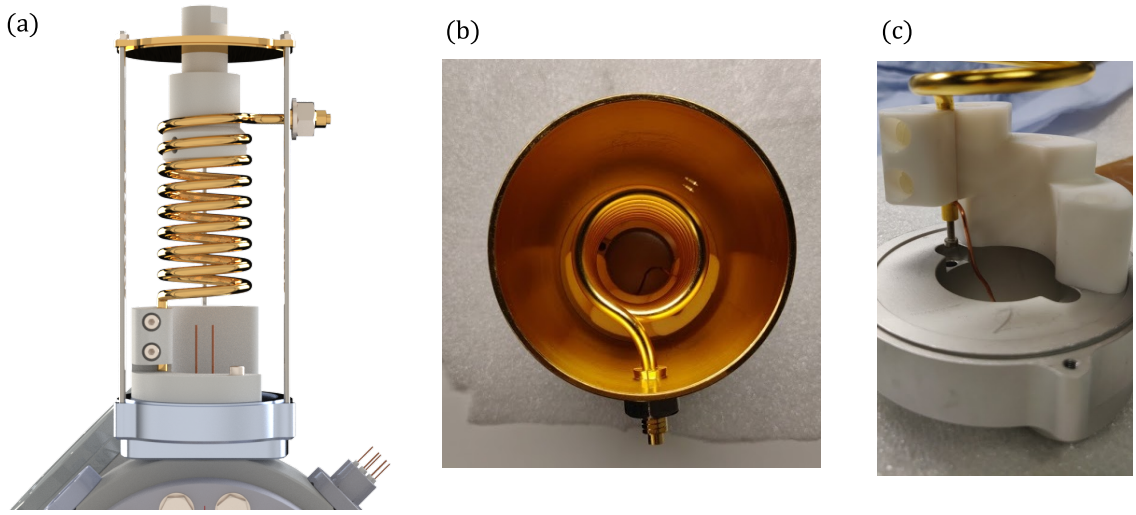

Figure 3.8: Helical resonator setup. (a) 3d rendering of the front view of the resonator with opaque shield on top of the vacuum chamber. The Teflon slider provides a spring-loaded electrical contact to the helical resonator coil. (b) Top view with open lid and without Teflon slider. (c) The resonator coil is clamped by the Teflon holder on the bottom of the resonator. On of the two wires from the electrical feedthrough (shown straight in (a)) is bent and inserted into a hole through the radial direction of the coil wire. It is fixed with a screw in a threaded hole from the bottom of the coil. The other wire is grounded via the vacuum chamber.

and a thickness of 2 mm. All copper parts are coated[41] with 30 μm of silver and 0.5 μm of gold on top to increase the long-term stability of the circuit. Oxidation of the copper could otherwise change the quality (Q) factor over time. To connect the resonator coil to the rf vacuum feedthrough, the feedthrough pin is inserted into a hole through the 5-mm-wire in the lower part of the coil and clamped with a screw (see Fig. 3.8(c)). Teflon parts[42] on the bottom of the resonator are used to clamp the coil and mount it in an upright position. The input signal is coupled to the resonator via a spring-loaded sliding contact mounted in a threaded cylindrical Teflon part. This Teflon slider is screwed into the inner part of the coil. The sliding contact allows for impedance matching by adjustment of the point of electrical contact along the coil.

To characterize the performance of the resonant circuit, the Q factor was determined. To this end, using a network analyzer, the scattering parameter of the reflected signal S_{11} is measured as a function of the frequency. With $\Delta\omega_S$ being the $1/\sqrt{2}$-full-width S_{11} bandwidth, the Q factor is calculated as $Q = 2\frac{\omega_0}{\Delta\omega_S}$ [128]. The Q factor, in turn, is related to the voltage gain of the circuit via $G_\mathrm{V} = \sqrt{Q/(Z_\mathrm{wave}\Omega_\mathrm{rf}(C_\mathrm{trap} + C_\mathrm{self}))}$, where we assume the source impedance Z_wave to be 50 Ohm and the trap circuit to be perfectly

[41] Ögussa GmbH, Liesinger-Flur-Gasse 4, 1230 Vienna, Austria

[42] Polyoxymethylene (POM), which is easier to machine than Teflon, was tested as a material for the coil mount and the slider but resulted in a fewfold reduction of the resonator's Q factor.

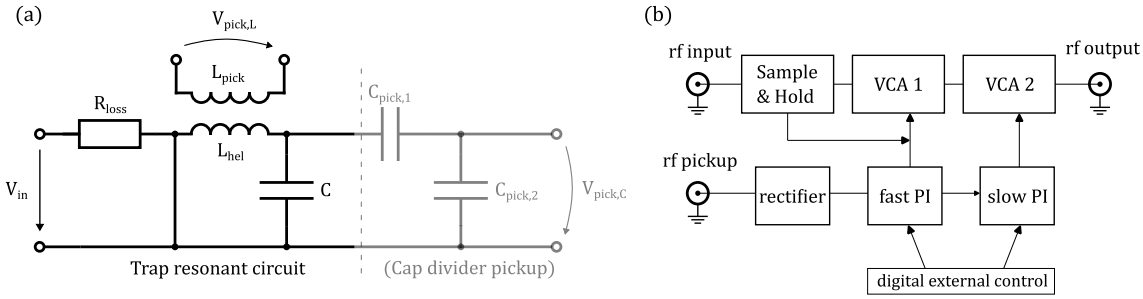

Figure 3.9: (a) Schematic of the trap rf circuit. The capacitance C is composed of the trap's capacitance C_{trap} and the helical resonator's self capacitance C_{self}. The pickup for rf power stabilization is done inductively via pickup coil. The grayed out part shows the initial setup with a capacitive divider used for the voltage pickup. (b) Working principle of the circuit for rf power stabilization. A description is provided in the main text.

matched. The resonator's self capacitance is determined from repeated measurements of the resonance frequency ($\Omega_{\text{res}} = 1/\sqrt{L(C_{\text{self}} + C_{\text{def}})}$ using various defined capacitive loads C_{def} yielding $C_{\text{self}} \approx 6.5$ pF. The resonance frequency of the loaded circuit, i.e. including the trap and its wiring, is about $2\pi \times 43$ MHz and the Q factor is determined to $Q \approx 140$. A measured voltage gain of $G_V \approx 24$ yields a total capacitance of the resonant circuit of $C = C_{\text{trap}} + C_{\text{self}} \approx 18$ pF suggesting an upper limit for the trap capacitance of $C_{\text{trap}} \approx 12$ pF[43].

3.4.2 rf power stabilization

rf stabilization circuit

In the quantum simulation experiments, the entangling interactions are mediated by the out-of-plane motional modes. Along with the dc voltages, the rf power applied to the trap rf electrodes determines these secular oscillation frequencies. Therefore, the rf power is stabilized to ensure motional coherence (on the order of hundreds of milliseconds) during entangling interactions and to guarantee the long-term stability of the mode frequencies. To this end, a small fraction of the trap drive voltage is picked up, either capacitively or inductively, serving as input signal for a home-built stabilization circuit. This circuit was developed by Matthias Bock based on a design by Gerhard Hendl. A schematic of the circuit's working principle is shown in Fig. 3.9(b).

In the current setup, the rf signal is picked up inductively (see next subsection for a short discussion about the pick-up) before being rectified and amplified. The stabilization of the rf power is based on two serial PI circuits, a slow and a fast one, acting on voltage-variable attenuators (VVA). The slow PI circuit compensates slow changes, e.g. due to thermal drifts, and maintains the set point of the fast PI circuit. This avoids the necessity to change the PI parameters of the fast circuit over the dynamic range resulting from a strong nonlinear behavior of the VVA. The fast PI circuit is purely analog while the slow

[43] The given value of the trap capacitance C_{trap} also includes the capacitances from the trap connections and wiring, presumably on the order of a few pF.

one is implemented digitally using the SPI interface of an Ethernet-controlled Arduino as well as ADCs and DACs. The interface allows for almost all parameters to be remotely controlled, among them the setpoint of the rf power, the PI parameters and the state of the sample-and-hold circuit. This opens up the ability to perform a controlled and precise attenuation of the trap potential, e.g. to kick out ions of the trap, which is crucial for fast deterministic loading of large ion crystals. Only the PI parameters of the fast PI circuit have to be modified via dip switches changing the feedback capacitance and resistance.

To achieve a good resolution of the rf power's setpoint (corresponding to a secular frequency step size on the order of a few Hz) a 20-bit DAC is used to generate the setpoint voltage of the fast PI. The stabilization of the rf power can be switched on and off by an external trigger signal (sample-and-hold), which digitally deactivates the slow PI circuit and bypasses the update of the error signal in the fast PI circuit using an analog switch[44]. At typical trapping conditions, the rf output power of the signal generator is chosen such that the output voltage of the slow PI circuit is about 9 V corresponding to a regime of low attenuation close to the limit of the VVA. This prevents the unintentional application of high voltages to the trap. To minimize the effect of thermal drifts, the temperature of the circuit board is stabilized.

rf pick-up

An active stabilization of the rf voltage used to drive the trap requires a pick-up of a small fraction of the applied voltage. A reliable pick-up can also be useful to estimate the voltage applied to the trap rf electrode in contrast to relying on the pre-determined value of the voltage gain of the resonant circuit. However, this necessitates a proper calibration of the pick-up, which is not straightforward and often requires an active probe.

The rf pick-up can be realized either capacitively or inductively. A capacitive voltage divider consisting of at least two serial capacitors (see Fig. 3.9(a)) has the disadvantage that the capacitors add up to the total capacitive load of the circuit, decreasing the Q factor and thus the voltage gain of the system. In addition, the capacitors can be susceptible to changes in the surrounding temperature. However, a capacitive pick-up is easy to implement and the pick-up ratio can be easily adjusted since it is given by the ratio of capacitances $\frac{V_\mathrm{p}}{V_\mathrm{trap}} = \frac{C_\mathrm{pick,1}}{C_\mathrm{pick,1}+C_\mathrm{pick,2}}$. An inductive pick-up does not substantially contribute to the circuit's load and is not as sensitive to thermal drifts. Another major advantage is that it is easy to galvanically isolate the pickup from the trap circuit, which is beneficial to avoid grounding problems. On the other hand, the inductive pick-up might be more difficult to set up and a change in the geometry of the pick-up coil or its placement entails a change in the coupling ratio, adding to the complexity of calibration.

In our experiment, an initially installed capacitive pickup[45] turned out to be insufficiently stable[46] and was replaced by an inductive pickup. Given good knowledge of the gain of

[44]The fast PI circuit's output voltage corresponds to the last value before triggering and is governed by a capacitor. In the absence of leakage current the output would be kept constant. In practice, the capacitor discharges slowly and the rf output voltage drops to zero.

[45]The employed capacitive divider had a voltage ratio of 1000 given by $C_{p,1} = 0.2$ pF (4 capacitors with 0.8 pF in series) and $C_{p,2} = 200$ pF.

[46]Simply using a bidirectional coupler[47] to pick off the signal instead of the capacitive divider improved

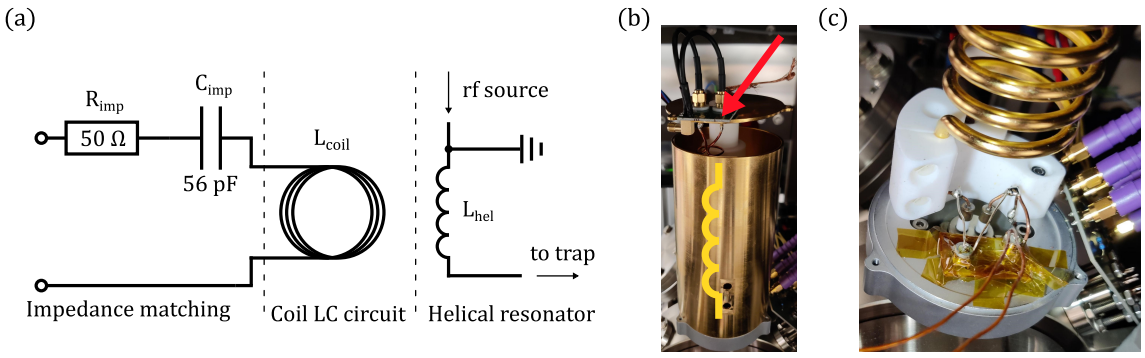

Figure 3.10: (a) Impedance matching circuit for the rf pickup. (b) Photograph of the first prototype of the inductive pickup coil, showing the position of the coil mounted on the lid of the helical resonator (red arrow). The position of the helical resonator coil is indicated in yellow. The small PCB on top of the lid serves for impedance matching. (c) Photograph of the PCB hosting the capacitive divider for rf pickup. The PCB is fixed via Kapton tape to the bottom mount of the helical resonator. Connections are soldered to the two pins of the vacuum feedthrough (rf + ground). Two Kapton-insulated, stranded copper wires are used as a twisted pair to guide the rf pickup signal from the capacitive divider PCB inside the helical resonator to the outside.

the circuit obtained from previous measurements, a precise calibration was not required and the pick-up coil could just be optimized to provide a good signal-to-noise ratio for active stabilization. A small coil[48] was mounted on the lid of the helical resonator to pick up the signal in the upper part of the resonator. A small PCB with an RC-impedance-matching circuit ($Q \approx 1$, $R = 50$ Ohm, $C = 56$ pF) is placed in a brass housing on top of the resonator lid. This ensures that the circuit's resonance frequency is fixed at the trap drive frequency as the 50-Ohm resistor ensures a purely Ohmic impedance matched to the BNC cable. This renders the pick-up, to first order, insensitive to changes of the cable's capacitance.

3.4.3 dc supply

The dc voltages on the eight endcap segments and the four middle segments are supplied by a precise high-voltage multi-channel power supply[49], often referred to as *iseg box*. The voltage source is mounted in a crate and controlled by an Ethernet-compatible controller[50]. Since voltages of only up to a few tens of volts are required, we use voltage dividers to exploit the iseg module's stability at higher voltages. In typical trapping operation, about 300 V are generated by the voltage source. The choice of the components for the voltage dividers is restricted by the current limit of the iseg box of $I_{\mathrm{lim}} = 4$ mA. For the

the motional coherence significantly.

[48] A copper wire with a diameter of 1.5 mm was wound by hand to form a coil with a few windings and a diameter of about 1.5 cm.

[49] iseg Spezialelektronik GmbH, EHS F2 20p_SHV

[50] iseg Spezialelektronik GmbH, CC 24 MASTER controller

endcap segments the dividers consist of $R_{\mathrm{div},1} = 100$ kΩ[51] and $R_{\mathrm{div},2} = 10$ kΩ[52], and $R_{\mathrm{div},1} = 100$ kΩ and $R_{\mathrm{div},2} = 5$ kΩ[53] for the middle segments, yielding a splitting ratio of about 1:10 and 1:20 for the endcaps and middle segments, respectively. The voltage applied to the middle segments is roughly a factor of 2 lower than the voltage on the endcap electrodes. A parallel capacitor with $C_{\mathrm{div}} = 2.2$ nF serves as a moderate filter with a cut-off frequency of about 7 kHz. Since the resistance of the high-voltage resistors vary in a specified range of ±1 %, the dc channels were calibrated individually using a high-precision voltage meter.

In order to reduce high-frequency noise on the dc electrodes, potentially heating the ion crystals at their secular frequencies, we use first-order RC low-pass filters with a cut-off frequency of about 300 Hz. The two filter PCBs are mounted directly on top of the two dc vacuum feedthroughs. Each RC filter line consists of a resistor with $R_{\mathrm{filter},1} = 100$ kOhm and a capacitor with $C_{\mathrm{filter}} = 4.7$ nF. To enable faster switching between applied voltages, a parallel resistor with $R_{\mathrm{drain}} = 10$ MOhm connected to ground was introduced to the filter design allowing a fast discharge of the filter capacitor on the order of $\tau = R_{\mathrm{drain}}C \approx 4.7$ ms, the discharge time of the RC circuit. Subsequently, the voltage dividers were added to the setup resulting in an even faster drain via the second resistor of about 50 ns and 25 ns for the endcap and middle segments, respectively.

Initially, an additional resistor with $R_{\mathrm{filter},2} = 100$ kOhm was placed before the trap to serve as a second RC filter stage in conjunction with the trap capacitance. However, the additional resistors introduced Johnson noise on the trap dc electrodes and, moreover, may have impaired the grounding of parasitic rf voltage on the dc electrodes. These resistors were found to be the dominant cause of a high heating rate of about 16 phonons/s in the experiment. After removing them from the circuit the heating rates could be improved substantially to about 0.6 phonons/s. Note that a full re-design and exchange of the PCBs is a delicate task since the filter PCBs are connected to the feedthrough pins via metal sleeves, which are soldered into vias in the PCBs. The sleeves are pushed onto the feedthrough pins to create the electrical connection. This causes mechanical stress on the pins and repeated manipulation is considered risky in view of a vacuum leak.

3.4.4 dc electrode control

Given a perfectly symmetric trap, to trap a crystal in a 2d configuration, one voltage is applied to all endcap electrodes and a different voltage to all middle segments. Due to imperfections in the trap geometry, additional dc voltages need to be applied to some of the electrodes to align an ion crystal with the trap center and adjust rotations of the crystal to minimize the micromotion in out-of-plane direction. The voltage sets required for specific actions, such as rotations and shifts of the crystals, as well as adjustments in confinement, are calculated based on finite-element simulations[54] of the electric field

[51] 100 kΩ: Vishay RH050100K0FE02
[52] 10 kΩ: Vishay RH05010K00FE02
[53] 5 kΩ: Vishay RH0505K000FE02
[54] The simulations were carried out using COMSOL Multiphysics design suite. More detailed information on finite-element simulations of our trap can be found in [61]

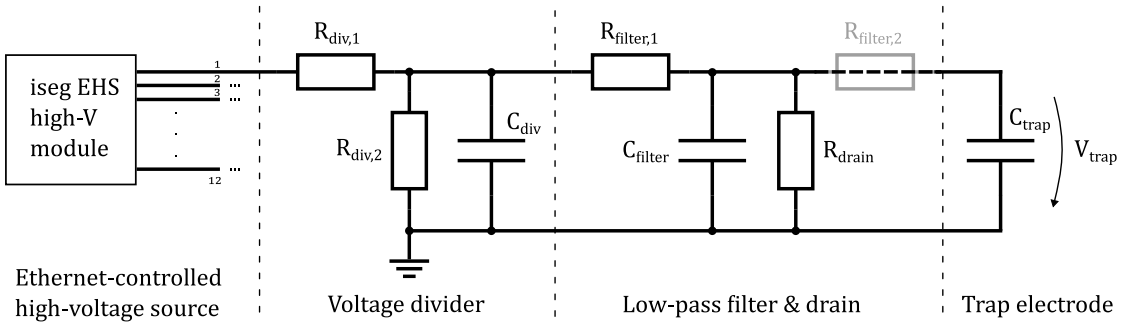

Figure 3.11: Schematic circuit of a single dc supply line from the high-voltage module to the trap electrode. The circuit of all other dc lines are equivalent.

created by the trap electrodes. This procedure coarsely follows Refs. [129] and [130] and is described in the following.

As a first step, finite-element simulations for all twelve dc electrodes are carried out individually by simulating a voltage of 1 V on one electrode while keeping the others at ground. The electrostatic potential $\phi_k(x, y, z)$ created by each electrode k is determined on a mesh of discrete coordinate triplets (x_i, y_i, z_i). The electrode potentials can be expanded into $n_m = 9$ terms including 3 linear terms, 3 harmonic terms and 3 terms describing rotations, given by

$$\begin{aligned}\phi_k = \alpha_{1,k}x + \alpha_{2,k}y + \alpha_{3,k}z + \alpha_{4,k}x^2 + \alpha_{5,k}y^2 + \alpha_{6,k}z^2 + \\ + \alpha_{7,k}xy + \alpha_{8,k}yz + \alpha_{9,k}xz,\end{aligned} \tag{3.1}$$

where $\alpha_{k,1}, \ldots, \alpha_{k,9}$ are the expansion coefficients for each electrode k. The Laplace equation $\Delta\phi = 0$ forces at least one of the harmonic coefficients of the total electrostatic trap potential to be negative[55]. Therefore, the potential of each of the k electrodes can also be written in form of only $n_m = 8$ spherical harmonic terms as

$$\begin{aligned}\phi_k(x, y, z) = \beta_{1,k}x + \beta_{2,k}y + \beta_{3,k}z + \beta_{4,k}(x^2 - y^2) + \beta_{5,k}(2z^2 - x^2 - y^2) + \\ + \beta_{6,k}xy + \beta_{7,k}yz + \beta_{8,k}xz \quad .\end{aligned} \tag{3.2}$$

The harmonic terms in Eq. (3.2) are intuitive to interpret when considering the classical design of a linear Paul trap: The endcap electrodes create a potential in the form of $\propto 2z^2 - x^2 - y^2$ confining in z-direction while repelling in $x-$ and $y-$direction. The dc voltages on the blade electrodes create potentials of the form $\propto x^2 - y^2$ responsible for the radial anisotropy (radial mode splitting). The equations (3.2) can be rewritten as

$$YM = \phi \ , \tag{3.3}$$

where the $n_i \times n_k$ matrix ϕ contains the electrostatic potentials $\phi_k(x_i, y_i, z_i)$ as columns, M is an $n_m \times n_k$ matrix containing the $m = 8$ coefficients $\beta_{m,k}$ for each electrode k and

[55] An electrostatic potential cannot trap a charged particle in all three directions, which is known as *Earnshaw's theorem*.

Y is an $n_i \times n_m$ matrix containing the n_m bare terms (without the coefficients $\beta_{m,k}$) in Eq. (3.2) evaluated at the coordinate triplets (x_i, y_i, z_i) of the simulated grid. Equation (3.3) represents an overdetermined problem, which can be solved for M by determining the pseudoinverse[56] Y^{-1} based on a singular-value decomposition. This step corresponds to a fitting of the simulated potentials ϕ_k by Eq. (3.2). Finally, the voltage sets required for control of the total potential can be obtained by calculating another pseudoinverse M^{-1}. The matrix M^{-1} contains the eight voltage sets that must be applied to the 12 electrodes to control the eight individual terms in Eq. 3.2, while minimizing the impact on all other components of the potential. These eight "unit" voltage sets U_k for control of the individual actions on the potential are given by

$$U_k = M^{-1}\hat{\mathbf{m}}_\mathbf{k} \ , \tag{3.4}$$

where $\hat{\mathbf{m}}_\mathbf{k} \in \{(1, ..., 0), (0, 1, ..., 0), ..., (0, ..., 1)\}$.

Instead of calculating the pseudoinverse, one could use a minimum norm least-squares solution[57] to solve the linear equation (3.3) or apply a *Tikhonov* regularization, which essentially smooths the truncation of singular values compared to the Moore-Penrose pseudoinverse. For the presented trap, however, the various methods yielded the same results and were almost independent of the used regularization parameter.

In the presented experiments, we apply pre-calculated voltage sets solely to the endcap segments. This was necessary because, during the initial phase of the project, the voltage control of the middle segments suffered from a time lag in the communication between the experiment control PC and the power supply[58]. Consequently, the voltages on the middle segments are currently adjusted manually to position the ion crystal along the y direction. Only after that, we control the potential by applying multiples of the pre-calculated voltages to the endcap electrodes, e.g. to shift or tilt the crystal. By doing so, we accept that these voltage sets are not optimal in reducing the impact on other spherical harmonic terms. In the future, voltage sets including the middle segments will be applied with the goal of controlling the potential in a more deterministic way. However, certain electrode geometries as well as imperfections in the alignment lead to undesired effects on other terms of the trapping potential. This cannot be completely avoided unless the impact of voltage changes on the individual electrodes are fully mapped out in experiments.

3.5 Experiment control

The states of the ions are manipulated by laser pulses of typically a few tens to hundreds of microseconds using acousto-optic modulators. The required phase coherent and precisely timed radio-frequency pulses are generated by a commercial FPGA-based Sinara system from M-LABS[59] in combination with *Advanced Real-Time Infrastructure for Quan-*

[56] The MATLAB function *pinv* is used for this task. It calculates the Moore-Penrose pseudoinverse.
[57] MATLAB's *lsqminnorm* was used.
[58] W-IE-NE-R MPV 8120I
[59] The Sinara hardware platform is manufactured by Creotech Instruments S.A., ul. Jana Pawła II 66, 05-500 Piaseczno, Poland

tum physics (ARTIQ) featuring a python-based high-level programming language (ARTIQ python). Both hardware and software components are described in the following sections.

3.5.1 Experiment control hardware

The modular Sinara system features an FPGA-based *carrier* module[60] as the main device communicating with up to 12 modules plugged into the same backplane of the rack-mountable crate. To extend the number of modules, a second Sinara crate containing an additional carrier module is used as a synchronized satellite device, accommodating up to 12 additional modules usable for the experiments. The system allows for generating signals with a timing accuracy on the ns-scale. Four modules[61] hosting four direct digital synthesis (DDS) chips each are used to generate the rf signals required to drive and switch the AOMs creating the laser pulses used for photoionization, Doppler and EIT cooling, and repumping from metastable states. For coherent qubit manipulation 3 modules[62] hosting 2 arbitrary waveform generators each (AWG) are used for global manipulation and future single-ion addressing at 729 nm as well as for driving stimulated Raman transitions at 395 nm. The AWGs allow for amplitude shaping of the laser pulses in order to avoid off-resonant carrier excitation. All rf output signals are amplified by network-controlled amplifiers[63]. The ARTIQ *SU Servo* feature is used to stabilize the intensity of the lasers used for cooling and repumping. The light is sampled by photodiodes[64] in combination with an 8-channel ADC module[65]. The sampled signals are used by the servo to control the amplitude of the Urukul's DDS rf output driving the AOMs. A thorough characterization of the circuit and its performance has not been conducted.

Digital I/O channels[66] are used to trigger external devices such as mechanical shutters, electronic rf switches (e.g., to switch between various laser beams connected to the same DDS output channel), and the EMCCD camera. For the experiments presented in this work, a NIDAQ card [67] built into the experiment control PC generated the signals triggering individual laser pulses from the ablation laser used for ion loading and controlling the servo-motor of a rotation mount adjusting the power of ablation laser pulses. A photodiode detects the ablation laser pulses and triggers the generation of a 375-nm laser pulse (second photoionization step) via the NIDAQ card in order to reduce the time of illumination with UV light potentially creating free electrons from the trap electrodes. In the meantime, however, the electronic setup for ablation laser loading has been updated and is now also controlled by the Sinara hardware. The NIDAQ card has thus been removed from the setup.

[60] Sinara 1124 Carrier "Kasli 2.0"
[61] Sinara 4410 DDS "Urukul"
[62] Sinara 4624 AWG "Phaser"
[63] Creotech Instruments Booster, 8-channel rf power amplifier
[64] Thorlabs PDA10A2 and Thorlabs PDA36A2
[65] Sinara 5108 "Sampler"
[66] Sinara 2128 8-channel isolated TTL cards
[67] National Instruments (NI) PCIe- PCIe-6363, X Series DAQ

3.5.2 Experiment control software

The experiment control software used in the experiment, named *Serles*, is owned and continuously developed by AQT[68]. The main framework of Serles is adapted and extended to the needs of the experiments with 2d crystals described in this work. The control software is written in *Python* interfacing naturally with the ARTIQ-Python language. A local, in-memory key-value database enables rapid querying and storage of the experimental parameters as well as the latest data set. The software comprises standard Python code and runtime-critical code implemented as ARTIQ kernels. The code written in the ARTIQ kernel environment is compiled into machine code by the ARTIQ compiler and executed on the FPGA chip, which forms the core of the ARTIQ sinara hardware.

The experimental setup is controlled by two PCs: one main control PC hosting and executing the Serles software and a second PC dedicated to Piezo mirror control, laser control, and wavemeter readout, with the help of which the lasers are locked. We use a separate PC to avoid runtime-critical interference with the main control PC. Beyond that, all components in the experiment can be controlled via Serles. In the graphical user interface (GUI), all relevant experimental parameters can be set, ions can be loaded and kicked out with just a few mouse clicks, and the trap dc and rf voltages can be controlled and monitored. Experimental sequences with adjustable parameters can be integrated directly into the GUI window. More complex measurements, e.g. scans over multiple parameters, are run using dedicated Python scripts. In general, the software allows to scan each adjustable parameter in a measurement sequence. Each scan is saved as a single file in *JSON* format.

A camera widget features the calibration for quantum state detection, and monitoring of live crystal images. Furthermore, various crystal configurations can be detected and classified automatically to post-process data and to monitor the stability of a crystal over time. An overview on the state detection and read-out is given in Sec. 3.5.4; for more details on the analysis and classification of lattice crystal configuration please refer to Sec. 4.5.

3.5.3 Electrical connections and grounding

When looking at typical trapped-ion experimental setups, it might come as a surprise that organized wiring and well-defined connections of lab devices are crucial for the performance of a trapped-ion apparatus. Electric-field noise on the trap electrodes, e.g. due to technical noise or Nyquist-Johnson noise, can lead to an increase in the heating rate whereas magnetic-field noise at various frequencies can lead to decoherence and shot-to-shot variations during measurements. In many cases a poor performance can be traced back to noisy power supplies or ground loops. An insightful review of electric field noise in ion-trap experiments can be found in [119].

In the experimental setup presented here, great care is taken to ensure well-defined and isolated ground connections to prevent ground loops. The connections between the devices involved in the experiment control are schematically shown in Fig. 3.12. All devices in

[68] Alpine Quantum Technologies GmbH, spin-off company of the Innsbruck ion-trapping group

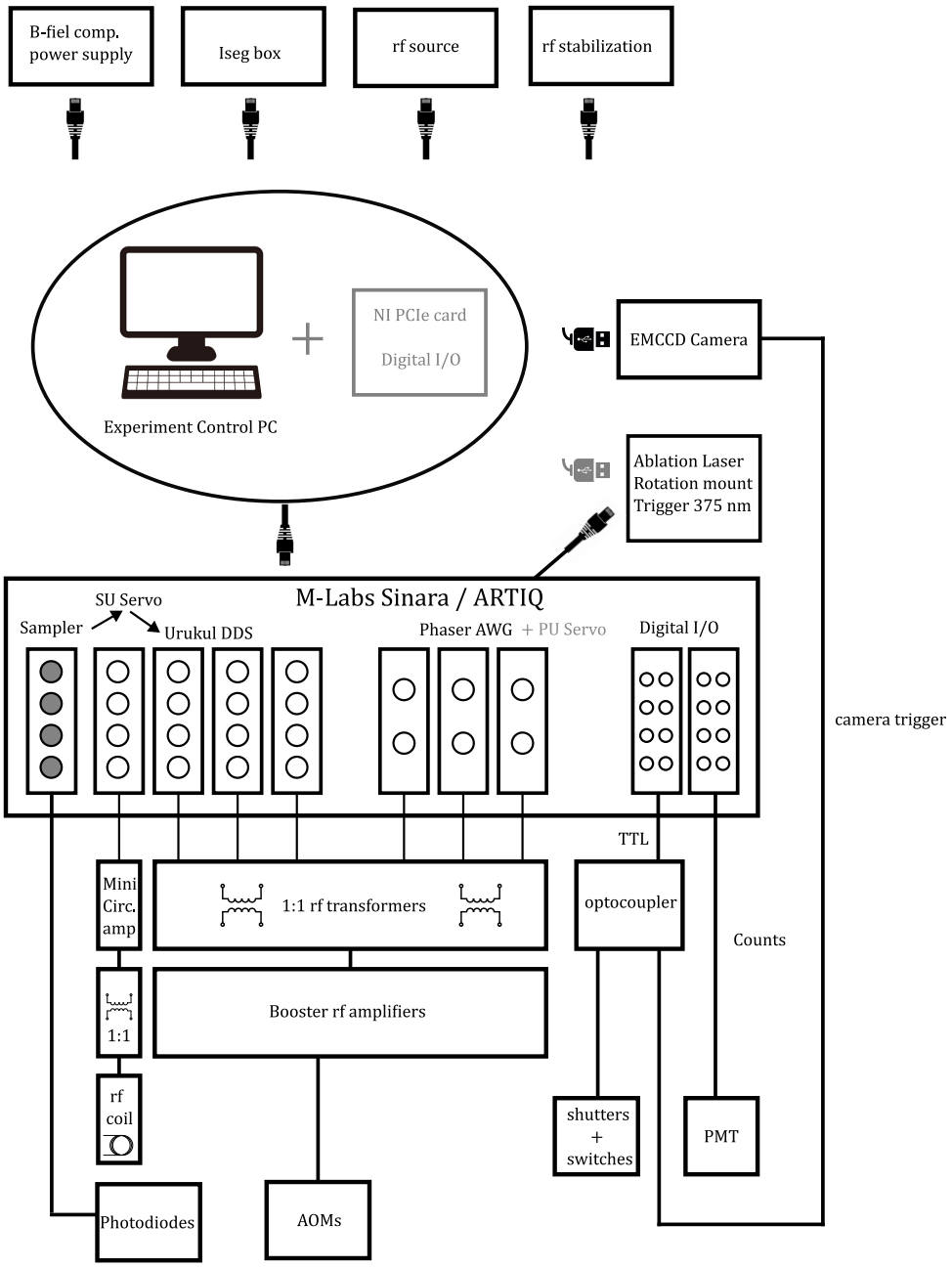

Figure 3.12: Schematic diagram of the experiment control system. The image shows all devices connected to and controlled by the main control PC. Ethernet connections, indicated by Ethernet connectors, are galvanically isolated through Ethernet-to-optical converters and *vice versa*. Additionally, optocouplers and 1:1 rf transformers are employed to isolate TTL and rf signals, respectively. USB connections, represented by USB Type-A connectors, are the only non-isolated connections. A second control PC, used for laser frequency stabilization (via wavelength meter) and control of piezo-driven mirror mounts, is not depicted in this image. For more detailed information about the experiment control system, refer to the main text.

the setup are connected to a total of only two power outlets, i.e. two separate electrical grounds. The devices connected to the vacuum chamber, including the vacuum pump and voltage supplies, are powered by a single socket, which is secured by an uninterruptible power supply (UPS). All other devices are connected to another separate socket. Within each of these two circuits, several measures have been taken to prevent ground-loops: Ethernet connections are isolated via Ethernet-to-optical converters[69], e.g. to isolate the control PCs from the Sinara box. A break-out board populated with optocouplers is employed to galvanically isolate TTL signals from the controlled devices. To separate the Sinara box from the rf coil mounted at the vacuum chamber, a 1:1 transformer is introduced (see Sec. 3.7). The aluminium profiles holding the vacuum chamber as well as the posts holding the breadboard around the trap are put onto feet made of PEEK[70], ensuring isolation from the lower breadboard and the rest of the optical table. All AOMs are either mounted on insulating posts[71] made of polyoxyehylene (POM) or ceramic pedestals posts.

Proper grounding of the helical resonator and the coaxial cable guiding the rf input turned out to be essential for the reduction of electronic noise, and thus the heating rate. To this end, multiple connections are introduced on the outside of the helical resonator, from the rf input coaxial cable to the resonator shield and from the helical resonator to the vacuum chamber (see Fig. 3.6). All efforts result in a single-ion heating rate of about 0.6 phonons/s.

Further aiming at the reduction of magnetic-field noise to improve the electronic coherence, the number dc power supplies has been reduced. Multiple laboratory devices are powered by a single linear power supply[72] at 24 V in combination with dc-dc converters, e.g. 12 V[73] for Thorlabs photodiodes. This way, many of the switched-mode power supplies, which are known sources of decoherence, are replaced. The rf stabilization circuit is powered separately by a 4-channel linear power supply (5V , ±15 V, 24 V)[74]. The coils for magnetic-field gradient compensation are supplied by a low-noise digital bipolar power supply[75].

3.5.4 Quantum-state readout

A key requirement for quantum experiments is a high-fidelity discrimination between two qubit states. To read out the quantum state of the ions in the presented experiments, a fluorescence measurement at 397 nm, driving the $4^2S_{1/2} \leftrightarrow 4^2P_{1/2}$ transition, is carried out in each single-shot experiment. The ions' fluorescence is detected on the chip of an EMCCD camera, enabling the site-resolved imaging of ion crystals[76]. The quantum state is determined by evaluating whether an ion is in a fluorescing (bright) or non-fluorescing (dark) state. Using an optical qubit, encoded in the $S_{1/2}$ and $D_{5/2}$ states,

[69] TP Link MC200CM, Gigabit-Ethernet media converter
[70] Polyether ether ketone
[71] Radiant Dyes Laser & Accessoires GmbH, Friedrichstrasse 58, 42929 Wermelskirchen, Germany
[72] Elektro-Automatik PS 3000 B series
[73] CUI Inc., PYBE20-Q24-D12-T
[74] Rohde&Schwarz NGP824, 4-channel power supply
[75] CAENels easy-driver 1020
[76] Additionally a PMT can be used, e.g. for the detection of a single ion.

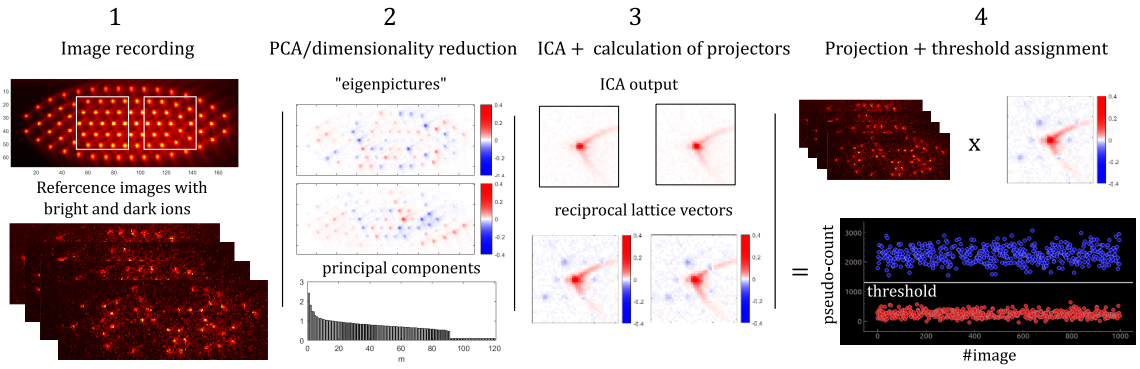

Figure 3.13: Calibration scheme for quantum state readout. For a detailed description, refer to the main text. (1) A set of typically a few thousand reference images is recorded. (2) A PCA of the reference images yields N eigenpictures corresponding to the N largest eigenvalues. (3) An ICA of the eigenpictures reveals the contributions of individual ions. The reciprocal lattice vectors of the single-ion image vectors yield an orthogonal basis set, which are used as projectors. (4) The reference images are projected onto the reciprocal lattice vectors. The distribution of pseudocounts is used to define a threshold between the dark and bright states of the individual ions. These threshold can then be used for the discrimination of states in new data images.

the detection is done immediately at the end of an experimental sequence. Using the qubit encoded in the two Zeeman states of the $S_{1/2}$ manifold, the population of one of the two Zeeman states (here: $|m = -1/2\rangle$) is coherently transferred to the $D_{5/2}$ state prior to the fluorescence measurement. This shelving is done via multiple pulses addressing different $D_{5/2}$ sublevels to ensure a high-fidelity population transfer, which is robust to slight miscalibrations of the 729-nm beam parameters. For the state-readout of a single ion, the bimodal distribution of photon counts can be used to set a threshold between the bright and the dark state, which is easy to implement. In experiments with multiple ions in a crystal, in particular planar crystals, this becomes more challenging as light scattering crosstalk can corrupt the state discrimination. Optical aberrations or a low numerical aperture can cause overlapping point-spread functions on the camera chip. Compared with linear strings of trapped ions, this results in an increase in readout errors for 2d crystals due to a higher number of neighboring ions. Furthermore, the state readout needs to be easily applicable to arbitrary 2d crystal lattice configurations. For these reasons, we use a novel approach based on statistical image analysis of a set of reference images, effectively implementing an unsupervised learning algorithm. This section provides a brief overview of the algorithm. A more detailed description of the procedure can be found in Ref. [61] and will also be subject to an upcoming publication.

Unsupervised learning of state discrimination

First, a set of typically a few thousand reference images, displaying roughly one half of the ions in a bright and the other half in a dark state, are recorded (step 1 in Fig. 3.13). To this end, a $\pi/2$-pulse is applied using either light at 729 nm or the rf coil in conjunction with shelving of one Zeeman state population before imaging. The pixel counts

of each image is represented by a linear vector $\mathbf{x_i}$ and the vectors of all images are assembled into a matrix X. A principal component analysis of X is done for the purpose of dimensionality reduction: A singular value decomposition of the covariance matrix $C_{XX} = \frac{1}{n}XX^T - \mu_{\boldsymbol{x}}\mu_{\boldsymbol{x}}^T$, normalized using the average pixel brightness $\mu_{\boldsymbol{x}}$, yields *eigenpictures* of the image sets (step 2 in Fig. 3.13). For an N-ion crystal, a small number of N eigenpictures, corresponding to the N largest eigenvalues, is sufficient to capture the quantum-state-dependent correlations necessary for the quantum state readout as all other eigenvalues are much smaller than the few most significant ones. Each recorded image can be approximately represented by a linear combination of these eigenpictures. However, the eigenpictures do not provide a very intuitive representation and, moreover, do not form an orthogonal basis set, which is required for a crosstalk-free discrimination. A mapping to an orthogonal single-ion basis, where each image represents the spatial distribution of fluorescence of an individual ion in the crystal, is therefore favorable. This is achieved in the next step, where an independent component analysis of the N eigenpictures is used to find a single-ion picture basis S, which captures the contributions of individual bright ions. In the presence of fluorescence crosstalk, the single-ion pictures contained in S still do not form an orthogonal basis set and thus the reciprocal lattice vectors of S are calculated as $\mathbb{1}_N = K^T S$ (step 3 in Fig. 3.13) to obtain one. The (reciprocal lattice) images forming the columns of K now represent an orthogonal basis and account for crosstalk between the ions via negative values at the location of the ions that cause the unwanted crosstalk (blue pixels in the projector images shown in the steps 3 and 4 of Fig. 3.13). Finally, all reference images are projected onto the N projectors, defining the reduced state space, to obtain a distribution of pseudocounts for each ion. These single-ion distributions then allow to determine pseudocount thresholds for each ion by fitting a bimodal Gaussian function (step 4 in Fig. 3.13). The N projectors in combination with their thresholds can finally be used for the state discrimination of a newly recorded image.

In addition to fluorescence crosstalk, we identified another source of error in our experiments occurring during the quantum-state readout: The ion crystals sometimes heat up during imaging and consequently compromise the readout of individual images. This problem is addressed in the following way: The distributions obtained from the pseudocounts of projected reference images yield a mean value $\mu_{\mathrm{b,d}}$ and a standard deviation $\sigma_{\mathrm{b,d}}$ for the bright and the dark state of each ion. The distribution of normalized pseudocounts for 5000 reference images of a 19-ion crystal is shown in Fig. 3.14(a). The pseudocounts can be expressed as the deviation from the mean value μ in units of the standard deviation $\sigma_{\mathrm{b,d}}$ of the respective bright and dark state distribution separately. By doing so, we obtain normalized pseudocounts with similar values irrespective of the ions being in a bright or dark state. For each reference image, we sum up the normalized pseudocounts of all N ions to obtain a new pseudocount, which we call *anomaly parameter* (see Fig. 3.14(b)). The distribution of the anomaly parameters for all reference images now allows to define a threshold to distinguish between "cold" and "hot" ion crystals in individual images (see Fig. 3.14(c)). Before carrying out experiments, this procedure is performed automatically along with the calibration routine described above. After successful calibration, if the anomaly parameter of a recorded image is larger than the set threshold, the experiment is automatically rejected and repeated by the experiment control. Alternatively, this method

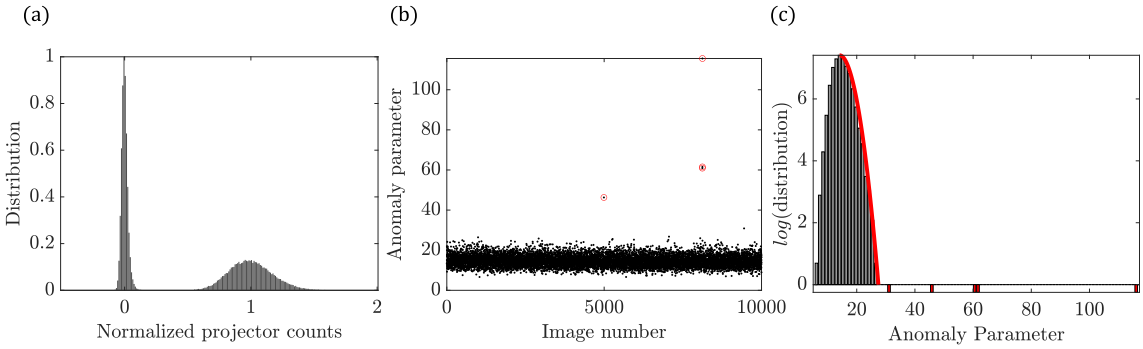

Figure 3.14: (a) Distribution of projector counts for 5000 reference images. All values are normalized to the mean values of the dark ($\mu_\mathrm{d} = 0$) and bright ($\mu_\mathrm{b} = 1$) distributions. (b) Anomaly parameters for a set of 10000 images of a 19-ion crystal. (c) Logarithmic histogram of anomaly parameters shown in (b). The bars, representing a single occurrence of an image within a bin ($log(1) = 0$), are shown as negative values on the y-axis to distinguish them from the zero line. The distribution allows to set a threshold between regular (cold crystal) and compromised (hot crystal) images using a Gaussian function (solid red line).

can be applied to sort out compromised data in post-processing.

The last component in our detection scheme is the in-sequence classification of the crystal lattice configuration, as the arrangement of the ions in a 2d crystal can change during measurements. In experiments conducted so far, we use symmetric and stable crystals, which are found in the same configuration in > 99 % of experiments. To detect and reject the residual experiments impaired by configuration changes, in addition to the image for quantum state-readout taken at the end of each sequence, we record an image with all ions in the bright state at the beginning of each experiment. This image is used to classify the crystal configuration and initiate the repetition of an experiment if needed. A detailed description of the analysis of crystal configurations is given in Sec. 4.5.

3.6 Optical setups

3.6.1 Overview of the laser systems and beam geometry

Laser systems

The following subsections describe the laser setups used for various purposes in our experiment. A brief overview of the laser systems and beam geometry is provided upfront: For photoionization (422 nm), Doppler and EIT cooling (397 nm), and repumping from metastable states (854 and 866 nm), a 19"-rack-based Toptica multi-diode laser (MDL) system[77], containing four external cavity diode lasers (ECDL), is used. The lasers are fiber-coupled[78]. Two Toptica *DLC pro* controllers are each controlling two of the lasers of the MDL system. The stimulated Raman transition used for entangling interactions is driven by a frequency-doubled diode-based laser system[79] with an output power of about 1.4 W at 396 nm. Narrow laser light at 729 nm (∼1 Hz level), referenced to an ultra-high-finesse cavity, is shared by another laboratory in the same building via a SM/PM fiber and amplified by a tapered amplifier[80] (see Sec. 3.6.6 for more details). It is used for coherent manipulation of the optical qubit and population shelving prior to the quantum-state readout of the ground-state qubit. For ablation loading, a ns-pulsed laser at 515 nm is used and a compact single-mode diode laser at 375 nm[81] is employed for the second photoionization step.

The MDL lasers as well as the Raman laser are monitored and locked using an 8-channel wavelength meter[82], which is calibrated with light from the 729-nm laser. The software provided along with the wavelength meter generates an error signal and enables feedback to the piezo voltage of the locked laser via an Ethernet connection to the laser controller. The locking bandwidth of this "digital" locking scheme is limited by the update rate of the wavelength measurement which is typically on the order of several milliseconds. Consequently, this scheme is not capable of narrowing down the free-running linewidth of the ECDL lasers (on the order of a few hundred kHz), but it effectively corrects for slow frequency drifts. The wavelength meter has a specified absolute accuracy of < 10 MHz[83]. Considering the natural linewidth of the $S_{1/2} \leftrightarrow P_{1/2}$ transition of $\Gamma = 21.4$ MHz, the stabilization of the lasers is sufficient for our experiments.

Each of the ECDL lasers provides about 40 mW of output power ex-fiber with a specified short-term linewidth of 150 kHz over 5 μs for the 423-nm and 397-nm and 100 kHz over 5 μs for the 854-nm and 866 nm lasers. A beat measurement of the locked 854-nm laser with a second 854-nm laser[84] suggests an upper bound for the linewidth of about 237 kHz

[77] Toptica MDL pro, all ECDL, 4 x DL pro at 397 nm, 423 nm, 854 nm and 866 nm, output power: ≈38 mW ex-fiber

[78] Toptica *FiberDock*

[79] Toptica DLC TA-SHG PRO, design wavelength: 396 nm ± 2 nm, output power: > 1.4 W, linewidth: <200 kHz over 5 μs

[80] Toptica MTA BoosTA pro

[81] Toptica iBeam smart 375 nm

[82] HighFinesse WS8-10, 19"-rack compatible

[83] The typical accuracy is on the order of a few MHz over many hours.

[84] Light from the 854-nm laser at lab 1 at IQOQI was used, which has an expected linewidth of about

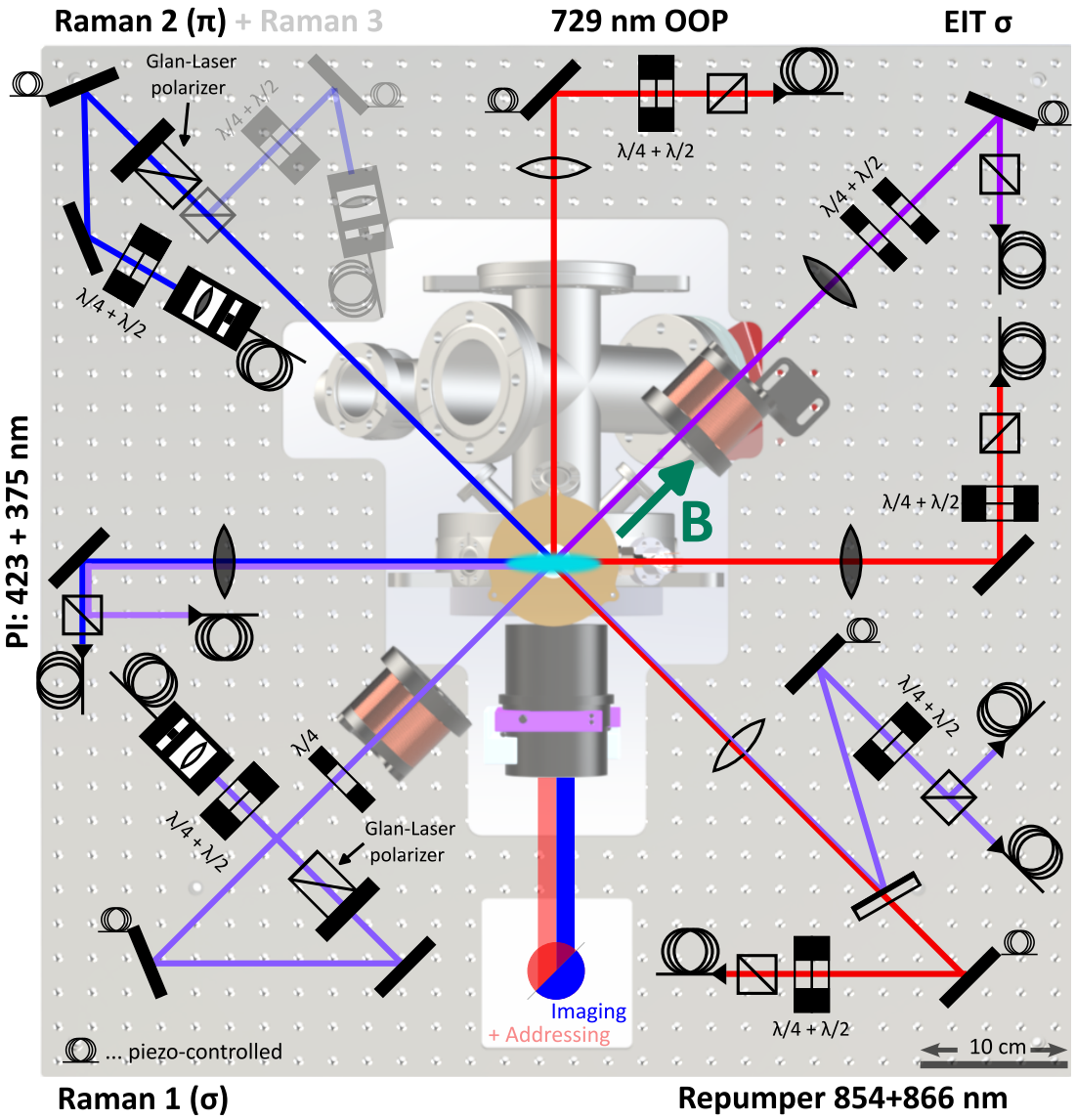

Figure 3.15: Schematic image, illustrating the top view of the optical setup surrounding the vacuum chamber. Only laser beams within the horizontal plane (xz-plane) are shown. The ions are trapped in the center of the vacuum chamber's main corpus. The two permanent magnet holders, including coils for field compensation, are placed to the front and to the back of the main corpus along a diagonal in this image. They create the quantization field at an angle of 45° with respect to the crystal plane (yz-plane). The objective lens assembly, held by a purple mirror mount, is placed in front of the vacuum chamber's front window for imaging and addressing perpendicular to the crystal plane. The square hole in the front of the breadboard allows the collected fluorescence image to be reflected downwards (perpendicular to the image plane of this figure) and enables the passage of the addressing beam, propagating from the bottom breadboard towards the ion crystal. The optics for the Raman 3 beam (grayed out) have been removed from the setup, as it has no intended use in any foreseen experiments.

measured over 17 minutes. During this time the beat signal's center frequency exhibited a drift of < 1 MHz. Due to air pressure fluctuations[85] the frequency measured by the wavelength meter can experience jumps on the order of a few MHz, stabilizing within less than one second. This time can be minimized by adjusting the measurement time of each channel to the minimum of 1 ms, thereby maximizing the update rate of the frequency stabilization.

Laser beam geometry

Figure 3.15 shows the geometry of the laser beams surrounding the trap and the magnetic field. Piezo-driven mirror mounts[86] in all beam paths around the trap allow for beam alignment without the need for opening the μ-metal shield. All laser beams shown in Fig. 3.15 enter the vacuum vessel within the horizontal plane and are unaffected by micromotion, which occurs only in vertical direction (y). Three beams enter from other directions and are not displayed in the figure: The ablation laser beam enters the vacuum chamber from the bottom viewport. An additional spectroscopy beam at 729 nm, entering the chamber from the top at an angle of 45° with respect to the horizontal plane, couples also to the in-plane modes of motion[87]. Akin to this spectroscopy beam, a second Doppler cooling beam, at an angle of about 20° with respect to the horizontal plane and about 45° with respect to the crystal plane, also couples to the motional modes with mode vectors along the vertical direction. In the experiments, we find that planar crystals consisting of more than a few ions can be cooled efficiently with the primary Doppler cooling beam along a direction within the horizontal plane at 45° with respect to the crystal plane. The ability to efficiently cool larger crystals without an overlap of the cooling laser's k-vector with the y-direction is unexpected and currently not understood. For single ions and small ion crystals, however, we observe a hot vertical COM mode, which is solved by using the second Doppler cooling beam instead.

3.6.2 Laser ablation loading and photoionization

Laser ablation loading

Routinely performing experiments with larger ion crystals requires the ability to load ions in a deterministic and fast manner. In general, there are three options for loading ions into traps: using a resistively heated oven, laser ablation with a pulsed laser, or a 2d magneto-optical trap (MOT). Heating up an oven is a slow process, which can take up to several minutes for a single loading cycle. It is therefore not suited for frequent reloading of larger ion crystals while setting up a 2d MOT requires much more resources and potentially affects the vacuum quality of the system [131]. We therefore choose pulsed laser ablation as it is actually the simplest and least cumbersome method to set up and operate. It has been implemented and proved reliable in various trapped-ion setups [132–134]. Control of the applied laser pulses combined with precise control of the rf trap potential enables

100 kHz.

[85] This was experienced at the IQOQI when the door to the laboratory section was opened.

[86] Lioptec SR100-HS-100-2PZ, PiezoSTAR with 2 piezos (Physik Instrumente piezos)

[87] with the exception of the COM mode in axial direction

us to deterministically load and remove ions. More details on the characterization of the loading process are given in Sec. 4.1.

For ablation loading of Ca^+ ions, a pure calcium target is placed in vacuum in the proximity of the ion trap. Individual ns-laser pulses are guided onto the target to create an atomic beam directed to the trap center. At the same time, the calcium atoms in the trap center are ionized in a two-photon process: The first photon from a laser beam at 423 nm isotope-selectively drives a cycling transition to a highly excited state. From this state, the electron is further excited to the continuum by a photon from a second laser beam at 375 nm.

The laser pulses are generated by a passively Q-switched diode-pumped solid-state (DPSS) laser[88] at 515 nm. A visible wavelength is beneficial for alignment. The laser is able to generate pulses of about 1 ns at a maximum repetition rate of 2 kHz. The maximum pulse energy of a single pulse is about 300 μJ. The optical setup for the ablation laser is shown in Fig. 3.16(a). A motorized $\lambda/2$-waveplate in combination with a high-power polarizing beam splitter (PBS) cube is used to control the intensity of the laser pulses sent to the target through the window on the bottom of the vacuum chamber. A parabolic mirror[89] with a focal length of about 150 mm[90] is mounted below the window and is used to focus the beam onto the target with an estimated spot diameter of about 300 μm.

Ablation laser alignment

For a rough alignment we use the lowest power and lowest repetition rate (16.7 Hz). The ablated atomic beam is constrained by a 300-μm hole at the tip of the funnel aperture, which requires fine tuning of the laser beam's position on the target to allow the atom beam to reach the trap center. The fine adjustment of the beam position on the target is done with the help of a time tagger[91] recording the fluorescence of neutral atoms (at 423 nm) in the trap center. The time-resolved fluorescence signal detected by the PMT is repeatedly measured while adjusting the beam alignment onto the target. In the absence of a fluorescence signal in case of misalignment, the power of the laser is increased progressively while adjusting the mirror until a signal is detected by the PMT. This signal can then be maximized. After successful alignment, the power can be reduced to values, at which only single or few ions are trapped with a single laser pulse. A problem that arises during the alignment procedure is the significant beam pointing instability of the laser during continuous operation. During alignment, the laser is therefore turned on repeatedly for only several seconds at a time while adjusting the mirror, which helps mitigate large drifts of the beam position due to thermal effects. After maximizing the fluorescence signal, the laser is turned off for about a minute before checking the fluorescence once again. This ensures proper alignment in the "cold" state of the laser, which is more relevant later when triggering individual pulses.

Note that atoms can be directly ionized by an ablation pulse when using a high laser pulse

[88] Coherent Flare NX, 515 nm, pulse duration: 1.3 ± 0.2 ns

[89] Thorlabs MPD169-P01

[90] Due to the divergence of the laser beam we estimated a focal point at a distance of about 160 mm from the parabolic mirror.

[91] ID Quantique ID900 time controller

intensity. The trap could thus be loaded without photoionization lasers. However, there are two concomitant problems: First, direct ionization is not an isotope-selective process and, therefore, other isotopes may be loaded as "dark" ions. Second, atoms ionized by this process arrive at the trap with a much higher kinetic energy. Consequently, they require more time to be cooled and trapped stationarily. In our experiment, photoionized atoms are loaded within one second whereas directly ionized ions appear on the camera image only several seconds after the ablation laser pulse was triggered. For these reasons, we adjust the pulse energy to typical values between 50 and 100 μJ, ensuring that photoionization occurs as the primary ionization mechanism. To load ions into the trap, we typically trigger a small number (typically 1-10) of ablation laser pulses at low power.

Photoionization

The applied laser powers for the two photoionization steps are typically about 300 μW for 423 nm and about 8 mW for 375 nm. A high-power fiber[92] is used to guide the light from the optical table to the trap inside the magnetic shield. Both beams have a beam diameter of about 300 μm at the trap center. The two photoionization beams (423 nm and 375 nm) are combined using a PBS cube and sent to the ions through the left axial hole. The 423-nm light is controlled by a mechanical shutter [93]. The 375-nm laser can be switched on and off rapidly by a TTL signal modulating the laser output[94]. By using fast switching, the exposure of the trap surface to scattered UV light is minimized to prevent the creation of free electrons that could ionize the background gas and create dark ions. The optical setups for the two photoionization laser beams at 423 nm and 375 nm are shown in Fig. 3.16(b).

3.6.3 Doppler cooling and state detection at 397 nm

The light for Doppler cooling is generated by one of the Toptica MDL pro ECDL lasers at 397 nm, delivering an output power of approximately 38 mW after the fiber. During Doppler cooling, light at 866 nm (see Sec. 3.6.5) is applied along with the 397-nm laser to repump population from the metastable $3^2D_{3/2}$ state. The light at 397 nm is used for both Doppler and EIT cooling, as well as quantum state detection, driving the $4^2S_{1/2} \leftrightarrow 4^2P_{1/2}$ dipole transition. A schematic drawing of the optical setup is shown in Fig. 3.17(a). 397-nm-light is guided from the rack to the optical table in a single-mode (SM) polarization maintaining (PM) fiber. A small fraction of the light (a few percent) is split off, coupled into another fiber and sent to the wavelength meter for monitoring and locking. After that, the light is split up using a $\lambda/2$-waveplate and a PBS cube between the Doppler cooling and the EIT cooling setup. For Doppler cooling, the beam is further split into three beams: the primary Doppler cooling beam in the horizontal plane, a second beam at an angle of about 20° w.r.t. the horizontal plane for cooling single ions, and a third far-red-detuned ($\Delta = 2\pi \times 300$ MHz) beam for recrystallization of melted ion crystals, referred to as *refreeze*

[92] Oz Optics QPMJ-A3AHPCA3AHPC-400-3/125-3AS-5-1, 3/125 μm, high power PM patchcord for 400 nm, end-capped, high-power air gap FC connectors on both ends

[93] Radiant Dyes, Titanium Mini Servo Motor

[94] Our model of the iBeam smart laser (2018) was modified by Toptica to activate the optional *digital modulation* feature. The specified maximum modulation frequency for completely switching the laser on and off is 100 MHz.

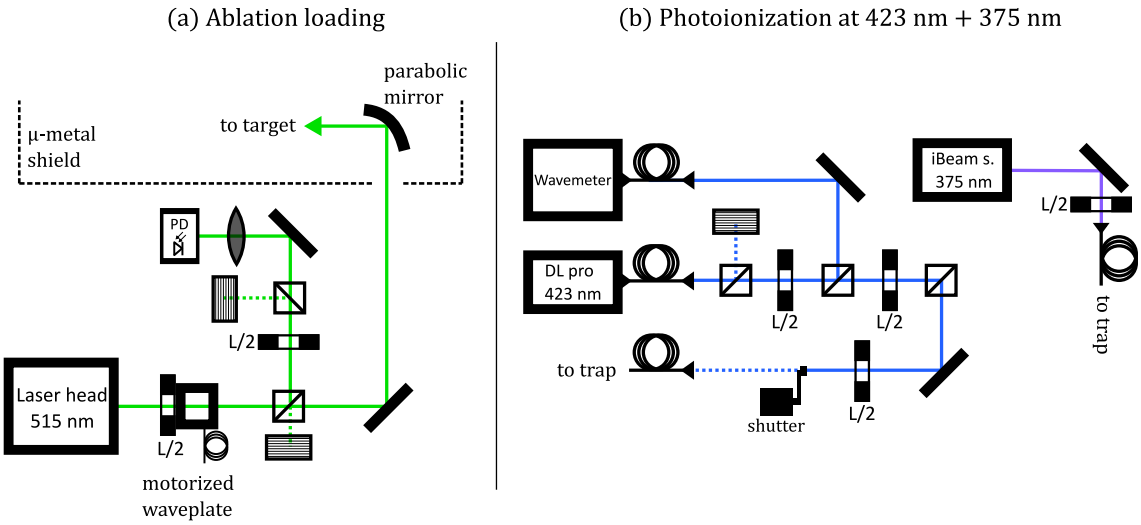

Figure 3.16: Optical setups for (a) pulsed laser ablation at 515 nm and (b) photoionization at 423 nm and 375 nm.

beam. With the exception of a $\lambda/2$-waveplate, all PBSs and waveplates in the high-power arm (before the first Doppler cooling double-pass and before the EIT cooling setup) are dedicated high-power components from B. Halle[95] and Lens-Optics[96]. All three beams are individually controlled using AOMs[97] in a double-pass configuration for frequency scanning and suppression of light leakage. In addition, mechanical shutters block residual leaking light from the unused beam paths. The refreeze beam is combined with the primary beam and coupled into the same PM fiber. A 10-nm-bandpass filter around 400 nm[98] is introduced in front of the fiber coupler to suppress unwanted frequency components at 393 nm (from amplified spontaneous emission) pumping into the metastable $3^2D_{5/2}$ state. At the trap, the beams are overlapped with the already combined 854-nm and 866-nm beam using a dichroic mirror. The beams are entering the front viewport in the horizontal plane at 45°. The second cooling beam is coupled out at an angle of approximately 20° relative to the horizontal plane and sent to the ions through a 125-mm planoconvex lens[99]. For detection, the Doppler cooling beams are used at higher power to saturate the fluorescence of the illuminated ions.

3.6.4 Electromagnetically induced transparency cooling at 397 nm

EIT cooling is used to cool the out-of-plane modes of motion close to the ground state. To this end, the 397-nm light from the ECDL is split between the Doppler cooling and the EIT cooling setup (Fig. 3.17(a)). A schematic drawing of the EIT cooling setup is shown

[95] Bernhard Halle Nachfl. GmbH, Hubertusstrasse 10, 12163 Berlin, Germany
[96] LENS-Optics GmbH, Bürgermeister-Neumeyr-Strasse 7, 85391 Allershausen, Germany
[97] Gooch & Housego, AOM model: 3080-125
[98] Edmund Optics 65132, bandpass filter, 400/10 nm, OD4, 25 mm
[99] Thorlabs LA1986-A

(a) Doppler cooling

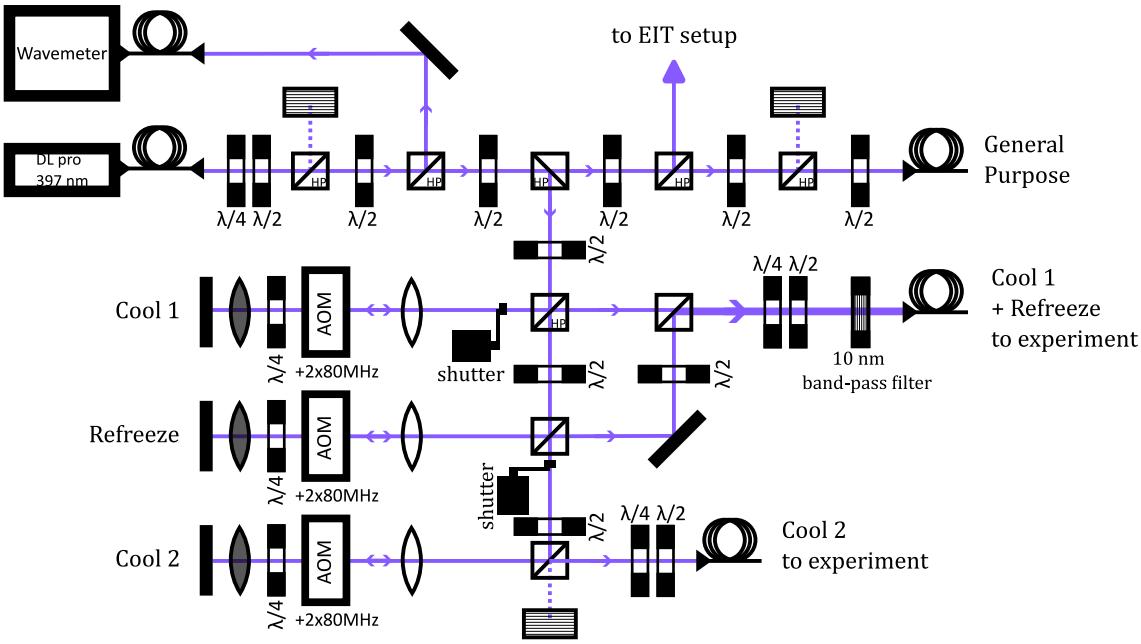

(b) EIT cooling

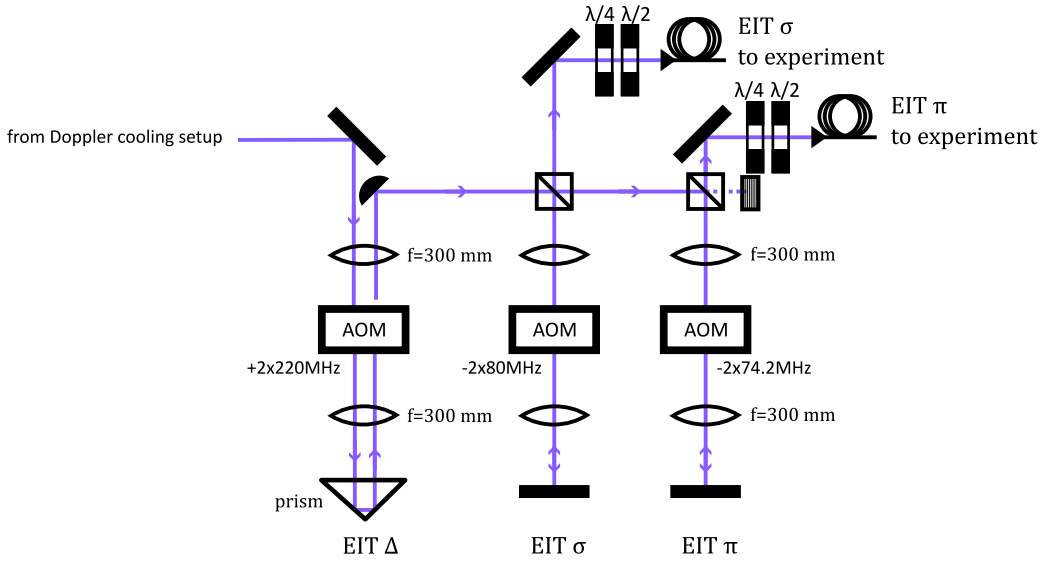

Figure 3.17: Optical setups for (a) Doppler cooling and (b) EIT cooling.

in Fig. 3.17(b). First, the beam is sent through an AOM[100] in double-pass configuration, which is used to set the detuning from the $4^2S_{1/2} \leftrightarrow 4^2P_{1/2}$ transition ("EIT Δ" in Fig. 3.17(b)). This AOM requires vertical linear polarization, prohibiting the separation of the output beam at a PBS by introducing a $\lambda/4$-waveplate in the double pass. It is thus spatially separated by a prism and a small D-shaped mirror. Subsequently, the beam is split into a σ-polarized beam ("EIT σ") and a π-polarized beam ("EIT π"), with each beam being controlled by an additional double-pass AOM[101] before being sent to the trap via fiber. The first double-pass AOM is operated at $+2 \times 220$ MHz, which together with the double-pass setup operated at -2×80 MHz generates a total frequency detuning of $\Delta = 110$ MHz from the $4^2S_{1/2} \leftrightarrow 4^2P_{1/2}$ carrier transition. The double-pass of the π-beam is set to 2×74.2 MHz to match the Zeeman splitting of the two $S_{1/2}$ ground states. The σ-polarized light could be used to optically pump into the $|S_{1/2}, m = -1/2\rangle$ state by extending the σ-light pulse as done in Ref. [135]. However, spurious polarization components can corrupt this method, which is why we use the narrow 729-nm laser driving the $|S_{1/2}, m = +1/2\rangle \leftrightarrow |D_{5/2}, m = -3/2\rangle$ transition along with 854-nm light to pump into the $|S_{1/2}, m = +1/2\rangle$ ground state subsequent to EIT cooling.

The two EIT cooling beams address the ions perpendicular to each other entering at an angle of 45° with respect to the crystal plane. The resulting differential k-vector is perpendicular to the crystal plane enabling ground-state cooling of the out-of-plane modes of motion. The π-beam is overlapped with the primary Doppler cooling beam on a PBS cube and enters through the front window. The σ-beam enters through a 45° window at the rear side of the chamber. The σ-beam's polarization is adjusted using a combination of a $\lambda/2$- and a $\lambda/4$-waveplate in precision rotation mounts[102]. For a description of the calibration routines for polarization and power of the EIT cooling beams, please refer to Sec. 5.2.2.

3.6.5 Optical pumping at 854 nm and 866 nm

During cooling and imaging, a laser beam at 866 nm is applied along with the 397-nm light to repump from the metastable $3^2D_{3/2}$ state back into the $4^2S_{1/2}$ manifold. A 854-nm laser, along with a 729-nm laser that couples the $D_{5/2}$ state, is used to initialize a quantum state through optical pumping. This process transfers the ion from the $|S_{1/2}, m = -1/2\rangle$ into the $|S_{1/2}, m = +1/2\rangle$ state via the $|P_{3/2}, m = +1/2\rangle$ level. The optical setup for both the 854-nm and the 866-nm lasers are shown in Fig. 3.18. Two ECDL lasers provide about 40 mW of light at 854 nm and 866 nm, respectively. A small fraction ($\sim$1 %) of the light is split off by a fused-fiber splitter[103] and sent to the wavelength meter for frequency stabilization. The high-ratio output ports are spliced with a 5-meter PM fiber to guide the light onto the optical table adjacent to the lasers in the 19"-rack. Each beam is switched on and off by an AOM[104] in a double-pass configuration. The setups for both lasers are completely analogous before the two beams are combined on a PBS cube and directed to

[100] IntraAction Corp., AOM model: ASM-2002B8
[101] Gooch & Housego, AOM model: 3080-125
[102] Thorlabs PRM1 precision rotation mount
[103] Thorlabs PN850R1A1, 99:1 Fiber coupler 850 ±15 nm
[104] Gooch & Housego, AOM model: 3200-124

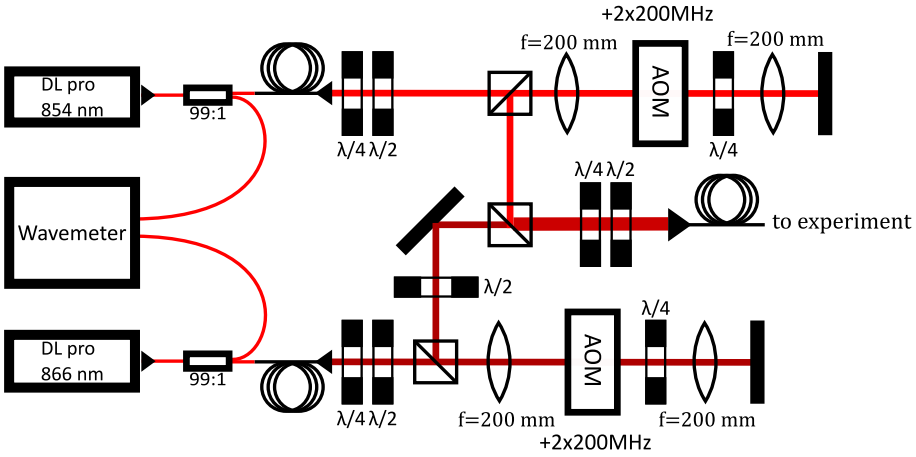

Figure 3.18: Optical setup for lasers at 854 nm and 866 nm.

the experiment through an optical fiber. At the trap, the beams are overlapped with the Doppler cooling beam before being sent to the ions.

3.6.6 Spectroscopy and coherent control of the optical qubit at 729 nm

To manipulate the optical qubit on the $S_{1/2} \leftrightarrow D_{5/2}$ transition, we use shared frequency-stabilized laser light at 729 nm. In the course of this work, several 729-nm sources were used. For most measurements, which were done before moving from the IQOQI to the UIBK building in 2022, we used light from the QSIM experiment in lab 1 at the IQOQI. After the move, a laser system [136] hosted in the neighboring lab (group of Ben Lanyon) was shared. Due to frequent issues with this system, at the time of writing, we were using shared light from the "big lab" (linear experiment) on the ground floor of the Technikerstrasse 25. These systems were all based on Ti:Sapphire lasers referenced to an external ultra-high finesse cavity via Pound-Drever-Hall scheme. A completely new laser system based on a laser diode[105] will be set up in the 2d crystals lab in the near future.

Due to thermal fluctuations and acoustics, phase noise is introduced to the light passing through an optical fiber. For several tens of meters of fiber, it results in a typical frequency broadening of a few kHz. Therefore, the phase of the shared light guided to our laboratory, is actively stabilized using a dedicated *fiber noise cancellation* (FNC) setup. The phase is stabilized interferometrically using a home-built phase-locked loop circuit following the approach presented originally in Ref. [137].[106] A small fraction of the light is split off by a 90:10 non-polarizing beam splitter and retroflected by a mirror onto a photodiode. The beam is then sent through an AOM at a drive frequency of 80 MHz ($+1^{\text{st}}$ order) before entering the fiber. The second arm of the interferometer is given by the light, which is back-reflected at the FC/PC fiber facet after passing through the fiber twice. This weak beam passes through the AOM again and is overlapped with the retroflected 10%-arm on the photodiode yielding a beat signal at 160 MHz. Using home-built electronics, an

[105] Toptica MTA pro

[106] More details on the implementation in trapped-ion experiments in Innsbruck can be found in Ref. [138].

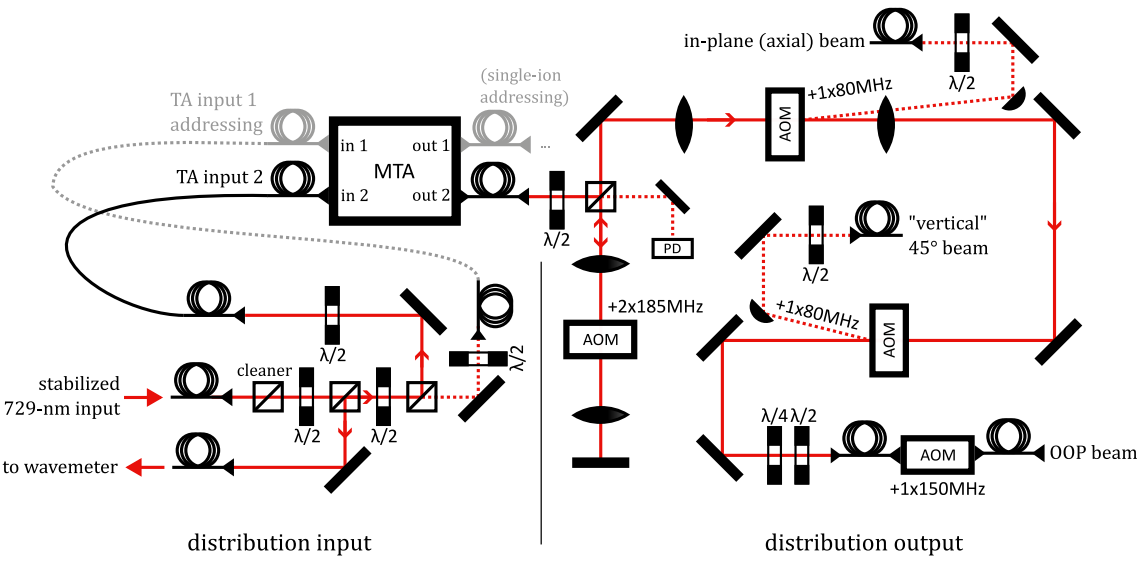

Figure 3.19: Optical setup for the 729-nm laser.

error signal is generated by comparing the beat signal to a reference signal from a stable frequency source (>160 MHz, locked to a GPS reference) and mixed down to dc. In a phase-locked loop, the phase difference is fed back to a voltage-controlled oscillator (VCO) that drives the AOM at about 80 MHz. An additional AOM (-1st order) is used in the FNC setup to cancel the frequency shift introduced by the other AOM.

A schematic of the optical setup used to prepare the beams that are sent to the ions is shown in Fig. 3.19. On the experiment table, the incoming beam is amplified by a rack-mountable system containing two tapered amplifiers (TAs)[107]. About 20 mW of frequency-stabilized light is currently used to seed one of the two TAs. The TA output is sent through a double-pass AOM and afterwards split up into three beams, which are used globally on the ion crystal: a beam perpendicular to the ion crystal plane, a beam sent through the axial hole of the trap, and a beam addressing the ions at 45° from the top (relative to the horizontal plane) coupling to both the out-of-plane and the in-plane modes (with the exception of the axial COM mode). These three beams can be controlled individually by single-pass AOMs. The in-plane beam and the top beam pass a free-space AOM[108]. The out-of-plane 729 beam is coupled into a fiber-AOM[109]. The fiber AOM is fast (rise time $\leq$ 50 ns) and guarantees stable coupling of the modulated light into the output fiber. While the 729-nm light in our setup is typically not used to bichromatically drive the ions, the fiber-coupled AOM helps to reduce the power imbalance between the two light field components, which can arise from unequal coupling to a fiber after a longer free-space beam path following the free-space AOM. In experimental sequences, the beams are switched using the global double-pass configuration. Focusing the beam with a 150-mm planoconvex

[107] Toptica MTA BoosTA pro
[108] Gooch & Housego, AOM model: 3080-125
[109] Gooch & Housego, fiber AOM model: MM080-1C2V14-5-F2SH-B

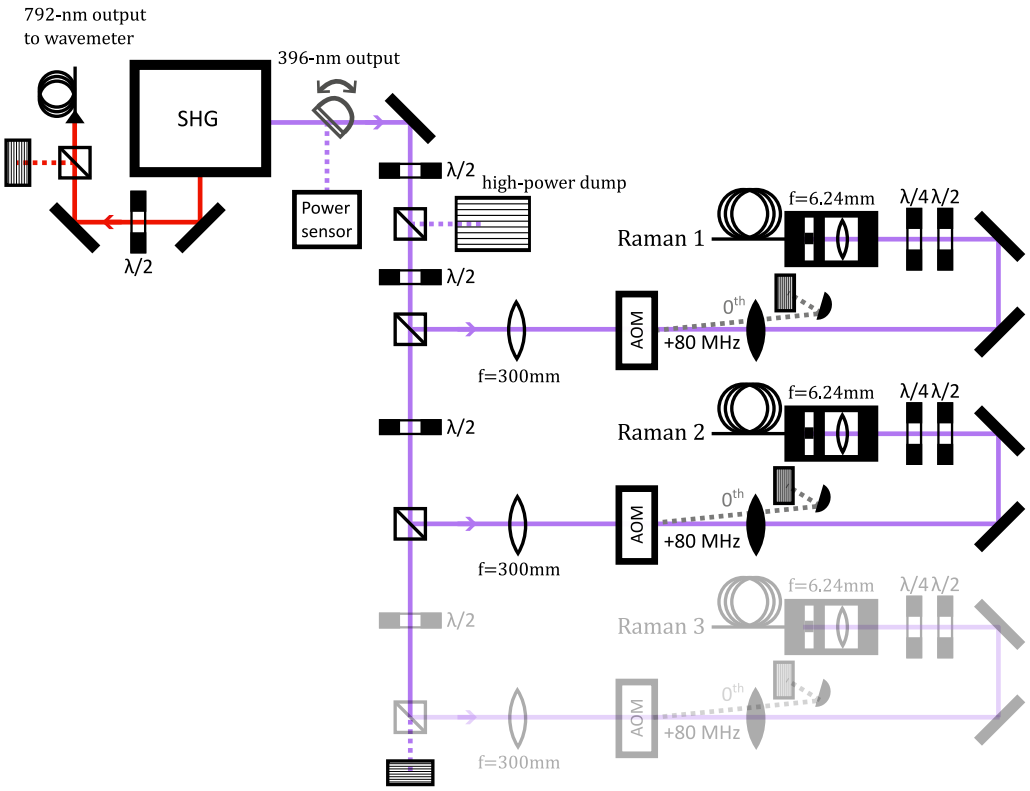

Figure 3.20: Optical setup for stimulated Raman transitions at 396 nm. The Raman 3 beam was used only in the initial setup.

lens [110] into the AOM thereby enables a fast modulation. During measurements, the fiber AOM is never switched off completely and remains in an idle state. The leakage through the double-pass is negligible. 10-meter-long fibers guide the three beams from the optical table to the experiment. At the trap, the polarization is cleaned using a PBS cube after the fiber and can be adjusted with a combination of a $\lambda/2$- and a $\lambda/4$-plate before the beams are focused onto the ion crystal using 300-mm planoconvex lenses.

In the near future, the output of the second TA will be used for single-ion addressing with a tightly focused laser beam. Addressing in two dimensions will be realized using two crossed AODs. An additional AOM will compensate for the frequency shift introduced by the two AODs.

3.6.7 Stimulated Raman transition for entangling interactions at 396 nm

A stimulated Raman transition is used to couple the two Zeeman sublevels of the $4^2S_{1/2}$ manifold (ground-state qubit). Details on this interaction are presented in Chap. 6. The

[110] Thorlabs LA1433-B

light for driving this transition is provided by a frequency-doubled diode laser[111] at 396 nm that off-resonantly couples the qubit states to the $4^2P_{1/2}$ and $4^2P_{3/2}$ states. The three-level scheme used for the stimulated Raman transition requires simultaneous excitation with two beams of different polarization with respect to the quantization axis: one beam ($\boldsymbol{\sigma}$) coupling the transition with Δm= $\pm$1 and a second beam ($\boldsymbol{\pi}$) coupling the transition with Δm= 0. The beam geometry is shown in Fig. 3.15, with more details provided in Fig. 6.2. In the presented experiment, we use two counterpropagating beams. The σ-beam (Raman 1) is parallel to the magnetic-field axis and enters the front viewport at 45° with respect to the crystal plane. It is linearly polarized and thus contains a balanced ratio of σ^+- and σ^--components. The π-beam (Raman 2) enters the vacuum chamber on the rear side through a 45°-window. It is linearly polarized in the horizontal plane, and aligned perpendicular to the σ-beam, and thus to the magnetic field. This geometry results in a differential k-vector that is perpendicular to the ion crystal plane. Therefore, we can make use of sideband transitions, coupling to the OOP motional modes to create entanglement across an ion crystal. An additional beam (Raman 3) was initially set up as a secondary σ-beam but has since been removed from the setup, as it was not required for any planned measurements. The Raman 3 beam was co-propagating with the π-beam (Raman 2) but vertically polarized. In combination with the Raman 2 beam it could be used to drive solely the electronic transition between the two $S_{1/2}$ sublevels without coupling to the motional modes, as the differential k-vector vanishes.

The linear polarization of the beams is cleaned using Glan-Laser polarizers[112]. The frequency difference between two Raman beams is chosen such that the Raman process is induced by the σ^+ component of the Raman 1 (or Raman 3) beam in conjunction with the π-polarized Raman 2 beam resulting in a transition with $\Delta m = +1$ between the two $S_{1/2}$ Zeeman states. In order to cancel the differential ac-Stark shift on the two $S_{1/2}$ Zeeman sublevels, the Raman 1 beam is linearly polarized (orthogonal to the quantization B-field). The balanced ratio of σ^--polarized and σ^+-polarized light results in equal light shifts on the two qubit states, due to symmetric coupling to the Zeeman sublevels of the $P_{1/2}$ and $P_{3/2}$ states. Furthermore, the detunings of the beams are set corresponding to a so-called magic wavelength at 395.799 nm, canceling light shifts on the $S_{1/2} \leftrightarrow D_{5/2}$ clock transition [139, 140].

A drawing of the optical setup for the preparation of the Raman beams is shown in Fig. 3.20. In general, the beam paths are kept as compact as possible, as differential optical path lengths between two Raman beams can lead to relative phase instabilities that impair the coherence of the light field interacting with the ions. The absolute phase of the beams does not affect the interactions. The fibers from the preparation setup to the trap breadboard are guided closely to each other to restrict phase noise (due to thermal drifts and vibrations) to noise that is predominantly common-mode to both fibers. The Raman beams are individually controlled using AOMs[113] in single-pass configurations. Each beam is focused in the center of the AOMs using a 300-mm lens to decrease the rise

[111] Toptica DLC TA-SHG PRO, design wavelength: 396 nm ± 2 nm, output power: > 1.4 W, linewidth: < 200 kHz over 5 μs

[112] Thorlabs GLB10-405, Glan-Laser polarizer, α-BBO, 405-nm coated

[113] Gooch & Housego I-M110-2C10T-3-GH72, Crystal Quartz, 355 nm, 110 MHz

time during modulation. After the AOM, another 300-mm lens re-collimates the beam[114], which is then coupled into a PM-fiber using home-built fiber couplers[115]. An aspheric lens with a focal length of 6.24 mm is employed to couple the light into the fiber with an efficiency of about 70 %. Additional custom aluminium parts are introduced to the coupler assembly to shield the fiber end facets from dust particles, which could be adsorbed and burned. In order to further reduce the risk of damage of the fiber end, we use fibers with high-power connectors[116]. In these connectors, an uncladded, bare piece of fiber core is exposed to the light. This helps prevent the evaporation of adhesive used to fix the glass core to the cladding, which could adhere to the fiber end and ultimately result in damaged (burnt) end facets. Home-built couplers are also used for outcoupling the light at the experiment. Rather than collimating the beam, the lens in the coupler directly refocus the light from the fiber onto the ions, reducing the number of optical elements between the fiber and the ions. In the experiments presented in this work, we used aspheric lenses[117]. Recently, these lenses have been identified to introduce aberrations in the beam profile and cause inhomogeneous coupling across the crystal. Simulations with *Zemax Optical Studio* have confirmed such aberrations. In the meantime, triplet collimators have replaced the aspheric lenses at the trap, which improved the beam quality and thus the homogeneity of the coupling across an ion crystal.

3.6.8 Imaging and state detection

For imaging and quantum-state detection, fluorescence from the ions at 397 nm is collected using a custom aberration-corrected objective lens assembly. At the same time, the objective is designed for 729-nm light to enable addressing of individual ions in a crystal with a tightly focused laser beam, whose focus is diffraction-limited by the given numerical aperture (NA). In the course of this work two different objective lenses have been employed. For the majority of the presented measurements, we initially used a *Sill Optics*[118] objective with NA = 0.29, before installing a new custom objective lens assembly from *PhotonGear*[119]. Since the Sill Optics objective has already been removed from the setup, this section will focus on details of the new imaging setup.

The objective is placed in front of the big front window (CF100) orthogonal to the crystal plane (see Fig. 3.15). The PhotonGear objective was specifically designed and optimized for the setup described in this work. It features a diffraction-limited design optimized for wavelengths of 397, 532 and 729 nm. The design for 532 nm will be beneficial in the future for applying strong light fields at 532 nm in the out-of-plane direction. The objective has a working distance of 45.42 mm and a numerical aperture of NA = 0.44. Its outer diameter and thus the NA is geometrically limited by the surrounding laser beams with an incidence

[114] Due to space constraints the distance of the second lens to the focal point is less than 300 mm.

[115] The couplers are composed of cage-compatible components from Thorlabs including an xy-translation mount for the fiber adapter and a z-translation mount for the coupler lens.

[116] Oz Optics QPMJ-A3AHPCA3AHPC-400-3/125-3AS-X-1, X = 3 or 5 (meters), 3/125 μm, high power PM patchcord for 400 nm, end-capped, high-power air gap FC connectors on both ends

[117] Asphericon GmbH, AFM12-15-U-K-285, EFL 15 mm, fused silica, AR coating: 355 nm

[118] Sill Optics GmbH, Germany. The objective was designed by Jan Benhelm [141] in 2004 for the trapped-ion group in Innsbruck and is used in several experiments to date.

[119] PhotonGear Inc., USA

angle of 45° with respect to the ion plane. The increased NA, compared with the Sill Optics objective, is beneficial for photon collection and for diffraction-limited focusing of a laser beam at 729 nm for single-ion addressing. The field of view is 300 μm in diameter and the specified wavefront errors for 397, 532 and 729 nm are $< 0.075\lambda$ rms, $< 0.06\lambda$ rms and $< 0.05\lambda$ rms, respectively. The objective is equipped with a 3-inch-thread[120] close to the center of gravity and is screwed into a custom threaded 3-inch-mirror mount[121]. The mirror mount is placed on top of an xyz-translation stage[122]. In addition to translations in three directions, the mirror mount allows for tilting of the objective to minimize optical aberrations.

For spatially resolved imaging, the collected fluorescence light is focused onto the chip of an EMCCD camera[123]. The PhotonGear objective is infinity-corrected for 397 nm[124]. A lens with a focal lens of 1000 mm[125], mounted inside the magnetic shield, is used as a tube lens to focus the image onto the camera chip. A 3-inch dichroic mirror[126]reflects the fluorescence light at 397 nm towards the camera while transmitting light at 729 nm for single-ion addressing from the other direction. Complementary to the camera, a photon-multiplier tube[127] (PMT) is employed to count fluorescence photons from the ions. A 90/10 beam splitter sends 90 % of the collected light to the EMCCD camera and 10 % to the PMT. The PMT proves particularly helpful during the first attempts to trap ions in a new setup. It has a larger chip (22 mm) than the camera (8.2×8.2 mm chip size), which facilitates the alignment of the collected light. A slit aperture[128] is installed in front of the PMT to cut off potential stray light at the edges of the incoming beam. Furthermore, the PMT can be used for fast measurements with a single ion when spatial resolution is not required.

With the new objective we were able to reduce the aberrations of the individual signals substantially and therefore decrease the fluorescence cross-talk between the ions in a crystal. This is of particular importance for experiments with larger 2d crystals with more than several tens of ions. The higher NA as well as the reduction of aberrations allows to reduce the exposure time for imaging to about $300 - 500\mu$s while maintaining a high-fidelity quantum state readout compared to typically between 3 and 7 ms used with the previously installed Sill Optics objective.

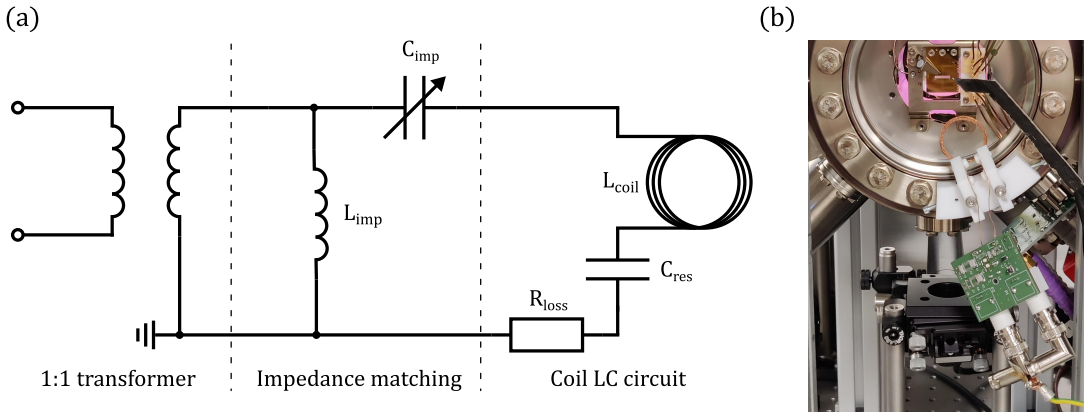

Figure 3.21: (a) Schematic circuit of the rf coil used for global coherent manipulation of the $|S_{1/2}, m = -1/2\rangle \leftrightarrow |S_{1/2}, m = +1/2\rangle$ transition. (b) Photo of a prototype of the rf coil setup mounted to the vacuum chamber's front viewport.

3.7 rf coil for coherent manipulation of the ground-state qubit

In addition to using stimulated Raman transitions, we can use an electromagnetic field at radio frequency to couple the ground-state qubit, whose states are separated by approximately 11.5 MHz. As a result of the longer wavelength compared to optical transitions, we can benefit from a more homogeneous coupling across an ion crystal as well as an enhanced coherence. In our setup, a handmade coil is used as an rf antenna to drive the transitions between the two Zeeman sublevels $|S_{1/2}, m = -1/2\rangle$ and $|S_{1/2}, m = +1/2\rangle$. It consists of 5 windings of a standard enameled copper wire (0.4 mm wire diameter) with an approximate coil diameter of 35 mm. The coil is mounted below the front viewport to an aluminium profile holding the vacuum chamber. Teflon parts keep the coil in place while ensuring electrical isolation from the aluminium profile and the vacuum chamber. A home-built circuit board with multiple SMD pads allows for tuning the circuit by adding combinations of parallel and serial capacitors and inductors. A schematic of the circuit and a photo of the setup is shown in Fig. 3.21. The sinusoidal rf signal at $\omega_{\text{res}} \approx 11.5$ MHz, used to drive the qubit transition, is generated by a DDS of the Sinara Urukul module. Although the DDS allows for fast switching, an additional electronic switch[129], controlled by a TTL signal, suppresses signal leakage from the DDS when the coil is not used. The

[120] Thorlabs SM3 thread
[121] Liop-tec SR100-HS-100-2S-RE, STAR series 3" with SM3 thread
[122] Newport M-562F-XYZ
[123] Andor iXon Ultra 897, 512x512 pixels, pixel size: 16 μm, NUV-optimized AR coated window
[124] The object conjugate plane for 729 nm is at -2.23m and for 532 nm at -3.61m.
[125] Thorlabs LA4337-UV-ML, 2" UVFS plano-convex lens, f = 1000mm
[126] LaserOptik L-20094, HR at 390-400 nm, HT at 729 nm and 532 nm
[127] Sens-Tech P25PC
[128] Owis SP40, max. 7x7 mm slit aperture
[129] MiniCircuits ZASWA-2-50DRA+

signal is preamplified[130] by > 29 dB. A rf transformer[131] is installed in the supply line to galvanically isolate the rf coil from the source. The other end of the coil is grounded to the vacuum chamber. Without the isolating transformer, we observed excessively large heating rates of the out-of-plane COM mode on the order of thousands of phonons/s. The origin of this behavior is currently unknown.

Impedance matching of the load to the line impedance of 50 Ω is performed with a single LC network (C_{imp} and L_{imp}). A resistor of 1 Ω is introduced into the circuit (here contained in R_{loss}) to maintain a sufficiently low Q factor and thus a relatively broad resonance. The capacitance of the resonant circuit is $C_{res} = 98$ pF. Based on the given values, the coil's inductance is estimated to be $L_{coil} \approx 1.95$ μH (from $\omega_{res} = \frac{1}{\sqrt{LC}}$). The circuit's quality factor Q is measured to be around 18. The effective resistance can thus be determined to be $R_{loss} \approx 7.8$ Ω (from $Q = \frac{1}{R}\sqrt{\frac{L}{C}} = \frac{\omega_{res} L}{R}$), of which 6.8 Ω are attributed to parasitic losses. With this circuit, we achieve a Rabi frequency of $\Omega \approx 2\pi \times 100$ kHz with a maximum relative variation of about 3.5 % across a 91-ion crystal.

Overall, the circuit's components are given by:

Component	**Value**	**Composition**
$\mathbf{C_{imp}}$	231–271 pF	1 nF || 220 pF || 10—50 pF (variable)
$\mathbf{L_{imp}}$	244 nH	220 nH + 12 nH + 12 nH
$\mathbf{C_{res}}$	98 pF	(150 pF || 22 pF) + 220 pF
$\mathbf{L_{coil}}$	~ 1.95 μH	-
$\mathbf{R_{loss}}$	~ 7.8 Ω	1 Ω (built-in) + 6.8 Ω (losses)

[130] MiniCircuits ZHL-1-2W-S+, Gain Block, 5-500 MHz, 50 Ω
[131] MiniCircuits TC1-1-T+, 1:1 core & wire transformer, 0.4-500 MHz, 50 Ω

Chapter 4

System characterization

This chapter discusses various measurements that characterize the presented system and its performance. The loading and ionization process via laser ablation is described in Sec. 4.1. A brief phenomenological overview of the operation of the ion trap is given in Sec. 4.2 prior to a discussion of measurements of the ions' micromotion (Sec. 4.3), which allow for the minimization of excess micromotion and ensure the planarity of the trapped crystals. Furthermore, the stability of ion crystals is investigated. Section 4.4 presents quantitative measurements for characterization of the melting and recrystallization behavior of planar crystals with various ion numbers. After that, Sec. 4.5 outlines a method for the analysis of distinct crystal lattice configurations, enabling the minimization and filtering of unwanted occurrences of metastable lattice configurations during a measurement. Numerical simulations, described in Sec. 4.5.3, substantiate these findings. The last three sections present details on the single-ion heating rate (Sec. 4.6), the electronic coherence (Sec. 4.7) and the motional coherence (Sec. 4.8) observed in the system.

4.1 Ablation Loading

In order to characterize and optimize the ablation loading, the fluorescence of neutral calcium atoms at 423 nm is detected as a function of the arrival time at the PMT while scanning the frequency of the laser. The detected photon counts are analyzed using a time controller for time-correlated photon counting (time tagger)[1]. The presented measurements are essentially time-of-flight (TOF) measurements and they are used to find suitable laser parameters to deterministically load $^{40}Ca^+$ as well as $^{44}Ca^+$ ions. The initial motivation for loading $^{44}Ca^+$ ions, was to measure the swapping rate of a mixed-isotope crystal, comprised of one $^{40}Ca^+$ (bright) and one $^{44}Ca^+$ (dark) ion, in order to characterize the pressure in the vacuum system.

Loading $^{40}Ca^+$ ions

In the current setup, the two PI laser beams (423 nm and 375 nm) are overlapped on

[1] ID Quantique ID900 time controller

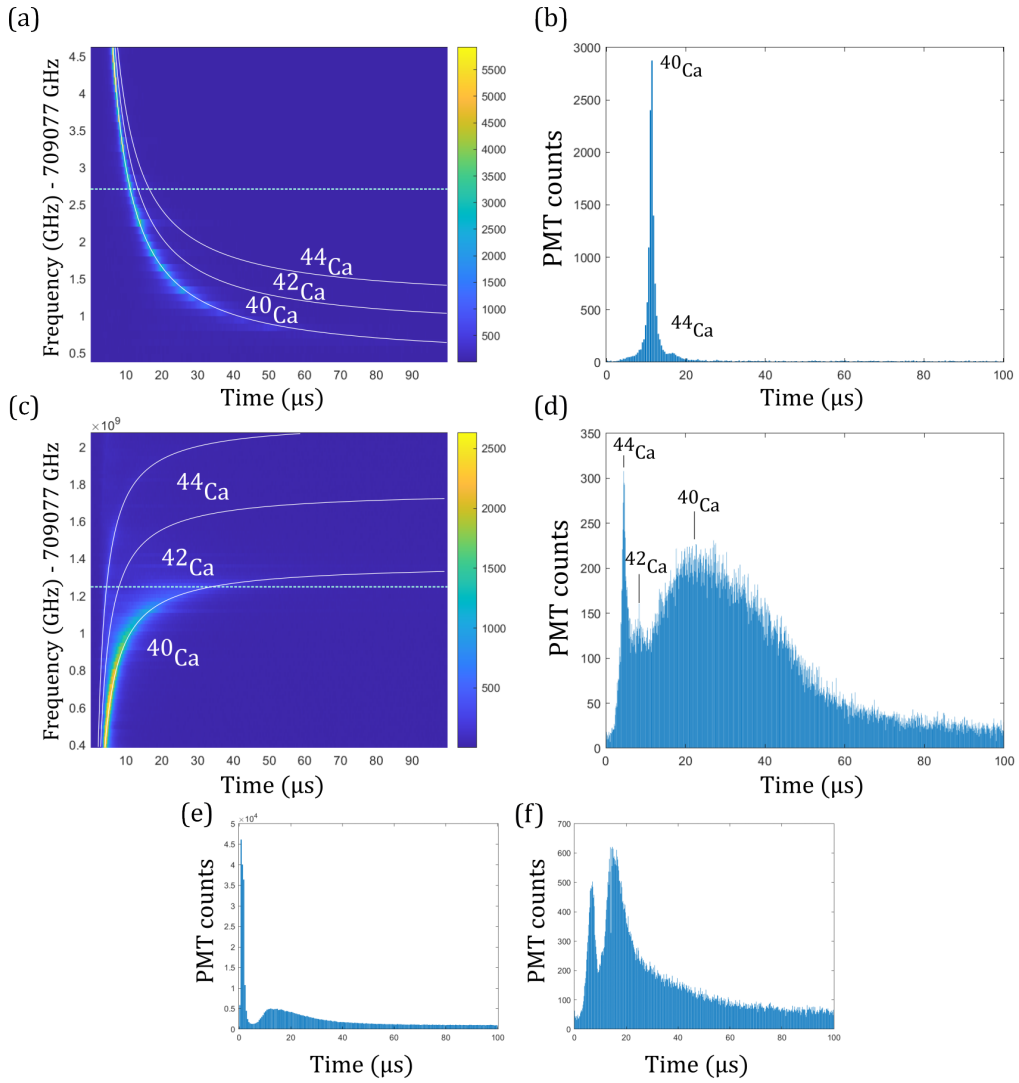

Figure 4.1: Time-correlated photon counts of neutral atom fluorescence at 423 nm detected on the PMT. a) The photon counts are shown for varying detuning of the PI laser beam. The angle between the atom beam and the PI laser beam is 45°. The resonance of ^{44}Ca atoms is barely visible to the right of the more prominent ^{40}Ca signature. The geometry (blue Doppler shift superimposing the blue isotope shift) does not allow to suppress the loading of ^{40}Ca atoms. The white solid lines represent the expected Doppler-shifted resonances based on the arrival time. b) Photon counts for a single PI laser frequency (dashed line in a)). The small spike to the right of the main peak (^{40}Ca) is attributed to ^{44}Ca atoms. c) Same as a) but for an angle of 83° between the atoms and the laser coming from the opposite direction (red Doppler shift). Two distinct curves for ^{40}Ca and ^{44}Ca are visible. A third, very subtle line corresponds to ^{42}Ca atoms. This geometry enables selective loading of isotopes other than ^{40}Ca. d) Photon counts for a single PI laser frequency (dashed line in c)). There are two main peaks for ^{44}Ca and ^{40}Ca. A third small peak in-between corresponds to ^{42}Ca atoms. e) PMT counts for high pulse power with dominant direct ionization. f) PMT counts at reduced power. A further reduction of laser power leads to a trace as shown in a). Note that fluctuations of the laser's position on the target cause large fluctuations in fluorescence and background counts.

a PBS cube and sent to the trap through the left axial viewport (see Fig. 3.15). The angle between the PI beams and the neutral atom beam coming from the target is 45°. For this configuration, a time-resolved measurement of the neutral atomic fluorescence as a function of the arrival time and frequency detuning is shown in Fig. 4.1(a). To load $^{40}Ca^{+}$ ions, the frequency of the first PI laser is currently set to 709.079362 THz (422.791120 nm), resonant with an atom population that has a peak velocity of about 600 m/s, corresponding to a peak arrival time of about 25 μs at the PMT[2]. For trapping, it is beneficial to choose a PI laser frequency, which is resonant with a slow population of neutral atoms as they are easier to trap and require less kinetic energy to be removed through laser cooling. Increasing the laser frequency tunes the laser into resonance with faster atoms as they are moving away from the light source. In this configuration, $^{40}Ca^{+}$ ions can be loaded isotope-selectively. In Fig. 4.1(a), the ^{44}Ca atoms appear only as a subtle line next to the dominant ^{40}Ca line. In Fig. 4.1(b), an exemplary single trace corresponding to the dashed line in subpanel (a) is displayed, which represents a histogram of the time-correlated signal at a single PI laser frequency of 709.080704 THz. The ^{44}Ca signature appears as a small peak next to the main peak from ^{40}Ca atoms. For loading, the PI laser beam at 423 nm is controlled by a mechanical shutter whereas the second PI laser beam at 375 nm is switched on rapidly with a time delay of 10 μs with respect to the ablation laser pulse. This prevents excessive exposure of the trap electrodes to UV light, which could create charges on the trap surface and, potentially lead to dark ions by ionizing the background gas through free electrons. Furthermore, the delayed 375-nm pulse is suppressing the loading of fast ions, thereby eliminating the necessity to remove their higher kinetic energy.

Loading $^{44}Ca^{+}$ ions

The geometry described above (PI beams through left axial trap hole) does not allow for the exclusive selection of ^{44}Ca atoms as the red Doppler shift of the resonance frequency (several GHz for fast atoms) has an opposite sign than the blue isotope shift of 773.8(3) MHz [142]. This results in coincident resonances for ^{40}Ca and ^{44}Ca atoms that are slower compared to ^{40}Ca. In order to change the Doppler shift's sign and decrease its magnitude, we set up another beam entering from the right rear viewport at 45° with respect to the crystal plane, resulting in an angle of about 83° between atom beam and 423-nm laser beam. In contrast to the configuration used to produce Fig. 4.1(a), the modified geometry enables deterministic loading of ^{44}Ca isotopes, which can be seen in Fig. 4.1(c). By tuning the laser frequency to values > 709.0783 THz, the ^{44}Ca line can be accessed without being resonant with ^{40}Ca atoms. Figure 4.1(d) shows a single trace, measured at a frequency that is on resonance with both fast ^{44}Ca and slower ^{40}Ca atoms. A third small peak in-between, visible as fine line in Fig. 4.1(c), can be attributed to ^{42}Ca atoms (isotope shift: 393.5(2) MHz, natural abundance: 0.647 % [142]). Note that, given the availability of a rapidly switchable 375-nm laser beam, one could select the slower ^{40}Ca distribution by activating the laser after the arrival of the main fraction of other isotopes, e.g. after 15-20 μs in the example of Fig. 4.1(d).

[2]The distance between the calcium target and the trap center is about 1.5 cm.

Avoiding direct ionization by the ablation laser

At the time of carrying out these measurements, we did not succeed in deterministically loading mixed-isotope crystals due to a non-optimal alignment and power setting of the photoionization laser beams. The loading process was therefore dominated by direct ionization through the ablation laser pulse. As a result of the natural abundance of 97 % of ^{40}Ca compared to 2 % of ^{44}Ca target, we predominantly loaded $^{40}Ca^{+}$ ions. After adjustment of the PI laser beams, the ablation pulse power was set to a level below the power threshold for direct ionization, at which efficient loading using the PI beams is achieved, rendering photoionization the predominant loading mechanism. This enables isotope-selective loading of ^{40}Ca (Fig. 4.1(a)) or ^{44}Ca ions (Fig. 4.1(c)). In typical operation, the power of the ablation laser pulse for loading is about 25 %[3] of the maximum power of 300 μJ per pulse. The PI beams at 423 nm and 375 nm are set to a power of about 300 μW and 8 mW, respectively. With these settings, ions are loaded and Doppler cooled within a second whereas without the use of the PI lasers, but at higher ablation laser power, the laser cooling to a localized spot appearing on the camera image takes up to a few seconds, as a higher kinetic energy of the ions has to be removed. Figure 4.1(e) shows a time-resolved measurement at a high ablation laser power. A peak at an arrival time of < 1 μs is observed corresponding to fast ions, which are ionized directly by the ablation laser. This peak is removed by lowering the power per ablation laser pulse. Figure 4.1(f) shows a measurement at intermediate power. Further reduction of the power leads to a trace as shown in Fig 4.1(a).

4.2 Ion trap potential, ion number, trapping lifetime

In addition to a short description of the trap and characteristic simulated values that was given in Sec. 3.1.2, this section briefly presents the most important experimental parameters as well as phenomenological observations. A detailed description and characterization of the ion trap and its potential is presented in Ref. [61].

Trap potential

The trap is typically operated at rf voltages of around 1 kV peak-to-peak with a trap drive frequency of $\Omega_{\mathrm{rf}} \approx 2\pi \times 43.2$ MHz. The dc voltages applied to the dc trap electrodes are on the order of 15 V on the middle segments and 30 V on the endcap electrodes. The typical trapping potential we work with is characterized by the oscillation frequencies $\omega_{\mathrm{s}} = 2\pi \times 2.2$ MHz in the strongly confining direction and $\omega_{\mathrm{w1,w2}}$ of a few hundred kHz in the two weakly confining directions. The trap is designed to confine planar crystals in the yz-plane. The rf electrodes create a confining potential in the xy-plane. Additional confinement in axial direction is achieved by applying positive voltages to the eight endcap dc segments. The potential created by the endcaps is confining in x- and z-direction while being repulsive in y-direction. For the purpose of micromotion compensation, these voltages on the endcaps are not equal (see Sec. 3.4.4. Positive voltages on the middle segments create the anisotropic potential, with strong confinement along x and weak confinement along y and z, required for trapping planar crystals.

[3] estimated from the angle of the half-wave plate used to attenuate the laser power

Simulations of the trap potential suggest a potential depth of about 4 eV for an rf voltage of 1 kV peak-to-peak. From image analysis it can be inferred that anharmonic contributions to the trapping potential are only minor in the presented setup. More details on the principles of this analysis can be found in Sec. 2.1.5 and Refs. [60, 61]. As the principal axes of the trap potential are well aligned with the trap's geometrical axes, x, y, and z, the notation (ω_{w1}, ω_{w2}, ω_{s}) and (ω_x,ω_y,ω_z) is used interchangeably in this thesis.

Ion number (N)

In the presented trap, planar ion crystals of up to $N \approx 100$ ions have been trapped routinely throughout this work. As quantum measurements require stable crystal lattice configurations, we trap elongated highly symmetric crystal configurations with two symmetry axes (y and z), which are realized only by specific ion numbers for a given trap potential. More details on the analysis of crystal lattice configurations are given in Sec. 4.5. The trapping of stable 2d crystals with ion numbers beyond $N = 105$ has not yet been attempted in presented apparatus. Although there is no fundamental constraint to do so, it currently requires manual and iterative adjustment of the trap voltages to find stable configurations, which becomes increasingly difficult with higher N. In principle, the system should be capable of trapping substantially more than 100 ions. In particular, relaxing the potential in axial direction (z) provides a way to maintain planar crystals before the heating of low-frequency in-plane modes may become a problem. Recently, experiments reported in Ref. [36] demonstrated the stable trapping of 2d crystals consisting of up to 512 ions, using a similar trap design and a comparable trap oscillation frequency in out-of-plane direction of about $2\pi \times 2.2$ MHz. Hence, disregarding changes in the lattice configuration, it should be feasible to trap such larger planar ion crystals with the accessible trap parameters in the setup presented here.

An upper limit for the secular oscillation frequency in out-of-plane direction, and effectively for the number of ions, is given by the applicable rf voltage[4]. Increasing the confinement in OOP direction using higher voltages on the endcap or middle segments is restricted to the point, at which the confinement in y-direction becomes too weak. Both the endcap and middle segments increase the confinement in x- while decreasing it in y-direction. Applying negative voltages on the middle segments, on the other hand, would result in a stronger confinement in y-direction while weakening the confinement in x-direction. At some point, this would lead to the condition for trapping 2d crystals ($\omega_{\mathrm{s}}/\omega_{\mathrm{w}} > 1.23N^{\frac{1}{4}}$) no longer being satisfied.

Lifetime of trapped ion crystals

The lifetime of trapped ion crystals in our setup is limited only by the occurrence of "dark" ions[5]. During continuous operation of the trap and laser cooling of the ions, provided that there is no malfunction, ions do not get lost. The life time of a trapped crystal with $N \approx 100$ usually exceeds many hours and has even exceeded several days in the past

[4]Keeping the rf voltage around 1 kV peak-to-peak is a precaution since the trap has already been shorted during testing at voltages of approximately 1.7 kV and 1.2 kV peak-to-peak.

[5]Dark ions are either a different isotope or atomic species, or a molecular ion, e.g. CaH^+ or $CaOH^+$, formed in a reaction with a residual background gas atom or molecule.

before a dark ion occurred. We observe that dark ions almost always appear in addition to the already trapped ions, preserving the number of bright ions in a crystal. These dark ions are preferentially residing at the edge of the crystal pointing to atomic species or molecules that are heavier than ^{40}Ca as they experience a lower confinement. After resuming the operation of the trap, following a full ramp-down of the rf voltage, we usually observe an increased number of dark ions within the first day of operation. This may be related to the release of contaminants from the trap electrode surface during the heat-up process. In contrast to the dark ions appearing during continuous trap operation, these dark ions preferentially occupy positions between the bright $^{40}Ca^{+}$-ions, pointing to lighter ionic species.

4.3 2d crystal alignment and orientation

In a 2d crystal trapped in a rf trap, micromotion of ions displaced from the rf null is inevitable. To first-order, in our trap geometry (see Sec. 3.1.2), micromotion occurs solely along the y-direction (perpendicular to the horizontal plane) enabling micromotion-free optical access within the entire horizontal plane. However, this applies only to ion crystals that are perfectly aligned with the yz-plane of the trap. Imperfections in the trap geometry as well as stray electric fields, e.g. due to charges on the trap surface, can lead to a misplacement of the ions with respect to the rf trap center. Displacement along the strongly confining direction as well as tilts about arbitrary axes result in phase modulated laser-ion interactions. By measuring the excitation on the micromotion sidebands, the ions' micromotion can be minimized via application of suitable voltages, which is described in Sec. 4.3.1. In Sec. 4.3.2, measurements of the micromotion sidebands are further used as a tool to ensure the planarity of ion crystals.

Note that in case of a strongly focused laser beam, the micromotion along y can also leads to an amplitude modulation of the interaction [143]. For example, in a 105-ion crystal as shown in Fig. 4.2, the ions furthest away from the rf-zero line experience a micromotion amplitude of about 3 μm peak-to-peak. However, the laser-ion interaction is governed by the accumulated intensity that the ion experiences during the interaction time. Given that the applied laser pulse is long (e.g. 10 μs) compared to the period of the rf drive (about 23 ns in our experiments), the shot-to-shot variations in intensity caused by the modulation, are negligible.

4.3.1 Micromotion compensation

For most experiments, minimizing micromotion is crucial to maintain resonance between atomic transitions and light fields. There are several ways to do so, which are, for instance, discussed in Ref. [53] and in section 5.3 of Ref. [99]. Here, resolved sideband measurements of the micromotion sidebands are carried out to quantify and minimize the ions' micromotion. Provided that a narrow-linewidth laser is available and optical access from relevant directions is feasible, a resolved-sideband measurement is the most accurate and thus favorable method. We make use of the narrow $S_{1/2} \leftrightarrow D_{5/2}$ quadrupole transition at 729 nm to determine the micromotion modulation index β, which is related to the

Rabi frequency of the carrier transition Ω_{carr} and the Rabi frequency of the micromotion sideband transition Ω_{sb} in the following way [53, and references therein]:

The first-order solution of the ion motion with secular frequency ω_{s} is given by (cf. Eqs. 2.6 and 2.28)

$$x(t) = x_0 \cos(\omega_{\mathrm{s}} t)\,(1 + q/2 \sin(\Omega_{\mathrm{rf}} t))) \;, \tag{4.1}$$

where x_0 is the ion's distance from the yz-plane containing the rf-null. The micromotion-modulated electric field of a laser beam propagating in the rest frame of an ion can be expanded into Bessel functions J_n as

$$\begin{aligned} E(t) &= E_0 \exp\{-i\omega_{\mathrm{laser}} t\} \exp\left\{ i k_x x \frac{q}{2} \sin(\Omega_{\mathrm{rf}} t) \right\} \\ &= E_0 \exp\{-i\omega_{\mathrm{laser}} t\} \sum_{n=-\infty}^{\infty} J_n(\beta) \exp\{in\Omega_{\mathrm{rf}} t\} \quad , \end{aligned} \tag{4.2}$$

with the laser frequency ω_{laser}, the rf drive frequency Ω_{rf} and the trap's q parameter. For simplicity, the laser beam is assumed to propagate along the x-direction. Expression 4.2 relates the micromotion amplitude to the modulation index, given by $\beta = k x_0 q/2$. In the low intensity limit and for $\beta \ll 1$, we find

$$\frac{\Omega_{\mathrm{sb}}}{\Omega_{\mathrm{carr}}} = \frac{J_1(\beta)}{J_0(\beta)} = \frac{\beta}{2} + O(\beta^2) \;, \tag{4.3}$$

which represents a useful figure of merit in experiments as Ω_{carr} and Ω_{sb} can be measured easily via resolved-sideband spectroscopy. To this end, a pulse length scan on the carrier as well as on the micromotion sideband is fitted with a sinusoidal function to obtain the Rabi frequencies Ω_{carr} and Ω_{sb}, respectively.

Micromotion compensation procedure

When the crystal is optimally positioned at the center of the trap and aligned with the yz-plane, the modulation indices are expected to be minimized. Several imperfections, however, can lead to a non-optimal placement and orientation of the ions. They may not be confined well in a single plane but instead extended into the third dimension. The crystal plane could also be misaligned with respect to the trap center or tilted with respect to the principal axes. These issues may arise from asymmetries in the trap geometry as well as electric stray fields, e.g. caused by charges or dust on the trap surface. We compensate for these imperfections by applying pre-calculated voltage sets to the trap dc electrodes (see Sec. 3.4.4 for the calculation of these voltage sets).

The compensation procedure is routinely carried out, e.g. after changing the trap voltages, and is described in the following. So far, we adjust the crystal's position in y-direction by changing voltages only on the middle segments whereas the alignment in x and z is adjusted by using only on the endcap electrodes.[6] When the voltages required for compensation are completely unknown, the initial coarse compensation is performed iteratively in all three spatial directions using a single ion. In the first step, only linear translations of the

[6] Note that these additional voltages modify the confinement in all three directions.

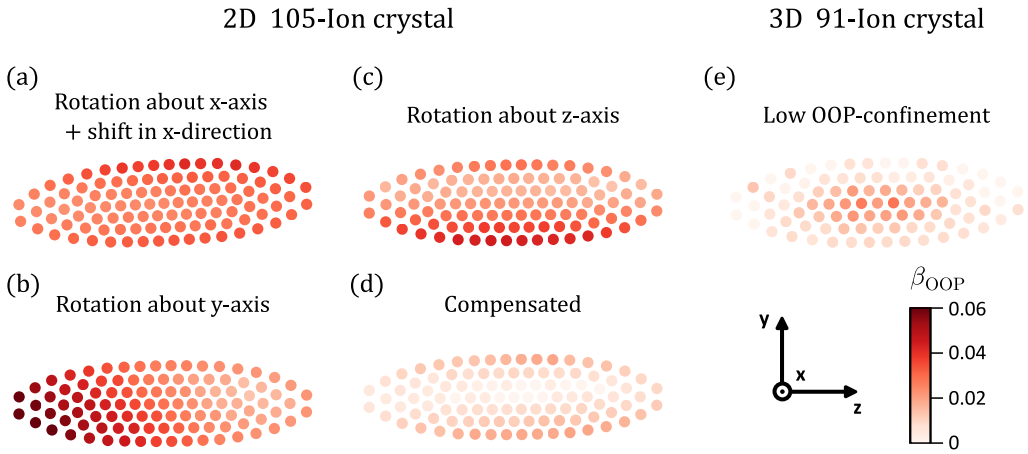

Figure 4.2: Micromotion modulation index in the out-of-plane direction. (a)–(c) Examples of planar 105-ion crystal displaying undesirable shifts along and rotations about various axes, resulting in increased modulation indices. The labels indicate the main contribution to the crystals' misalignment. (d) The micromotion can be compensated by the application of precalculated voltage sets, counteracting the unwanted shifts and rotations. The displayed ion crystal is aligned with the trap center and the yz-plane, minimizing the micromotion modulation indices for all ions. (e) Modulation indices of a slightly three-dimensional 91-ion crystal. The ions in the center are pushed out of the crystal plane due to low confinement in x-direction.

ion are induced. The modulation index in z-direction is measured with the axial *in-plane* beam and minimized by shifting the ion along the trap axis. Analogously, the x-direction is minimized using the out-of-plane beam. We minimize the modulation in y-direction using the "xy-beam" (at an angle of 45° with respect to the horizontal xz-plane). As the xy-beam couples to both the x- and y-directions, minimizing the excitation on the micromotion sideband using this beam does not necessarily minimize the micromotion in both directions equally. This can be achieved through an iterative procedure, alternating between the out-of-plane beam and the xy-beam. However, the displacement and tilt involving the y-direction can also be diagnosed with the out-of-plane beam probing a larger crystal. After locating the rf trap center with a single ion, in the second part of the compensation procedure, a larger crystal (typically $N > 50$) is used to detect rotations and shifts of the crystal plane using the out-of-plane beam as the primary tool. The modulation indices β_i of the individual ions are repeatedly measured while shifting and rotating the ion crystal to align it with the yz-plane.

Fig. 4.2 shows various scenarios of a 91-ion crystal and a 105-ion crystal. Subpanels (a) to (c) of Fig. 4.2 show the modulation indices $\beta_{\mathrm{OOP}}^{(i)}$ for 105-ion crystals displaying undesirable shifts along and rotations about arbitrary axes. In our setup, the main operations, which are applied to obtain the optimum configuration, are translations along the x-axis in combination with rotations about the z-axis. Since the pre-calculated voltage sets are based on the assumption of an ideal electrode alignment, the operations do not resemble pure translations or rotations. Therefore, a translation in x-direction usually adds unwanted

rotations about the z- and y-axis. By iteratively adjusting the compensatory voltages, the micromotion indices can be minimized to $\beta^{(i)}_{\mathrm{OOP}} < 0.02$ for all ions (Fig. 4.2(d)). The slightly increased modulation indices of the outer ions hint to a small misalignment of either the laser beam or the ion crystal.[7] However, these effects are small, reflected in the overall low modulation indices, and do not restrict any envisaged experiment.

4.3.2 Planarity of an ion crystal

Another possible reason for increased micromotion in out-of-plane direction is an insufficient trap anisotropy to keep the ions confined within a plane. So far, a perfectly planar crystal has been assumed. In practice, the crystal's planarity cannot easily be claimed from analyzing its image recorded perpendicular to the crystal plane. To investigate the planarity of the crystals, one can also exploit a measurement of the micromotion modulation indices using the OOP 729-nm beam. Figure 4.2(e) shows a 91-ion crystal that is not perfectly planar. Due to a low confinement in x-direction, the ions in the center of the crystal are pushed out of the plane. The third dimension manifests itself in a higher modulation index of these ions. Figure 4.3 shows the transition between a 3d and 2d configuration for a 91-ion crystal in more detail: Single-ion resolved pulse length scans of the carrier and the micromotion sideband reveal the coupling strength to the individual ions. At lower confinement along x, the ions in the middle row of the crystal (indicated in red) display a weaker coupling on the carrier, as the laser-ion interaction is modulated at Ω_{rf}, and a stronger coupling on the micromotion sideband. After increasing the voltages on the dc middle segments, the ions are pushed back into the plane and, consequently, show a more homogeneous coupling overall and a weaker coupling on the micromotion sideband. For the 2d crystals in optimal placement, shown in Fig. 4.2, consisting of 91 and 105 ions, the trap oscillation frequencies are $\omega_{x,y,z} = 2\pi \times (2196, 680, 343)\,\mathrm{kHz}$ and $\omega_{x,y,z} = 2\pi \times (2188, 528, 248)\,\mathrm{kHz}$, respectively.

4.4 2d crystal stability I - Melting and recrystallization

Most findings described in this section have been published in Ref. [60].

Background gas collisions

Two kinds of collisions with residual background gas can impact the ion crystal in the following way [58]: Inelastic processes may alter the internal state of the ion, lead to the formation of molecular ions in chemical reactions, e.g. CaH in case of Ca^+-ions, or cause a charge exchange with the neutral background gas. Elastic collisions, on the other hand, only add kinetic energy to the system. Its impact can result in a systematic uncertainty in frequency measurements [144], motional heating, changes in the crystal configuration of planar crystals and their melting into a non-crystalline cloud. Elastic Langevin collisions of the ions with residual background gas can transfer large amounts of energy onto the ions and are able to induce a transition to a non-crystalline phase, in which an additional energy

[7] In case of a misalignment of the beam with respect to the horizontal axis, the light would be modulated by the micromotion in y that has a larger amplitude for the outer ions.

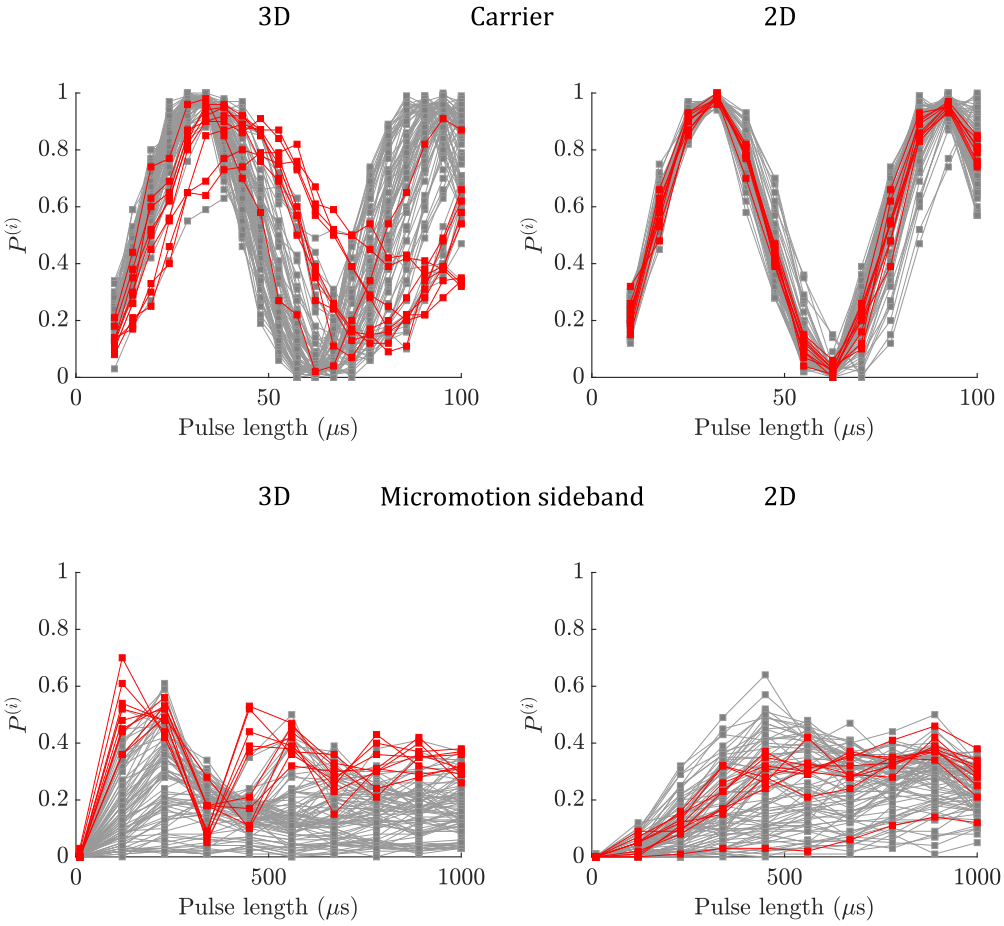

Figure 4.3: Carrier (top row) and micromotion sideband (bottom row) excitation dynamics of the individual ions of a slightly three-dimensional (left) and a well-compensated two-dimensional (right) 91-ion crystal. In the slightly 3d crystal, we observe a decreased coupling on the carrier as well as faster oscillations on the micromotion sideband for the ions in the central row of the crystal (marked in red). By increasing increasing the dc voltages on the middle segments and thus the confinement in out-of-plane direction, the ions in the center of the crystal are pushed back into a planar configuration. This scenario corresponds to the crystals shown in Fig. 4.2(d) and (e).

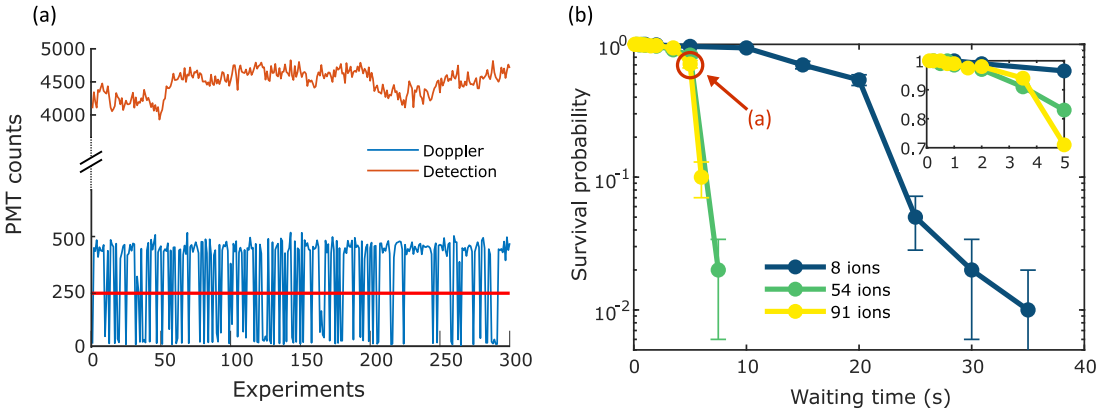

Figure 4.4: Melting behavior of planar crystals. (a) Exemplary data set for a 91-ion crystal and a wait time of 5 seconds corresponding to a single data point in (b). The PMT counts after the specified wait time (labeled *Doppler*) are used to detect melting events via a predefined threshold (red solid line). In addition, the PMT counts after application of a recrystallization pulse (labeled *Detection*) are used to ensure that the ions are again in crystalline phase before the next experiment. In all individual experiments, no dips (indicating a melted crystal, as seen in Fig. 4.5(a)) of the *Detection* counts were observed and the rejection of data by setting another threshold was not required. In 87 out of the 300 carried out experiments, we detect a melted crystal. The drift of the PMT counts is due to the unstabilized laser power of the 397-nm beam used for detection. (b) Probability of not melting into an ion cloud within a certain wait time with all laser cooling beams being switched off for 2d ion crystals consisting of 8, 54 and 91 ions. The inset shows the survival probabilities for short times in more detail.

transfer can occur from the trapping rf field to the ions in the cloud (rf heating) [47, 145]. Once the crystal is melted, a quantum measurement is fully corrupted. For this reason, it is essential for any measurement that an ion crystal maintains its crystalline structure during the experimental sequence. A stable and well-known lattice structure is crucial for individual-ion readout and laser addressing, as the calibration of these processes relies on the stable positions of the ions.

4.4.1 Melting of planar ion crystals

When exciting a melted ion cloud with light at 397 nm, the non-localized, hot ions scatter fewer photons than ions in the crystalline phase. This phenomenon can be used to automatically detect a melting event during data taking by identifying a drop in fluorescence counts on the PMT during Doppler cooling[8]. In our experiments, the detection of such an event interrupts the sequence and triggers a far-red-detuned ($\Delta = 2\pi \times 330$ MHz) Doppler

[8]The photon counts on the PMT were used when there was still a 70/30 beam splitter between camera and PMT. After installing a new objective and a 90/10 beam splitter, the signal on the PMT is too low for a robust automated detection of the drop in photon counts. Therefore, the "auto refreeze" feature is now implemented using a second in-sequence image with fully bright ions enabling the analysis of the lattice configuration as well as detecting melted crystals easily.

cooling beam (*refreeze* beam) to be switched on for 100 ms along with the primary Doppler cooling beam. The compromised experiment will then be repeated.

To characterize the melting behavior of planar ion crystals, we investigate the survival time of a crystal in the absence of any cooling. For this purpose, after cooling, all ions are initialized in the electronic ground-state (bright state). After that we introduce a variable wait time τ, during which all cooling beams are turned off. Subsequently, the fluorescence counts are recorded on the PMT by exciting the ions with a 397-nm pulse. Theses counts are used to distinguish between the melted and crystalline phase, making use of sudden drops in fluorescence as described above. Afterwards, the primary Doppler cooling and refreeze beams are turned on for 100 ms to recrystallize a potentially melted crystal. Finally, the PMT counts are recorded again and a threshold could be used to ensure that the ions are recrystallized before the next measurement. In the measurements presented in Fig. 4.4, the ions were recrystallized in each individual experiment, rendering the definition of a threshold unnecessary.

In Fig. 4.4(a) the PMT counts after a waiting time of 5 s (labeled *Doppler*) as well as after application of the refreeze pulse (labeled *Detection*) are shown for 300 individual experiments with a 91-ion crystal. Figure 4.4(b) shows the results for planar crystals consisting of 8, 54 and 91 ions. The survival probability, i.e. the fraction of single-shot experiments, in which the ions maintained their crystalline structure, is presented as a function of the waiting time τ between 0.1 and 60 seconds. For each given waiting time, between 100 and 300 experiments were carried out to determine the survival probability. For the smaller 8-ion crystal, we observe a relatively stable crystal lattice up to 10 s and 100 % melting after a waiting time of 40 s. For larger crystals, the time required to obtain melted crystals in 100 % of the experiments is significantly reduced; however, the ions maintain their crystalline structure with high probability for several seconds, as shown in the inset of Fig. 4.4(b). It is evident that the data does not follow a purely exponential decay, which would be expected from melting events caused solely by Langevin collisions. We associate this nonexponential decay with rf heating as an additional mechanism in the melting process. Rather than being caused only by background gas collisions, rf heating following these collisions could lead to the observed decay and a nonlinear dependence on the number of ions.

In our experiments, we mitigate rf-heating effects to a certain degree by operating the trap with a low q parameter of $q \approx 0.1$. For the long timescales investigated in these experiments, however, these effects seem to become considerable. Molecular dynamics simulations performed in Ref. [146] suggest a scaling of the rf-heating rate with q^n, where $n > 4$.[9] The nonlinear dependence on the number of ions found in this reference is supporting our observations. Irrespective of these mechanisms, the observed crystal survival times of several seconds for larger crystals is long compared with the time of the envisaged experiments, presumably on the order of ≤ 1 s.

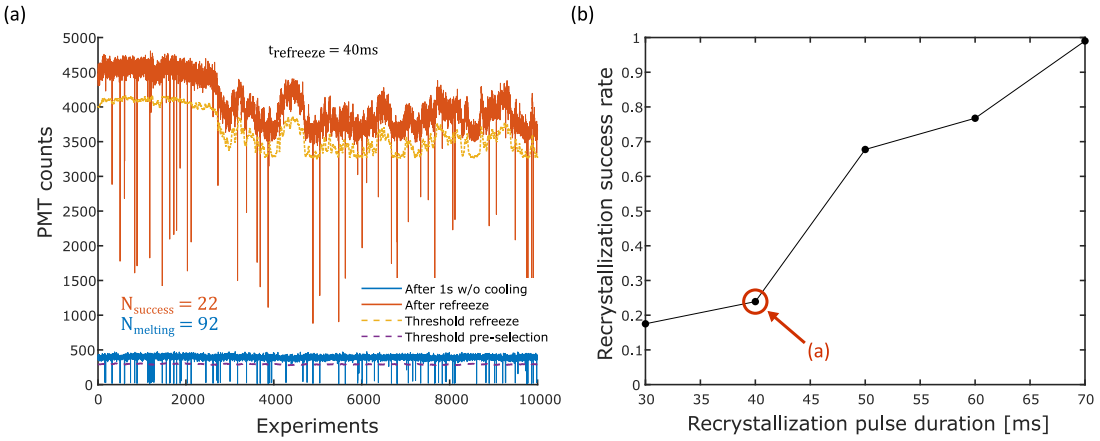

Figure 4.5: Refreeze measurements with a planar 91-ion crystal. (a) Exemplary data set of a measurement with a refreeze pulse length of 40 ms corresponding to the second data point in (b), showing a low recrystallization success rate of about 24 %. After a free evolution time of 1 s, the fluorescence PMT counts (*After 1 s w/o cooling*) are detected and evaluated by comparison with a threshold. Fewer scattered photons indicate a melted crystal. Subsequently, the refreeze Doppler pulse is applied. The success of the recrystallization attempt is evaluated by comparing the fluorescence counts (*After refreeze*) to a predefined threshold. The thresholds are dynamically defined as a specified fraction of the PMT counts detected in each experiment, which accounts for the drift of the unstabilized laser power. The data shows 92 melting events occurring in 10000 single-shot experiments. Using a refreeze pulse of 40 ms, out of these 92 experiments, a successful recrystallizaton was achieved in only 22 cases. (b) Recrystallization success rate for pulse lengths between 30 and 70 ms. After 70 ms, about 99 % of the melted crystals are recrystallized.

4.4.2 Recrystallization of an ion cloud

We performed further experiments, similar to the ones described in the previous section, to estimate the required duration of a recrystallization (refreeze) pulse, i.e. a far red-detuned ($\Delta = 2\pi \times 330$ MHz) Doppler cooling pulse at 397 nm, that is applied to recrystallize an ion cloud consisting of 91 ions. To this end, after initial cooling and ground-state preparation, the cooling lasers are switched of for a duration of 1 s, representing a realistic upper limit for the sequence length of future experiments. After 1 s, the fluorescence is detected on the PMT to distinguish whether the ions are in a crystalline or melted phase. After detecting a melting event, a recrystallization pulse is applied before detecting the photon counts on the PMT to check the success in recrystallization[10]. The success rate is repeatedly measured as a function of the refreeze pulse length.

Figure 4.5(a) displays exemplary data of a measurement run with a planar 91-crystal

[9]The theory based on Coulomb pair collisions predicts a scaling of the rf-heating rate of q^n, where $n = 4$ [147], which is expected to be applicable to higher temperatures ($n = 4.5$ for $T = 5$K in Ref. [146]).

[10]In addition, the ions were imaged on the EMCCD camera, which was used to cross-check the success in recrystallization.

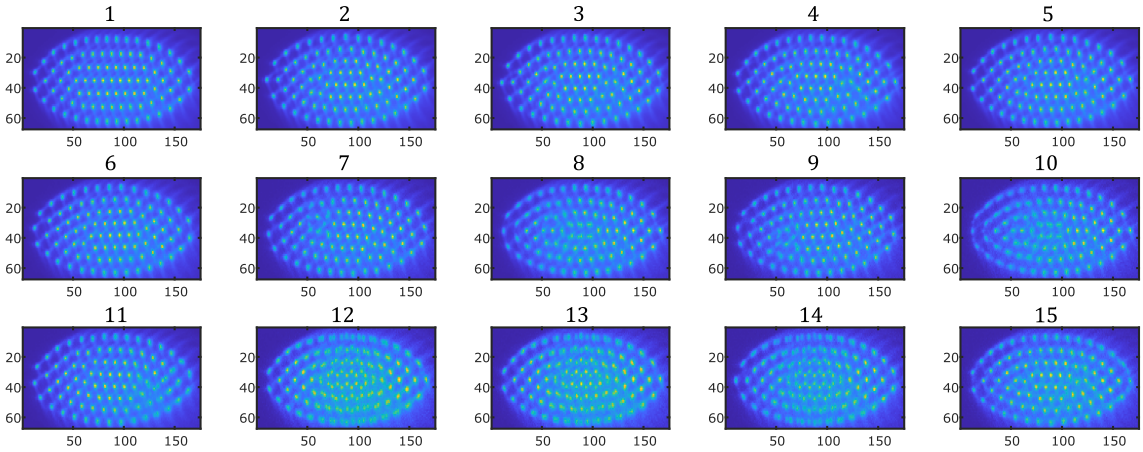

Figure 4.6: Images of a 91-ion crystal in various configurations, illustrating the need for an automated image analysis to detect distinct configurations in experiments with large planar crystals.

using a refreeze pulse duration of 40 ms. The data presented in (a) corresponds to the second data point in Fig. 4.5(b) showing the recrystallization success rate for various pulse lengths between 30 and 70 ms. A melting of the 91-ion planar crystal within 1 s of waiting time occurs in about 1 % of the cases, which is consistent with the experiments described in Sec. 4.4.1 and shown in Fig. 4.4. Hence, around 10000 experiments were conducted for each refreeze pulse duration to obtain approximately 100 usable data points. If a melting event occurs within 1 s without cooling, the experiment reproduces a realistic free evolution time for the ion cloud before applying a recrystallization Doppler cooling pulse. For the 91-ion crystal, we observe recrystallization after 70 ms in 101 out of 102 recorded melting events. Based on these findings, our standard measurements sequences use a refreeze pulse length of 100 ms whenever a melting event is automatically detected by the experiment control system. This value is sufficient for crystals of size $N \lesssim 100$. For substantially larger crystals, which have not yet been used in any measurement, a longer refreeze pulse may be required.

4.5 2d crystal stability II - Crystal lattice configurations

Most findings described in this section have been published in Ref. [60].

In contrast to high-energy collisions with background-gas molecules or atoms leading to the melting of an ion crystal, transitions between distinct Coulomb lattice configurations could be induced by low-energy collisions or by motional heating, in particular rf heating [40, 41]. The transferred energy leads to a rearrangement of the ions' equilibrium positions associated with local minima in the potential energy landscape governed by the number of ions in a given potential. In some cases, two or more crystal configurations can be degenerate in energy: For example in a so-called "zigzag" crystal, the two mirror-symmetric configurations "zig" and "zag" both correspond to a minimum in potential

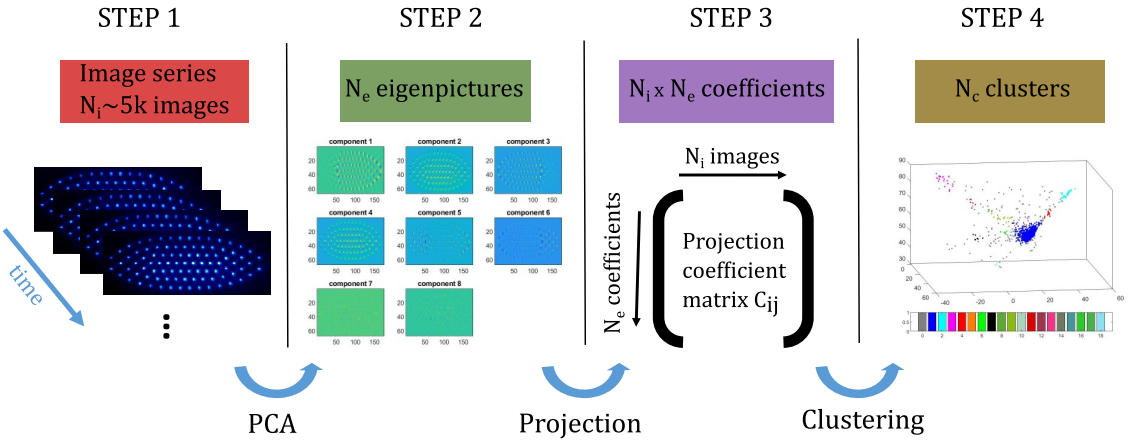

Figure 4.7: Overview of the clustering algorithm used for analysis of crystal lattice configurations. A description of the individual steps is provided in the main text.

energy [40, 64]. Figure 4.6 shows various images of an elliptical 91-ion crystal, exhibiting distinct configurations. In many cases the differences between two configurations are subtle and can be challenging to spot by eye.

In general, we find an increasing number of distinct crystal configurations for larger, less elongated 2d ion crystals culminating in completely unstable lattices in round crystals due to librational modes of the shell-like structures. However, there are highly stable elliptically shaped 2d crystal structures with two symmetry axes, exhibiting only a single configuration most of the time. In our experiments the quantum-state readout and its calibration (see Sec. 3.5.4) relies on fixed positions of the ions. At a later stage, addressing of individual ions with a tightly focused laser beam will also be sensitive to positional changes after calibrating the beam deflection to a specific configuration. Moreover, crystal lattice changes modify the motional mode spectrum, which in turn modifies the entangling interaction mediated by the ions' motion. All these unwanted effects, if not detected, can corrupt measurement outcomes. It is therefore essential that changes between lattice configurations are either mitigated beforehand or detected with high fidelity to exclude the corresponding data from further analysis.

In Sec. 4.5.1, the analysis of distinct crystal lattice configurations via clustering is presented. The detection and quantification of the crystal configuration changes further allows for mitigation and filtering of unwanted occurrences of metastable lattice configurations during a measurement, which is described in Sec. 4.5.2. Section 4.5.3 supports these findings with numerical simulations based on simulated annealing of ion crystal lattices.

4.5.1 Analysis of 2d ion crystal configurations via clustering

Clustering algorithm

The analysis of the configuration changes is based on the recording of a time series of ion crystal images and the assignment of these images to distinct configurations using

statistical and machine-learning tools. More precisely, a dimensionality reduction is carried out using a principal component analysis (PCA) followed by the application of a clustering algorithm[11] [148]. Figure 4.7 shows a schematic diagram of the individual steps, which are described in the following:

STEP 1 A series of N_P images of an N-ion crystal, taken about 0.5 s apart, is recorded. For a comprehensive analysis, typically a number of images on the order of $N_P \approx 10^4$ is recorded. If the goal is not to capture as many configurations as possible but rather to use the analysis to quickly check the crystal stability over shorter time scales, one can use a reduced set of images recorded over a shorter amount of time. The pixel brightness values of each recorded image j is represented as a column vector $\mathbf{x}_j$ and put into a matrix $M = [\mathbf{x}_1 \dots \mathbf{x}_{N_P}]$ representing all images and pixels as columns and rows, respectively. **STEP 2** A PCA is applied to the data for the purpose of dimensionality reduction, as the information contained in each image is on the order of 10^4 pixel values. To this end, a singular value decomposition (SVD) of the covariance matrix of $C_M = MM^T$ of the kind $C_M = Y\Sigma^2 Y^T$ is performed, where Σ is a rectangular diagonal matrix containing the N_P squared positive singular values of M, and Y contains the corresponding eigenvectors $\mathbf{y}_i$ that are in the following denoted as *eigenpictures*. By truncating these matrices according to only a small number of the largest n singular values, the individual images can be represented as superpositions $\mathbf{x}_j \approx \sum_{i=1}^{n} c_{ij}\mathbf{y}_i$, with $c_{ij} = \mathbf{y}_i^T \mathbf{x}_j$. Empirically we find that the observed crystal configurations in our experiment can be sufficiently described and distinguished using $n \geq 8$ eigenpictures. **STEP 3** The coefficients c_{ij} are calculated by projecting each image onto the n most significant eigenpictures. Hence, each image is now represented by only n coefficients. **STEP 4** In a final step, the clustering algorithm DBSCAN is applied to all images in the reduced state space of n eigenvectors, i.e. applied to the matrix c_{ij}. This way, each image is assigned to a cluster in the reduced state space, where each cluster corresponds to a distinct crystal configuration.

The DBSCAN algorithm uses two input parameters: The parameter *minpts* defines the minimum number of points to form a dense region (ϵ-neighborhood), in which all points are mutually separated by less than a distance of ϵ, with ϵ being the second input parameter. All *core points* of a cluster have to have $minpts - 1$ other points within the distance of ϵ. In addition, points with a distance to these core points that is less than ϵ also belong to the same cluster and are regarded as *density-reachable* even if they have $< minpts$ points within ϵ. While DBSCAN was used in the presented analysis, a Bayesian Gaussian mixture model can be used in the current experiment control software[12] as an alternative clustering method.

Analysis of a planar 91-ion crystal

Figure 4.8 illustrates the configuration analysis of a planar 91-ion crystal, which is trapped in a non-optimal potential, resulting in an increased probability of finding metastable configurations. The analyzed data set consists of $N_P = 4100$ images recorded with an exposure time of 100 ms over several hours. Eight eigenpictures (displayed in Fig.4.8(a)) associated

[11] Density-based spatial clustering of applications with noise (DBSCAN)

[12] Implemented using the scikit-learn package in Python: *sklearn.mixture.BayesianGaussianMixture*

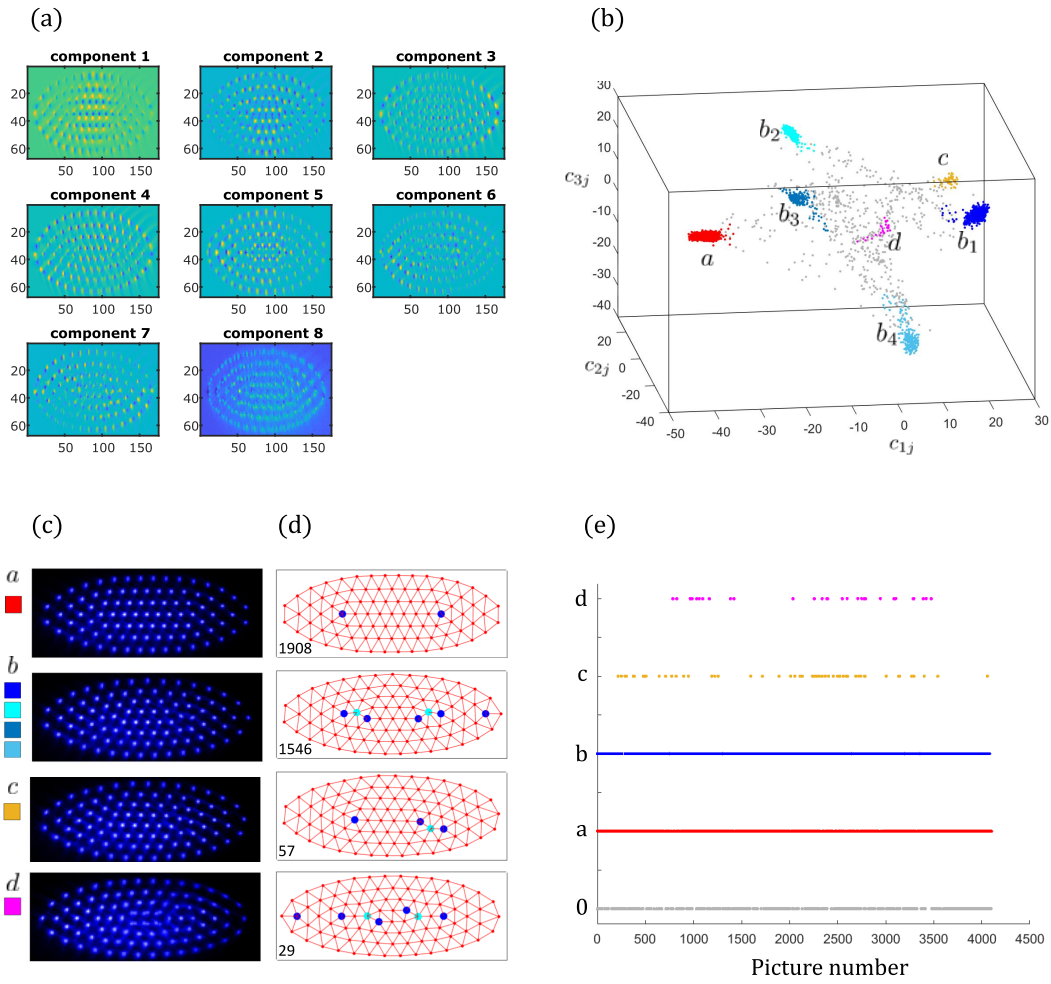

Figure 4.8: Configuration analysis 91-ion crystal based on 4100 camera images. (a) Eight eigenpictures are used as projectors for the purpose of dimensionality reduction. (b) Each image is plotted as a point in a three-dimensional state space corresponding to the projection coefficients c_{ij} of three highest eigenvalues. The clustering algorithm identified seven different clusters (a, $b_1, \ldots b_4$, c, d) indicated by colors. Gray points are unlabeled and associated with images, in which the ions are either hot or undergoing a configuration change during the image acquisition time. (c) Camera images, representing the cluster centers of four distinct configurations that are found in the analysis. The clusters b_i are mirror-symmetric representations of the same lattice configuration. The blurred ions in cluster d appear in all images of this cluster and are attributed to either hot in-plane motional modes, or to transitions between two (near-)degenerate non-equilibrium configurations occurring during imaging. (d) Planar graphs representing the ions as vortices, with edges linking nearest neighbors. Defects in the triangular lattice with five or seven instead of six nearest neighbors are indicated by dark blue and light blue vertices, respectively. The number of occurrences of the four distinct configurations are displayed in the lower left corner. (e) "Time series" of classified images. The plot shows the cluster label assigned to the images recorded over time.

with the eight largest eigenvalues are used as projectors for dimensionality reduction prior to clustering. Values of $minpts = 7$ and $\epsilon = 15$ are used as input parameters[13] for the DBSCAN clustering algorithm. In Fig. 4.8(b), each point represents one of the recorded images that is assigned to a cluster indicated by different colors. To illustrate the clusters in a way perceptible to humans, they are represented in a three-dimensional space, which is spanned by the coefficients corresponding to the most significant eigenpictures found by the PCA. The algorithm finds seven different clusters. A representative image corresponding to the innermost data point of each cluster is given in Fig. 4.8(c). It should be noted that the clustering algorithm does not account for mirror symmetries. Therefore, the clusters labeled b_i in Fig. 4.8(b) represent the same crystal lattice configuration, as they contain mirror images of the same configuration with respect to the y- and z-axes. The association of multiple clusters to a single configuration (as for b_i) is done by comparing the ion positions in different pictures[14]. For each configuration, the probability of occurrence p_i is determined by counting the number of images N_i in the associated cluster and normalizing it as $p_i = N_i/N_P$. In the presented data set, the main configuration (cluster a) is found with $\max(p_i) < 0.5$, which would be problematic in view of quantum simulation experiments requiring only a single configuration. Even with reliable post-processing and filtering, the data acquisition rate remains unfavorable. However, the stability can be improved substantially by fine-tuning the trap anisotropy ($\zeta = \omega_y/\omega_z$) and, by doing so, increasing the energy gap between the ground-state and the metastable configurations. This optimization is further described in Sec. 4.5.2.

In cluster d, some ions in the crystal's center appear blurred (see Fig. 4.8(c)). The corresponding ions in all individual images of cluster d show such an elongated fluorescence profile. This effect could be attributed to the following mechanisms: First, hot in-plane vibrational modes at low frequencies may heat the center ions. Second, these images could show a non-equilibrium state, where fast transitions between two (near-)degenerate configurations occur on a timescale faster than the camera exposure time in these measurements (100 ms). In Ref. [149], such non-equilibrium configurations have been found in both simulations and experiments. In addition, hot in-plane modes may enhance these transitions.

Nearest-neighbor and defect analysis

Prior to the nearest-neighbor analysis of each ion in a crystal lattice, the ion positions need to be determined. To this end, in the initial step, the autocorrelation function of an image is calculated and the first minimum of the radially averaged autocorrelation function r_{ex} is used as an estimate for the half-distance between two ions in the crystal. Next, provisional ion positions are determined by repeatedly searching for the brightest pixel while excluding an area of $r_{\mathrm{ex}}^2\pi$ around the identified pixels. This procedure is terminated

[13] The values of $minpts$ and ϵ have to be adjusted according to the crystal stability in the experiment.

[14] First, for each ion in an image, the minimum distance to any other ion in another picture is calculated. The maximum of these distances is taken as a measure for the maximum deviation of an ion position in two distinct pictures. If this maximum distance is less than a predefined threshold, the pictures are considered to belong to the same configuration. This threshold might depend on the stability of the experimental apparatus. For the present data set a threshold of $t_p = 2$ pixels was used. The maximum distance is calculated for the horizontally and vertically mirrored images.

as soon as the value of the remaining brightest pixel drops below a specified fraction of the global brightness maximum. Subsequently, the ion positions are determined more accurately via two-dimensional Gaussian fits of the individual spots around the provisional positions. Based on the fitted ion positions, a Voronoi tesselation is performed to determine the nearest neighbors of each ion. This ultimately enables the analysis of defects in the crystal lattice. A planar graph representation of the identified configurations is displayed in Fig. 4.8(d). The vertices correspond to ions and the edges link the nearest neighbors. The figure highlights nearest-neighbor defects, facilitating to spot differences in the lattice structures. The value in the lower left corner gives the total number of occurrences N_i of a certain configuration in the recorded image series. In general, the ions form a triangular lattice structure with six nearest neighbors per ion. All configurations contain a number of defects, exhibiting five or seven nearest neighbors. In the highly symmetric main configuration, the triangular structure is discontinued only at the two outer ions of the central row, which have five nearest neighbors. Other less likely configurations show more defects in various locations, leading to a broken symmetry along the horizontal and vertical axis of the crystal plane.

4.5.2 Mitigation of configuration changes in experiments

Optimization of the trap anisotropy

Highly stable planar crystals in our experiments are characterized by symmetry along the horizontal and vertical axes of the crystal plane, which - for given trapping parameters - can be realized only by specific numbers of ions. This is why the most commonly used planar crystals in the presented experiments are comprised of 8, 19, 91 and 105 ions. Searching for stable configurations in simulations with various trap anisotropies and ion numbers is time-consuming. However, we empirically find stable crystals by tuning the trap's rf and dc voltages to adjust the trap potential anisotropy, as well as by adding and removing ions from the crystal. Once relatively stable parameters are found, the analysis method described above proves very effective in further reducing the occurrences of metastable configurations. As shown in Fig. 4.9(a), the potential anisotropy can be fine-tuned by changing the trap rf voltage to maximize the time spent in the main configuration. By repeating the clustering analysis for several values of the trap anisotropy, the optimum value can be estimated. Here, we simply use a quadratic fit. For the 91-ion crystal, the occurrences of metastable configurations are mitigated to a probability of ≤ 1 % during the measurements. Moreover, the metastable crystal configurations occurring close to or at the optimum potential anisotropy tend to have a short lifetime, often not exceeding 10 ms.

Automated detection of crystal configuration changes

After optimization of the trap anisotropy, remaining configuration changes during measurements are identified in between cycles of N repetitions of single-shot experiments by the control program and the affected cycle is automatically repeated. For the calibration of this configuration filter, an image series is recorded prior to a measurement. The cluster analysis, as described in Sec. 4.5.1, yields a number of eigenpictures and the analyzed clusters associated with different configurations. After this calibration procedure, the actual

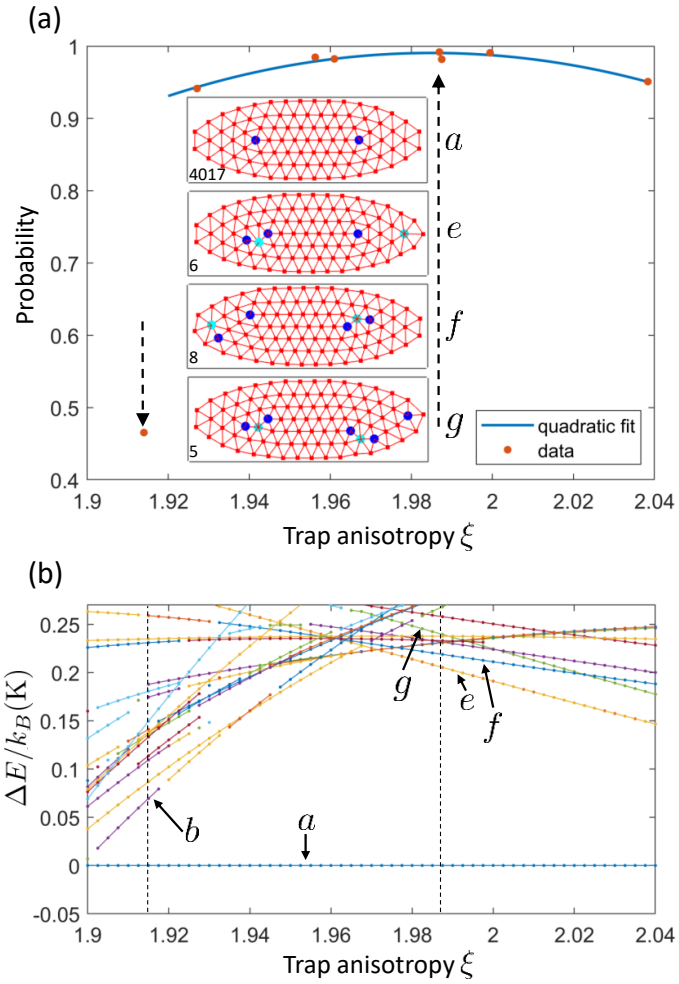

Figure 4.9: Crystal configurations versus trap potential anisotropy for a 91-ion crystal. (a) The experimental data for the probability of finding the main configuration $\max(p_i)$ is shown as a function of the trap anisotropy ξ and indicated by red points. A stable regime with $\max(p_i) > 0.9$ is identified, where the probability of being in the main configuration (labeled "a") exceeds 90 %. A quadratic fit of the points within this regime (blue line) is used to estimate the optimum anisotropy. At this optimum point (upward-pointing arrow), more than 99 % of all 4050 recorded images are found in the main configuration whereas configurations e–g, shown along with the number of occurrences, are found in only a few cases. The leftmost data point in the unstable regime (downward-pointing arrow) corresponds to the data shown in Fig. 4.8. (b) Numerical simulations based on simulated annealing yield the energy gaps ΔE between the main configuration and other metastable configurations. The gap becomes maximal close to the optimum value of ξ seen in the experiments. All experimentally observed configurations are reproduced by the simulations.

measurements are carried out. By taking an additional image with all bright ions at the beginning of each single-shot experiment, the images can be assigned to a configuration and dismissed in case of a mismatch with the desired main configuration. To this end, the recorded image is projected onto the eigenpictures to obtain the corresponding coefficients and, finally, the Euclidean distance to the center of the identified clusters. If the configuration associated with an identified cluster is not the desired one, based on the distance to the main cluster, the data is excluded from further analysis and the whole cycle of N single-shot experiments is repeated. Moreover, this approach enables tracking of the configuration state during long measurements, which facilitates the detection of symptoms of undesired changes in the experiment.

An additional potential tool for maximizing the time in the main configuration may be the deliberate destabilization of undesired metastable configurations by transiently changing the laser cooling parameters. The crystal could thereby be vibrationally excited before inducing a transfer to the main configuration during subsequent recooling. However, such an "annealing routine" has not yet been required in the conducted experiments.

In conclusion, the presented strategies allow us to almost completely eliminate the effect of undesired configuration changes on the measurement outcome. Still, low energetic background gas collisions may cause ions to swap positions without undergoing a melting of the crystal or a change of the lattice structure. These events cannot be detected by the presented methods but are rare in our setup. This phenomenon also occurs in linear ion strings and has been investigated in an experiment in the quantum simulation experiment with linear strings[15] in Innsbruck. Such changes were tracked in experiments with a linear string of 22 ions, where these swapping events occurred in 5 out of 1000 experiments, each lasting 20 ms. Although never quantified thoroughly, the background gas collision rate in our experiment is lower than in the one with linear strings and, therefore, we estimate the measurement errors caused by such swapping events to be well below 10^{-3}. In setups with higher collision rates, however, it may be an option to dedicate some ions to the detection of these collisions occurring during measurements. For example, one could use these ions to probe the temperature of the ions in the out-of-plane direction.

4.5.3 Numerical simulations - Simulated annealing

For a better understanding of the trap anisotropy's influence on the occurrence of various crystal lattice configurations, numerical simulations, based on a simulated annealing routine [150], are performed to search for the most stable ground-state configuration as well as other metastable configurations of a 91-ion crystal. In these simulations, a conservative anisotropic harmonic potential with oscillation frequencies $\omega_{\mathrm{x}} \gg \omega_{\mathrm{y,z}}$ is assumed. The energy function to be minimized $E_{\mathrm{tot}}(y_i, z_i) = E_{\mathrm{pot}}(y_i, z_i) + E_{\mathrm{coul}}(y_i, z_i)$ is comprised of the trapping potential energy E_{pot} and the Coulomb energy between the ions E_{coul} (cf. Sec. 2.1.2). After execution of the annealing routine, the result is further refined by

[15] QSIM experiment, Lab 1 at IQOQI

searching for a local minimum[16] of the energy function.

The simulation parameters are chosen such that the ground-state configuration (the *main configuration* in the experiment) is found in about 15 % of the simulation runs. To reproduce a large number of metastable configurations, 500 annealing runs each are carried for 6 six values of the trap anisotropy ξ in the range of $1.9 \leq \xi \leq 2.06$. In order to deterministically find similar configurations for similar trapping potentials, a configuration found for a particular anisotropy in a previous simulation run, is used as a starting configuration in additional runs with a slightly modified trap anisotropy and a slower *cooling* schedule. This way, the energy gaps for various configurations can be tracked across a range of the trap anisotropy (connected lines in Fig. 4.9(b)).

The simulation results are illustrated in Fig. 4.9(b), where the energy difference with respect to the ground-state configuration is plotted as a function of the trap anisotropy ξ. Points corresponding to the same configuration are connected by solid lines. The simulations generate a larger number of distinct configurations than seen in the experimental data. However, in the simulated data, we are able to identify all experimentally observed configurations close to the optimum anisotropy at $\xi = 1.987$, as well as the most frequent configurations at $\xi = 1.915$. The energy gap between the ground state and the first metastable configuration is indeed close to its maximum at $\xi = 1.987$, where we detect the main configuration with the highest probability in the experiments (Fig. 4.9(a)). The maximum energy gap is equivalent to a temperature of about 200 mK, in contrast to only about 50 mK at $\xi = 1.915$, suggesting that for non-optimal anisotropy, metastable configurations can be reached more easily, e.g. due to insufficient laser cooling or low-energy Langevin collisions.

4.6 Single-ion heating rate

An important quantity characterizing an ion trapping apparatus is its motional heating rate $\dot{\bar{n}}$ that describes the increase of the mean phonon number per time unit. There are various mechanisms leading to electric field noise and consequently to motional heating in an ion-trapping apparatus. Many of these mechanisms are still poorly understood. An extensive review of potential noise sources and measurements can be found in [119]. The heating rate may yield information about the level of electronic noise at the trap and ultimately sets an upper limit to the motional coherence time. For a single ion in a thermal state of motion, the heating rate can be determined by the sideband ratio technique, described in Sec. 5.8, which is based on an analytically correct relation between the mean phonon number and the excitation probability on the red and the blue sidebands. The mean phonon number is determined by $\frac{P_r(\bar{n},t)}{P_b(\bar{n},t)-P_r(\bar{n},t)} = \bar{n}$ (cf. Eq. 5.22). In a measurement, the red and blue sidebands are probed sequentially for a varying probe pulse delay t_{delay} after cooling and state initialization. The frequency of the delayed probe pulse is scanned over the sideband frequency and fitted by a Gaussian function to obtain the excitation probabilities P_r and P_b. For each value of t_{delay} we calculate

[16] For the local minimum search, the MATLAB built-in function *fminunc*, a nonlinear programming solver, is used.

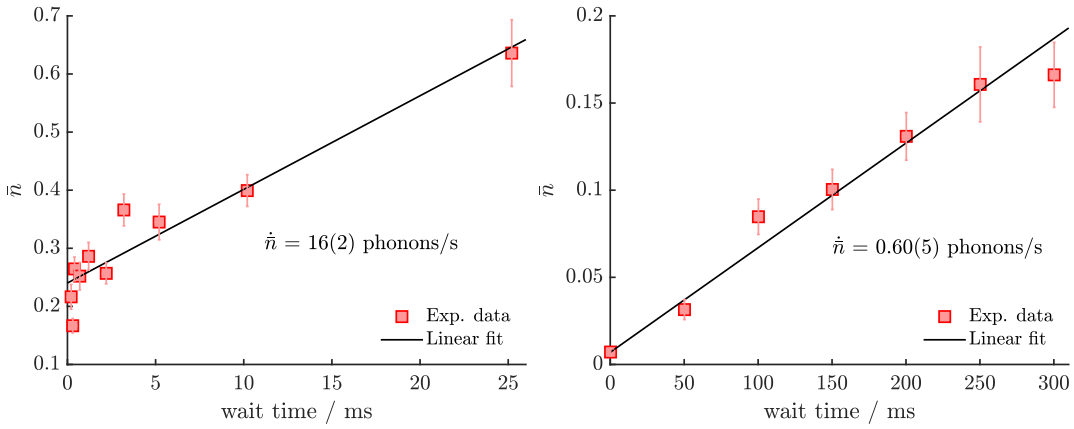

Figure 4.10: Heating rate measurement via sideband ratio thermometry with a single ion trapped in a potential with $\omega_x = 2\pi \times 2.189$ MHz (corresponding to the out-of-plane direction of 2d crystals). The mean phonon number $\bar{n}$ is estimated for various waiting times introduced before the spectroscopic measurement on the motional sidebands. Linear fits of the data yield the heating rate (a) before and (b) after a modification of the dc filter boards. The heating rate $\dot{\bar{n}}$ could be reduced from about 16 phonons/s to about 0.6 phonons/s.

the mean phonon number $\bar{n}$. The single-ion heating rate is then determined by fitting the mean phonon number as a function of t_{delay} by a linear function. In the course of this work, multiple heating-rate measurements have been carried out in various electronic environments, i.e. different configurations for devices and grounding. Great efforts have been made to reduce electronic noise on the trap electrodes by galvanic isolation and proper grounding. Repeated measurements with a single ion yielded a heating rate of about 16 phonons/s consistent with measurements based on other methods for estimating $\bar{n}$ (see Sec. 5.3). One heating rate measurement using the single-ion sideband ratio technique is shown in Fig. 4.10(a), where the motional sidebands were probed on the $S_{1/2} \leftrightarrow D_{5/2}$ transition. For an EIT-cooled ion trapped in a potential with $\omega_x/(2\pi) = 2.189$ MHz, corresponding to the out-of-plane direction of a planar crystal, the heating rate is estimated to be $\dot{\bar{n}} = 16(2)$ phonons/s. This value was subsequently improved by a modification of the dc filter boards. A resistor generating Johnson noise on the trap dc electrodes was removed (see Sec. 3.4.3) and the current heating rate in the out-of-plane direction was reduced to 0.60(5) phonons/s per ion, which is shown in Fig. 4.10(b). In the latter experiments, the motional sidebands were excited on the stimulated Raman transition coupling the two $S_{1/2}$ Zeeman states (see Ch. 6). Moreover, the ion was ground-state-cooled using resolved-sideband cooling, which manifests itself in a lower temperature after cooling, in contrast to EIT cooling that was used in panel (a). Further thermometry measurements with 8-ion and 19-ion crystals have been carried out before and after the modification of the filter boards and are discussed in Sec. 5.3.

4.7 Electronic coherence

The coherence time is one of the most important characteristic quantities of a quantum device. In essence, it defines the time window allowing for coherent manipulation of quantum states without the loss of information encoded in these states. The electronic decoherence in the apparatus therefore limits the number of high-fidelity operations in a single experiment. There are two sources of decoherence occurring in experiments: dephasing and spontaneous decay, the latter of which is equivalent to one qubit state changing the another.

Dephasing occurs as the quantum system interacts with its environment and manifests itself in a loss of well-defined phase relations. The loss of these phase relations can occur between an ion's electronic state and a laser field, or more generally, between the energy eigenstates of the ions. The dephasing time is often referred to as the T_2 time, associated with the spin-spin relaxation time in nuclear magnetic resonance (NMR) measurements, and specifies the time, when these coherent phase relations drop to $1/e$ of the original value. In trapped-ion systems, the coherence time usually refers to the measured contrast decay in a Ramsey experiment, in which the initially prepared state $|+\rangle$ evolves into a thermal mixture of the states $|+\rangle$ and $|-\rangle$. In contrast to the T_2 time related to dephasing, the thermal relaxation time T_1 defines the decoherence due the spontaneous decay of a qubit's excited state to the ground state changing one qubit state into the other one. The T_1 time is therefore directly linked to the spontaneous scattering rate or the lifetime of a qubit state. The fundamental limit for the T_2 time of a qubit is given by $T_2 < 2T_1$.

For future quantum simulation experiments, the ground-state qubit encoded in the two Zeeman states $|\mathrm{S}_{1/2}, m = -1/2\rangle$ and $|\mathrm{S}_{1/2}, m = +1/2\rangle$ will be used. In the absence of an electromagnetic field, the qubit exhibits an infinite T_1 time, i.e. no spontaneous decay. However, pontaneous scattering during stimulated Raman interactions (see Sec. 6.4) as well as the ground-state qubit's susceptibility to magnetic-field fluctuations constitute the dominant mechanisms for decoherence.

Coherence of the ground-state qubit

We determine the coherence time T_2 of the ground-state qubit in a Ramsey experiment using either the rf coil or the stimulated Raman transition at 396 nm to transfer populations between the two states. After optically pumping into the $|S_{1/2}, m = -1/2\rangle$ state, a $\pi/2$-pulse prepares an equal superposition of $|S_{1/2}, m = -1/2\rangle$ and $|S_{1/2}, m = +1/2\rangle$. A second $\pi/2$-pulse is applied after a Ramsey wait time τ_R. Finally, the quantum state readout at 397 nm is done after shelving the $|m = -1/2\rangle$ population to the $D_{5/2}$ state. The phase of the second $\pi/2$-pulse is scanned to obtain a sinusoidal Ramsey fringe pattern, which is fitted with a sine function to extract the contrast. The measurement is repeated for varying wait times such that the contrast decay over time can be found using an exponential or Gaussian fit[17] to extract the 1/e time constant. Figure 4.11(a) presents Ramsey experiments on the ground-state qubit, showing the measured contrast as a function of the waiting time τ_R. Measurements were performed using both the rf coil and the

[17] White Lorentzian noise would lead to a purely exponential decay whereas other noise components can alter the shape of the decoherence curve, such that a Gaussian function fits better.

stimulated Raman transition, yielding comparable results. Using a Gaussian fit, we obtain a coherence time T_2^* of about 130 ms for the ground-state qubit, which can be extended to about 370 ms (T_2 time) using a standard spin-echo pulse sequence[18].

Coherence of the optical qubit

The same measurement scheme can be used to determine the coherence time of the optical qubit by using the 729-nm laser to drive the $S_{1/2} \leftrightarrow D_{5/2}$ transition. In the course of this thesis, various shared 729-nm laser setups provided light for the experiments, the latest of which did not show excellent frequency stability (estimately on the order of 10 kHz) due to an absent fiber-noise cancellation. As this is limiting the coherence time, no measurements on the coherence of the optical qubit are presented here. A new 729-nm setup (shared with the Lanyon lab) will be set up in the near future in the 2d crystals lab. In the experiments presented in this thesis, however, the coherence of the optical qubit does not play a crucial role as the quadrupole transition is used only in short sequences, where a relatively short coherence time is not limiting. Moreover, for the ground-state preparation by optical pumping as well as for the shelving of one of the ground-state populations for quantum state readout, a long coherence time is not required. In future experiments, the optical quadrupole transition is planned to be used mainly for off-resonant qubit manipulation via ac-Stark shift gates. However, in more complex measurement schemes involving novel approaches for full quantum state tomography and entanglement characterization in large ion crystals, e.g. as described in [151], good coherence for additional manipulation of states in the $D_{5/2}$ state manifold is required.

4.8 Motional coherence and long-term stability of the trap oscillation frequency

Akin to the electronic coherence time, the motional coherence time T_{m}^* sets a limit for coherent interactions mediated by the ions' motion, such as quantum logic operations or entangling interactions in quantum simulation experiments. T_{m} denotes the motional coherence time determined in a Ramsey measurement with a spin-echo pulse. Several mechanisms may affect the motional state of an ion and lead to a reduction of its coherence. Here, we limit the discussion to two mechanisms that are most relevant to the presented ion-trap experiments: secular frequency instabilities caused by rf power fluctuations of the trap drive signal, and motional heating due to electric-field noise. The latter becomes particularly important in experiments with many ions. Fluctuations in the secular oscillation frequencies are reduced by active stabilization of the rf voltage. Using a home-built PI circuit (Sec. 3.4.2), fast modulation (on the order of kHz) and slow drifts of the trap oscillation frequencies can be mitigated effectively.

Measurement of the motional coherence time

The measurement to characterize the motional coherence using a single ion is based on the

[18] In the standard *Hahn* spin-echo sequence, a single π-pulse is added in the middle of the wait time, which refocuses the spin and thereby reduces the effect of slow noise processes occurring in the first half of the wait time.

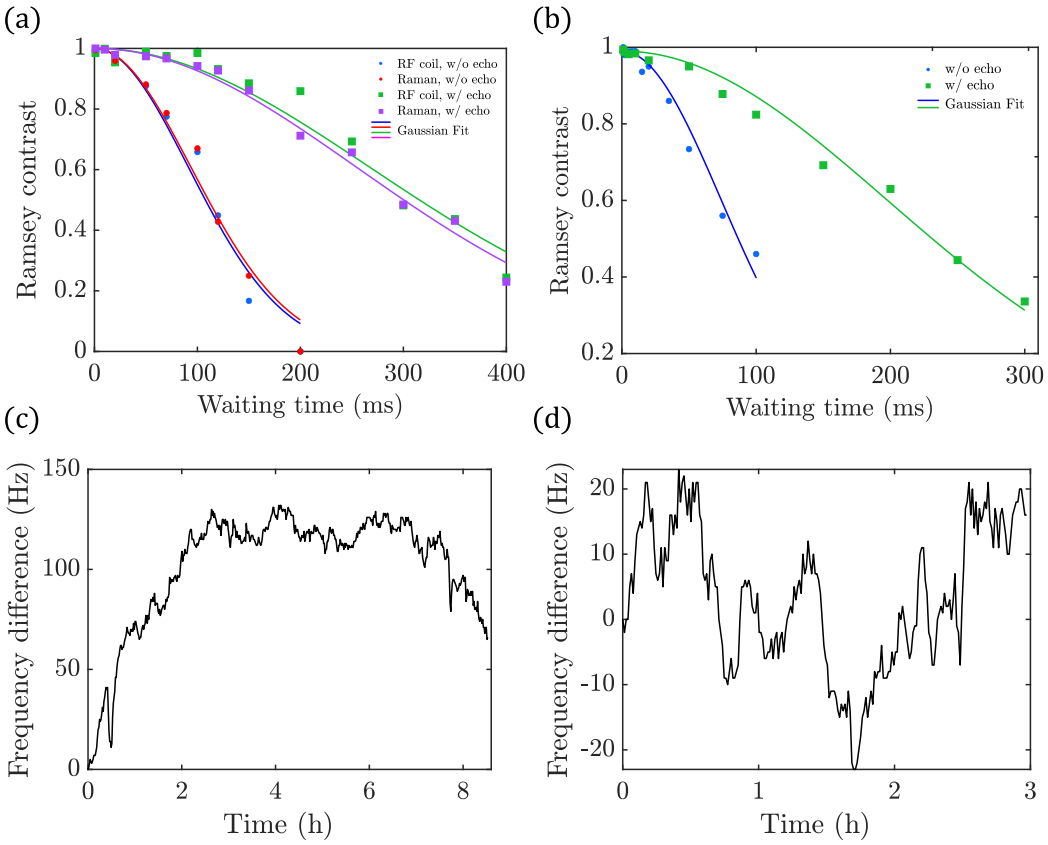

Figure 4.11: Electronic coherence, motional coherence and long-term stability of the trap frequency. (a) Ramsey measurements of the electronic coherence time T_2^* (without spin echo) and T_2 (with spin-echo pulse) of the ground-state qubit using both the rf coil and the stimulated Raman transition. Gaussian fits reveal coherence times of $T_2 \approx 130$ ms and $T_2^* \approx 370$ ms. (b) Motional Ramsey measurements yield motional coherence times of $T_\mathrm{m}^* \approx 105$ ms and $T_\mathrm{m} \approx 279$ ms. (c–d) The long-term stability of the trap oscillation frequency ω_x is measured in motional Ramsey experiment with a fixed waiting time t_R of 5 ms (c) during the day and (d) during the night, showing drifts on the order of 150 Hz and 50 Hz, respectively.

creation of a superposition of two motional Fock states sharing the same electronic state. This is done in a Ramsey-type experiment. After initialization in the $|S_{1/2}, m = -1/2\rangle$ state, the first carrier $\pi/2$-pulse creates an equal superposition of $|\uparrow\rangle = |m = +1/2\rangle$ and $|\downarrow\rangle = |m = -1/2\rangle$ using the rf coil[19]. Subsequently, using the Raman laser, a π-pulse on the blue sideband of the desired mode transfers the population in the electronic ground state (the part of the superposition in $|\downarrow\rangle$) to the motionally excited $|\uparrow\rangle$-state, creating the desired superposition $|\uparrow, n = 0\rangle + |\uparrow, n = 1\rangle$. Here, we probe the mode in x-direction, which corresponds to the out-of-plane direction of planar crystals. After a Ramsey wait time t_R, another π-pulse is applied on the blue sideband to transfer the motionally excited population back to the ground state. This is followed by another $\pi/2$-pulse on the carrier. The phase of the last pulse is scanned to create a fringe pattern, which is fitted by a sinusoidal function to obtain the signal contrast. This measurement is repeated for various wait times t_R and the decay of contrast over time is found using a Gaussian fit, where the motional coherence time $T_\mathrm{m}^{(*)}$ is given by the $1/e$ time. The contrast decay of the "out-of-plane mode" of a single ion with $\omega_x = 2\pi \times 2.2225$ MHz is shown in Fig. 4.11(b) measured both with and without an additional spin-echo pulse (π-pulse in the middle of the waiting time). We find a motional coherence time of $T_\mathrm{m}^* \approx 105$ ms without spin echo and $T_\mathrm{m} \approx 279$ ms with spin echo. The current single-ion heating rate of about 0.6 phonons/s is not limiting the motional coherence at this point. Note that before the modification of the dc filter boards, the motional coherence time T_m was approximately 40 ms and, in fact, limited by motional heating at a rate of about 16 phonons/s. The current motional coherence may be limited by electronic components that cause mainly low-frequency noise on the order of μV, affecting the set point voltage of the rf stabilization circuit, or by the voltage stability of the dc electrodes. The current coherence, however, does not pose any limitation to the planned experiments and compares very well to other setups. A further investigation of the rf stabilizations circuit's performance is therefore not envisaged in the foreseeable future.

Long-term stability of the motional modes

In order to determine the long-term stability of the secular oscillation frequency, motional Ramsey experiments are repeatedly performed with a fixed waiting time of $t_\mathrm{R} = 5$ ms over the course of several hours. The measured phase shift $\delta = \Delta\omega\tau_\mathrm{R}$ reflects the changes in the secular frequency as the electronic state is entirely in the $|\uparrow\rangle$ state, which is largely unaffected by laser frequency changes or magnetic-field fluctuations. The drift of the motional oscillation frequency over time is shown in Fig. 4.11(c–d) for a single ion with a secular frequency of $\omega_x = 2\pi \times 2.225$ MHz. We find a frequency drift of < 50 Hz peak-to-peak over the course of 3 hours during the day (Sunday early afternoon) and < 150 Hz peak-to-peak over the course of more than 8 hours during the night. The origin of these drifts is unknown but they are suspected to be caused by thermal fluctuations of the rf stabilization circuit, the helical resonator[20] or the trap electrodes. Without active stabilization, we observe secular frequency drifts on the order of one kHz over the course of a few minutes, due to the temperature fluctuations around the experiment.

[19] Alternatively, the stimulated Raman transition could also be used for this purpose.

[20] Temperature changes could slightly change the geometry and thus the resonance properties of the resonator.

Chapter 5

Ground-state cooling and thermometry of 2d ion crystals

A fundamental feature of trapped-ion experiments is the fact that ions are confined and oscillating in an approximately harmonic potential. This is well understood both theoretically and experimentally. The excellent controllability of the electronic as well as motional degrees of freedom make trapped ions such a powerful platform. For experiments involving quantum gates mediated by the ions' motion, good knowledge and control of the ions' motion is generally required. Moreover, a thermal occupation of motional states can adversely affect the induced interactions and should be mitigated. An excellent level of control has been demonstrated for linear strings of up to several tens of particles in numerous experiments. However, as the number of ions increases, the number of vibrational modes grows accordingly, resulting in a number of challenges: First, sequential sideband cooling of individual modes - the most commonly applied cooling technique in trapped-ion experiments - becomes time-consuming and eventually infeasible. However, over the years, the methodology of cooling techniques has evolved, and faster multi-mode cooling techniques, such as polarization-gradient cooling [48] and EIT cooling [152], have been successfully applied to larger ion crystals ranging from several tens to hundreds of ions [135, 153, 154]. Second, techniques for measuring the temperature of an ion crystal cooled close to the ground state are less developed for larger crystals. The established techniques generally rely either on the calculation of the full time propagation of the sideband dynamics or on the interrogation of individual ions in a crystal. Both approaches are not easy to scale up and complex many-body interactions make exact calculations practically infeasible for ion crystals exceeding several tens of ions. Therefore, new thermometry methods are required to estimate the temperature of arbitrarily large ion crystals that are cooled near the ground state, e.g. for evaluating cooling techniques or determining the heating rates for ion crystals. In experiments with planar crystals, an additional challenge for cooling and thermometry may be given by the inevitable micromotion of ions. In the presented setup, however, the ions can be addressed from directions perpendicular to the direction of micromotion.

In the first part (Sec. 5.1) of this chapter various numerical methods to determine the motional mode frequencies and vectors of ion crystals are discussed. The second part (Sec. 5.2) focuses on ground-state cooling of 2d ion crystals via polarization-gradient cooling and electromagnetically induced transparency (EIT) cooling. In the third part (Sec. 5.3 and following), various approaches for thermometry measurements are discussed, starting with the resolved-sideband technique, which represents the primary tool to carry out thermometry measurements with a single ion. In section 5.9 the generalization of the single-ion sideband thermometry technique as well as its experimental realization with a 19-ion crystal is presented, demonstrating its applicability to globally addressed, near-ground-state cooled ion crystals of arbitrary size.

5.1 Numerical simulations of motional modes

Throughout this chapter, simulations of motional mode spectra are presented in conjunction with experimental results. An overview of various approaches to simulate the motional mode frequencies and vectors is given in the following.

In a crystal confined in an ion trap, the ions' motion is determined by the trapping potential and the mutual Coulomb interactions between them. A good knowledge of the ions' equilibrium positions in the potential is essential to accurately simulate the normal modes. Therefore, the simulation of normal modes usually consists of two steps: First, the determination of the equilibrium positions, around which the ions oscillate, and, second, the actual simulation to identify the motional mode frequencies and vectors (Lamb-Dicke parameters).

Equilibrium positions

In this work, two different methods for the simulation of the equilibrium positions of 2d ion crystals were used: i) Solving the ions' equations of motion including a damping term, and ii) simulated annealing. The first method is essentially a *molecular dynamics* simulation. Initially, the ion positions are randomly distributed across a predefined area. Starting from these positions, the coupled equations of motion in the time-dependent potential (see Sec. 2.1.1) are solved for a number of time steps. By the introduction of a damping term $\frac{\mathrm{d}v_i}{\mathrm{d}t} = -C_{\mathrm{cool}} v_i$, akin to homogeneously and isotropically laser cooling all three directions[1], the ions' coordinates converge towards their equilibrium positions. In the simulated annealing routine, the energy function, consisting of the potential energy in the trapping potential and the mutual Coulomb interactions, is minimized. Such a routine can also be used for the simulation of various crystal configurations (see Sec. 4.5.3 for further details). Simulated annealing is generally faster than solving the equations of motion but, depending on the simulation parameters, one can end up in undesired metastable crystal lattice configurations. The simulated annealing runs may therefore have to be repeated multiple times to find the stable main configuration used for experiments, which renders this method slower in some cases.

[1] Note that in reality, very high ion velocities can reduce the cooling force if the Doppler shift exceeds the detuning of the laser. This behavior is not reproduced by the described simulations.

Pseudopotential simulations

Most simulations of normal mode frequencies and vectors shown in this thesis are simulated using pseudopotential theory. These simulations are based on the approximation of the trapping potential by a time-independent harmonic potential, which is described in more detail in Sec. 2.1.2. While there are other approaches that are potentially more accurate by taking the time-dependent rf potential into account (see following paragraphs), pseudopotential simulations have proven to be sufficiently accurate for the presented experiments. Examples of mode spectra from pseudopotential simulations can be found in Fig. 5.1 or Fig. 5.4.

Fourier transformation of simulated ion trajectories

Another approach to extract the normal mode frequencies and the mode vectors entails the (fast) Fourier transformation (FFT) of the numerical solution of the equations of motion (Eq. (2.11)). For this purpose, either simple integration schemes[2] like $\vec{x}_{n+1} = \vec{x}_n + \vec{v}_0\Delta t + \frac{1}{2}\vec{a}_n\Delta t^2$ or numerical solvers for differential equations[3] are used to stepwise compute the trajectories of N ions for a time interval t_{sim} on the order of a few hundreds of μs to several ms. The obtained trajectories are then subjected to a FFT to determine the frequency spectrum of the secular oscillations.

To extract the N out-of-plane mode frequencies and mode vectors, an independent component analysis[4] (ICA) is applied to the N ion trajectories stored in F_{in} ($N \times d$ matrix with d being the number of time steps of the individual trajectories). The fastICA yields $F = W^{\mathrm{T}}F_{\mathrm{in}}$, where F is a $N \times d$ matrix containing the N independent (spectral) components corresponding to the N out-of-plane mode frequencies. The frequencies are finally found by fitting the absolute values of the individual columns of F with Gaussian functions. The N mode vectors can be extracted from the $N \times N$ matrix W (un-mixing matrix)[5].

A simulated frequency spectrum obtained from the FFT of the individual ion trajectories of a 19-ion crystal is shown in Fig. 5.1(a), where the mode frequencies obtained from the ICA are indicated by vertical lines at the bottom of the plot. Figure 5.1(b) illustrates the simulated mode vectors, once obtained from pseudopotential simulations and once from the ICA of the simulated ion trajectories in the full rf potential. The values from the two approaches agree very well ($< 3.5\%$). Slight discrepancies between the two methods can be seen in Fig. 5.1(c), where they are compared with the measured OOP mode frequency spectrum of a 19-ion crystal, trapped in a potential with trap oscillation frequencies of $\omega_{\{x,y,z\}} = 2\pi \times \{2188.4, 643.2, 340.0\}$ kHz. The spectrum shows a more noticeable discrepancy between the pseudopotential- and the FFT/ICA-based values for lower mode frequencies. In the simulations, the axial potential was slightly modified to $\omega_z = 2\pi \times 342$ kHz to improve the match between simulations and experiment.

[2] Other algorithms such as the Verlet or Forest-Ruth algorithm might be used to increase the accuracy of the simulations.

[3] e.g. MATLAB built-in solver *ode113*

[4] fastICA [155]

[5] The fastICA algorithm computes F as $F = T(W^{\mathrm{T}})^{-1}F_{\mathrm{in}} + M$, where the unmixing matrix W is normalized by T and M contains the N sample means of F_{in}.

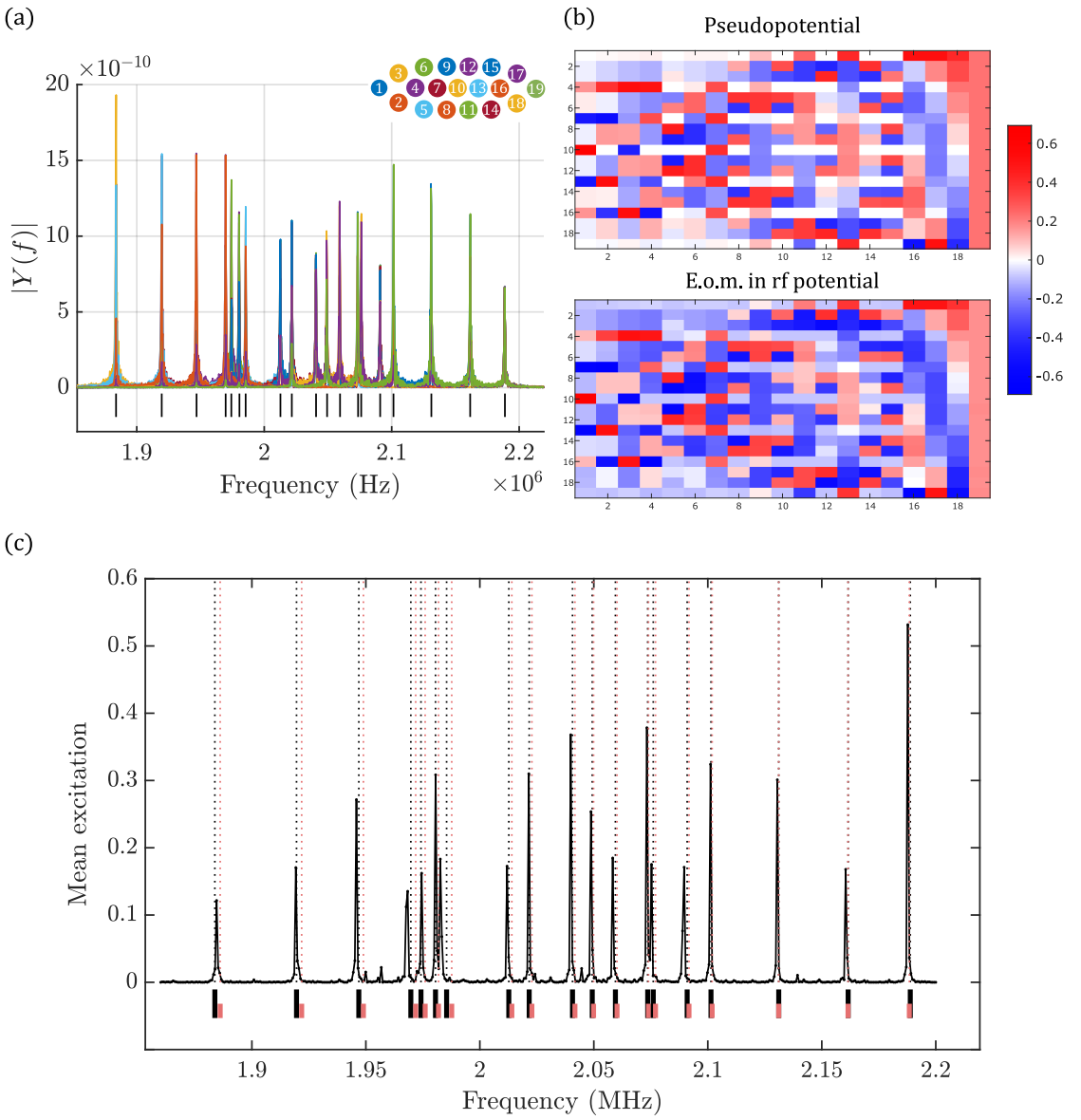

Figure 5.1: Simulation of the out-of-plane modes of motion via molecular dynamics simulation in the rf potential and comparison to pseudopotential theory and experimental data. (a) Simulated single-ion resolved motional "spectrum" obtained via ICA of the Fourier-transformed simulated ion trajectories. $|Y(f)|$ corresponds to the amplitude of motion in the out-of-plane direction. The fitted mode frequencies are indicated by vertical bars at the bottom. (b) Comparison of the single-ion Lamb-Dicke factors obtained from pseudopotential theory (top) and molecular dynamics simulations (bottom). (c) Measured blue sideband frequency spectrum of the out-of-plane motional modes of a planar 19-ion crystal. The vertical black dotted lines and bars at the bottom indicate the mode frequencies obtained from pseudopotential simulations. The vertical red dotted lines and short bars at the bottom show the frequencies derived from the simulated ion trajectories in the rf potential.

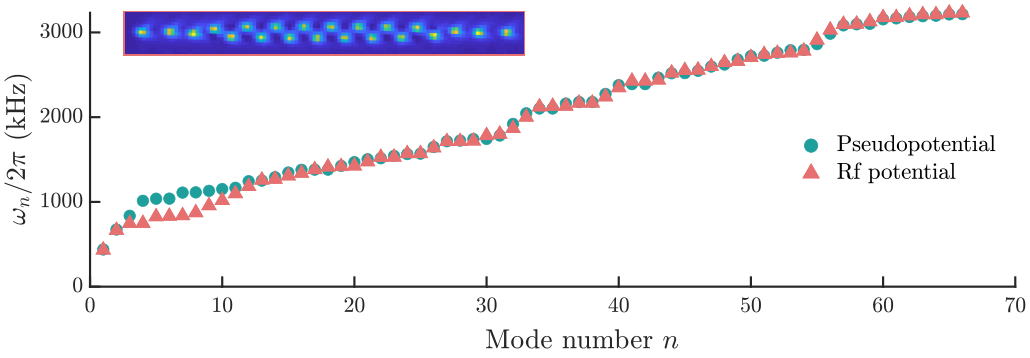

Figure 5.2: Comparison of the simulated normal mode frequencies of a 22-ion zig-zag crystal using the pseudopotential approximation as well as Floquet-Lyapunov theory. The code of the Floquet-Lyapunov simulations used to produce this plot was gracefully provided by Haggai Landa.

Floquet-Lyapunov approach

The mathematical foundation of the Floquet-Lyapunov method for solving the coupled Mathieu equations is summarized in the Appendix A following Refs. [56,59]. The Floquet-Lyapunov theory is a way to solve dynamical systems described by periodic, linear differential equations, such as the Mathieu equations. It thereby takes the full rf field into account. However, compared to pseudopotential as well as molecular dynamics simulations, the Floquet-Lyapunov approach did not improve the agreement with experimental data of planar 8-, 16- and 22-ion crystals. As an example, the discrepancy between the simulated mode frequencies using pseudopotential theory and Floquet theory for a 22-ion zig-zag crystal[6] is shown in Fig. 5.2. In particular at low oscillation frequencies, the two methods do not yield consistent results. The origin of this discrepancy is currently not understood.

5.2 Ground-state cooling of 2d crystals

Cooling single or multiple ions close to the ground state is a key requirement for high-fidelity quantum operations with trapped ions. In a first step, the ions are usually Doppler cooled to a mean phononic occupation number on the order of $\bar{n} \sim 10$ quanta. Subsequently, the ions are further cooled near the ground state. The most popular technique to do so is resolved-sideband cooling, which has first been implemented experimentally about 30 years ago; see Ref. [156] for a single ion in one dimension, Ref. [157] for a single ion in all three spatial directions via Raman sideband cooling, and Ref. [158] for the first sideband cooling of a two-ion crystal. Although this technique is well established and widespread, it becomes impractical for larger systems with many ions. To cool multiple modes in a large ion crystal close to the ground state, e.g. all axial/radial modes in a linear ion chain or all out-of-plane/in-plane modes in a 2d crystal, one has to sequentially

[6] A measured spectrum and results from pseudopotential simulations of the in-plane modes are presented in Fig. 5.4 in the context of polarization gradient cooling.

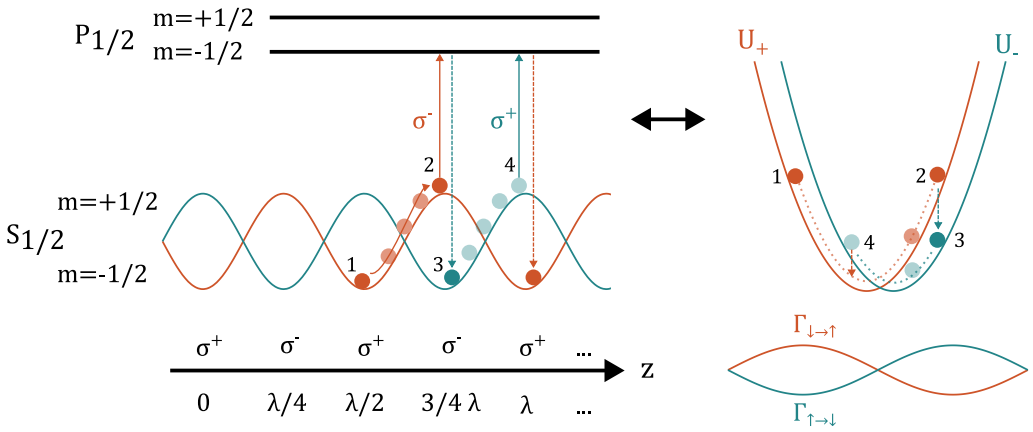

Figure 5.3: Polarization gradient cooling principle. Two counterpropagating beams in a lin-perp-lin configuration create a periodic polarization pattern. The polarization gradient causes a state-dependent displacement of the trapping potential and, in addition, gives rise to a spatial dependence of the pumping rates favoring energy-decreasing transitions. The illustration shows an ion in the $|S_{1/2}, m = +1/2\rangle$ state (1) moving within the polarization gradient through a region with linear polarization towards the field with predominantly σ^--polarized light (2), where it gets excited to the $|P_{1/2}, m = -1/2\rangle$ state (3). Due to the state-dependent displacement of the potentials for the two ground states, the ion decays favorably to the $|S_{1/2}, m = -1/2\rangle$ state (4) before the cycle can start from anew (with opposite signs). The right part illustrates the process for an ion residing in one of the potential wells.

cool these modes using individual pulses resonant with the red sidebands of single modes. This procedure is time-consuming and can get inefficient for a large number of particles, in particular in traps subjected to a large heating rate. However, there are other ground-state cooling techniques allowing the simultaneous cooling of multiple modes, which are scalable and thus applicable to larger ion crystals. Two established techniques, namely polarization-gradient (PG) cooling and electromagnetically induced transparency (EIT) cooling, are discussed in the following. Note that there are ongoing efforts to increase the efficiency of sideband cooling through novel cooling protocols [159, 160], although the scalability of these methods is unfavorable in view of the relatively simple implementation of PG or EIT cooling[7].

5.2.1 Polarization-gradient cooling

The theoretical framework and the data summarized in this section have been published in Reference [153].

PG cooling is a Sisyphus cooling technique and was reported first in 1988 in the context of cooling free atoms in neutral atomic molasses to sub-Doppler temperatures in Ref. [161], although at that time the mechanism was not understood. Only after that, it was described

[7] assuming the absence of geometrical or space constraints

theoretically in 1989 [162]. Besides an early demonstration with weakly bound trapped ions in one dimension [163], there has not been much interest in the application of PG cooling to bound atomic systems. However, the endeavors to scale up such systems led to realizing the potential of multimode cooling techniques. Here, we briefly discuss the principles of PG cooling and its application to a planar, zigzag-shaped 22-ion crystal, which was published in Ref. [153] along with experiments on cooling linear crystals consisting of up to 51 trapped $^{40}Ca^{+}$ ions. The experiments were performed in the quantum simulation experiment (QSIM) at the IQOQI Innsbruck. Details on the experimental setup can be found, for example, in Refs. [81].

Theoretical descriptions of PG cooling of trapped ions were established in Refs. [48, 164] with a focus on atomic transitions with $J_g = \frac{1}{2} \leftrightarrow J_e = \frac{3}{2}$, where $J_{\{g,e\}}$ are the total angular momenta for the ground and the excited states. A description of PG cooling using a $J_g = \frac{1}{2} \leftrightarrow J_e = \frac{1}{2}$ transition ($S_{1/2} \leftrightarrow P_{1/2}$ in $^{40}Ca^{+}$) was derived in Ref. [153], which the following paragraphs are briefly reviewing.

As its name suggests, PGC is based on the exploitation of a polarization gradient. In the presented experiments, a gradient is created by two off-resonant counterpropagating beams with mutually orthogonal linear polarization (*lin-perp-lin* configuration). They propagate along the trap symmetry axis z, coincidental with the quantization axis. The beams create an alternating polarization pattern of σ^{+}- and σ^{-}-polarization along the beam propagation axis. This leads to a state-dependent trapping potential for the illuminated ions that are either in state $|S_{1/2}, m = +1/2\rangle = |+\rangle$ or $|S_{1/2}, m = -1/2\rangle = |-\rangle$. The periodically varying ac-Stark shifts, which are π out of phase with respect to each other, modify the total potential energy of the two states to

$$U_{\pm} = \frac{1}{2} m\omega_z^2 z^2 + \frac{1}{3}\Delta s \mp \frac{1}{3}\Delta s \sin(2kz + 2\phi), \tag{5.1}$$

where k is the wave number, Δ the detuning from the dipole-allowed transition, ϕ the position of the polarization gradient with respect to the trap center (linear polarized light at the trap center for $\phi = 0$), and s the so-called saturation parameter $s = \frac{\Omega^2/2}{\Gamma^2/4+\Delta^2}$. The saturation parameter represents a measure for the intensity of the light field relative to the natural linewidth of the transition Γ. In addition to creating a Stark shift that displaces the potential into opposite directions due to the additional optical potential, the laser beam gives rise to spatially varying transition probabilities

$$\Gamma_{\pm\leftrightarrow\mp} = \frac{1}{9}\Gamma s(1 \mp \sin(2\phi)). \tag{5.2}$$

The displacement of the minima of the total potential $U_{\pm}$ lead to a favoring of transitions that cause an energy reduction over the reverse processes. In a more descriptive language: An oscillating ion moving along the z-direction experiences the periodic light shift as a potential hill. While climbing up the hill, the ion loses kinetic energy and at the same time experiences the maximum transition probability to the other Zeeman state at the maximum potential energy. Being optically pumped into the other state and, consequently, the other potential well, the ion finds itself in a lower lying potential energy level and the Sisyphus process will start all over again. This cooling mechanism is illustrated in Fig. 5.3.

Within the Lamb-Dicke regime, where the ions are localized to less than the wavelength of the interacting laser, the resulting heating processes limiting the cooling performance can be described using carrier and sideband transitions. There are two processes leading to heating: First, absorption on the carrier transition and subsequent spontaneous emission on the upper or lower motional sideband and, second, absorption on the upper or lower sideband and subsequent spontaneous emission on the carrier transition. Note that heating can also be caused by dipole force fluctuations or random scattering events, leading to transitions from one Zeeman ground state to the other. However, these processes are not taken into account. Based on these heating processes, rate equations can be derived to yield the cooling rate and cooling limit (see [48, 153] for details). For a single ion, the maximum cooling efficiency occurs at $\phi = 0$, i.e. the ion is located at the steepest slope of the optical potential. For this configuration, the mean phonon number in steady state is found to be

$$\langle n_0(\zeta)\rangle = \zeta + \frac{1}{4\zeta} - \frac{1}{2}\,, \tag{5.3}$$

where $\zeta = \frac{\Delta s}{3\omega_z}$. For $\zeta = \frac{1}{2}$, the optical well depth $\frac{2\Delta s}{3}$ becomes equal to the trap frequency ω_z and leads to the minimum achievable phonon number of $\langle n_0\rangle^{(\min)} = \frac{1}{2}$. Considering a larger ion crystal, the ions are sampling the phases of the polarization gradient such that the position of the gradient with respect to the ions becomes irrelevant. In this case, the heating and cooling rates can be averaged (integral over all phases), yielding a cooling limit of $\min\langle n\rangle \approx 0.87$ [153].

Experimental realization - Moving polarization gradient

In the experiments presented here, $^{40}Ca^{+}$ ions are trapped in a macroscopic blade-style linear Paul trap. Before PG cooling, the ions are precooled with a Doppler cooling beam at 45° overlapping with all collective modes of motion. The same 397-nm laser provides light for the two PGC beams cooling on the $S_{1/2} \leftrightarrow P_{1/2}$ transition. A laser beam at 866 nm is used along with the cooling beams to repump spontaneously decayed ions from the metastable $D_{3/2}$ state into the $P_{1/2}$ manifold. A polarization gradient along the trap's axial direction (z) is created with two beams that are linearly but mutually orthogonally polarized. They enter the trap through holes in the endcap electrodes with a diameter of 0.5 mm from both sides, coupling to the in-plane modes of a planar crystal trapped in the yz-plane, with the exception of the COM mode in the vertical direction (y). The two counter-propagating beams are blue-detuned by $\Delta = 2\pi \times 210$ MHz from the $S_{1/2} \leftrightarrow P_{1/2}$ cooling transition. Positioning an ion at an exact phase of a polarization gradient with a stability of a small fraction of the wavelength is an experimentally very challenging task. However, there are other ways to realize PGC in the lab. Instead of a static polarization gradient, a moving polarization gradient can be used. Such a traveling standing wave is implemented by introducing a detuning of one of the two counterpropagating beams with respect to the other of $\delta < \omega_z^{(\min)}$. The detuning is smaller than the lowest motional frequency but larger than the cooling rate to avoid an adiabatic change of $\langle n\rangle$ according to the steady-state value for the changing phase. This way, the ions will be cooled as they are sampling different values of the polarization gradient's phase. Here, the detuning between the two beams is set to $2\pi \times 60$ kHz. After cooling, a narrow 729-nm laser (along with a 854-nm laser) is used for ground-state preparation via optical pumping to

the $|S_{1/2}, m = +1/2\rangle$ state. The same laser is used to drive coherent oscillations and map the motional state onto the electronic states via pulses on either a carrier or a motional sideband of the $S_{1/2} \leftrightarrow D_{5/2}$ transition prior to quantum-state readout.

Cooling the in-plane modes of a 22-ion zig-zag crystal

In order to test PGC of a planar ion crystal, the in-plane modes of a 22-ion zigzag-shaped crystal aligned with the yz-plane were cooled using a moving polarization gradient in axial direction (z), as described above. The center-of-mass frequencies were measured to be $\omega_{(x,y,z)} = 2\pi \times (2.76, 2.51, 0.438)$ MHz. Figure 5.4 displays the blue sideband spectrum measured on the $S_{1/2} \leftrightarrow D_{5/2}$ transition after 1 ms of PG cooling. The global mean excitation $\overline{p}$ (Fig. 5.4(a)) as well as the mean excitation $\overline{p}_j$ of the individual ions (Fig. 5.4(b)) are shown and compared with numerical simulations (Fig. 5.4(c)). Pseudopotential simulations of the normal modes agree well with the measured mode frequencies and single-ion excitations. In addition, Floquet-Lyapunov simulations were carried out, leading to very similar results but showing a discrepancy for modes with frequencies in the range between $2\pi \times 500$ and $2\pi \times 1000$ kHz (Fig. 5.2). 40 out of 44 ($= 2N$) in-plane modes can be identified in the spectrum. The center-of-mass mode in the vertical y-direction does not have any overlap with the axial spectroscopy beam. Furthermore, the pseudopotential simulations suggest that three modes are degenerate in frequency. Qualitatively, the axial parts of the simulated mode vectors (Figure 5.4(c)) agree well with the measured excitation probabilities. This can be easily inferred from the illustration of the mode vectors for two modes in Fig. 5.4(a). The ions with longer white arrows in axial (horizontal) direction, corresponding to larger Lamb-Dicke factors, show a higher excitation probability in the measured spectrum compared to the ions whose motion is predominantly in other directions.

To evaluate the cooling performance, we measured collectively driven Rabi oscillations on the $S_{1/2} \leftrightarrow D_{5/2}$ carrier transition. Figure 5.5 shows the site-resolved dynamics of the ions in the 22-ion 2d crystal, once after Doppler cooling for 3 ms (a) and again after additional PG cooling for 1 ms (b). A micromotion-induced broadening of the cooling transition leads to a poor Doppler cooling performance and instant damping of the oscillation. After PGC, however, we observe persistent Rabi oscillations. The mean phonon number can be determined by fitting the global carrier Rabi oscillations, thereby assuming thermal states of motion for the N modes $\bar{\mathbf{n}} = (\langle n_1 \rangle, \ldots, \langle n_N \rangle)$. The effective Rabi frequency $\Omega^j_{n,n}$ depends on the motional state and therefore contains information about the phonon distribution $p_{\bar{n}}(n)$ of all motional modes involved. Expressions for the Rabi frequency $\Omega^j_{n,n}$ and the excitation probability of the individual ions p_j are given in Sec. 5.5.3. A fit of these carrier oscillations (Eq. (5.20)) is computationally expensive and the application of standard fitting routines impractical. Thus, a dividing rectangles algorithm (see [8] and references therein) was used; details on the parametrization are given in [153]. Figure 5.5(c) displays the evaluated mean phonon numbers of the individual modes, where we estimate $\langle n \rangle$ to be about 15 phonons for the COM mode and 8 or fewer phonons for all other modes.

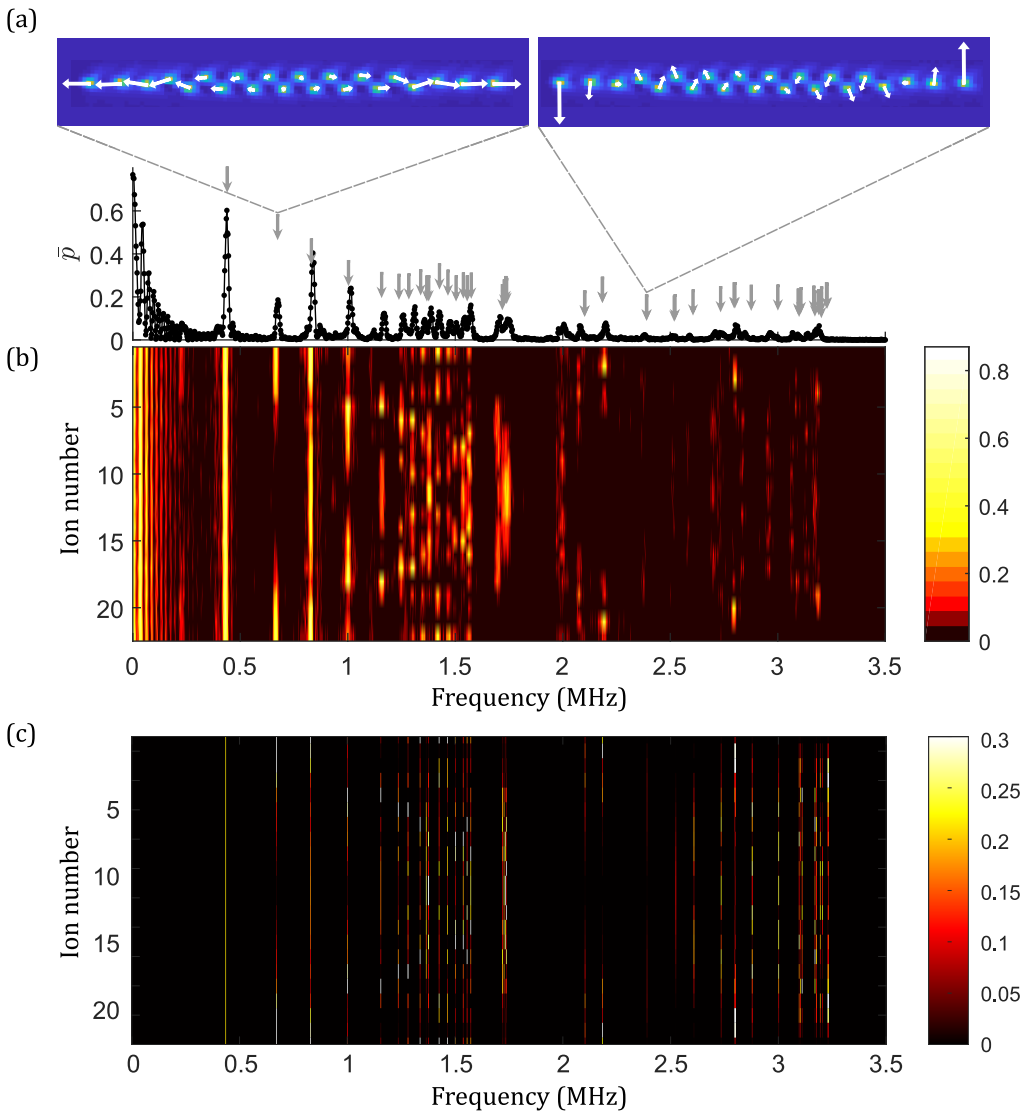

Figure 5.4: In-plane motional mode spectrum of a 22-ion zig-zag crystal. (a) The excitation probability is measured on the blue sidebands of the narrow $S_{1/2} \leftrightarrow D_{5/2}$ transition using a global beam in axial direction. The spectrum was taken after 3 ms of Doppler cooling followed by 1 ms of polarization gradient cooling. The black dots show the mean excitation of all 22 ions. The black solid line is just a guide to the eye. The gray arrows on top of the spectrum indicate simulated mode frequencies an their axial coupling weight obtained from pseudopotential simulations. The mode vectors of two exemplary modes are visualized by white arrows. The mode structure qualitatively agrees with the measured single-ion excitations shown in the 2d plot in (b). (b) The single-ion resolved excitation probabilities reveal information about the mode structure via their coupling strengths in axial direction. The numbering of the ions is from left to right in axial direction. (c) The simulated spectrum showing the Lamb-Dicke factors of the individual ions agrees well with the measured excitation in (b).

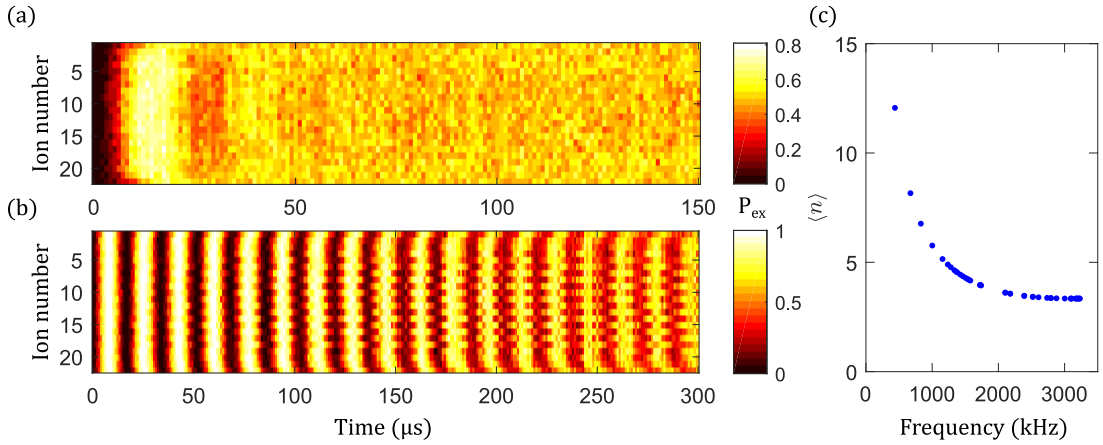

Figure 5.5: Carrier Rabi oscillations of a 22-ion zig-zag crystal (a) after only Doppler cooling and (b) with additional PG cooling. The ions are excited with a global beam in axial direction on the $S_{1/2} \leftrightarrow D_{5/2}$ transition. After Doppler cooling, barely any oscillation is visible. Additional PG cooling for 1 ms results in persistent Rabi flops. (c) The mean phonon number for the individual modes is estimated from fits of the carrier oscillations.

5.2.2 Electromagnetically induced transparency cooling

The results presented in this section have been partially published in Ref. [60].

Electromagnetically induced transparency (EIT) cooling is a ground-state cooling technique, which is applicable to precooled trapped particles. From an experimental point of view, it is significantly less demanding than resolved-sideband cooling on a narrow quadrupole transition. At the same time, it is known for the highest achievable cooling rates compared to other techniques and it is suitable for simultaneously cooling multiple modes. In principle, there is no restriction on the transition linewidth. However, depending on the laser parameters, the frequency range that that can be efficiently cooled may be limited, which can be significant for systems with large ion numbers.

The idea of using EIT as a mechanism for cooling trapped particles was originally proposed and described in 2000 in Ref. [152], along with the experimental demonstration of cooling up to two degrees of freedom in a single trapped $^{40}Ca^{+}$ ion [165]. After being relatively unnoticed for more than 10 years, EIT cooling was applied to sympathetically cool mixed-species ion crystals with two and four ions [166], as well as to cool neutral atoms in a cavity-QED setup [167] and in a quantum-gas microscope [168]. More recently, it has attracted more interest in view of experiments involving a higher number of particles for quantum simulation [135]. It has since been employed in various experiments, including the cooling of multiple degrees of freedom in single or multiple ions simultaneously [169], multi-mode cooling of larger systems, such as about 190 ions in a Penning trap [154], cooling up to 40 ions in a long linear chain [170], and cooling planar ion crystals of up to 12 ions in rf traps [42]. Some of these experiments [42,169] apply advanced protocols based on a double-EIT scheme [171], making use of an additional state in a tripod configuration,

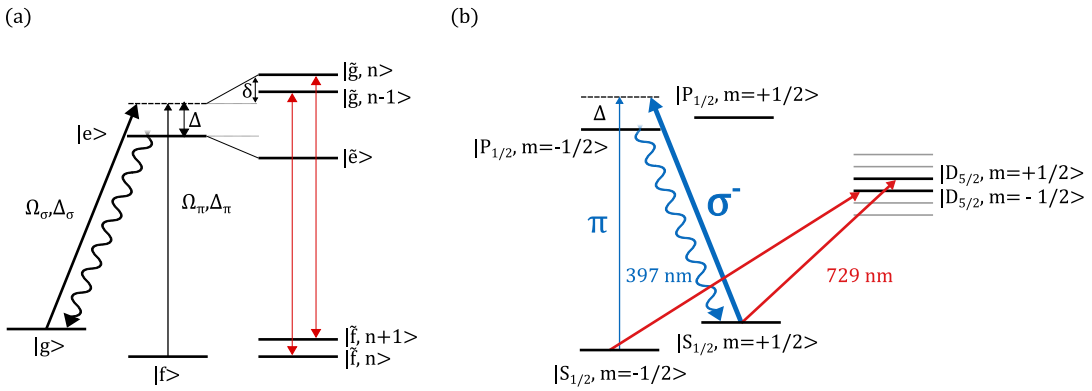

Figure 5.6: (a) General Λ-type level scheme for EIT cooling. A high-intensity beam (σ) creates dressed states. The weaker probe beam (π) preferentially drives the red sidebands of the asymmetric absorption profile. (b) Level scheme used for EIT cooling in the presented experiments with $^{40}Ca^{+}$ ions.

as opposed to three states in a λ or ladder scheme in "single-EIT" experiments. This way, the cooling limit can be lowered while extending the cooling range. Most recently, experiments with large 2d crystals containing up to 512 ions in a rf trap, cooled close to the ground state (< 1 phonon), have been reported in Ref. [36]. In these experiments, EIT cooling was applied, along with additional sideband cooling targeting the 10 highest-frequency modes in out-of-plane direction.

In this section, a summary of the basic mechanism of EIT cooling, following the theoretical description in Ref. [152], precedes the experimental implementation and results on EIT cooling of small and large 2d crystals with up to 105 ions. Details on the optical setup for preparation of the EIT beams are given in Sec. 3.6.4 whereas Sec. 3.6.1 presents details on the beam geometry and the optical setup around the trap.

EIT cooling mechanism

EIT cooling is based on a modification of the absorption profile on the cooling transition, exploiting the effect of electromagnetically induced transparency. This mechanism, also known as *coherent population trapping* or *dark resonance*, occurs in a three-level system, where coherently driving one of the two transitions leads to the cancellation of absorption on the other one. It is a quantum interference effect and can be seen as the destructive interference of the two pathways to the excited state. It can be used to enhance the absorption on red sideband transitions while suppressing absorption on the carrier and blue sideband transitions.

We consider a Λ-type level scheme, where the two ground states $|g\rangle$ and $|f\rangle$ are coupled via the excited state $|e\rangle$, as shown in Fig. 5.6(a). The $|g\rangle \leftrightarrow |e\rangle$ transition is driven by an intense laser field with Rabi frequency Ω_σ and detuning Δ, creating the dressed states $|\tilde{g}\rangle$ and $|\tilde{e}\rangle$. The induced ac-Stark shift is given by

$$\delta = \pm\frac{1}{2}\left(\sqrt{\Omega_\sigma^2 + \Delta^2} - |\Delta|\right). \tag{5.4}$$

For blue-detuned light, the state $|\tilde{g}\rangle$ is shifted upwards and state $|\tilde{e}\rangle$ downwards in frequency. Along with the dressing beam (σ), a second, weak probe beam with detuning Δ_π and Rabi frequency $\Omega_\pi \ll \Omega_\sigma$ drives the $|\tilde{f}\rangle \leftrightarrow |\tilde{g}\rangle$ transition[8]. Figure 5.7 shows the resulting absorption profile as a function of the detuning Δ_π, where the narrow feature represents a Fano interference profile [172]. The absorption profile is asymmetric for $\Delta_\sigma \neq 0$. For $\Delta_\pi = \Delta_\sigma$, the system is transparent for the probe beam. A broad resonance emerges around $\Delta_\pi \approx 0$ (resonant with the Stark-shifted carrier), while a narrow resonance near $\Delta_\pi \approx \Delta_\sigma$ can be exploited for cooling. Taking the secular motion of the trapped ions into account, one can choose the detuning $\Delta_\sigma > 0$ and the Rabi frequency Ω_σ such that the transparency corresponds to the $|\tilde{f}, n\rangle \leftrightarrow |\tilde{g}, n\rangle$ transition, and the narrow resonance, exhibiting a high excitation probability, corresponds to the red sideband transitions $|\tilde{f}, n\rangle \leftrightarrow |\tilde{g}, n-1\rangle$ of the modes to be cooled. In turn, the blue sideband transitions $|\tilde{f}, n\rangle \leftrightarrow |\tilde{g}, n+1\rangle$ reside within the onset of the broad resonance and therefore have a low excitation probability. Consequently, the particles are preferentially cooled via the red sideband transitions while the carrier as well as blue sideband transitions are suppressed. The laser parameters are chosen according to the conditions

$$\Delta_\pi = \Delta_\sigma \quad \text{and} \quad \delta \approx \omega_{\text{osc}}, \tag{5.5}$$

such that the light shift (governed by Ω_σ) equals ω_{osc}, the oscillation frequency of the vibrational mode to be cooled. To cool multiple modes of motion over a range of frequencies in a multi-ion crystal, the light shift can be set to the center of the desired frequency spectrum, assuming that the width of the absorption profile covers the whole range of mode frequencies. The cooled frequency range is determined by the detuning $\Delta_{\sigma,\pi}$, which, at the same time, defines the decay rate of the dressed state $|\tilde{g}\rangle$ and thus the minimum achievable temperature. This results in an inevitable trade-off between the frequency range that can be cooled efficiently and the achievable minimum temperature.

In the weak excitation regime, the cooling dynamics can be expressed in the form of a rate equation, yielding expressions for both the achievable phonon number and the cooling rate. The process, involving absorption and emission, is described by

$$\frac{\mathrm{d}}{\mathrm{d}t}\langle n\rangle = -\eta^2 \left(A_- - A_+\right)\langle n\rangle + \eta^2 A_+ \,, \tag{5.6}$$

with rate coefficients

$$A_\pm = \frac{\Omega_\pi^2}{\Gamma} \frac{\Gamma^2\omega^2}{\Gamma^2\omega^2 + 4\left(\frac{\Omega_\sigma^2}{4} - \omega(\omega \mp \Delta)\right)^2} \,, \tag{5.7}$$

where Γ is the linewidth of the transition and η the Lamb-Dicke factor of the mode of interest. From this expression, the steady-state solution for the mean phonon number $\langle n\rangle$ is given by

$$\langle n\rangle = \frac{A_+}{A_- - A_+}, \tag{5.8}$$

[8]Note that in this scheme (strong σ-polarized dressing beam and weak π-polarized probe beam), the state $|\tilde{f}\rangle$ is approximately $|f\rangle$.

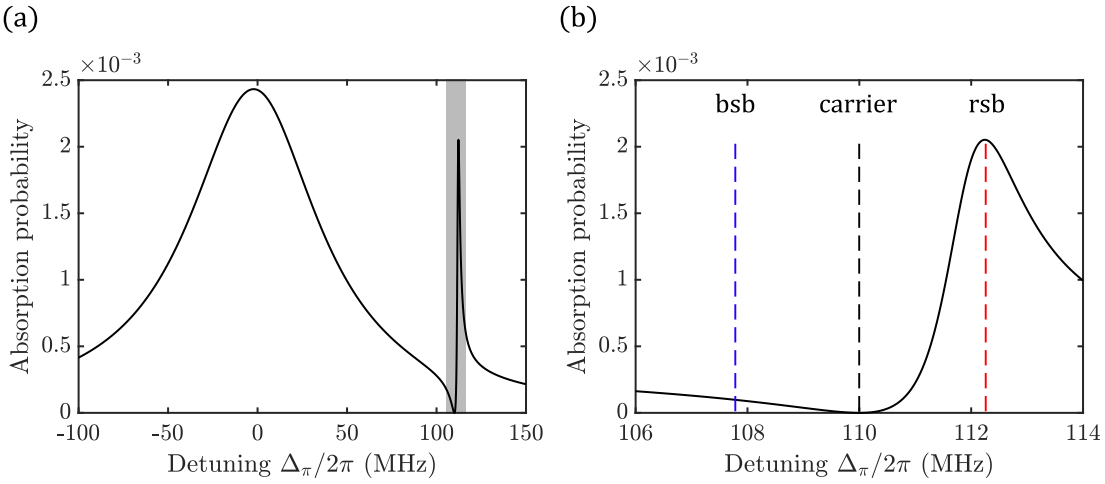

Figure 5.7: Simulated absorption profile for EIT cooling as a function of the detuning of the EIT π-beam from the bare $S_{1/2} \leftrightarrow P_{1/2}$ transition. The gray-shaded area indicates the region around the electromagnetically induced transparency with an absorption probability of zero. Panel (b) shows this region in more detail. The absorption probability on the red sideband is enhanced compared to the probability on the carrier and the blue sideband. The absorption profile was simulated according to Eq. (3.27) in Ref. [173]. The detuning Δ_σ of the σ-beam is 110 MHz. Ω_σ is set to optimize absorption for a mode frequency of $\omega_m = 2\pi \times 2.2$ MHz, while $\Omega_\pi = 0.1\Omega_\sigma$.

and the cooling rate by

$$R = \eta^2 \left(A_- - A_+\right). \tag{5.9}$$

Ground-state cooling of 2d crystals

In the experiments with planar $^{40}Ca^+$ crystals, we use EIT cooling to prepare the N out-of-plane modes of motion near the ground state. The transitions involved in these measurements are shown in Fig. 5.6(b). A suitable three-level system in Λ configuration is given by the two Zeeman levels of the $4S_{1/2}$ manifold, coupled off-resonantly via the $3P_{1/2}$ state. The quantization axis is oriented at an angle of 45° with respect to the crystal plane and allows for an optimal geometry for EIT cooling. Given sufficient optical access, undesired polarization components of the laser beams can be suppressed while the effective cooling k-vector aligns with the ion crystal's transverse direction. With this in mind, we use two perpendicular beams, each having a k vector with an angle of 45° with respect to the crystal plane. The beam geometry at the trap is shown in Fig. 3.15. A strong σ^--polarized beam at 397 nm propagates along the magnetic-field axis and couples the $|S_{1/2}, m = +1/2\rangle$ state to the $|P_{1/2}, m = -1/2\rangle$ state, acting as a dressing light field. At the same time, a weak π-polarized probe beam ($\Omega_\pi \sim \frac{\Omega_\sigma}{10}$) couples the $|S_{1/2}, m = -1/2\rangle$ to the $|P_{1/2}, m = -1/2\rangle$ state and predominantly drives red sideband transitions of the out-of-plane modes.

Figure 5.8 shows the simulated cooling rate and the achievable minimum temperature in

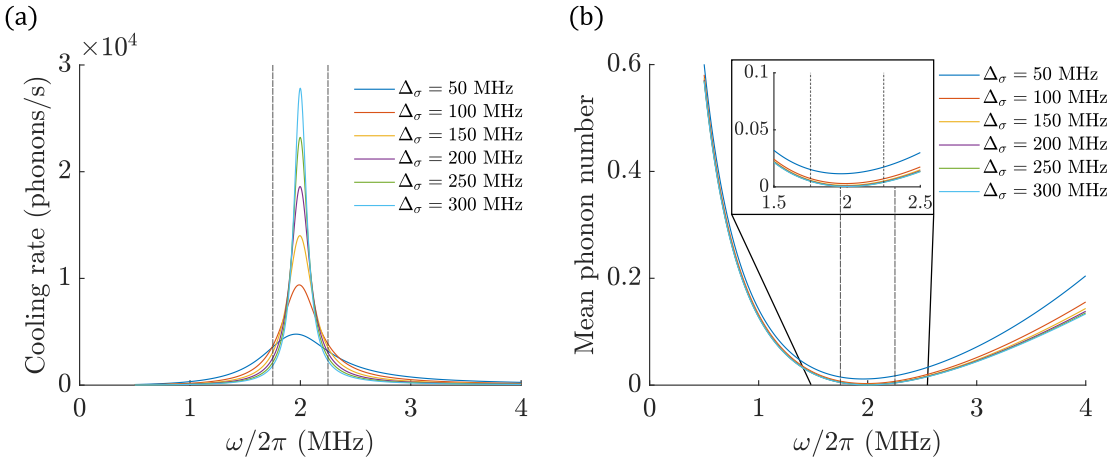

Figure 5.8: Simulations of (a) cooling rate and (b) cooling limit in the steady state. The Rabi frequency Ω_σ of the dressing beam is set such that the induced light shift matches a frequency of 2 MHz. The Rabi frequency of the probe beam Ω_π is set to $\Omega_\sigma/20$. The detuning of the two beams from the bare transition is varied from 50 to 300 MHz. A frequency range of 500 kHz centered around 2 MHz is indicated with dashed vertical lines. Then inset in (b) shows a close-up of the same plot around 2 MHz.

the steady state, according to Eq. (5.6) and Eq. (5.8) for a light shift matching a sideband frequency of 2 MHz and various detunings Δ from the bare $S_{1/2} \leftrightarrow P_{1/2}$ transition. It reveals that a change in detuning primarily affects the cooling rate, which decreases with larger values of Δ, while having only a minor impact on the achievable steady-state temperature over a wide frequency range. In the experiments with larger 2d crystals presented herein, motional mode spectra with a typical frequency range of approximately $2\pi \times 300$ kHz need to be covered. We use a blue detuning of $2\pi \times 110$ MHz to ensure an absorption spectrum broad enough to accommodate a motional frequency spectrum of a few hundred kHz. The power of the σ-beam is adjusted such that the induced light shift matches the center frequency of the out-of-plane spectrum. This ensures that all OOP modes are well within the absorption spectrum, enabling efficient simultaneous cooling of all modes.

Techniques for calibrating laser parameters to optimize the cooling performance were developed and presented in Refs. [135, 173]. The following sections review and discuss these methods in the context of experiments with 2d crystals.

Calibration I: Polarization of the σ^--beam

Spurious σ^+-polarized light leads to undesired pumping into the $|S_{1/2}, m = +1/2\rangle$ state, in which the ions do not participate in the cooling cycle. The polarization of the EIT σ^--beam is linear out of a PM fiber arriving at the trap breadboard. It is cleaned by a polarizing beam splitter before being converted into circular polarization using a combination of a $\lambda/2$- and a $\lambda/4$-waveplate mounted in high-precision rotation mounts. To optimize the polarization of the circularly polarized beam, a Ramsey-type experiment is carried out,

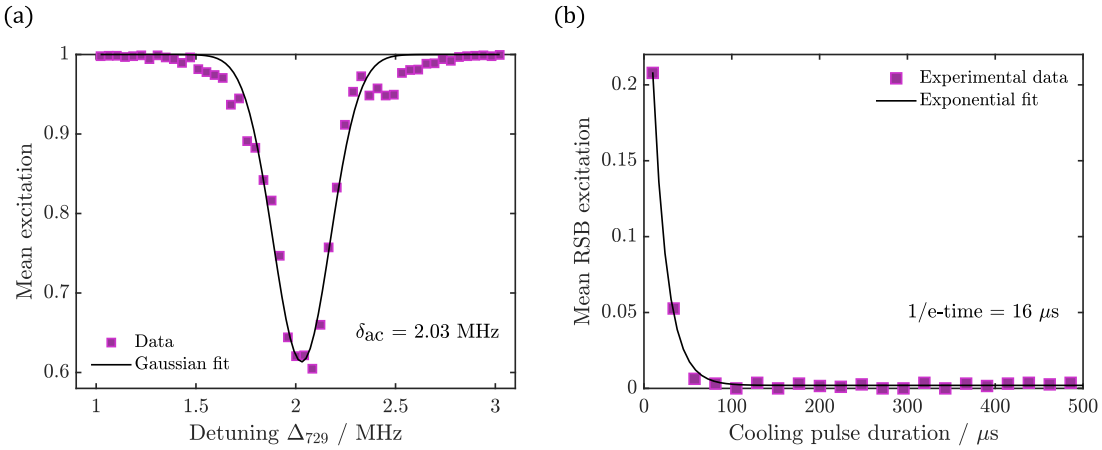

Figure 5.9: EIT dressing calibration and cooling dynamics for a 19-ion crystal. (a) Spectroscopy on the $S_{1/2} \leftrightarrow D_{5/2}$ transition (at 729 nm) while simultaneously illuminating with the EIT σ-beam (driving the $S_{1/2} \leftrightarrow P_{1/2}$ transition). The 729-nm laser beam probes the ac-Stark shift induced by the EIT σ-beam. The mean excitation of all ions is given as a function of the detuning from the bare $S \leftrightarrow D$ transition. The power of the σ-beam is adjusted such that the induced light shift matches the center of the motional out-of-plane frequency spectrum of the 19-ion crystal, here $\omega_{\text{center}} \approx 2\pi \times 2.030$ MHz determined via Gaussian fit (solid line). (b) The mean excitation on the red sideband is shown as a function of the EIT cooling duration. After about 100 μs, the RSB excitation reaches values close to zero. A cooling pulse length of > 300 μs is chosen for further experiments to ensure a steady state temperature at the end of cooling.

where the EIT σ^--pulse is sandwiched between two $\pi/2$-pulses at 729 nm. The first $\pi/2$-pulse prepares an equal superposition of the $|S_{1/2}, m = -1/2\rangle$ and the $|D_{5/2}, m = -5/2\rangle$ state. Then, the σ^--beam is switched on for a variable time t_σ. Subsequently, a second $\pi/2$-pulse is applied, with a phase shifted by $\pi/2$ with respect to the first pulse. For perfect σ^--polarization, we expect an excited state population of 0.5. However, unwanted σ^+-components induce a light shift δ_{σ^+} on the $|S_{1/2}, m = -1/2\rangle$ state and cause pumping out of this state. Measuring the excitation as a function of the σ^--pulse length t_σ (see Fig. 3(d) in Ref. [135]), these unwanted effects result in an exponentially decaying periodic signal, oscillating at the frequency of the induced light shift δ_{σ^+}. The measured oscillation frequency thus yields information about the strength of the σ^+ component and allows for suppression of it.

A simpler, though less accurate, alternative would be to transfer the $|S_{1/2}, m = +1/2\rangle$ population to the $D_{5/2}$ state after cooling using a π-pulse at 729 nm while minimizing the $D_{5/2}$ population. Furthermore, one could minimize the fluorescence induced by the σ-beam [173]. Both methods are not as accurate as the one described above and have not been used in the context of the presented measurements.

Calibration II: Light shift

In order to cool a particular vibrational mode, the mode frequency has to be well within

the narrow absorption spectrum generated by the two EIT beams. For a single ion, one can set the light shift δ induced by the σ^--beam to equal the ion's oscillation frequency ω_{osc}. For a planar crystal, however, assuming a large enough cooling range, the light shift δ is set to match the center frequency of the frequency spectrum to be cooled. In case of the presented 2d crystal experiments, it is set to the center of the out-of-plane spectrum, spanning several hundreds of kHz. In the experiment, the induced light shift is controlled by adjusting the intensity ($\propto \Omega_\sigma^2$) of the EIT σ-beam, which results in an ac-Stark shift of equal magnitude but opposite sign on both the $|\mathrm{S}_{1/2}, m = +1/2\rangle$ and $|\mathrm{P}_{1/2}, m = -1/2\rangle$ states. For calibrating the light shift, we use the following measurement sequence: First, the ion is prepared in the $|\mathrm{D}_{5/2}, m = +3/2\rangle$ state using a π-pulse at 729 nm. Afterwards the σ^--beam is switched on while simultaneously probing the $|\mathrm{S}_{1/2},\ m = +1/2\rangle \leftrightarrow |\mathrm{D}_{5/2},\ m = +3/2\rangle$ transition at 729 nm. If resonant with the ac-Stark-shifted 729-nm transition, the $\mathrm{D}_{5/2}$ state is depopulated by optically pumping into the $|\mathrm{S}_{1/2}, m = -1/2\rangle$ state by the 729-nm beam in conjunction with the EIT σ^--beam. A relatively low intensity of the 729-nm probe beam should be used to prevent broadening of the transition while still efficiently depleting the state. Finally, the population in the $\mathrm{D}_{5/2}$ state is measured. The light shift can be determined by finding the minimum excitation probability of the $\mathrm{D}_{5/2}$ state as a function of the frequency detuning from the undisturbed 729-nm transition. Such a measurement is shown in Fig. 5.9(a), where the light shift is set to about 2 MHz for measurements with a planar 19-ion crystal. In practice, we keep the frequency detuning of the 729-nm laser fixed at the desired value (corresponding to the motional mode frequencies) and scan the power of the dressing beam to find the desired power minimizing the signal.

The light shift calibration routine can be done using either a single ion or an ion crystal, the latter of which can yield additional information about the homogeneity of the laser beam's intensity profile across the crystal. Moreover, an analog measurement is used to set the intensity of the EIT π-beam to a small value, avoiding additional light shifts on the probed transition. Ω_πe is typically set to $\sim \frac{\Omega_\sigma}{10}$.

Note that another precise calibration method is based on measurements of optical pumping rates between the two $\mathrm{S}_{1/2}$ Zeeman states. These require precise knowledge of all laser parameters in addition to the decay rates of the excited states [114]. It was therefore not used in the experiments described here.

Cooling time

To determine a sufficient EIT cooling pulse length, we measure the excitation probability on the red sideband of the COM mode - using either the 729-nm OOP-beam or the Raman beams - as a function of the cooling pulse length. Such a measurement on the COM mode of a 19-ion crystal is shown in Fig. 5.9(b), where we observe an exponential decay with a 1/e time of about 16 μs. The cooling time for subsequent experiments is chosen well within the plateau near zero to ensure that the cooling dynamics have advanced to a steady state. We find that an EIT cooling time of 300 μs, in addition to 3 ms of Doppler cooling, is sufficient to cool up 105 ions in a planar crystal configuration close to the ground state.

EIT cooled 2d crystals

Figure 5.10 features red sideband spectra measured with and without an EIT cooling pulse for ion crystals consisting of 8, 19, 98, and 105 ions, the largest crystal cooled in our setup so far. Apart from the residual excitation of the COM mode, we observe a clear suppression of all other motional modes in the out-of-plane spectrum. The spectroscopic measurements were carried out using the narrow 729-nm OOP laser beam after cooling (3 ms Doppler + 300 μs EIT cooling) and optical pumping (100 μs). During optical pumping and the 729-nm pulse (1 ms), the crystal - preferentially the COM mode - heats up in proportion to $\dot{\bar{n}}N$. Considering a heating rate of about 16 quanta/s/ion at the time of the measurements, substantial heating of the COM mode is expected.

For the 8- and 19-ion crystals, pseudopotential simulations were performed to determine the motional mode frequencies and mode vectors. The simulated OOP mode frequencies of the 19-ion crystal match well with the spectroscopically measured oscillation frequencies. The simulated mode vectors are also used in thermometric measurements described in Sec. 5.9.1. Regarding the 8-ion crystal, we observe slight discrepancies between some of the simulated and experimentally determined mode frequencies. They might be attributed to a crystal lattice configuration close to a structural phase transition. Supplementary pseudopotential simulations suggest that slight modifications to the trap oscillation frequencies (on the order of a few kHz) lead to a modified crystal lattice structure, in which the otherwise vertically aligned square lattice in the center of the 8-ion crystal is tilted with respect to the y-axis, resembling a zig-zag configuration of the inner ions. The simulated mode frequencies for the tilted configuration result in a slightly better match with the experimental data, which is not shown here. Instabilities of the trap frequencies, e.g. due to rf power fluctuations at that time, might aggravate such a discrepancy between the measured and simulated values. Further simulations based Floquet-Lyapunov theory as well as Fourier transformation of the simulated ion motion did not improve the agreement between simulations and experiment, despite taking the full rf potential into account. In general, these deviations do not necessarily scale with the number of ions, as we obtain a better agreement for the 19-ion crystal as opposed to the 8-ion crystal and a 16-ion crystal (not shown here).

In conclusion, the presented motional sideband spectra qualitatively show that all modes in crystals with ion numbers of up to $N = 105$ are cooled close to the motional ground-state. However, due to complex quantum many-body interactions involved in the sideband dynamics, quantitative thermometric measurements with larger ion crystals are not straightforward and will be discussed in Sec. 5.3.

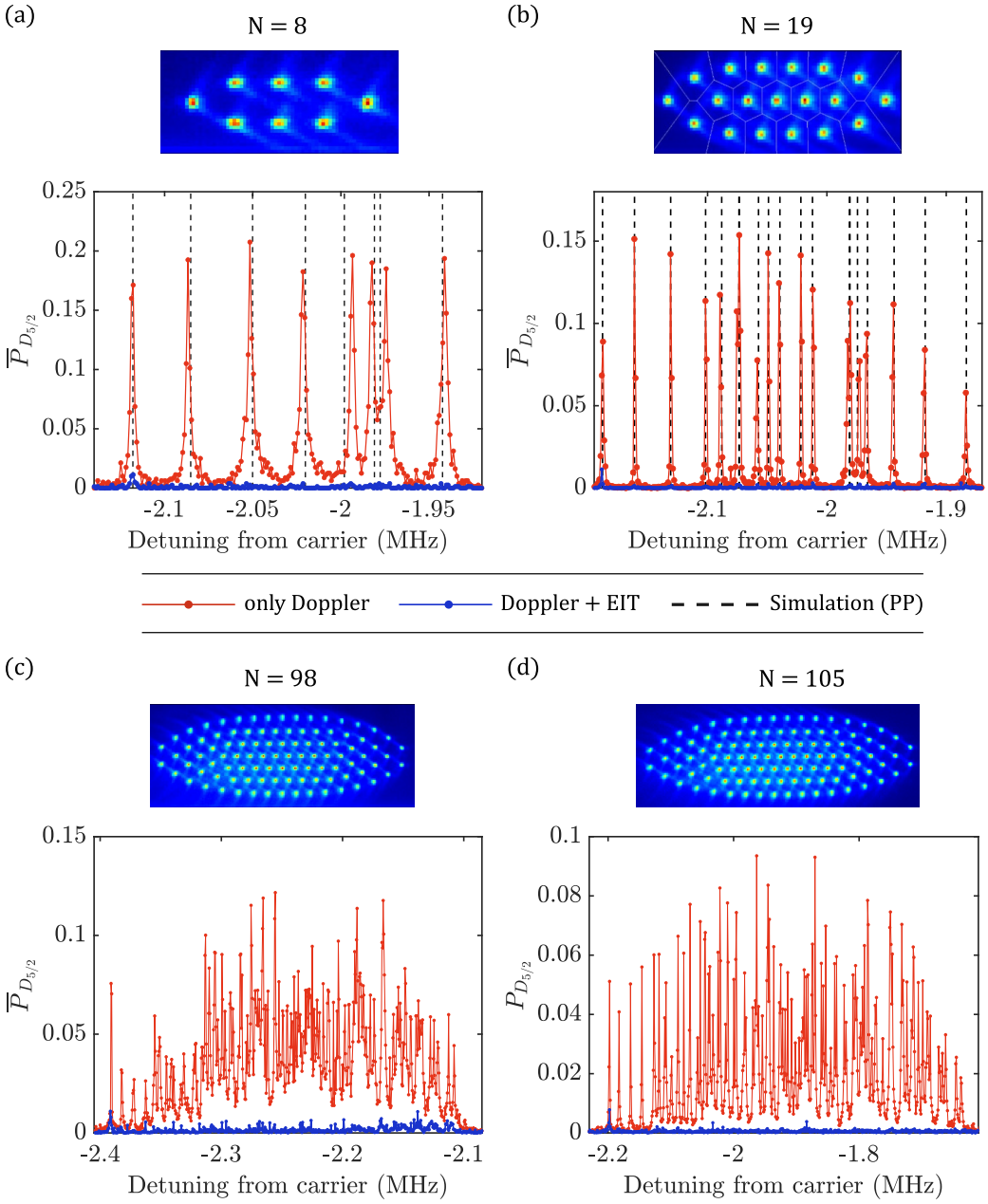

Figure 5.10: Red vibrational sideband spectra of the out-of-plane modes of 2d crystals consisting of (a) 8, (b) 19, (c) 98, and (d) 105 ions. All spectra are measured once after Doppler cooling (red data points) and again after an additional EIT cooling pulse of 300 μs (blue data points). For the smaller ion crystals in (a) and (b), simulated normal mode frequencies from pseudopotential simulations are indicated as vertical dashed lines. Generally, a good match is obtained for both spectra; however, for the 8-ion crystal, three modes at lower frequencies show a discrepancy, the origin of which is not fully understood (see main text for a discussion).

5.3 Thermometry of trapped ions

Scaling up quantum systems is generally a very demanding task, which is accompanied by numerous difficulties, ranging from entropy management to the physical control of many-qubit platforms. In trapped-ion systems, maintaining control of an increasing number of motional degrees of freedom is one of the major challenges that needs to be addressed. Besides the need for efficient ground-state cooling techniques, which was discussed in the previous sections, the accurate assessment of a prepared state of motion of ion crystals is another requirement. For many applications with trapped ions, this is essential to rule out spurious effects or to ensure efficient cooling of certain motional degrees of freedom, which may be used used to mediate entangling gates.

While the existing methodology for thermometry is sufficient for single ions and small crystals cooled to low phonon numbers, techniques applicable to large, ground-state cooled crystals are less developed. For single-ion thermometry, we can exploit simple analytical expressions based on the asymmetry of the red and blue sidebands, which is referred to as *sideband thermometry*. With sideband thermometry as the primary tool, further techniques, including singular value decomposition and numerical fits of the motional sideband dynamics, can provide estimates for single ions and small crystals [160, 174]. Note that far from the motional ground state, there are several techniques, such as time-of-flight, Doppler lineshape or image analyses [175–179], yielding satisfactory accuracy for practically arbitrary ion numbers. In contrast, thermometry of larger ion crystals close to the ground-state is not straightforward as ion-ion interactions lead to complex many-body correlations, which have to be addressed. Nonetheless, in many recently published experiments, these many-body interactions have been neglected [35,159,170,180,181] underlining the demand for accurate thermometry methods for ion crystals. Close to the ground state, applying the single-ion formula to the modes of a larger crystal usually leads to an underestimation of the occupation numbers due to the pronounced asymmetry in the spectrum. Figure 5.11 shows the blue and red sideband spectra of a 19-ion crystal after Doppler cooling. Naively applying Eq. (5.22) for single-ion sideband thermometry to modes in this spectrum, thereby fully neglecting any many-body effects, yields a mean phonon number of about $\bar{n} \approx 1$. However, after Doppler cooling we expect this number to be about 5-10 phonons, demonstrating that close to the ground state, the consideration of many-body interactions is crucial for a reliable temperature estimation. However, it is not required if individual ions in the crystal can be addressed. While, in this case single-ion techniques can be applied, it may become inefficient due to poor statistics. Moreover, experimentally, it can be challenging to implement single-ion addressing, in particular for large ion numbers, and in many experiments it may not be required otherwise. In this work, the presented methods rely solely on collective addressing and readout of ion crystals.

The following sections present techniques and results on thermometry of single ions, 8-ion crystals as well as a 19-ion crystal. In particular, the generalization of the sideband ratio technique from a single ion to ion crystals is described, following a collaborative work published in Ref. [182]. The discussed techniques are based on the assumption that the ions are in a thermal state. This approximation generally holds well for laser-cooled ions but it may not always provide an accurate description, especially when using short cooling

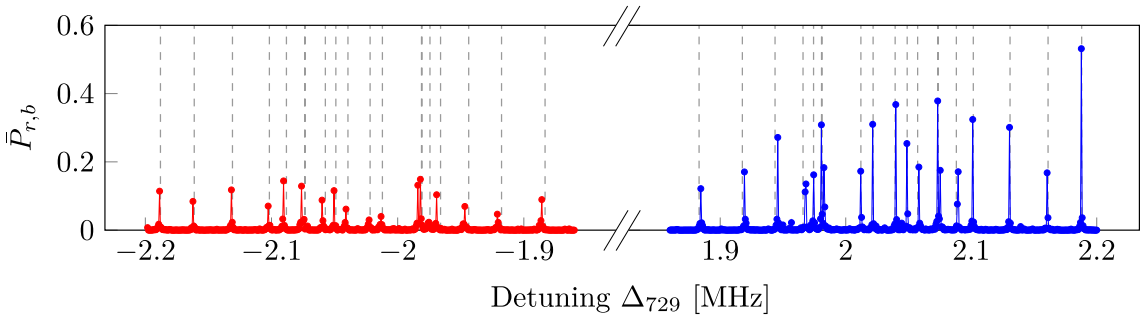

Figure 5.11: Red and blue sideband spectrum of the out-of-plane modes of a 19-ion crystal. The spectrum was measured on $S_{1/2} \leftrightarrow P_{1/2}$ transition after Doppler cooling for 3 ms, for which a mean phonon number of about 5-10 phonons would be expected. When simply applying the formula for single-ion sideband thermometry (Eq. (5.22)), the asymmetry in the spectrum would result in an underestimation of the phonon number due to many-body interactions between the ions. The generalization of the single-ion sideband thermometry technique to many-ion crystals, presented in Sec. 5.9, addresses this problem.

pulses or in the presence of micromotion [160, 183–185].

5.4 Coherent sideband dynamics

Single ion

A thermal state of motion for a single degree of freedom is given by

$$\rho(\bar{n}) = \sum_{n=0}^{\infty} p_n(\bar{n}) \left|n\right\rangle \left\langle n\right|, \tag{5.10}$$

where the probability to find a certain Fock state $|n\rangle$ is given as a function of the mean phonon number $\bar{n}$

$$p_n(\bar{n}) = \frac{\bar{n}^n}{(\bar{n}+1)^{n+1}}. \tag{5.11}$$

With the bosonic creation and annihilation operators a and $a^\dagger$, where $\hat{N} = a^\dagger a$ is the number operator, the mean phonon number is $\bar{n} = \mathrm{Tr}\left[\rho(\bar{n}) a^\dagger a\right]$. In the experiment the mean occupation can be inferred by measuring the excitation probability on the RSB and the BSB of a sideband-resolved transition, coupling the motional state to the electronic state of an ion. To this end, the ion is initialized in the state $\rho(\bar{n}) \otimes |\downarrow\rangle\langle\downarrow|$ before driving the sideband transition resonantly for a time t. For a single ion, the excitation dynamics of the vibrational sidebands are described by the Hamiltonians

$$H_r = g(\sigma_+ a + \text{h.c.}), \tag{5.12a}$$

$$H_b = g(\sigma_+ a^\dagger + \text{h.c.}), \tag{5.12b}$$

where the index $\{r, b\}$ denotes the red and blue sideband, respectively and the effective coupling strength is given by $g = \Omega_{n,n}\eta/2$, where the carrier Rabi frequency $\Omega_{n,n}$ is rescaled with the Lamb-Dicke factor ($\eta \ll 1$). The spin operators are defined as $\sigma_+ = |\uparrow\rangle\langle\downarrow|$ and $\sigma_- = |\downarrow\rangle\langle\uparrow|$. Using the evolution operator $U_\alpha(t) = \exp(-\mathrm{i}H_\alpha t)$, where $\alpha \in \{r, b\}$, the probability to find an ion in the excited state $|\uparrow\rangle$ is given by

$$P_\alpha(\bar{n}, t) = \mathrm{Tr}\Big[U_\alpha(t)\rho(\bar{n}) \otimes |\downarrow\rangle\langle\downarrow| \, U_\alpha^\dagger(t) \, |\uparrow\rangle\langle\uparrow|\Big]. \tag{5.13}$$

Explicitly, P_r and P_b for a single ion are given by

$$P_r(\bar{n}, t) = \frac{1}{2}\sum_{n=1}^{\infty} p_n(\bar{n})(1 - \cos(gt\sqrt{n}))\,, \tag{5.14a}$$

$$P_b(\bar{n}, t) = \frac{1}{2}\sum_{n=0}^{\infty} p_n(\bar{n})(1 - \cos\Big(gt\sqrt{n+1}\Big))\,. \tag{5.14b}$$

Ion crystals

For an ion crystal, we assume that each of the vibrational modes is in a thermal state. For a globally addressed ion crystal, the dynamics on the first-order red and blue sidebands are given by [182]

$$H_r = g(J_+ a + J_- a^\dagger), \tag{5.15a}$$

$$H_b = g(J_+ a^\dagger + J_- a), \tag{5.15b}$$

with the spin operators $J_\pm = \sum_{i=1}^{N} \eta_i \sigma_\pm^i$ and the average Rabi frequency[9] of the sideband transitions g, such that $\sum_i \eta_i^2 = 1$. Both the RSB and BSB Hamiltonians in Eqs. (5.15) have conserved quantities given by $\Big[H_r, a^\dagger a + J_0\Big]$ and $\Big[H_b, a^\dagger a - J_0\Big]$, where $J_0 = \sum_{i=1}^{N} \sigma_+^i \sigma_-^i$ yields the number of electronic spin excitations.

To simulate the exact sideband dynamics for a given system, the Schrödinger equation for the Hamiltonians (5.15) needs to be time-propagated. Explicitly, the probability of an ion crystal to remain in the motional ground state is given by

$$\mathrm{Tr}[|\mathbf{0}\rangle\langle\mathbf{0}| \, \rho_\alpha(\bar{n}, t)] = \sum_{n=0}^{\infty} p_n(\bar{n}) |\langle \mathbf{0}, n| \, U_\alpha(t) \, |\mathbf{0}, n\rangle|^2. \tag{5.16}$$

where $|\mathbf{0}\rangle = |\downarrow \ldots \downarrow\rangle$ is the collective spin ground state, and $\rho_\alpha(\bar{n}, t) = U_\alpha(t)\rho(\bar{n}) \otimes |\mathbf{0}\rangle\langle\mathbf{0}| \, U_\alpha^\dagger(t)$ the time-propagated full density matrix of the system excited on the red or blue sideband ($\alpha \in \{r, b\}$), and $p_n(\bar{n})$ is the thermal occupation probability of Fock states (Eq. (5.11)). For large ion crystals, this calculation becomes intractable as its complexity is growing exponentially with the ion number N. However, considering only the COM mode, all ions have equal Lamb-Dicke factors ($\eta_i \propto 1/\sqrt{N}\ \forall i$), allowing the sideband dynamics

[9] In this description, the Lamb-Dicke factors η_i account for all coupling inhomogeneities to the ions, which, in general, can be calibrated.

to be calculated in a symmetric Hilbert subspace using the symmetric spin Dicke basis of states

$$|\mathbf{M}\rangle = \frac{1}{M!}\binom{N}{M}^{-1/2} S_+^M |\mathbf{0}\rangle\,, \text{ with } S_+ = \sum_{i=1}^{N} \sigma_i^+ \,. \tag{5.17}$$

This approach bypasses the problem's exponential scaling and renders a numerical fit of the COM mode feasible even for higher ion numbers. Such a fit of the out-of-plane COM mode of a 19-ion crystal is shown in Fig. 5.15(c).

5.5 Fitting of coherent dynamics

The expressions given in the previous section can be used to extract the mean phonon number from the sideband excitations measured as a function of the interrogation time t, which is discussed in the following section 5.5.1. Similarly, a numerical fit can be performed for carrier oscillations, which is briefly described in Sec. 5.5.3. However, for an ion crystal, a fit of the system dynamics is a computationally complex task due to the exponentially growing state space of N coupled harmonic oscillators. As the propagation of the full density matrix has to be computed for varying mean phonon numbers in order to fit the data, this approach is only feasible for small ion numbers. Moreover, a mean-field approximation neglecting higher-order ion-ion correlations was pursued in the course of the work for Ref. [182] to simulate the sideband dynamics of a 19-ion crystal; however, we did not succeed in fully reproducing the experimental data. This attempt is briefly discussed in Sec. 5.5.2.

5.5.1 Fitting of sideband oscillations using numerical simulations

Assuming knowledge of the secular frequencies and, in the case of an ion crystal, the mode vectors, the dynamics of a thermal state can be numerically fitted using the mean phonon number as a free parameter. To this end, a thermal state distribution (Eq. (5.11)) with phonon numbers of $n_{\max} \gg \bar{n}$ is considered. The system dynamics are simulated for varying mean phonon numbers and a least-squares optimization is used to find the best fit to the data. Provided single-ion addressing, Eqs. (5.14) could be used to extract the mean phonon number of individual modes in multi-ion a crystal. However, many experiments are lacking coherent control of individual ions, which also applied to the experimental setup presented in this work[10].

Concerning the accuracy of the estimation of $\bar{n}$, a Fisher information analysis of the sideband dynamics of a single ion reveals that it is most beneficial to fit the measured excitation on the red sideband as the red sideband data contains most information about the thermal state of the ion and therefore yields the lowest Cramér-Rao bound compared with the excitation on the blue sideband or a combined measurement scheme such as the sideband-ratio estimator (Eq (5.23) in Sec. 5.8) [182]. From a practical point of view, however, the sideband-ratio technique can be advantageous as the blue sideband excitation therein acts as a gauge for the measurement in the presence of technical noise.

[10] The foreseen single-ion addressing optics have not yet been set up in the course of this work.

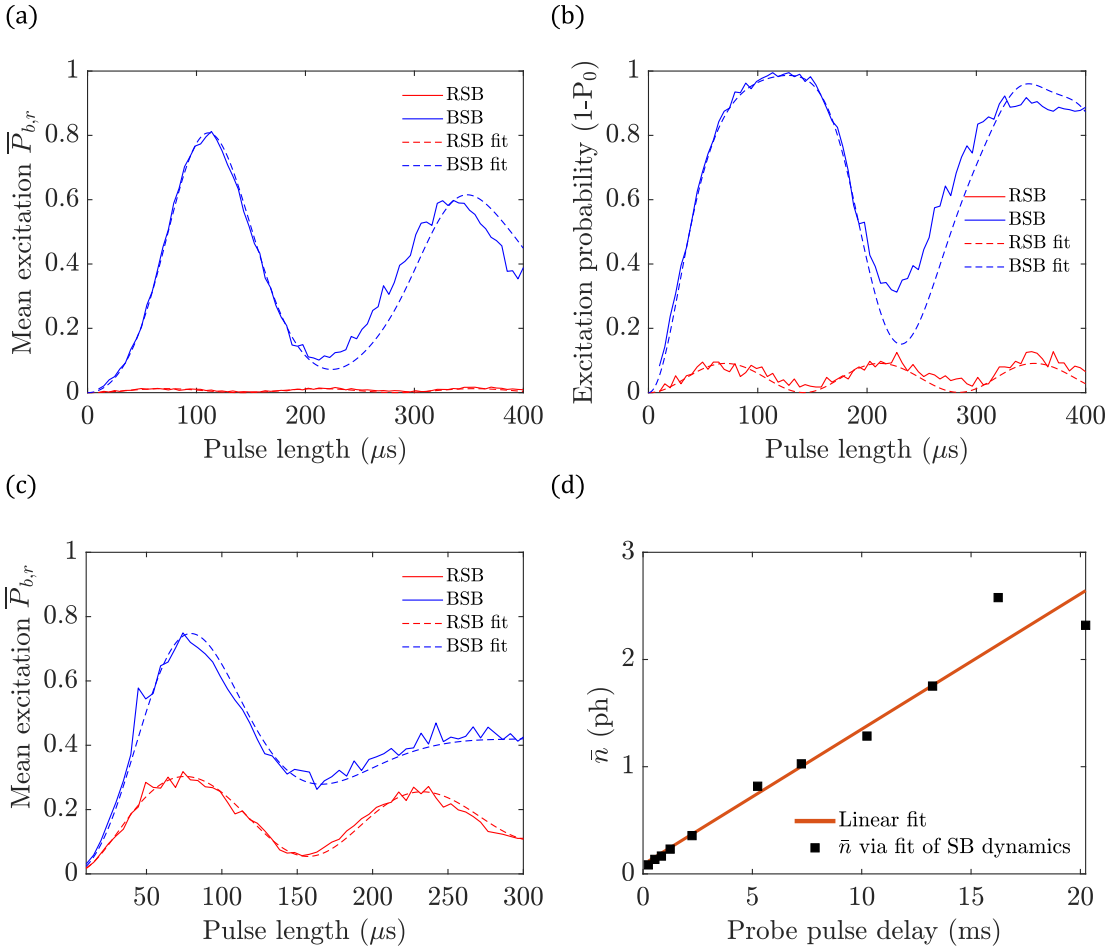

Figure 5.12: Sideband dynamics and heating rate measurement for an 8-ion crystal. (a) Mean excitation probabilities on the red and blue sideband as a function of the probe pulse length. Least-squares fits of the red sideband dynamics are used to determine the mean phonon number $\bar{n}$. (b) Global excitation probability as defined in Eq. (5.13), being the quantity of interest for sideband thermometry of ion crystals (Sec. 5.9). (c) Same as (a), but with a probe pulse delay of 20 ms. (d) Heating rate measurement. The mean phonon number is determined using fits of the red sideband dynamics for varying probe pulse delays. A linear fit (solid red line) is used to determine the heating rate of $\dot{\bar{n}} = 15.8 \pm 1.1$ phonons/s/ion.

Sideband dynamics of a planar 8-ion crystal

Figures 5.12(a) and (b) show fits of the sideband dynamics of the out-of-plane COM mode of an 8-ion crystal recorded immediately after EIT cooling. The crystal was trapped in a potential with trap oscillation frequencies $\omega_{\{x,y,z\}} = 2\pi \times \{2.118, 0.702, 0.370\}$ MHz. 729-nm light was used to excite the first order red and blue motional sidebands of the $S_{1/2} \leftrightarrow D_{5/2}$ transition. To measure the heating rate of the COM mode, the experiments were repeated for varying delays introduced before the probe pulse. Fits of the red sideband data are used to estimate the mean phonon numbers for various delays. A linear fit of the mean phonon number as a function of the probe pulse delay yields a heating rate of $\dot{\bar{n}} = 15.8 \pm 1.1$ phonons/s/ion. Note that these measurements were carried out before a modification of the dc filter boards, which lead to a substantially lower heating rate of about 0.6 phonons/s/ion (see Sec. 4.6).

5.5.2 Mean-field approximation for ion crystals

In order to validate the thermometry measurements with a 19-ion crystal presented in Sec. 5.9.1, a mean-field approximation of the sideband dynamics was pursued. In this approach, higher order ion-ion correlations are neglected and the ground-state probability

$$P_g = \langle \otimes_i \sigma_i^{gg} \rangle \simeq \prod_i (1 - \langle \sigma_i^{ee} \rangle) \ , \tag{5.18}$$

where σ_i^{gg} and σ_i^{ee} are projectors to the ground and excited states, respectively, can be computed via a closed set of differential equations, which are given in Appendix B. Figure 5.13 shows the sideband dynamics of a planar 19-ion crystal. Here, the mean occupation number $\left\langle a^\dagger a \right\rangle = \bar{n}$, used as initial condition in the mean-field approximation, is set to the value that was obtained from sideband thermometry measurements (Sec. 5.9.1. At the onset of the excitation dynamics, the simulated curve agrees well with the experimental data and successfully reproduces the dynamics at the single-ion level. However, for longer interrogation times ($t > 100\mu$s), the approximation fails to replicate the measured data and even results in unphysical values. It is thus not feasible to use this approximation for a reliable fit of the data to estimate the temperature. This showcases the complexity of approximating the multi-ion correlations in the dynamics of even relatively small ion crystals and underscores the need for reliable thermometry methods for larger crystals. Although not pursued here, considering higher order terms in the approximation could potentially yield more accurate results.

5.5.3 Fitting of carrier oscillations using numerical simulations

There is also a weak dependency of the carrier transition's Rabi frequency on the phonon number n_m of the motional mode m, which is given by [49]

$$\Omega_{n,n}^{(j)} = \Omega_0 \prod_{m=1}^{N} L_{n_m}(\eta_{m,j}^2) \ , \tag{5.19}$$

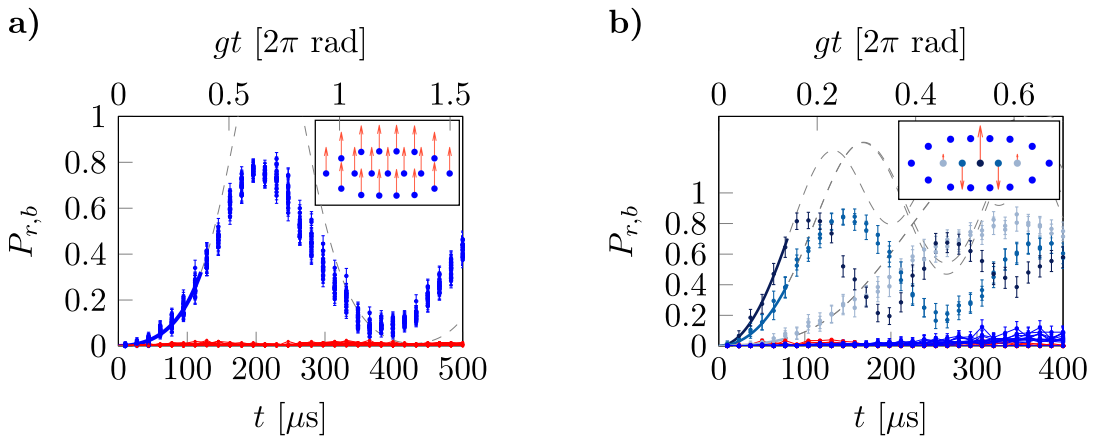

Figure 5.13: Attempt to fit the sideband dynamics of a planar 19-ion crystal using a mean-field approach. (a,b) Fit of the single-ion resolved sideband dynamics measured on (a) the COM mode and (b) the lowest-frequency mode of the out-of-plane motional spectrum. The solid lines highlight the regions with good overlap whereas the grayed out, dashed lines show a substantial discrepancy between experiment and simulation up to unphysical values for longer evolution times. The insets illustrate the structure of the investigated modes with arrows proportional to their mode vectors.

where Ω_0 is the single-ion Rabi frequency[11], L_{n_m} is a Laguerre polynomial, $\eta_{m,j}$ is the Lamb-Dicke parameter for ion j and mode m. The excited state probabilities $p_j(t)$ of the jth ion on the carrier transition, assuming thermal states for N modes with mean phonon numbers $\bar{\mathbf{n}} = (\bar{n}_1, \bar{n}_2, ..., \bar{n}_N)$, is given by

$$p_j(t) = \sum_{\bar{\mathbf{n}}} p_{\mathrm{th}}(\bar{\mathbf{n}}) \sin^2(\Omega_{n,n}^{(j)}(\bar{\mathbf{n}})t/2) \ . \tag{5.20}$$

As with the sideband dynamics, an increasing number of ions drastically raises the computational cost of simulating the carrier dynamics for various phonon numbers. To estimate the mean phonon number from carrier Rabi oscillations of a 22-ion crystal after PG cooling (Fig. 5.5), a semi-quantitative approach was pursued, using a gradient-free minimization algorithm to find a parameter set fitting the experimental data. Details on this approach can be found in Ref. [153] and references therein.

5.6 Rapid adiabatic passage

A rapid adiabatic passage (RAP) in trapped ions can be realized by a frequency-chirped laser pulse with a time-dependent Gaussian amplitude envelope [186]. Being robust to instabilities in experimental parameters, it can transfer the population from one internal state to another with high fidelity. It has further been used to generate Dicke states in a two-ion crystal [187]. Multiple RAPs can be applied to measure the Fock state of a

[11] Note that Ω_0 might vary for different ions, e.g. due to an inhomogeneous laser beam profile, and therefore becomes $\Omega_{0,j}$ taking these variations into account.

single ion [188]. In an ion crystal, prepared in the electronic ground state, a globally applied RAP can be used to transfer the phononic excitation to an electronic excitation using the red sideband transition. For $\bar{n} < N$, there is a 1:1-mapping, such that the count of electronic excitations in the crystal is a direct measure for $\bar{n}$. However, it has been reported in Refs. [135, 173] that for modes other than the COM mode, this approach is only reliable when $\bar{n} < N/2$. Thermometry based on RAP is also plagued and limited by quantum correlations induced via the common coupling of the spins to the modes of motion. A reliable inference of the occupation number would require a sufficiently accurate description of the adiabatic quantum many-body dynamics, which is again not feasible for large crystals.

5.7 Thermometry using a collective bichromatic drive

Alternatively, the temperature of an ion crystal could be estimated using a bichromatic laser beam simultaneously driving the red and blue sidebands of a particular mode in combination with a single-ion readout. By reading out only one particular ion in the crystal, one can circumvent the increased complexity in the measurement due to quantum many-body interactions. This approach is briefly summarized in the following; a more detailed discussion can be found in Ref. [182].

The red and blue sideband dynamics are governed by the Hamiltonian $H = H_r + H_b = \sum_i H^i$ with commuting single-particle Hamiltonians $H^i = g\eta_i(a + a^\dagger)\sigma_x^i$. For a crystal that is initially prepared in the state $\rho_0 = |\mathbf{0}\rangle\langle\mathbf{0}| \otimes \rho(\bar{n})$, where the mode is assumed to be in a thermal state with mean phonon number $\bar{n}$, the probability to find ion i in the excited state after bichromatically driving the crystal for a time t is

$$\begin{aligned} P^i(\bar{n}, t) &= \mathrm{Tr}\Big[e^{-\mathrm{i}H^i t}\,|\downarrow\rangle\langle\downarrow| \otimes \rho(\bar{n}) e^{\mathrm{i}H^i t}\,|\uparrow\rangle\langle\uparrow|\Big] \\ &= \frac{1}{2}\Big(1 - e^{-2(gt\eta_i)^2(2\bar{n}+1)}\Big). \end{aligned} \tag{5.21}$$

This exponential loss of contrast can be exploited to extract the mean phonon number $\bar{n}$ without the burden of many-body correlations across the crystal. However, such a measurement requires larger statistics, as it measures only single-ion excitations, as well as longer interrogation times due to a reduced single-ion coupling that scales with η_i, especially for larger crystals. A quantitative comparison presented in Ref. [182] shows that the bichromatic method and the sideband thermometry, discussed in the following sections, are advantageous in complementary regimes. The sideband thermometry of ion crystals yields better statistics at low temperatures whereas the bichromatic approach can be beneficial at higher temperatures of $\bar{n} \gtrsim 1$.

5.8 Sideband thermometry of a single ion

This section closely follows the theory presented in Ref. [182].

In Sec. 5.4, we saw that the sideband excitation of a particular mode measured as a function of the interrogation time t can be fitted to obtain the mean phonon number.

However, for a single ion in a thermal state of motion with small vibrational excitation, a simpler and more convenient relation can be used to infer the mean occupation number by measuring the RSB and BSB excitation probabilities at only a single interrogation time [49, 58, 156, 189]. Considering a single degree of freedom, the mean phonon number is given by

$$\bar{n} = \frac{P_r(\bar{n}, t)}{P_b(\bar{n}, t) - P_r(\bar{n}, t)} \,. \tag{5.22}$$

This formally correct analytical expression[12] relates theory and experiment in a simple way and represents the essence of the widely employed *sideband-ratio thermometry technique*. Since this identity is an analytical expression based on exact statistical averages, it holds only for an infinite number of measurement samples. For this reason, P_α is henceforth replaced by the relative statistical frequency f_α, representing the sampled values of P_α. The expression for $\bar{n}$ given in Eq. (5.22) transforms into the statistical estimator for the mean occupation number

$$\hat{\bar{n}} = \frac{f_r}{f_b - f_r}. \tag{5.23}$$

Dealing with statistical estimates entails both a statistical error and a bias for the given estimator $\hat{\bar{n}}$. Assuming a finite sample size $\mathcal{N}$ (with $\mathcal{N}/2$ measurements on the RSB and $\mathcal{N}/2$ measurements on the BSB transition), the estimate f_α is normally distributed and the statistical variance and bias can be calculated as

$$\delta\bar{n} = \langle\hat{\bar{n}}\rangle - \bar{n} = \frac{1}{\mathcal{N}} \frac{2P_bP_r(2 - P_b - P_r)}{(P_b - P_r)^3}, \tag{5.24a}$$

$$\Delta\bar{n}^2_{\mathrm{err}} = \langle(\hat{\bar{n}} - \bar{n})^2\rangle = \frac{1}{\mathcal{N}} \frac{2P_bP_r(P_b + P_r - 2P_bP_r)}{(P_b - P_r)^4} \,. \tag{5.24b}$$

5.9 Sideband thermometry of ion crystals

Large parts of the theory and results presented in this section have been published in Ref. [182].

The sideband dynamics of an ion crystal consisting of N ions are described by Eqs. (5.15). In contrast to the single-ion case, we now have to account for the many-body interactions of the coupled N-particle system to adequately describe its dynamics. For large N, computing the exact dynamics by propagation of the Schrödinger equation becomes an extremely expensive problem due to the exponential growth of the Hilbert space. Due to the many-body dynamics, a simple analytical expression, as given by Eq. (5.22) for a single ion, does not exist for ion crystals. However, according to Ref. [182], we can extend the single-ion sideband-ratio technique to the case of ion crystals by approximating the onset of the N-body system's sideband dynamics, which will be described in the following.

[12] It can be easily verified using the presented expressions for $P_\alpha(\bar{n}, t)$ and $\frac{p_{n+1}(\bar{n})}{p_n(\bar{n})} = \frac{\bar{n}}{\bar{n}+1}$ for thermal states.

For convenience we first redefine the ion crystal excitation probability as the complement of the probability for all ions to remain in the ground state (see Eq. (5.16)), i.e. the probability of a single or more ions to be excited, as

$$P_\alpha(\bar{n},t) = 1 - \mathrm{Tr}[|\mathbf{0}\rangle\langle\mathbf{0}|\,\rho_\alpha(\bar{n},t)], \tag{5.25}$$

where $|\mathbf{0}\rangle = |\downarrow\ldots\downarrow\rangle$ is the collective spin ground state and $\rho_\alpha(\bar{n},t) = U_\alpha(t)\rho(\bar{n}) \otimes |\mathbf{0}\rangle\langle\mathbf{0}|\,U_\alpha^\dagger(t)$ the time-propagated full density matrix of the system excited on the red or blue sideband ($\alpha \in \{r,b\}$). In Eq. (5.16), we can see that only diagonal elements of the time propagation operator U_α contribute to the excitation probability on the sideband $P_\alpha(\bar{n},t)$. In the next step these diagonal elements are expanded into a time power series,

$$\langle\mathbf{0},n|\,U_\alpha(t)\,|\mathbf{0},n\rangle \simeq \sum_{k=0}^{4} \frac{(-it)^{2k}}{(2k)!}\,\langle\mathbf{0},n|\,H_\alpha^{2k}\,|\mathbf{0},n\rangle + o(t^{10}). \tag{5.26}$$

Terms of up to eighth order in time are found to sufficiently cover the first fringe of the sideband excitation, yielding an accurate temperature estimate within this time window. In the given series expansion only even powers of H_α are non-vanishing and thus contribute to the global excitation probability. Within this approximation, the matrix elements become polynomials of a maximal degree of 4 in n and 8 in gt. The average of Eq. (5.26) with respect to n yields the excitation probability in Eq. 5.25 and finally results in the functional dependence of the conveniently measurable sideband ratio on the mean phonon number,

$$\frac{P_r(\bar{n},t)}{P_b(\bar{n},t) - P_r(\bar{n},t)} = \mathcal{R}_t(\bar{n}), \tag{5.27a}$$

where

$$\mathcal{R}_t(\bar{n}) = \bar{n} + (gt)^2\mathcal{P}_2(\bar{n}) - (gt)^4\mathcal{P}_3(\bar{n}) + (gt)^6\mathcal{P}_4(\bar{n}) + o(t^8)\,. \tag{5.27b}$$

The coefficients $\mathcal{P}_k(\bar{n})$ are known polynomials depending solely on the mode coupling coefficients η_i and can be computed efficiently. They are given explicitly for $k = 1, 2$ in Appendix B of Ref. [182]. Equations (5.27) are, in essence, a generalization of the single-ion sideband ratio (Eq. (5.22)) to the case of ion crystals, taking the quantum correlations between the ions into account. As in the single-ion case, for a finite number of measurements, the probabilities $P_{r,b}$ are replaced by the statistical frequencies $f_{r,b}$, yielding the temperature estimator for an ion crystal:

$$\hat{\bar{n}} = \mathcal{R}_t^{-1}\!\left(\frac{f_r}{f_b - f_r}\right). \tag{5.28}$$

This relation reduces the temperature measurement to solving the polynomial equation by finding the root of $\mathcal{R}_t(\bar{n}) - f_r/(f_b - f_r) = 0$, which yields the mean occupational number $\bar{n}$. Note that the calculation of the polynomial coefficients in Eq. (5.27b) causes the majority of computational overhead, which depends on the order of the series expansion used for the approximation. The systematic bias and the variance of the estimator, resulting from

the finite sampling of the red and blue sideband excitation probabilities $P_{r,b}$, are given by

$$\begin{aligned}\delta\bar{n} &= \langle\hat{\bar{n}}\rangle - \bar{n} \\ &= \frac{1}{\mathcal{N}}\Big[\frac{2P_bP_r(2-P_b-P_r)}{(P_b-P_r)^3}\frac{1}{\mathcal{R}_t'(\bar{n})} - \\ &\quad - \frac{P_bP_r(P_b+P_r-2P_bP_r)}{(P_b-P_r)^4}\frac{\mathcal{R}_t''(\bar{n})}{[\mathcal{R}_t'(\bar{n})]^3}\Big],\end{aligned} \tag{5.29}$$

and

$$\Delta\hat{\bar{n}}^2_{\text{error}} = \frac{1}{\mathcal{N}}\frac{2P_bP_r(P_b+P_r-2P_bP_r)}{(P_b-P_r)^4}\frac{1}{[\mathcal{R}_t'(\bar{n})]^2}\,, \tag{5.30}$$

respectively. The new estimator (5.28) is based on a truncation of the time evolution of the sideband excitation. For this reason, the estimator's error increases for longer interrogation times. For small ion crystals, this error can be calculated numerically, which revealed no dependence on the crystal size for crystals with $N < 12$ (details in [182]). Along the derivation of Eq. (5.28), no restrictions on the number of ions were imposed, suggesting that the estimator remains valid for ion crystals with large N.

5.9.1 Sideband thermometry of a planar 19-ion crystal

This section presents sideband thermometry measurements with a two-dimensional 19-ion crystal, based on the sideband ratio for ion crystals (Eq. (5.28)) that was derived in the previous section. In these measurement, the mean occupation numbers of the COM mode and the lowest-frequency (LF) mode of the out-of-plane sideband spectrum is determined. Besides the fundamental interest in thermometry with (2d) ion crystals and the characterization of heating in our setup, the purpose of these measurements is to demonstrate the application of the generalized sideband thermometry technique to a "larger" ion crystal. The size of the computational state space[13] required for the computation of exact excitation dynamics for the 19-ion crystal already surpasses the capabilities of most classical computers, or presents a substantial challenge at the very least.

Trapping and ground-state preparation

The planar 19-ion crystal was trapped in a potential with oscillation frequencies of $\{\omega_\text{s}, \omega_\text{w1}, \omega_\text{w2}\} = 2\pi \times \{2189, 645, 340\}$ kHz, where ω_s is the secular frequency in the strongly confining (OOP) direction, and ω_w1 and ω_w2 denote the secular frequencies in the two weakly confining directions. As in all other measurements with 2d crystals presented in this thesis, the w2-direction (z) is aligned with the rf-zero line. After Doppler cooling for 3 ms, all N out-of-plane modes are cooled close to their ground states via EIT cooling for 300 μs. The detuning of the EIT beams with respect to the bare $4\text{S}_{1/2} \leftrightarrow 4\text{P}_{1/2}$ transition is 110 MHz, enabling simultaneous and efficient cooling of all out-of-plane modes. The center of the EIT cooling range is aligned with the center of the out-of-plane RSB frequency spectrum, spanning about 300 kHz, by adjusting the power of the σ-polarized dressing beam (see Sec. 5.2.2 for details on the calibration procedures). Subsequent to cooling,

[13] 2^N complex numbers to represent an N-qubit state

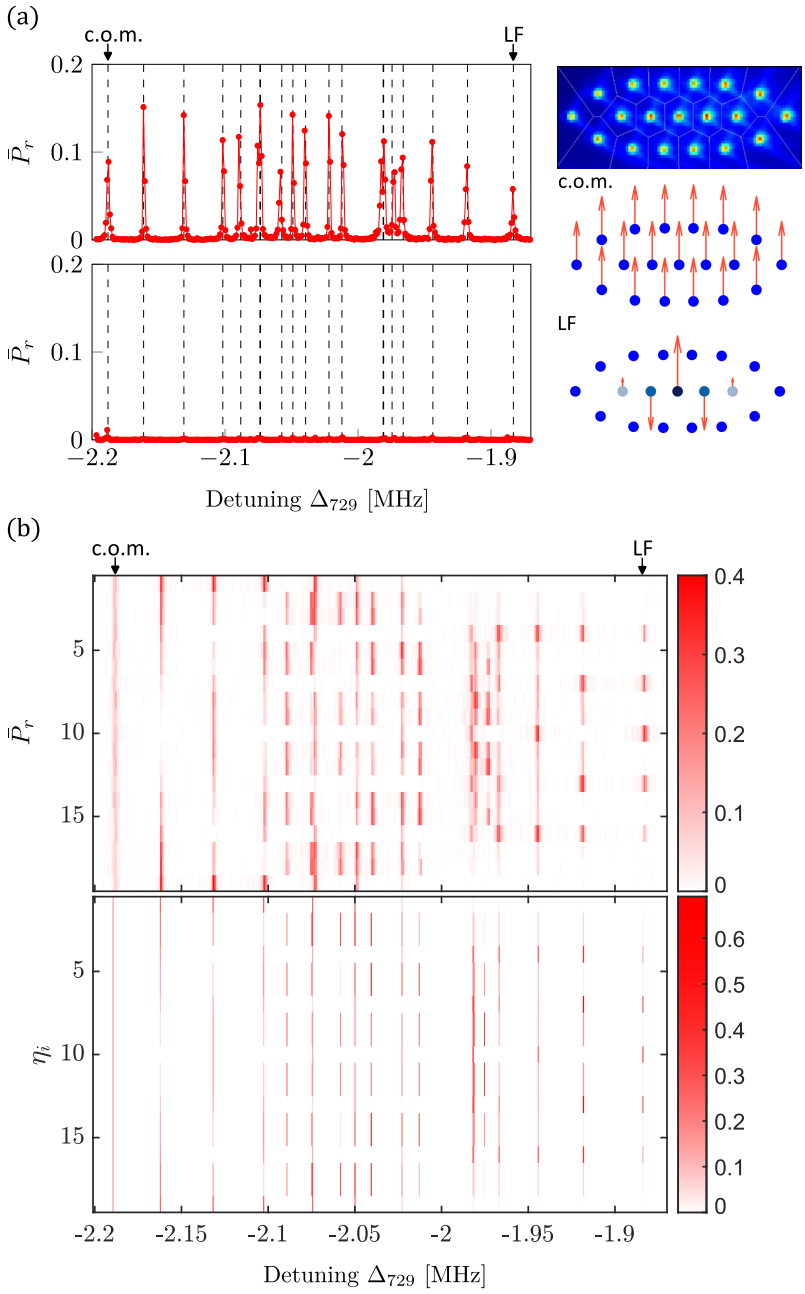

Figure 5.14: (a) Red sideband spectrum of the out-of-plane modes of a 19-ion planar crystal after Doppler cooling (top) and after an additional EIT cooling for 300 μs (bottom). The mean excitation is given as a function of the detuning from the carrier. The mode frequencies obtained from pseudopotential simulations are indicated by dashed lines. A false-color EMCCD camera image of the 19-ion crystal is shown at the top right. The mode vectors of the COM mode as well as the mode with the lowest out-of-plane frequency (LF) are represented by red arrows. Their lengths are proportional to the magnitude of the Lamb-Dicke factors η_i, with the direction indicating the sign of η_i. (b) Measured mean excitation (top) and simulated mode vectors (bottom) of the individual modes, demonstrating a good match between the simulations and experiments.

light at 729 nm is used to optically pump the ions into the $|S_{1/2}, m = -1/2\rangle$ state for 150 μs before each single-shot experiment.

Motional sideband spectrum and dynamics

The implementation of the generalized sideband thermometry protocol requires knowledge of the Lamb-Dicke factors of the individual ions for the motional mode to be analyzed. Therefore, numerical simulations based on pseudopotential theory were performed to determine all out-of-plane normal mode frequencies vectors. The obtained Lamb-Dicke factors are used to calculate the polynomial coefficients in Eq. (5.27b). To verify efficient cooling as well as the accuracy of the simulation outcome, before the actual thermometry measurements, the motional sideband spectrum and the sideband dynamics of the investigated modes are probed on the $4S_{1/2} \leftrightarrow 3D_{5/2}$ quadrupole transition. Figure 5.14 shows the red sideband spectrum of the 19-ion crystal, once after only Doppler cooling and again after an additional EIT cooling pulse. From a qualitative perspective, all modes are cooled close to the ground-state. The residual excitation on the COM mode originates from heating during state initialization (150 μs) and the spectroscopy measurement itself (1 ms). A good match between the simulated normal mode frequencies (dashed lines in Fig. 5.14) and the measured spectrum supports confidence in the simulation results used for subsequent temperature estimation. Note, however, that the pseudopotential approximation can sometimes fail to reproduce experimental data, in particular for planar crystals [56,57]. Alternative approaches might be more successful in some cases (cf. Sec. 5.1).

The measured sideband excitation dynamics, shown in Fig. 5.15, reveal the mode structure as well as the global excitation probabilities $P_{r,b}$ of the interrogated modes. The red and blue sideband transitions were each probed at a fixed carrier Rabi frequency ($\Omega_{\mathrm{carr}} = 2\pi \times 38.8$ kHz) as a function of the pulse length. The structure of the investigated modes manifests itself in the single-ion resolved data shown in Fig. 5.15(a) and (b) for the COM mode and the lowest-frequency mode, respectively. The global excitation probabilities $P_{r,b}$, being the quantities of interest in the sideband thermometry measurements, are shown in Fig. 5.15(c) and (d).

Reference measurements

For arbitrary modes of an ion crystal with as few as 19 ions, it is already challenging to provide a reliable reference estimate for $\bar{n}$ or to determine the error in $\bar{n}$ that is attributed to a finite interrogation time. This contrasts with smaller crystal sizes, e.g. consisting of 4 ions in Ref. [182], where it is feasible to compute the exact system dynamics within a reasonable time. The system dynamics of the COM mode, however, can be computed efficiently within the symmetric Hilbert subspace as described in Sec. 5.5.1. This is done for the data displayed in Fig. 5.15(c), where a least-squares fit of the RSB dynamics of the COM mode yields a mean phonon number of $\bar{n} = 0.147 \pm 0.02$ phonons. We use the first 20 points ($\lesssim 350\mu$s) to fit the curve, where we find a good match with the experimental data. For longer interrogation times, the data is impaired by a limited motional coherence due to motional heating and instabilities in the trap oscillation frequencies. Note that these measurements were taken before a modification of the dc filter boards and a revision of the rf power stabilization circuit, which substantially improved the motional

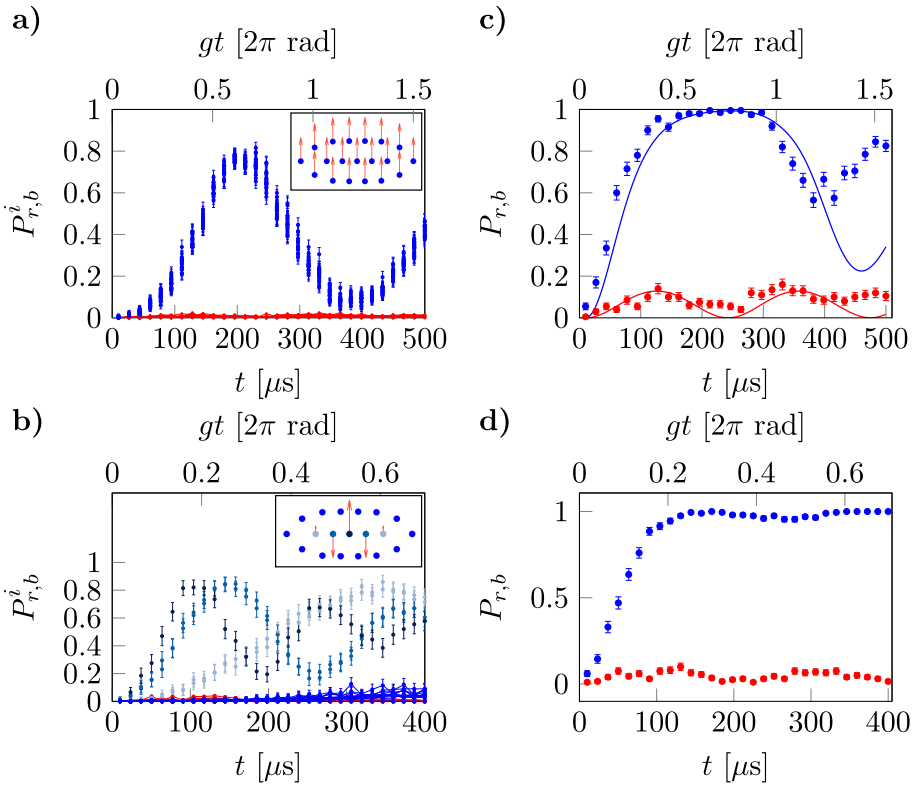

Figure 5.15: Sideband dynamics of a planar 19-ion crystal. (a,b) Single-ion excitation probabilities $P^i_{r,b}$ for (a) the COM mode and (b) the lowest-frequency mode. (c,d) The global excitation probabilities $P_{r,b}$, being the quantities of interest for the thermometry measurements, are shown for (c) the COM mode and (d) the lowest-frequency mode. The measured dynamics of the COM mode are fitted via least-squares by simulations in the symmetric Hilbert subspace of the COM mode. The solid line shows the simulated dynamics for the fitted value of the mean phonon number ($\bar{n} = 0.147 \pm 0.02$ phonons), which is used as a reference for subsequent sideband thermometry measurements (cf. Fig. 5.16).

coherence (Sec. 4.8).

Another comparative value is provided by measurements with a single ion using sideband-ratio thermometry. For the transverse mode of motion with a frequency of $\omega_x = 2\pi \times 2.188$ MHz, corresponding to the out-of-plane direction of a planar ion crystal, we find a mean phonon number of $\bar{n} = 0.06$ quanta after EIT cooling. The single-ion heating rate, at the time of these measurements, was approximately 16 phonons per second. These values are complemented with measurements and numerical fits of the sideband dynamics of a planar 8-ion crystal. For this crystal, the exact dynamics can be efficiently calculated, suggesting a heating rate of 15.8 phonons/s/ion.

Sideband thermometry of a planar 19-ion crystal

The sideband thermometry measurements of the COM mode and the lowest-frequency mode in out-of-plane direction were performed after EIT cooling and after optical pumping (adding a probe pulse delay of 150 μs after ground-state cooling). A global beam perpendicular to the crystal plane excites the ions with a maximum variation in the single-ion carrier Rabi frequencies of about 6% across the crystal. The excitation probabilities $P_{r,b}$ on the $|\mathrm{S}_{1/2}, m = -1/2\rangle \leftrightarrow |\mathrm{D}_{5/2}, m = -5/2\rangle$ transition with a 729-nm laser, were probed using various carrier Rabi frequencies and interrogation times. The excitation was measured in $\mathcal{N}/2 = 4000$ individual measurements each on the red and the blue sideband. Equation (5.28) is used to calculate the mean occupation number $\bar{n}$. The bias and errors are determined using Eq. (5.29) and Eq. (5.30), respectively. The estimated phonon numbers of the COM mode and the LF mode are displayed for various values of gt in Fig. 5.16(a) and (b), respectively. The bias-corrected mean phonon number is estimated to be $\bar{n} = 0.149(3)$ for the COM mode and $\bar{n} = 0.081(3)$ for the lowest-frequency mode. The magnitude of the bias is well below the error bar for all data points (see paragraph on *Statistical bias* below for a discussion). The obtained results are consistent across the probed parameter space. However, spurious excitation of neighboring modes at higher Rabi frequencies leads to an overestimation of the mean phonon number, particularly of the LF mode. This issue is further explored below; see paragraph on *Crosstalk*.

Heating-rate measurement

In addition to the characterization of the ground-state population directly after EIT cooling, the generalized sideband ratio technique was applied to determine the heating rate in measurements of vibrationally excited states with higher mean occupation numbers ($1 < n < 10$). To this end, sideband thermometry measurements, as described above, were carried out after a predefined waiting time between 0 and 20 ms following the ground-state preparation. A linear fit of the estimated mean phonon numbers, weighted with the inverse variance obtained from Eq. (5.30), finally yields the heating rate. The data is shown in Fig. 5.16(c) and reveals a heating rate of 15.3(1.7) quanta/s per ion for the COM mode. This value is in accordance with previous measurements with a single ion and an 8-ion crystal. The LF mode does not exhibit significant heating within tens of milliseconds and, therefore, a heating rate measurement for this mode is not shown.

Another heating rate measurement of the COM mode was carried out after the improvement of the dc filter boards[14], which led to a substantial reduction of Johnson noise on the dc electrodes. The measurement procedure was equivalent to the previous heating rate measurement. The red and blue sideband excitations were probed in $\mathcal{N}/2 = 5000$ experiments each. The 729-nm laser power was set corresponding to a carrier Rabi frequency of $2\pi \times 31.25$ kHz. The crystal was trapped in a potential with COM mode frequencies of $\omega_{x,y,z} = 2\pi \times \{2188.8, 644.4, 337.4\}$ kHz measured with the 19-ion crystal, being only slightly different from the ones used in the previous measurement ($\Delta\omega/(2\pi) < 3$ kHz in all directions). With the improved dc filters, we measure a reduced heating rate of 0.64(8) phonons/s per ion. This result is backed up by a single-ion heating rate measurement,

[14] see Sec. 3.4.3 for details

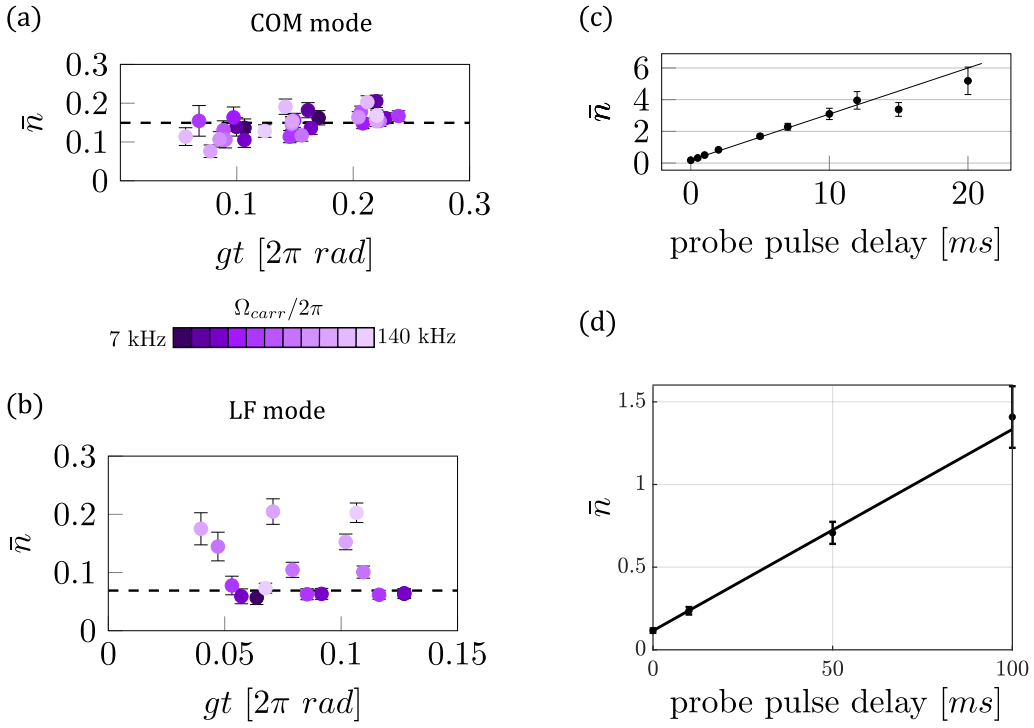

Figure 5.16: (a,b) Sideband thermometry for varying carrier Rabi frequencies (indicated by color) and interrogation times of the (a) COM and (b) the lowest-frequency mode. The mean values are indicated by dashed lines. The dependency of $\bar{n}$ on the carrier Rabi frequency is attributed to the unwanted excitation of neighboring modes (see *Crosstalk* in main text). Therefore, in the calculation of the mean value for the lowest-frequency mode in (b), we exclude all data points that are lying outside a range of 1σ from the mean value obtained from all data points. This affects five data points with the highest values of $\bar{n}$, corresponding to measurements at high Rabi frequency. The error bars of individual thermometry measurements are obtained from Eq. (5.30). (c) Heating rate measurement of the COM mode. The mean phonon number is measured as a function of the probe pulse delay. The solid line shows a weighted linear fit used to determine $\dot{\bar{n}}$. (d) Same as (c), but after the modification of the dc filter boards, resulting in a substantial reduction of the heating rate.

yielding 0.60(5) phonons/s (Sec. 4.6).

Crosstalk with neighboring modes

When using probe pulses at high laser intensities to measure the red and blue sideband excitation probabilities, unwanted excitation (*crosstalk*) of the neighboring modes can affect the mean phonon number estimate. This effect is evident in Fig. 5.16(b), where systematically higher mean phonon numbers are observed at increased Rabi frequencies. In the 19-ion out-of-plane spectrum, the neighboring modes of the COM mode as well as the lowest-frequency mode are separated by less than 30 kHz. Zooming into the excitation of individual ions in this data set, we can relate the bias at high laser intensities to a spurious excitation of neighboring modes. Figure 5.17 shows the red and blue sideband excitation of the individual ions in the 19-ion crystal as well as the global excitation probabilities for different carrier Rabi frequencies used in the thermometry measurement. In this subset of data, the blue sideband excitation was kept approximately constant at $P_b \approx 0.6$ by choosing the probe pulse length accordingly in the experiments. At higher Rabi frequencies, an increase in the red sideband excitation probability can be observed for ions that otherwise do not contribute at lower laser intensity. As an effect, the global excitation probability P_r increases. The modified excitation probabilities lead to an increased sideband ratio and, consequently, an overestimation of the mean phonon number. The structure of the LF mode and the adjacent mode in the frequency spectrum are illustrated in Fig. 5.13(c). However, bearing this effect in mind, it is relatively straightforward in experiments to avoid a bias from such crosstalk by measuring at a low Rabi frequency.

Statistical bias

Due to the finite sampling of the red and blue sideband excitations, a bias (Eq. (5.29)) and error (Eq. (5.30)) emerge in the estimate of the mean phonon number. For the 19-ion crystal, we analyze the statistical bias in subsamples of datasets with $\mathcal{N} = 8000$ experiments (4000 experiments on each sideband). The calculated bias (Eq. (5.29)) as well as the measured bias, based on the data set of all 8000 measurements, are both well below the error bar (Eq. (5.30)). In our measurements with a sample size of $\mathcal{N} = 8000$, the calculated bias $\delta\bar{n}/\bar{n}$ is about 10^{-3} (cf Fig. 3(b) in Ref. [182]). Using only subsamples of the full data set results in an expected increase of the bias. However, the ratio between the bias and the error remains well below 1, and for a sample size of $\mathcal{N} = 8000$, it is even below 10^{-2}. Therefore, the effect of the bias in these measurements is minor compared to the error due to finite sampling.

Experimental drift

Moreover, in order to investigate the influence of the sample size on the experimental outcome, we performed thermometry measurements with an 8-ion crystal. Figure 5.18 shows the mean phonon number estimated using the new sideband thermometry technique[15] for two exemplary laser intensity settings as a function of the number of consecutively performed experiments. For both settings, measurements at three different values of the blue

[15]For the 8-ion data, we used a polynomial up to cubic order in $\bar{n}$ (6^{th} order in gt) for the estimation - in contrast to 4^{th} order for the 19-ion data.

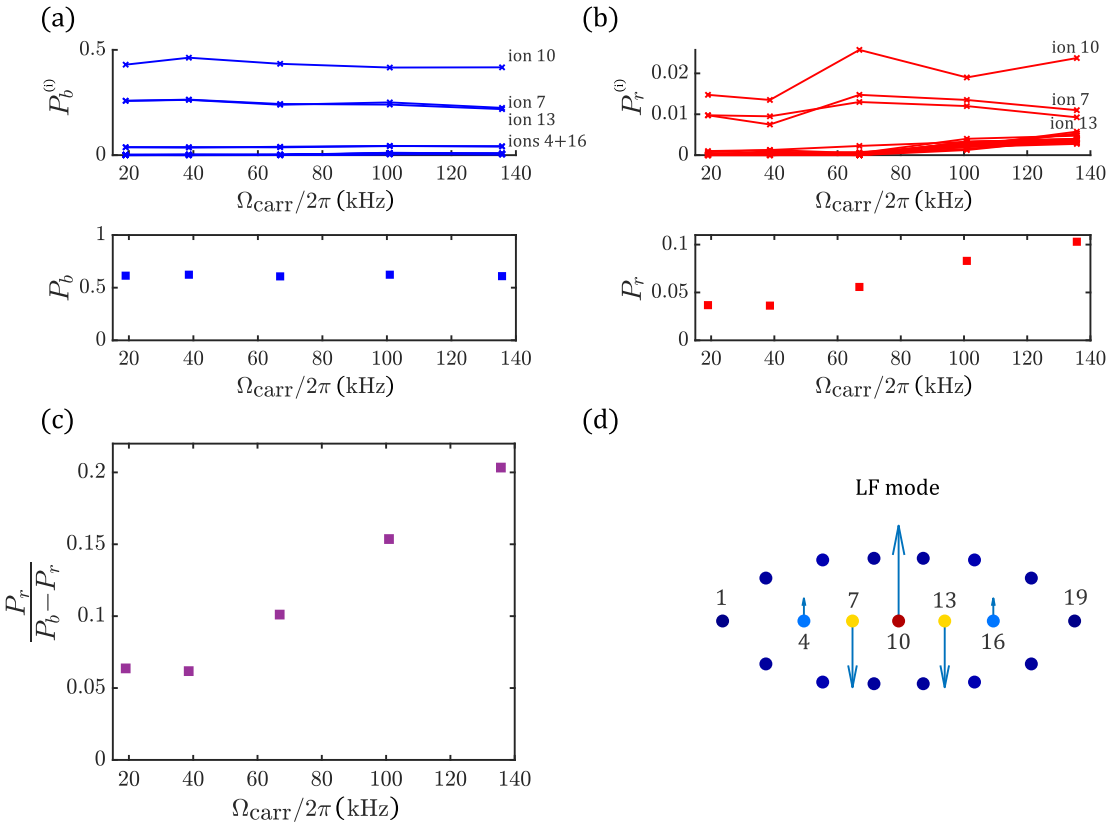

Figure 5.17: Analysis of power-dependent crosstalk with neighboring modes of the LF mode. (a) Single-ion (top) and global (bottom) excitation probabilities on the blue sideband of the lowest-frequency mode. The global blue sideband excitation probability is kept around $P_b = 0.6$ across varying laser intensities. (b) Red sideband excitations analogous to those shown in (a). (c) Sideband ratio. Parasitic red sideband excitations on the neighboring modes leads to an increase in the measured sideband ratio (5.13), resulting in an overestimation of the mean phonon number (cf. Fig. 5.16(b)). (d) Simulated mode structure of the investigated LF mode in the out-of-plane spectrum. The lengths of the arrows scale with the Lamb-Dicke factors. The overestimation of $\bar{n}$ at higher carrier Rabi frequency can be attributed to crosstalk with other motional modes with higher oscillation frequencies. As a result, the excitation pattern in (b) does not purely match the LF mode's pattern of motion.

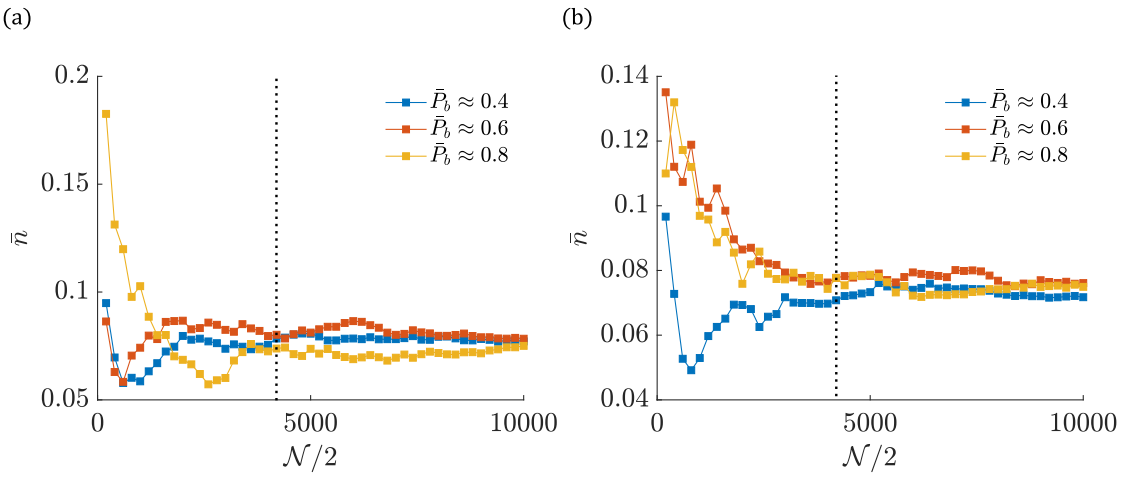

Figure 5.18: Sideband thermometry of the COM mode of an 8-ion crystal with a carrier Rabi frequency of (a) $\Omega_{\text{carr}} = 2\pi \times 18$ kHz and (b) $\Omega_{\text{carr}} = 2\pi \times 86$ kHz. The data is presented as a function of the number of experimental repetitions $\mathcal{N}/2$ on each sideband. While the bias and variance due to finite sampling are reduced with an increasing number of measurements, the measurements are limited by instabilities in the experimental setup due to thermal drifts. The dashed line indicates $\mathcal{N}/2 = 4000$ repetitions, which is the minimum number of experiments used in subsequent measurements. The indicated color corresponds to the approximate value of the blue sideband excitation probability P_b, which is determined by the interrogation time in the experiments.

sideband excitation probability ($P_b \approx \{0.4, 0.6, 0.8\}$) were carried out. Following initial oscillations, the curves converge towards values that drift as a result of instabilities in the experimental setup at that time. The main contribution to these drifts is suspected to stem from temperature variations in the lab that lead to fluctuations in rf power and, consequently, in the motional mode frequencies. Based on these measurements, we chose $\mathcal{N}/2 > 4000$ experiments each on the red and the blue sideband for all subsequent measurements with the 19-ion crystal. $\mathcal{N} = 4000$ is well within the plateau of the measurement outcome, limited by the instability of the motional mode frequencies rather than statistical shortcomings due to finite sampling. Note that these measurements were conducted at the IQOQI prior to relocating the experiment to a new laboratory at the University of Innsbruck. The new laboratory, equipped with an improved air conditioning system, as well as a number of improvements in the setup lead to an enhanced stability of the entire apparatus.

5.10 Summary and discussion

In the first part of this chapter, EIT cooling of the out-of-plane modes of ion crystals with up to 105 ions near the ground-state was presented as a prerequisite for future quantum simulation experiments. In addition to the stability of the trapped ion crystals discussed in Chapter 4, precise knowledge and control of the out-of-plane motional modes

is crucial for mediating entangling interactions. The presented results prove that a large number of modes, spanning a frequency range of several hundreds of kHz, can be efficiently cooled close to the ground-state. At the time of the publication of Ref. [60], the ground-state cooling of complete motional mode spectra (here, in the OOP direction) of crystals with about 100 ions was about an order of magnitude more than in other experiments with 2d crystals in rf traps and about a two-fold increase compared to experiments with linear strings. It was also the first experiment showing sideband-resolved spectra of such number of cold trapped ions. However, the engineered spin-spin interactions could still be impaired by hot in-plane modes, resulting in mode-mode couplings and an effective energy transfer from in-plane modes to the out-of-plane modes. This could lead to decoherence and adversely affect quantum simulation experiments. In turn, PG cooling of all in-plane modes can be integrated straightforwardly into the setup to mitigate these processes. So far, this has not been necessary in the new 2d crystals setup but was demonstrated with a 22-ion zig-zag crystal in another setup.

In order to characterize the motional state of larger ion crystals, a sideband thermometry method for ion crystals was presented as a generalization of the well-established single-ion sideband thermometry, taking many-body interactions in the system dynamics into account. The truncated power-series expansion in t of the evolution of the quantum many-body system yields accurate results for probe pulse times that provide a sufficient signal in experiments. In Ref. [182], the tolerable interrogation time is shown to be independent of the number of ions for $N = 4 \dots 12$. It may be reasonable to infer that this is also valid for larger ion crystals, as the derivation makes no assumptions on the number of ions. The new method enriches the toolbox for characterization measurements in quantum metrology, quantum information processing and quantum simulation. From an experimental point of view, it is easy to implement, although precise knowledge of the investigated modes as a prerequisite necessitates accurate simulations or single-ion addressed measurements. Parasitic crosstalk with neighboring modes is a problem that can be avoided easily by measuring at low laser powers. The statistical bias proves to be a minor problem, even for a relatively small number of measurements. In the presented results, the accuracy was limited by thermal drifts in the setup rather than by the theoretical error and bias from finite sampling.

Concerning the method's wider applicability, a current constraint is its limitation to canonical thermal states of motion. This assumption does not hold for all cooling techniques, in particular for sideband cooling or short cooling pulses [160, 183]. However, a noncanonical parametrization of the occupation probability and a systematic derivation of the corresponding estimators is, in principle, feasible. Additionally, one could extend the approach to correlated spin states to enhance the metrological accuracy, or use a bichromatic drive and consider many-body interactions to gain from measurements with multiple ions.

Chapter 6

Coherent control via stimulated Raman transitions

This chapter's purpose is to provide an overview of the characteristics and dynamics of the stimulated Raman transition used to implement entangling interactions in the presented apparatus. At the time of writing this thesis, the work on the optical setup as well as the characterization of the Raman interaction was still ongoing and, therefore, the number of measurements presented here is limited. A more comprehensive characterization will be part of future PhD theses and publications. In the following, after a brief review of the laser-ion interaction and the most relevant characteristics are discussed. The last section presents first experiments with a bichromatic field, demonstrating the build-up of quantum correlations in a 19-ion crystal during the application of an Ising-type interaction.

6.1 Laser-ion interaction of the stimulated Raman transition

Figure 6.1(a) shows a simple Λ-type level scheme consisting of levels $|1\rangle$ and $|2\rangle$ that are off-resonantly coupled via a third level $|3\rangle$ using two laser fields. In our experiments, we use a Raman transition to couple the two Zeeman states of the ground-state qubit. The wavelength of the Raman beams lies between the transition wavelengths of the dipole transitions to the $4P_{1/2}$ (397 nm) and the $4P_{3/2}$ (393 nm) state. We choose the wavelengths and polarizations of the two beams such that two-photon resonance is achieved with a combination of a σ^+-polarized and a π-polarized laser field. Figure 6.1(b) shows the relevant levels in $^{40}Ca^+$. Details on the optical setup are presented in Sec. 3.6.7. Section 6.2 provides more insights on the choice of the wavelength and polarizations, considering ac-Stark shifts.

Multilevel system interacting with off-resonant laser-field

For the treatment of the laser-ion interaction, let us first assume a simple Λ-type level scheme, as given in Fig. 6.1(a). In order to describe the interaction between the two off-

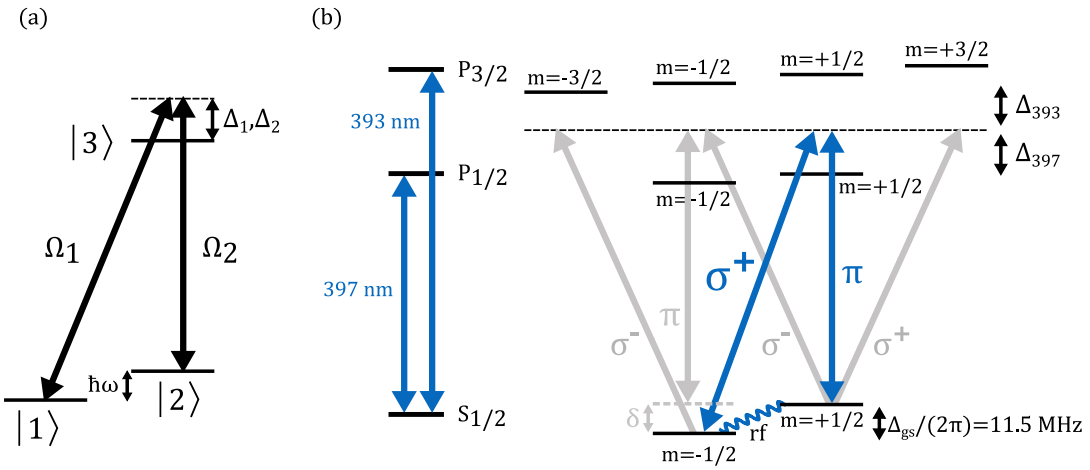

Figure 6.1: Level schemes relevant for stimulated Raman transitions used in this work. (a) Simplified Λ-type three-level scheme. (b) Involved sublevels and transitions in the $^{40}Ca^{+}$ ion. The $3D_{5/2}$ and $3D_{3/2}$ levels are not shown.

resonant Raman beams and an ion, we start from a Hamiltonian in the interaction picture considering the three levels and both laser beams

$$H_{\mathrm{I}} = \frac{\hbar}{2}\Omega_1 \left|3\right\rangle \left\langle 1\right| e^{-i\Delta_1 t} + \frac{\hbar}{2}\Omega_2 \left|3\right\rangle \left\langle 2\right| e^{-i\Delta_2 t} + h.c. \tag{6.1}$$

The Raman interaction is usually treated in an adiabatic elimination of the excited state level ($|3\rangle$), as done in Refs. [58, 190] and references therein, which yields an accurate description if the detuning from the third level is large. Another approach without adiabatic elimination is pursued in Ref. [191], leading to more accurate results for small detunings. Yet another convenient recipe is provided in Ref. [192] for deriving an effective Hamiltonian for the time-averaged dynamics of a detuned quantum system, which in the case of a Raman process, arrives at

$$\begin{aligned} H_{\mathrm{eff}} = &-\frac{\hbar\Omega_1^2}{4\Delta_1}\left(\left|3\right\rangle\left\langle 3\right| - \left|1\right\rangle\left\langle 1\right|\right) - \frac{\hbar\Omega_2^2}{4\Delta_2}\left(\left|3\right\rangle\left\langle 3\right| - \left|2\right\rangle\left\langle 2\right|\right) \\ &+ \frac{\hbar\Omega_1\Omega_2}{4\overline{\Delta}}\left(\left|1\right\rangle\left\langle 2\right| e^{i(\Delta_1-\Delta_2)t} - \left|2\right\rangle\left\langle 1\right| e^{-i(\Delta_1-\Delta_2)t}\right), \end{aligned} \tag{6.2}$$

where $\overline{\Delta} = \frac{\Delta_1\Delta_2}{\Delta_1+\Delta_2}$. The first two terms in this Hamiltonian can be associated with ac-Stark shifts that are induced by the two light fields. The third term describes coherent oscillations between the states $|1\rangle = |\downarrow\rangle$ and $|2\rangle = |\uparrow\rangle$ despite the absence of a direct interaction. Looking exclusively at the third term that represents the dynamics involving only the two qubit states $|1\rangle$ and $|2\rangle$, where $|1\rangle\langle 2| = \sigma^-$ and $|2\rangle\langle 1| = \sigma^+$, we can identify this term as an effective coherent Rabi oscillation between these states. This oscillation is described by Eq. (2.86), but with the Rabi frequency Ω being replaced by the effective Rabi frequency

$$\Omega_{\mathrm{eff}} \equiv \frac{\Omega_1\Omega_2}{2\overline{\Delta}}. \tag{6.3}$$

Using the effective Hamiltonian (6.2), the same formalisms as discussed in Secs. 2.5.2ff. can be applied to derive analogous expressions for spin-motion coupled interactions as well as entangling interactions via bichromatic light fields. In the case of the stimulated Raman transition, the phase of the light field ϕ_{L} used in Sec. 2.5 is replaced by the phase difference $\phi_1 - \phi_2$ between the two laser fields. In the presented experiments, we use a configuration with two counterpropagating Raman beams that are perpendicular to each other, with the difference wave vector $\mathbf{\Delta k} = \mathbf{k_2} - \mathbf{k_1}$ being aligned with the out-of-plane direction (x) of the crystal plane (see Fig. 6.2). For balanced intensities of the two Raman beams, with $|\mathbf{k_1}| = |\mathbf{k_2}| = k$, the coupling to the motional modes is enhanced by a factor of $\sqrt{2}$ as $|\Delta \mathbf{k}| = \sqrt{2}k$ compared to a single light field with k directly coupling to the out-of-plane modes.

Note that the given expressions are valid for an ideal three-level system, ignoring any coupling to additional electronic levels. A more general description would go beyond the scope of this thesis. However, for the treatment of the spontaneous scattering rate as well as the Raman Rabi frequency, both the $\mathrm{P}_{1/2}$ and the $\mathrm{P}_{3/2}$ levels are considered. A more general expression for the resonant two-photon Rabi frequency, taking other electronic levels and polarizations into account, is given by [193]

$$\Omega_{\mathrm{Raman}} = \frac{1}{2\hbar^2} \sum_k \sum_p \frac{\langle\uparrow| \mathbf{d_E} E_1 \hat{\mathbf{e}}_{\mathbf{1},\mathbf{p}} |k\rangle \langle k| \mathbf{d_E} E_2 \hat{\mathbf{e}}_{\mathbf{2},\mathbf{p}} |\downarrow\rangle}{\Delta_k} , \tag{6.4}$$

where the index k denotes the relevant electronic transitions, the index $p \in \pi, \sigma^+, \sigma^-$ accounts for all polarization components of the Raman laser beams, $\mathbf{d_e}$ denotes the electronic dipole moment, and $\hat{\mathbf{e}}_{\{\mathbf{1},\mathbf{2}\},\mathbf{p}}$ the polarization unit vectors of the electric fields with the amplitudes $E_{\{1,2\}}$.

6.2 Differential ac-Stark shift

A single off-resonant laser beam interacting with a two-level system results in a Stark shift of the transition frequency of

$$\delta_{\mathrm{ac}} \simeq \frac{\Omega^2}{2\Delta}. \tag{6.5}$$

In view of the stimulated Raman transition between the two $\mathrm{S}_{1/2}$ levels, the ac-Stark shifts of the two ground-state levels $|\downarrow\rangle = |\mathrm{S}_{1/2}, m = -1/2\rangle$ and $|\uparrow\rangle = |\mathrm{S}_{1/2}, m = +1/2\rangle$ have to be considered. In the presence of laser intensity fluctuations, power-dependent variations in the frequency shifts of the two states lead to decoherence and thus needs to be mitigated. For perfectly linearly polarized light, the differential Stark shifts of the qubit levels is zero ($\delta_{\mathrm{ac}}^{\downarrow} = \delta_{\mathrm{ac}}^{\uparrow}$), whereas any non-zero differential Stark shift ($\delta_{\mathrm{ac}}^{\downarrow} \neq \delta_{\mathrm{ac}}^{\uparrow}$) requires elliptical polarizations.

For two Raman beams interacting with a multi-level system, one has to consider the ac-Stark shifts from off-resonant coupling to all relevant transitions. Here, the levels of the $\mathrm{P}_{1/2}$ and the $\mathrm{P}_{3/2}$ manifold are taken into account. Relative to these levels, the coupling

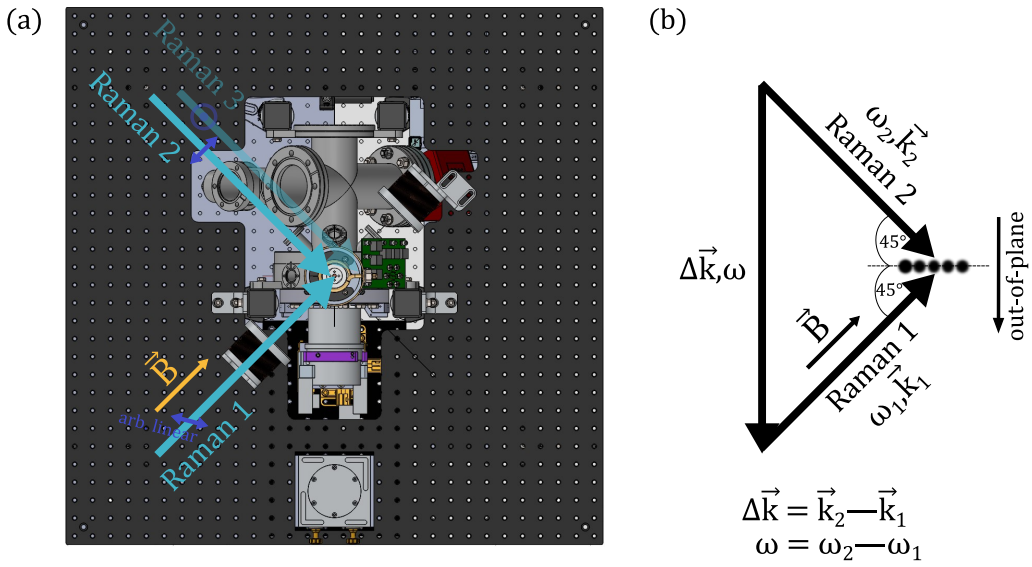

Figure 6.2: Beam and magnetic-field geometry for the stimulated Raman transition. (a) Geometry at the vacuum chamber (cf. Fig. 3.15). The Raman 3 beam was part of the initial setup but has since been removed. (b) Geometry of the Raman k-vectors with respect to the B-field and the ion plane.

to the $D_{5/2}$ and $D_{3/2}$ levels is small. However, in order to cancel the differential Stark shift on the $S_{1/2} \leftrightarrow D_{5/2}$ clock transition, the magic wavelength of 395.799 nm is used to drive the Raman transition [139, 140]. The light shifts for the two ground state levels are given by the sum over all dipole-allowed transitions considering all polarization components ($\sigma^{\pm}$ for Raman beam 1 and π for Raman beam 2)

$$\begin{aligned}
\delta_{\mathrm{ac}}^{\downarrow} &= \sum_{\substack{P_{3/2} \\ k}} \frac{\Omega^2_{|\downarrow\rangle \leftrightarrow k}}{2\Delta_k} + \sum_{\substack{P_{1/2} \\ l}} \frac{\Omega^2_{|\downarrow\rangle \leftrightarrow l}}{2\Delta_l} \\
&\quad \text{for } k \in \left\{ m = -\frac{3}{2}, m = -\frac{1}{2}, m = +\frac{1}{2} \right\} \text{ and } l \in \left\{ m = -\frac{1}{2}, m = +\frac{1}{2} \right\}, \\
\delta_{\mathrm{ac}}^{\uparrow} &= \sum_{\substack{P_{3/2} \\ k}} \frac{\Omega^2_{|\uparrow\rangle \leftrightarrow k}}{2\Delta_k} + \sum_{\substack{P_{1/2} \\ l}} \frac{\Omega^2_{|\uparrow\rangle \leftrightarrow l}}{2\Delta_l} \\
&\quad \text{for } k \in \left\{ m = -\frac{1}{2}, m = +\frac{1}{2}, m = +\frac{3}{2} \right\} \text{ and } l \in \left\{ m = -\frac{1}{2}, m = +\frac{1}{2} \right\}.
\end{aligned} \tag{6.6}$$

For perfectly linearly polarized light, the differential Stark shifts of the qubit levels is zero ($\delta_{\mathrm{ac}}^{\downarrow} = \delta_{\mathrm{ac}}^{\uparrow}$), whereas any non-zero differential Stark shift ($\delta_{\mathrm{ac}}^{\downarrow} \neq \delta_{\mathrm{ac}}^{\uparrow}$) requires elliptical polarizations. We now assume driving a stimulated Raman transition using a σ^+-polarized and a π-polarized beam, coupling the two $S_{1/2}$-ground states via the $|P_{1/2}, , = +1/2\rangle$ state as shown in Fig. 6.1 (b). Considering the $P_{1/2}$ manifold, the σ^+-beam would induce a light shift on the $|S_{1/2}, m_s = -1/2\rangle$ state but not on the $|S_{1/2}, m_s = +1/2\rangle$ state. This

imbalance can be lifted by using linearly polarized light to drive both the σ^+- and σ^--transition equally. This way, the differential Stark shift cancels. The beam geometry for doing so is shown in Fig. 6.2(a). The Raman 1 beam is linearly polarized and propagating parallel to the magnetic-field axis, driving both σ-components at the same time. In this configuration the orientation of the polarization vector can, in principle, be arbitrary within the plane perpendicular to the magnetic field[1].

Another effect causing a non-zero differential shift in our setup, is the off-resonant two-photon coupling of the two qubit states originating from the paths that involve the σ^--component of the Raman 1 beam. There is an off-resonant coupling with a positive detuning with respect to the $|m = -1/2\rangle$ state (shown in Fig. 6.1(b)) and an off-resonant coupling with a negative detuning with respect to the $|m = +1/2\rangle$ state (not shown). Both cases involve σ^--polarized light, resulting in unequal light shifts for the two states (on the order of 500 Hz at a Raman Rabi frequency of $\Omega \approx 2\pi \times 200$ kHz). This can be counteracted by a slight power imbalance of the two bichromatic components of the entangling interaction beams. In the presented experiments, we used a ratio of $\Omega_r/\Omega_b \approx 0.9$ between the red- and the blue-detuned components.

6.2.1 Measurement and minimization of ac-Stark shifts

The ac-Stark shift can be measured in a Ramsey-type experiment: The ion is first prepared in a superposition of one of the two $S_{1/2}$ sublevels by a $\pi/2$-pulse using the rf coil[2]. During the Ramsey wait time, one of the Raman beams is applied to the ion for a variable time τ_R. A second $\pi/2$-pulse at the end of the sequence concludes the Ramsey experiment. Repeating this experiment for varying Raman pulse lengths τ_R leads to oscillating Ramsey fringes, the frequency of which reveals the light shift induced by the detuned Raman beam. The measured signal is proportional to $\sin(\Delta_S \cdot t + \phi)$, where Δ_S is the ac-Stark shift. In order to determine the differential light shift, the measurement is performed once for the $|m = -1/2\rangle$ and once for the $|m = +1/2\rangle$ ground state. This scheme is also used to minimize the differential light shifts between ions in a crystal caused by the individual Raman beams.

6.3 Homogeneity of coupling

A homogeneous laser beam profile is crucial to ensure an equal coupling to the individual ions in a crystal and maintain coherence between the ions during interactions. In the current setup, we achieve a maximum variation of the Raman Rabi frequency of 15 % across a large 91-ion crystal[3]. During the time of this PhD work, the Raman laser setup was subject to frequent changes to optimize the coupling strength and reduce spatially varying ac-Stark shifts across the ion crystal. In the presented experiment, such ac-Stark

[1] The Raman 1 beam is entering the front viewport at 45°. Due to polarization-dependent transmission losses of the focused laser beam (the wave front is not perfectly planar), it can be beneficial to choose a certain orientation to minimize the inhomogeneity in the laser intensity.

[2] For this Ramsey experiment, also the $S_{1/2} \leftrightarrow D_{5/2}$ quadrupole transition, coupled via the 729-nm laser, could be used.

[3] The Rabi frequency of the outer ions is about 85 % of that of the innermost ions.

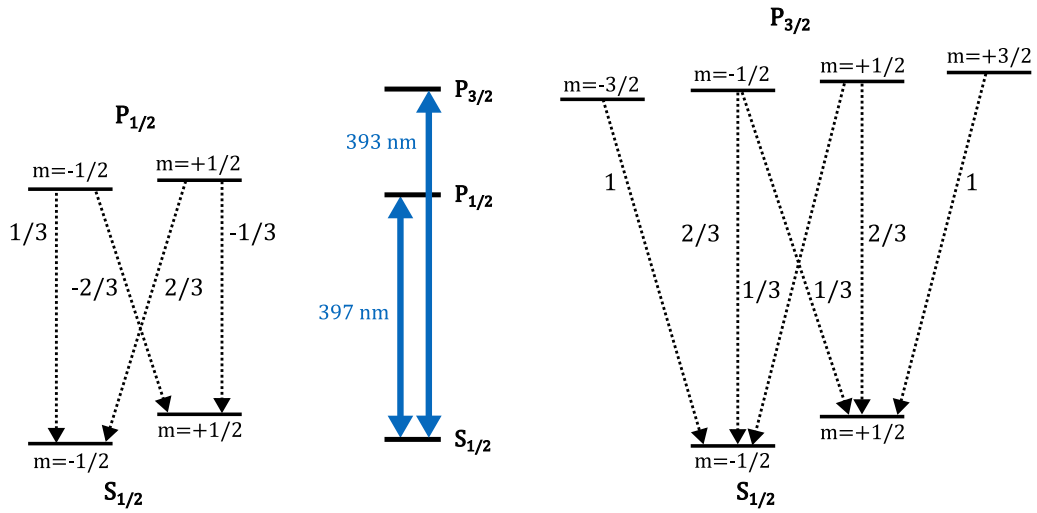

Figure 6.3: Zeeman sublevels of the $S_{1/2} \leftrightarrow P_{1/2}$ and $S_{1/2} \leftrightarrow P_{3/2}$ transitions with squared Clebsch-Gordan coefficients.

shifts are suspected to be caused by polarization-dependent losses at the surface of the vacuum chamber's front window, where the Raman 1 beam enters at 45°. At the window, the beam is not perfectly collimated, as it is focused onto the ion plane. It therefore exhibits spatially varying polarization components across the beam profile, which can translate to a spatially varying profile at the ions, causing some ions to decohere faster than others. Another potential cause for varying Stark shifts are back reflections of the beams creating interference patterns across the crystal plane. Although this effect cannot be excluded, in the geometry of the presented apparatus, this is regarded as unlikely due to the absence of (near)-parallel surfaces along the beam paths.

6.4 Spontaneous scattering

A finite detuning Δ causes spontaneous decay from the auxiliary level $|3\rangle$. The involvement of additional states may lead to further non-negligible scattering. This results in decoherence during laser-ion interactions, thereby introducing errors in quantum gates [194], which may pose a limitation to spin-spin interactions in future quantum simulation experiments.

In an off-resonantly driven two-level system, the photon scattering rate is given by

$$R = \Gamma \frac{\Omega^2}{2\Delta^2}, \tag{6.7}$$

where Γ is the natural decay rate (equivalent to the Einstein A coefficient), the detuning is $\Delta_1 = \Delta_2 = \Delta$, and $\Omega \ll \Delta$. In essence, this expression corresponds to the natural decay rate times the steady-state probability of finding the ion in the upper state. In the presented experiments with $^{40}Ca^+$ ions, we use the "magic wavelength" of 395.799 nm, which lies between the transition wavelengths of the $P_{1/2}$ and $P_{3/2}$ levels. Therefore, we consider the coupling to and the decay from the Zeeman sublevels of these states (see

Fig. 6.3). The total spontaneous scattering rate for the stimulated Raman transition can be calculated as the sum of the scattering rates from all relevant transitions [193]

$$R = \sum_i \Gamma_i P_i = \sum_{\substack{\alpha \\ 393,397}} \sum_{\substack{\beta \\ R1,R2}} \sum_{\substack{\gamma \\ l_1 \to l_2 \\ m_1 \to m_2}} \Gamma_\alpha \frac{P_{gs,\gamma} |\langle l_1, m_1 | \, \mathbf{d_E} E_{0,\beta} \hat{\mathbf{e}}_{\beta,\gamma} \, | l_2, m_2 \rangle|^2}{2\Delta^2_{\alpha,\beta}} \tag{6.8}$$

where $E_{0,\beta}$ are the peak electric fields of the Raman beams R1 and R2 and $P_{gs,\gamma}$ is the population in the respective level in the ground-state manifold with quantum number m_1 (l_1 is 0). In this expression, the coupling to the $D_{5/2}$ and $D_{3/2}$ state and the decay from them is neglected as the detuning from these states is large. The decay channels $P_{3/2} \to D_{5/2}$ with a branching ratio of 5.9% [195], $P_{3/2} \to D_{3/2}$ with a branching ratio of 0.7% [195], and $P_{1/2} \to D_{3/2}$ with branching ratio of 6.4% [196] are not taken into account. In practice, differences in the detuning due to the Zeeman splitting of 11.5 MHz can be neglected as it is small compared to the detuning from the P levels on the order of 10^6 THz ($\sim$ 2 nm). The calculation of Rabi frequencies, spontaneous scattering rates and decoherence rates of hyperfine qubits in various species can be found in Refs. [193, 194].

6.4.1 Measurement of the spontaneous decay rate

The spontaneous decay rate is measured separately for the π-beam and the σ-beam. In this measurement, the qubits are initially prepared in either the $|S_{1/2}, m = -1/2\rangle$ or the $|S_{1/2}, m = +1/2\rangle$ state. Then, one of the two Raman beams (σ or π) is turned on for a variable time. Finally, the population in the initial state is transferred to the $D_{5/2}$ state by a π-pulse prior to the readout of the $S_{1/2}$ population. The residual population in the $S_{1/2}$ state stems solely from the spontaneous decay from the P-levels, as there is only one Raman laser beam applied (no stimulated Raman transition). This measurement is carried out for both the σ- and the π-beam, and for each beam once after preparing the ions in the $|S_{1/2}, m = -1/2\rangle$ state and again after peparing them in the $|S_{1/2}, m = +1/2\rangle$ state. The population in the respective $S_{1/2}$ state as a function of the Raman pulse length is fitted by an exponential function $p_d(t) = 0.5(1 \pm e^{-\alpha t})$, approaching 0.5 in the equilibrium. The decay coefficient α measures the rate, at which population is exchanged between the two qubit states[4]. The neglection of decays from the P states to the D states affects only the steady-state population ($t \to \infty$) measured in the experiment and is a negligible offset from 0.5.

We measured scattering rates individually for the two beams and the two ground states, yielding a total scattering rate of approximately 20 s^{-1} per ion for a Raman Rabi frequency of $\Omega \approx 2\pi \times 200$ kHz. Further measurements involving randomized benchmarking of resonant single-ion gates suggest a slower decoherence than expected purely from the measured scattering rate. Investigations are ongoing and updates can be expected in future theses and publications.

[4]The rate equation for the two states is given by $\dot{\rho}_1 = \Gamma_{21}\rho_2 - \Gamma_{12}\rho_1$ and is solved by an exponential decay approaching $\Gamma_{12}/(\Gamma_{12} + \Gamma_{21})$.

6.5 Decoherence rate

Ramsey experiments with a variable waiting time between the two $R_x(\pi/2)$ pulses were performed to determine the coherence time of the Zeeman qubit using the rf coil as well as the Raman beams. Along with coherence measurements of the optical qubit, these measurements are presented in Sec. 4.7. They mainly account for dephasing of the Zeeman qubit due to magnetic-field fluctuations as well as interferometric phase instabilities between the Raman beams. To capture decoherence effects arising from spontaneous scattering and thermal occupation of motional modes, the decoherence rate was determined by applying an Ising-type XX interaction (using a bichromatic laser field, see Sec. 6.6) between the two Ramsey pulses and measuring the contrast decay as a function of the interaction pulse length, rather than the pure waiting time. Since the XX interaction is applied to its eigenstate, it decouples the state from the decoherence caused by magnetic and interferometric noise. We used Ising interaction pulse lengths ranging from 50 μs to 20 ms, with a sideband detuning of $\Delta_{\mathrm{sb}}/(2\pi) = 80$ kHz and no centerline detuning ($\delta = 0$). The phase of the second pulse was scanned to obtain Ramsey fringes, which were fitted by a sinusoidal function to determine the Ramsey contrast. The contrast decay for increasing interaction time was then fitted with a Gaussian function, yielding the decoherence rate γ_{dec}. The measurement was done with a 19-ion crystal with an out-of-plane COM mode frequency of $\omega_x = 2\pi \times 2.2225$ MHz. The carrier Rabi frequencies for the red and blue bichromatic components of the interaction were $\Omega_r/(2\pi) = 89.97$ kHz and $\Omega_b/(2\pi) = 99.35$ kHz, respectively.[5] The resulting decoherence rate is $\gamma_{\mathrm{dec}} = 17.8\ \mathrm{s}^{-1}$.

6.6 Bichromatic interaction

As introduced in Sec. 2.5.5 and Sec. 2.5.6, an Ising-type interaction can be realized using a bichromatic light field. Here, this is implemented by combining the red- and blue-detuned rf signals from two separate AWGs (Sinara Phasers), yielding the two-tone signal to drive the AOM for the σ-beam. Together with the π-beam, the Raman interaction couples the red and the blue motional sidebands simultaneously. With a sideband detuning of $\Delta_{\mathrm{sb}} = 80$ kHz, no centerline detuning and a carrier Rabi frequency of $\Omega_{\mathrm{carr}} \approx 123$ kHz, the ion-ion coupling constant is $J_0 \approx 2\pi \times 200$ Hz for an approximate power-law decay of the form $J_{ij} \simeq J_0/|i-j|^{\alpha}$. The exponent α, defining the tunable range of the interactions, is approximately 1 for these parameters. However, note that J_{ij} does not follow a pure power-law, in particular for larger ion-ion distances. Similar parameters have been used, for example, for spin-squeezing measurements presented in Ref. [61] and for further measurements that will be presented in an upcoming publication. For a sideband detuning of $\Delta_{\mathrm{sb}} = 320$ kHz and a carrier Rabi frequency of approximately $2\pi \times 245$ kHz, we find $\alpha \approx 2$ and $J_0 \approx 2\pi \times 130$ Hz. The current maximum achievable carrier Rabi frequency is about $2\pi \times 500$ kHz.

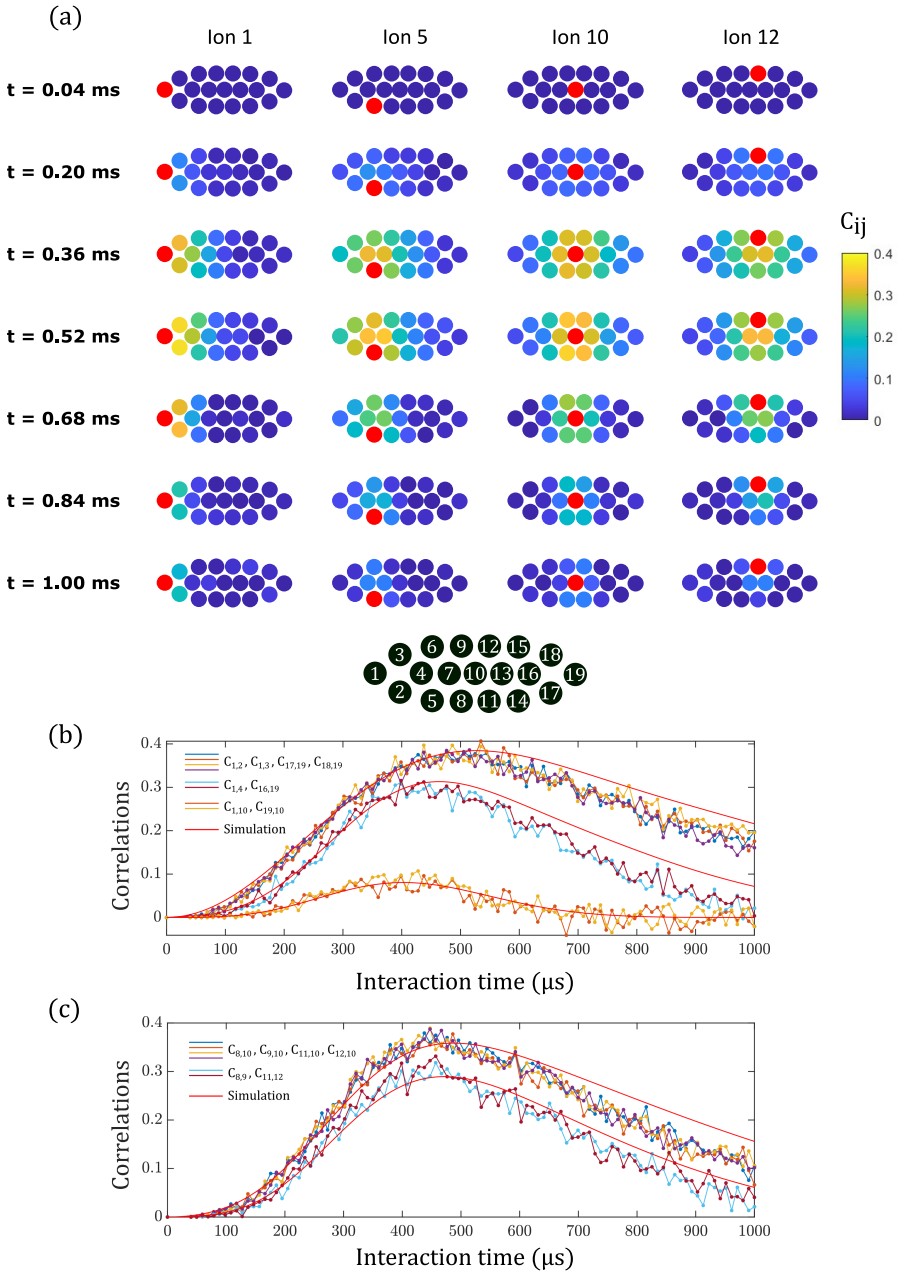

Figure 6.4: Build-up of correlations in a 2d 19-ion crystal interacting with an off-resonant bichromatic Raman laser field, creating Ising-type interactions. The ion numbering is shown in the center of the figure (black crystal). (a) Snapshots during the evolution illustrate the correlation coefficients $C_{ij}(t_k)$ at specific times for ions $i = \{1, 5, 10, 12\}$ marked in red. (b,c) Measured correlation coefficients for representative ion pairs as a function of the interaction time reveal a good agreement with numerical simulations (solid red lines) until decoherence effects impair the measurements at longer interaction times.

6.6.1 Build-up of quantum correlations under the Ising interaction

In the experiments presented in the following, we used a bichromatic light field with a sideband detuning from the COM mode of $\Delta_{\mathrm{sb}}/(2\pi) = 80$ kHz. The carrier Raman Rabi frequency was $\Omega/(2\pi) \approx 195.1$ kHz. The centerline detuning δ was 0, realizing a pure Ising model with interactions of the form $\propto \sigma_x^{(i)}\sigma_x^{(j)}$ without a transverse B-field term (cf. Eq. (2.110)). As the first experimental implementation of such an interaction in the presented apparatus, we apply it to a planar 19-ion crystal[6] and observe the build-up of correlations during the time evolution of up to 1 ms. Similar experiments have, for example, been carried out in Ref. [197]. In our experiments, the sequence consists of a resonant $\pi/2$-pulse about the x-axis ($R_x(\frac{\pi}{2})$), creating an equal superposition of $|\uparrow\rangle$ and $|\downarrow\rangle$, followed by the bichromatic Raman interaction pulse of variable length, which induces the coherent evolution of the Ising-Hamiltonian. Subsequently, a $R_y(\frac{\pi}{2})$ pulse is applied before the state is detected in the energy eigenbasis (z) to measure the spin-spin correlations in the x-basis. The correlations between all pairs of ions are then calculated as

$$C_{ij}(t) = \langle \sigma_i^x(t)\sigma_j^x(t)\rangle - \langle \sigma_i^x(t)\rangle\langle \sigma_j^x(t)\rangle. \tag{6.9}$$

The correlation coefficients C_{ij} of a few exemplary ions i are illustrated in Fig. 6.4(a). They are presented as snapshots at various time steps during the evolution of the interaction. We observe a clear build-up of correlations, reaching a maximum around 500 μs before decreasing again. We also performed simulations of the time evolution of the 19-ion crystal under the Ising Hamiltonian to compare them with the experimental data. The time evolution of correlations between a few selected ion pairs, along with the simulated dynamics, are displayed in Figs. 6.4(b-c), showing a good agreement between the measurements and simulations. The discrepancy at longer evolution times most likely originates from motional decoherence, which was still dominated by a noisy dc filter board at the time of these measurements.

6.7 Discussion and outlook

This chapter provided an overview of basic characteristics of stimulated Raman interactions in our setup and presented first measurements using a bichromatic interaction. These measurements demonstrated entanglement in a planar 19-ion crystal in the form of the build-up of spin-spin correlations under the time evolution of an Ising model. Numerical simulations support our findings and show that the applied interaction is well-defined and provides a suitable basis for establishing greater complexity in future experiments. This work therefore lays the foundation for quantum simulation with 2d ion crystals in the presented apparatus. The first experiments following those presented here, involve the creation of spin-squeezed states by the implementation of the one-axis twisting model (see Sec. 2.5.7). First results of these squeezing measurements are presented in Helene Hainzer's thesis Ref. [61], where spin-squeezed states of a 19-ion crystal are generated. The exper-

[5] They were imbalanced ($r : b \approx 0.9 : 1$) to compensate differential ac-Stark shifts; see Sec. 6.2.

[6] The 19-ion crystal was trapped in a potential characterized by the trap oscillation frequencies $\omega_{\{x,y,z\}} = 2\pi \times \{2222.5, 697.4, 360.2\}$ kHz.

iments are currently continued with larger ion crystals of about 100 ions. A variational approach is used to optimize the squeezing using the Wineland squeezing parameter as a cost function. These measurements will be subject of a forthcoming publication.

By using the ground-state qubit coupled via a stimulated Raman transition, we benefit from an increased coupling strength and coherence time compared to the optical qubit at 729 nm. However, note that between the time of the measurements and the submission of this thesis, the experimental setup has already been subjected to several changes, which led to further improvements. Modifications of the optical setup and beam parameters enhanced the coupling strength and homogeneity. In addition, the change of the dc filter boards (see Sec. 3.4.3) as well as modifications in the electronic setup, after tracking down a major source of magnetic-field noise created by the vacuum pump[7], considerably improved the motional and electronic coherence of the ground-state qubit. First measurements with spin-echo suggest a coherence time of about 950 ms, measured with the rf coil, and about 780 ms measured with the Raman beams. Details on an improved setup and further insights regarding the Raman interactions can be expected in the PhD thesis of Artem Zhdanov.

[7]The magnetic-field noise was caused by the connection between the NEG pump and the vacuum pump controller and could be removed simply by disconnecting the NEG.

Chapter 7

Summary and outlook

Summary and conclusion

This work presented a new ion-trap apparatus targeted at quantum simulation experiments with individually controllable particles in a planar configuarion to study 2d many-body physics intractable for classical computers. Prerequisites for such experiments include deterministic loading and stable trapping of two-dimensional ion crystals as well as maintaining a stable crystal lattice during the measurements. At the same time, one aims at minimizing the ions' micromotion to mitigate adverse effects on the laser-ion interactions. Quantum simulation experiments further require precise knowledge and control of the ions' motional modes as well as the ability to cool the motion close to the ground state. This is crucial, as the engineered entangling interactions are mediated by the ions' motion (here: in out-of-plane direction). These requirements entail a number of technical challenges that have been discussed and overcome in the course of this thesis.

After an overview of the foundations of ion trapping in rf traps as well as an introduction to quantum optics and quantum information with trapped ions in chapter 2, the experimental setup was presented in chapter 3. The novel rf trap design provides micromotion-free optical access in an entire plane, enabling high-fidelity quantum operations and an unobstructed quantum state read-out. The trap design and its geometry was briefly discussed before focusing on other parts of the setup, such as the vacuum apparatus, the trap electronics to control the dc and rf potentials, the experiment control, a new unsupervised-learning scheme for quantum-state readout, the optical setups, and the setup of the rf coil to manipulate the ground-state qubit.

Chapter 4 presented various characterization experiments, which demonstrated excellent control of the ions on a classical and quantum level. Laser ablation loading is combined with precise control of the rf potential depth to remove ions from the crystal. We thereby achieve deterministic loading of single ions and crystals containing up to about one hundred ions within typically less than a minute. Moreover, this work demonstrated that the micromotion modulation index can be reduced to $\beta_i < 0.02$ for all ions in a 105-ion crystal. Such measurements can be used further to ensure the planarity of ion crystals via adjustments of the voltages applied to the dc trap electrodes. In the absence of any cooling,

we achieve a crystal lifetime of several seconds for ion numbers of up to 91 ions - another major result. As crystal lattice configuration changes can compromise any quantum measurement, the stability of the crystal lattice was analyzed by an unsupervised classification of a recorded series of crystal images. The images were assigned to distinct crystal lattice configurations via a clustering algorithm. In this way, we found a finite number of crystal configurations occurring in large crystals of up to 91 ions. This method further allowed for the optimization of the rf potential to obtain stable elongated crystals, which reside in a single symmetric lattice configuration for more than 99 % of the time. These findings are supported by numerical simulations using simulated annealing. Overall, these measurement rule out rf heating as a detrimental cause of melting events or crystal lattice configuration changes in future experiments. Further characterization measurements with a single ion revealed a heating rate of about 0.6 phonons/s, an electronic coherence time of the ground-state qubit of about 130 ms without and 370 ms with a spin-echo pulse as well as a motional coherence time of 105 ms without and 279 ms with spin echo. Note, that these values have already been improved significantly since the experiments for this thesis were concluded (see *Outlook* below). Updated values will be provided in upcoming publications.

Chapter 5 first presented simulations of the motional mode spectrum of planar crystals as well as polarization gradient cooling of 22-ion zig-zag crystals as a first step towards ground-state cooling of planar crystals via a multi-mode cooling technique. Subsequent experiments demonstrated the ground-state cooling of crystals consisting of up to 105 ions via EIT cooling. In order to measure the temperature of individual modes in a 2d crystal, in a collaborative effort [182], a novel generalized sideband thermometry technique was applied to determine the mean phonon number of the COM mode and the lowest-frequency mode in out-of-plane direction of a 2d 19-ion crystal. Heating rate measurements of the COM mode revealed a heating rate of approximately 0.6 phonons/s per ion, which is consistent with single-ion measurements. The mode with the lowest mode frequency in the spectrum showed no significant heating after a waiting time of tens of milliseconds.

Chapter 6 gave an overview of the laser-ion interaction using a stimulated Raman transition to off-resonantly couple the two ground states in the $S_{1/2}$ manifold. The Raman transition will be used to implement entangling gates in future experiments, exploiting the ion-ion coupling due to Coulomb interactions. Besides the presentation of the optical setup and the geometry in our experiments, various aspects including differential ac-Stark shifts and spontaneous scattering were discussed as a starting point for further measurements. The chapter concluded with measurements that demonstrate the build-up of quantum correlations across a 19-ion 2d crystal under the action of a global bichromatic laser field, introducing finite-range spin-spin interactions for the first time in the new apparatus.

The results presented in this thesis are disarming several major challenges arising from working with 2d crystals, including effects induced by micromotion and rf heating, as well as the influence of crystal lattice instabilities. Previously, these aspects were considered risks of unknown severity. In the new apparatus, excellent classical and quantum control of planar ion crystals with up to 105 ions has been achieved, building a robust foundation for future experiments. By cooling 2d crystals of this size near the ground state and

conducting initial experiments with bichromatic spin-spin interactions, further milestones have been reached. Were one to set modesty aside and borrow another popular expression, one might conclude that the results presented in this work pave the way for future studies of quantum many-body physics in two dimensions, beyond the capabilities of classical computers.

Outlook

Despite considering many problems solved, there is still a number of challenges awaiting on the route to full-fledged quantum simulation with 2d crystals. However, as this thesis is being written, many of them are already being addressed by my colleagues Matthias Bock and Artem Zhdanov. Moreover, the PhD thesis of Helene Hainzer [61] may be seen as a complementary work that is covering other topics such as the analysis of anharmonicities in the trapping potential, a more detailed discussion of the quantum-state readout scheme, and a new scheme to probe phase differences in the presence of correlated phase noise based on N-ion correlation spectroscopy (published also in [76]).

The bichromatic interaction schemes, which have been applied for many years in experiments with linear ion crystals, can be transferred to 2d crystals straightforwardly. This was done in the first proof-of-principle experiments with bichromatic interactions presented in chapter 6. The laser system at 396 nm coupling the states of the ground-state qubit via a stimulated Raman transition is currently being optimized. Modified collimators are employed to ensure a homogeneous coupling across the crystals while minimizing the scattering of light at the trap electrodes. Spin squeezing experiments are used to benchmark the entangling interactions using the Wineland squeezing parameter as a figure of merit. In a variational fashion, an additional classical optimization algorithm is used to maximize the spin squeezing by acting on the parameters of the applied laser pulse sequence. These measurements will be part of a publication in the near future. Besides, an electrical connection between the controller and the NEG pump of the combined ion-NEG pump attached to the vacuum vessel, although sharing the same electrical ground, was identified as a major source of decoherence due to magnetic field fluctuations, with a main contribution at 792.66 mHz. By removing the unused cable, the electronic coherence time could be improved to nearly one second with the rf coil and 780 ms with the Raman beams (with spin-echo).

In view of the envisaged experiments, the last missing part in the experiment is the optical setup for manipulation of individual ions with a tightly focused laser beam. This setup was designed by Artem Zhdanov and has already been set up by him and Matthias Bock. It is currently being characterized. Two crossed acousto-optic deflectors (AODs) are used to steer a single narrow-frequency 729-nm laser beam in two dimensions before being focused by the objective to a diffraction-limited spot that interacts with single ions. Two AODs in a 4f-configuration ensure that the laser beam is guided into the objective without clipping as the deflection angle changes. A dichroic mirror allows for the separation of the addressing and the imaging beam. The single-ion addressing setup enables sequential single-qubit rotations as well as the preparation of arbitrary spin states. By shelving ions to the metastable $D_{5/2}$-state, where they are not participating in the entangling interactions induced by the Raman beams at 395 nm, the crystal lattice can be structured to realize

arbitrary spin geometries.

Another aspect, the exploration of which might yield an improvement of the setup's performance, is the heating of the in-plane motional modes. Cross-coupling could transfer energy from in-plane modes, which are currently only Doppler cooled, to the out-of-plane modes, leading to increased heating rates and, consequently, to motional decoherence. First measurements suggest a high heating rate in the vertical (y) direction. As a countermeasure, additional cooling via polarization-gradient cooling could be implemented by using two counterpropagating beams entering through the axial holes in the trap chip. Alternatively, sideband cooling could be used straightforwardly with the axial 729-nm beam to cool hot modes in the in-plane spectrum.

As a last note, a few suggestions on the modification of the trap chip shall be mentioned. In the presented setup, we expect to be able to trap several hundreds of ions, although ion crystals beyond 105 ions have not been explored yet. We encountered a limit for the applicable rf voltage of about 1 kV peak-to-peak, restricting the achievable trap frequency and eventually the number of ions that can be trapped in a two-dimensional crystal lattice configuration. As discussed in Sec. 2.1.5, the ratio between the trap frequencies in strongly and weakly confined directions have to obey a certain condition, which gets increasingly difficult with larger ion numbers. Increasing the applicable voltage, however, requires a modification of the trap design, in particular an increase of the distances between the electrodes to avoid voltage breakdowns due to shorts between two adjacent trap segments. In the current design, the width and depth of the trenches used for the electrode separation in the central area of the trap chip, is restricted by the substrate thickness. The etched trenches, separating the electrodes at the angled surfaces, need to leave enough substrate between the electrodes to ensure their mechanical stability. In order to keep the same geometry and benefit from a monolithic design, increasing the trench dimensions would require a thicker chip substrate, which could, in principle, still be processed effectively using selective laser-induced etching.

Appendix A

Floquet-Lyapunov theory

Floquet theory proposes solutions for a set of linear, ordinary differential equations (ODEs) with a periodic coefficient matrix. In Refs. [56, 59], it is used to solve Eq. 2.34, a set of Mathieu equations. A brief summary of this approach, following Refs. [56, 59], is given in this section.

For the f-dimensional Newtonian problem, where $f = 3N$ for N ions in three dimensions, the Floquet problem is stated in the $2f$-dimensional phase space as an ODE of first order using the definitions

$$\vec{\Phi}(t) = \begin{pmatrix} \vec{u}(t) \\ \dot{\vec{u}}(t) \end{pmatrix}, \quad \text{and} \quad \Pi(t) = \begin{pmatrix} 0 & \mathbb{1}_f \\ -(A - 2Q\cos(2t)) & 0 \end{pmatrix}, \tag{A.1}$$

with $\mathbb{1}_f$ being the f-dimensional identity matrix. The standard form of the e.o.m. is then given by

$$\dot{\Phi} = \Pi(t)\Phi. \tag{A.2}$$

There are $2f$ linearly independent column solutions constituting the fundamental matrix solution to equation A.2 . A fundamental matrix solution obeying $\Phi(0) = \mathbb{1}_{2f}$ is unique and can always be written as $\Phi(t) = \Gamma(t)e^{Bt}\Gamma^{-1}(0)$, where $\Gamma(t+T) = \Gamma(t)$ is periodic with the period of Π (period of the trap rf drive). The entries of the diagonal constant matrix B, which is given by

$$B = \mathrm{diag}(i\beta_1, \ldots, i\beta_{2f}) \ , \tag{A.3}$$

are known as characteristic exponents of the Floquet problem (Floquet exponents). With the transformation

$$\Phi(t) = \Gamma(t)\chi(t), \tag{A.4}$$

known as *Floquet-Lyapunov* transformation, Eq. A.2 transforms into the time independent diagonal form

$$\dot{\chi}(t) = B\chi. \tag{A.5}$$

Solutions to this equation are given by the Floquet modes,

$$\chi_\nu(t) = \chi_\nu(0)e^{i\beta_\nu t}. \tag{A.6}$$

The solution yields $2f$ $(6N)$ Floquet frequencies β_i, where for every β_i, there is a β_j with $\beta_j = -\beta_i$, leaving $3N$ mode frequencies - equivalent to the normal mode frequencies in the pseudo-potential calculation discussed earlier.

We are now looking for solutions in form of two linearly independent complex column vectors

$$\vec{u} = \sum_{n=-\infty}^{n=+\infty} \vec{C}_{2n} \left[be^{i(2n+\beta)t} + ce^{-i(2n+\beta)t} \right], \tag{A.7}$$

where b and c are complex constants determined by the initial condition. β will take real nonintegral values for stable modes and can be chosen in the range of $0 < \beta < 1$ for trapping parameters in the first stability zone [59]. We use $R_{2n} = A - (2n+\beta)^2$ to express $\vec{C}_{2n}$ by an infinite recursion relation

$$Q\vec{C}_{2n-2} = R_{2n}\vec{C}_{2n} - Q\vec{C}_{2n+2}, \tag{A.8}$$

which leads to two independent expansions of infinite continued matrix inversions

$$\vec{C}_2 = T_{2,\beta}Q\vec{C}_0 \equiv \left(\left[R_2 - Q \left[R_4 - Q \left[R_6 - \ldots \right]^{-1} Q \right]^{-1} \right] Q \right]^{-1})Q\vec{C}_0 \tag{A.9}$$

and

$$Q\vec{C}_2 = R_0\vec{C}_0 - Q\vec{C}_{-2} = \tilde{T}_{0,\beta}\vec{C}_0 \equiv \left(R_0 - Q \left[R_{-2} - Q \left[R_{-4} - \ldots \right]^{-1} Q \right]^{-1} Q \right) \vec{C}_0 \tag{A.10}$$

We define

$$Y_{2,\beta} \equiv \tilde{T}_{0,\beta} - QT_{2,\beta}Q, \tag{A.11}$$

and, by multiplying Eq. A.9 with Q, we obtain that all characteristic exponents β are zeros of the determinant of $Y_{2,\beta}$.

We are now seeking a the Floquet-Lyapunov transformation, which transforms the e.o.m. into a time-independent diagonal equation. As already hinted above the solutions for stable Floquet modes are oscillatory and represented by complex conjugate pairs simplifying many expressions. B can be expressed in block form $B = \begin{pmatrix} iB & 0 \\ 0 & -iB \end{pmatrix}$, where $B_{f\times f} = \mathrm{diag}\,(\beta_1, \ldots, \beta_f)$ and all β_i are positive.

Using the series of $3N$-dimensional vectors $\vec{C}_{2n,\beta_i}$ as column vectors, we can now define

$$U_{3N\times 3N} = \sum_n \vec{C}_{2n,\beta_i} e^{i2nt} \ \ldots \tag{A.12}$$

and similarly

$$V_{3N\times 3N} = i\sum_n (2n + \beta_i)\vec{C}_{2n,\beta_i} e^{i2nt} \ \ldots. \tag{A.13}$$

The $6N$-dimensional fundamental matrix solution can now be represented by

$$\Gamma(t) = \begin{pmatrix} U & U^* \\ V & V^* \end{pmatrix}, \tag{A.14}$$

where U^* and V^* denote the complex conjugates of matrices U and V, respectively. It transforms the Hamiltonian coordinates $\vec{u}$ and their conjugate momenta $\vec{p} = \dot{\vec{u}}$, to the variables $\chi = \begin{pmatrix} \xi \\ \zeta \end{pmatrix}$, where ξ is the $3N$-dimensional vector of coordinates and $-i\zeta$ are the conjugate momenta, obeying $\xi = \zeta^*$ due to the realness of $\vec{u}$ and $\vec{p}$. The time dependence is then given by Eq. A.6.

Appendix B

Mean-field approximation of sideband dynamics of an ion crystal

The equations in this section were derived by Ivan Vybornyi and Klemens Hammerer[1] to fit the sideband dynamics of a 19-ion crystal discussed in Sec. 5.9.1 and Ref. [182]. Due to discrepancies between the simulated and measured data (see Sec. 5.5.2), this approach was no longer pursued. Taking higher orders of ion-ion correlations into account could potentially reduce this mismatch.

The mean-field approach relies on neglecting the higher-order correlations in the system, thereby simplifying the dynamics of the spin-motion coupling. The sought-for ground state probability is approximated as

$$P_g = \langle \otimes_i \sigma_i^{gg} \rangle \simeq \prod_i (1 - \langle \sigma_i^{ee} \rangle). \tag{B.1}$$

Consider the red sideband case with the Hamiltonian 5.15(a). Using the standard commutator relations for the Pauli operators $[\sigma_i^-, \sigma_j^+] = (1 - 2\sigma_i^{ee})\delta_{ij}$, $[\sigma_i^\pm, \sigma_j^{ee}] = \mp\sigma_i^\pm \delta_{ij}$ and the Ehrenfest theorem, we obtain the following *closed* system of equations

[1] Institut für Theoretische Physik, Leibniz Universität Hannover

$$\partial_t \langle \sigma_i^{ee} \rangle = \mathrm{i} g_i \Big(\Big\langle a^\dagger \sigma_i^- \Big\rangle - \Big\langle a \sigma_i^+ \Big\rangle \Big), \tag{B.2}$$

$$\begin{aligned} \partial_t \Big\langle a \sigma_i^+ \Big\rangle &= \mathrm{i} g_i \Big\langle a^\dagger a \Big\rangle - 2\mathrm{i} g_i \langle a^\dagger a \sigma_i^{ee} \rangle \\ &\quad - \mathrm{i} g_i \langle \sigma_i^{ee} \rangle - \mathrm{i} \sum_{j:j\neq i} g_j \langle \sigma_i^+ \sigma_j^- \rangle , \end{aligned} \tag{B.3}$$

$$\partial_t \Big\langle a^\dagger a \Big\rangle = \mathrm{i} \sum_i g_i \Big(\Big\langle a \sigma_i^+ \Big\rangle - \Big\langle a^\dagger \sigma_i^- \Big\rangle \Big), \tag{B.4}$$

$$\begin{aligned} \partial_t \langle \sigma_i^+ \sigma_j^- \rangle &\simeq \mathrm{i} \Big(g_i \langle a^\dagger \sigma_j^- \rangle \left(1 - 2 \langle \sigma_i^{ee} \rangle \right) \\ &\quad - g_j \langle a \sigma_i^+ \rangle \left(1 - 2 \langle \sigma_j^{ee} \rangle \right) \Big), \end{aligned} \tag{B.5}$$

$$\partial_t \Big\langle a^\dagger a \sigma_i^{ee} \Big\rangle \simeq \mathrm{i} g_i \Big(\Big\langle a^\dagger \sigma_i^- \Big\rangle \Big\langle a^\dagger a \Big\rangle - \Big\langle a \sigma_i^+ \Big\rangle \big(\Big\langle a^\dagger a \Big\rangle - 1 \big) \Big). \tag{B.6}$$

In the equations (B.2-B.6) we defined $g_i = g\eta_i$ and applied further approximations to obtain a closed system, including factorization of the higher-order correlations: $\langle a \sigma_i^\dagger \sigma_j^{ee} \rangle \approx \langle a \sigma_i^\dagger \rangle \Big\langle \sigma_j^{ee} \Big\rangle$, $\Big\langle \sigma_i^- a^\dagger a^\dagger a \Big\rangle \approx \Big\langle \sigma_i^- a^\dagger \Big\rangle \Big\langle a^\dagger a \Big\rangle$. With initial conditions being $\Big\langle a^\dagger a \Big\rangle = \bar{n}$ and all the other variables set to zero, the system of equations is solved to obtain the dynamics for $\langle \sigma_i^{ee} \rangle$ and P_g. For the case of the blue sideband given by Eq. 5.15(b), an analogous system of equations can be derived.

Bibliography

[1] W. Kohn and L. J. Sham, "Self-Consistent Equations Including Exchange and Correlation Effects," Phys. Rev. **140**, A1133–A1138 (1965).

[2] R. Orús, "Tensor networks for complex quantum systems," Nature Reviews Physics **1**, 538–550 (2019).

[3] G. Carleo and M. Troyer, "Solving the quantum many-body problem with artificial neural networks," Science **355**, 602–606 (2017).

[4] R. P. Feynman, "Simulating physics with computers," International Journal of Theoretical Physics **21**, 467–488 (1982).

[5] Y. I. Manin, "Vychislimoe i nevychislimoe (in English: The computable and uncomputable)," Sovetskoye Radio, Moscow pp. 13–15 (1980).

[6] P. Benioff, "The computer as a physical system: A microscopic quantum mechanical Hamiltonian model of computers as represented by Turing machines," Journal of Statistical Physics **22**, 563–591 (1980).

[7] J. Preskill, "Quantum Computing in the NISQ era and beyond," Quantum **2**, 79 (2018).

[8] C. Kokail, C. Maier, R. van Bijnen, T. Brydges, M. K. Joshi, P. Jurcevic, C. A. Muschik, P. Silvi, R. Blatt, C. F. Roos, and P. Zoller, "Self-verifying variational quantum simulation of lattice models," Nature **569**, 355–360 (2019).

[9] F. Schmidt-Kaler, H. Häffner, M. Riebe, S. Gulde, G. P. Lancaster, T. Deuschle, C. Becher, C. F. Roos, J. Eschner, and R. Blatt, "Realization of the Cirac–Zoller controlled-NOT quantum gate," Nature **422**, 408–411 (2003).

[10] K. Kim, M.-S. Chang, S. Korenblit, R. Islam, E. E. Edwards, J. K. Freericks, G.-D. Lin, L.-M. Duan, and C. Monroe, "Quantum simulation of frustrated Ising spins with trapped ions," Nature **465**, 590–593 (2010).

[11] J. W. Britton, B. C. Sawyer, A. C. Keith, C.-C. J. Wang, J. K. Freericks, H. Uys, M. J. Biercuk, and J. J. Bollinger, "Engineered two-dimensional Ising interactions in a trapped-ion quantum simulator with hundreds of spins," Nature **484**, 489–492 (2012).

[12] J. G. Bohnet, B. C. Sawyer, J. W. Britton, M. L. Wall, A. M. Rey, M. Foss-Feig, and J. J. Bollinger, "Quantum spin dynamics and entanglement generation with hundreds of trapped ions," Science **352**, 1297–1301 (2016).

[13] B. J. McMahon, K. R. Brown, C. D. Herold, and B. C. Sawyer, "Individual-Ion Addressing and Readout in a Penning Trap," arXiv:2404.02105 (2024).

[14] R. Gerritsma, G. Kirchmair, F. Zähringer, E. Solano, R. Blatt, and C. Roos, "Quantum simulation of the Dirac equation," Nature **463**, 68–71 (2010).

[15] B. P. Lanyon, C. Hempel, D. Nigg, M. Müller, R. Gerritsma, F. Zähringer, P. Schindler, J. T. Barreiro, M. Rambach, G. Kirchmair *et al.*, "Universal digital quantum simulation with trapped ions," Science **334**, 57–61 (2011).

[16] P. Schindler, M. Müller, D. Nigg, J. T. Barreiro, E. A. Martinez, M. Hennrich, T. Monz, S. Diehl, P. Zoller, and R. Blatt, "Quantum simulation of dynamical maps with trapped ions," Nature Physics **9**, 361–367 (2013).

[17] P. Jurcevic, B. P. Lanyon, P. Hauke, C. Hempel, P. Zoller, R. Blatt, and C. F. Roos, "Quasiparticle engineering and entanglement propagation in a quantum many-body system," Nature **511**, 202–205 (2014).

[18] C. Hempel, C. Maier, J. Romero, J. McClean, T. Monz, H. Shen, P. Jurcevic, B. P. Lanyon, P. Love, R. Babbush, A. Aspuru-Guzik, R. Blatt, and C. F. Roos, "Quantum Chemistry Calculations on a Trapped-Ion Quantum Simulator," Phys. Rev. X **8**, 031022 (2018).

[19] M. K. Joshi, F. Kranzl, A. Schuckert, I. Lovas, C. Maier, R. Blatt, M. Knap, and C. F. Roos, "Observing emergent hydrodynamics in a long-range quantum magnet," Science **376**, 720–724 (2022).

[20] F. Kranzl, A. Lasek, M. K. Joshi, A. Kalev, R. Blatt, C. F. Roos, and N. Yunger Halpern, "Experimental Observation of Thermalization with Noncommuting Charges," PRX Quantum **4**, 020318 (2023).

[21] L. K. Joshi, J. Franke, A. Rath, F. Ares, S. Murciano, F. Kranzl, R. Blatt, P. Zoller, B. Vermersch, P. Calabrese, C. F. Roos, and M. K. Joshi, "Observing the Quantum Mpemba Effect in Quantum Simulations," Phys. Rev. Lett. **133**, 010402 (2024).

[22] F. Kranzl, M. K. Joshi, C. Maier, T. Brydges, J. Franke, R. Blatt, and C. F. Roos, "Controlling long ion strings for quantum simulation and precision measurements," Phys. Rev. A **105**, 052426 (2022).

[23] J. P. Schiffer, "Phase transitions in anisotropically confined ionic crystals," Phys. Rev. Lett. **70**, 818–821 (1993).

[24] D. H. E. Dubin, "Theory of structural phase transitions in a trapped Coulomb crystal," Phys. Rev. Lett. **71**, 2753–2756 (1993).

[25] A. M. Polloreno, A. M. Rey, and J. J. Bollinger, "Individual qubit addressing of rotating ion crystals in a Penning trap," Phys. Rev. Research **4**, 033076 (2022).

[26] R. C. Sterling, H. Rattanasonti, S. Weidt, K. Lake, P. Srinivasan, S. C. Webster, M. Kraft, and W. K. Hensinger, "Fabrication and operation of a two-dimensional ion-trap lattice on a high-voltage microchip," Nature Communications **5**, 3637 (2014).

[27] M. Mielenz, H. Kalis, M. Wittemer, F. Hakelberg, U. Warring, R. Schmied, M. Blain, P. Maunz, D. L. Moehring, D. Leibfried, and T. Schaetz, "Arrays of individually controlled ions suitable for two-dimensional quantum simulations," Nature Communications **7**, 11839 (2016).

[28] P. C. Holz, S. Auchter, G. Stocker, M. Valentini, K. Lakhmanskiy, C. Rössler, P. Stampfer, S. Sgouridis, E. Aschauer, Y. Colombe, and R. Blatt, "2D Linear Trap Array for Quantum Information Processing," Adv. Quantum Technol. **3**, 2000031 (2020).

[29] S. Jain, J. Alonso, M. Grau, and J. P. Home, "Scalable Arrays of Micro-Penning Traps for Quantum Computing and Simulation," Phys. Rev. X **10**, 031027 (2020).

[30] S. Jain, T. Sägesser, P. Hrmo, C. Torkzaban, M. Stadler, R. Oswald, C. Axline, A. Bautista-Salvador, C. Ospelkaus, D. Kienzler *et al.*, "Unit cell of a Penning micro-trap quantum processor," arXiv:2308.07672 (2023).

[31] B. Yoshimura, M. Stork, D. Dadic, W. C. Campbell, and J. K. Freericks, "Creation of two-dimensional Coulomb crystals of ions in oblate Paul traps for quantum simulations," EPJ Quantum Technology **2**, 2 (2015).

[32] Y. Wang, M. Qiao, Z. Cai, K. Zhang, N. Jin, P. Wang, W. Chen, C. Luan, B. Du, H. Wang, Y. Song, D. Yum, and K. Kim, "Coherently Manipulated 2D Ion Crystal in a Monolithic Paul Trap," Adv. Quantum Technol. **3**, 2000068 (2020).

[33] M. K. Ivory, A. Kato, A. Hasanzadeh, and B. B. Blinov, "A Paul trap with sectored ring electrodes for experiments with two-dimensional ion crystals," Rev. Sci. Instrum. **91**, 053201 (2020).

[34] Y. Xie, J. Cui, M. D'Onofrio, A. J. Rasmusson, S. W. Howell, and P. Richerme, "An open-endcap blade trap for radial-2D ion crystals," Quantum Sci. Technol. **6**, 044009 (2021).

[35] M. D'Onofrio, Y. Xie, A. J. Rasmusson, E. Wolanski, J. Cui, and P. Richerme, "Radial two-dimensional ion crystals in a linear Paul trap," Phys. Rev. Lett. **127**, 020503 (2021).

[36] S.-A. Guo, Y.-K. Wu, J. Ye, L. Zhang, W.-Q. Lian, R. Yao, Y. Wang, R.-Y. Yan, Y.-J. Yi, Y.-L. Xu *et al.*, "A site-resolved two-dimensional quantum simulator with hundreds of trapped ions," Nature pp. 1–6 (2024).

[37] F. v. Busch and W. Paul, "Über nichtlineare Resonanzen im elektrischen Massenfilter als Folge von Feldfehlern," Zeitschrift für Physik **164**, 588–594 (1961).

[38] R. Alheit, S. Kleineidam, F. Vedel, M. Vedel, and G. Werth, "Higher order non-linear resonances in a Paul trap," Int. J. Mass Spectrom. **154**, 155–169 (1996).

[39] R. B. Blakestad, "Transport of Trapped-Ion Qubits within a Scalable Quantum Processor," Ph.D. thesis, University of Colorado (2010).

[40] M. Block, A. Drakoudis, H. Leuthner, P. Seibert, G. Werth, M. Block, A. Drakoudis, H. Leuthner, and P. Seibert, "Crystalline ion structures in a Paul trap," Journal of Physics B **33**, L375 (2000).

[41] R. Blümel, C. Kappler, W. Quint, and H. Walther, "Chaos and order of laser-cooled ions in a Paul trap," Phys. Rev. A **40**, 808–823 (1989).

[42] M. Qiao, Y. Wang, Z. Cai, B. Du, P. Wang, C. Luan, W. Chen, H.-R. Noh, and K. Kim, "Double-Electromagnetically-Induced-Transparency Ground-State Cooling of Stationary Two-Dimensional Ion Crystals," Phys. Rev. Lett. **126**, 023604 (2021).

[43] R. F. Wuerker, H. Shelton, and R. V. Langmuir, "Electrodynamic Containment of Charged Particles," Journal of Applied Physics **30**, 342–349 (2004).

[44] W. Paul and M. Raether, "Das elektrische Massenfilter," Zeitschrift für Physik **140**, 262–273 (1955).

[45] F. Diedrich, E. Peik, J. M. Chen, W. Quint, and H. Walther, "Observation of a Phase Transition of Stored Laser-Cooled Ions," Phys. Rev. Lett. **59**, 2931–2934 (1987).

[46] D. J. Wineland, J. C. Bergquist, W. M. Itano, J. J. Bollinger, and C. H. Manney, "Atomic-Ion Coulomb Clusters in an Ion Trap," Phys. Rev. Lett. **59**, 2935–2938 (1987).

[47] R. Blümel, J. M. Chen, E. Peik, W. Quint, W. Schleich, Y. R. Shen, and H. Walther, "Phase transitions of stored laser-cooled ions," Nature **334**, 309–313 (1988).

[48] J. I. Cirac, R. Blatt, A. Parkins, and P. Zoller, "Laser cooling of trapped ions with polarization gradients," Phys. Rev. A **48**, 1434–1445 (1993).

[49] D. Leibfried, R. Blatt, C. Monroe, and D. Wineland, "Quantum dynamics of single trapped ions," Rev. Mod. Phys. **75**, 281 (2003).

[50] P. K. Ghosh, *Ion traps* (Clarendon press, 1995).

[51] J. Keller, H. L. Partner, T. Burgermeister, and T. Mehlstäubler, "Precise determination of micromotion for trapped-ion optical clocks," Journal of Applied Physics **118**, 104501 (2015).

[52] A. Bermudez, P. Schindler, T. Monz, R. Blatt, and M. Müller, "Micromotion-enabled improvement of quantum logic gates with trapped ions," New Journal of Physics **19**, 113038 (2017).

[53] D. Berkeland, J. Miller, J. C. Bergquist, W. M. Itano, and D. J. Wineland, "Minimization of ion micromotion in a Paul trap," Journal of Applied Physics **83**, 5025–5033 (1998).

[54] D. James, "Quantum dynamics of cold trapped ions with application to quantum computation," Applied Physics B **66**, 181–190 (1998).

[55] C. Marquet, F. Schmidt-Kaler, and D. F. James, "Phonon–phonon interactions due to non-linear effects in a linear ion trap," Applied Physics B **76**, 199–208 (2003).

[56] H. Landa, M. Drewsen, B. Reznik, and A. Retzker, "Modes of oscillation in radiofrequency Paul traps," New Journal of Physics **14**, 093023 (2012).

[57] H. Kaufmann, S. Ulm, G. Jacob, U. Poschinger, H. Landa, A. Retzker, M. B. Plenio, and F. Schmidt-Kaler, "Precise Experimental Investigation of Eigenmodes in a Planar Ion Crystal," Phys. Rev. Lett. **109**, 263003 (2012).

[58] D. J. Wineland, C. Monroe, W. M. Itano, D. Leibfried, B. E. King, and D. M. Meekhof, "Experimental issues in coherent quantum-state manipulation of trapped atomic ions," Journal of Research of the National Institute of Standards and Technology **103**, 259 (1998).

[59] H. Landa, M. Drewsen, B. Reznik, and A. Retzker, "Classical and quantum modes of coupled Mathieu equations," Journal of Physics A **45**, 455305 (2012).

[60] D. Kiesenhofer, H. Hainzer, A. Zhdanov, P. C. Holz, M. Bock, T. Ollikainen, and C. F. Roos, "Controlling Two-Dimensional Coulomb Crystals of More Than 100 Ions in a Monolithic Radio-Frequency Trap," PRX Quantum **4**, 020317 (2023).

[61] H. Hainzer, "Quantum correlations of large planar ion crystals in a novel monolithic radiofrequency trap," Ph.D. thesis, University of Innsbruck (2024).

[62] D. G. Enzer, M. M. Schauer, J. J. Gomez, M. S. Gulley, M. H. Holzscheiter, P. G. Kwiat, S. K. Lamoreaux, C. G. Peterson, V. D. Sandberg, D. Tupa, A. G. White, R. J. Hughes, and D. F. V. James, "Observation of power-law scaling for phase transitions in linear trapped ion crystals," Phys. Rev. Lett. **85**, 2466–2469 (2000).

[63] G. Piacente, I. V. Schweigert, J. J. Betouras, and F. M. Peeters, "Generic properties of a quasi-one-dimensional classical Wigner crystal," Phys. Rev. B **69**, 045324 (2004).

[64] S. Fishman, G. De Chiara, T. Calarco, and G. Morigi, "Structural phase transitions in low-dimensional ion crystals," Phys. Rev. B **77**, 064111 (2008).

[65] P. Jurcevic, "Quantum computation and many-body physics with trapped ions," Ph.D. thesis, University of Innsbruck (2017).

[66] O. D. Kellogg, *Foundations of potential theory* (Springer, 1929).

[67] D. H. E. Dubin and T. M. O'Neil, "Trapped nonneutral plasmas, liquids, and crystals (the thermal equilibrium states)," Rev. Mod. Phys. **71**, 87–172 (1999).

[68] W. M. Itano, J. C. Bergquist, J. J. Bollinger, J. M. Gilligan, D. J. Heinzen, F. L. Moore, M. G. Raizen, and D. J. Wineland, "Quantum projection noise: Population fluctuations in two-level systems," Phys. Rev. A **47**, 3554–3570 (1993).

[69] D. J. Wineland, J. J. Bollinger, W. M. Itano, F. L. Moore, and D. J. Heinzen, "Spin squeezing and reduced quantum noise in spectroscopy," Phys. Rev. A **46**, R6797–R6800 (1992).

[70] O. Hosten, N. J. Engelsen, R. Krishnakumar, and M. A. Kasevich, "Measurement noise 100 times lower than the quantum-projection limit using entangled atoms," Nature **529**, 505–508 (2016).

[71] J. Franke, S. R. Muleady, R. Kaubruegger, F. Kranzl, R. Blatt, A. M. Rey, M. K. Joshi, and C. F. Roos, "Quantum-enhanced sensing on optical transitions through finite-range interactions," Nature **621**, 740–745 (2023).

[72] D. M. Greenberger, M. A. Horne, A. Shimony, and A. Zeilinger, "Bell's theorem without inequalities," American Journal of Physics **58**, 1131–1143 (1990).

[73] H. Ollivier and W. H. Zurek, "Quantum Discord: A Measure of the Quantumness of Correlations," Phys. Rev. Lett. **88**, 017901 (2001).

[74] K. Modi, A. Brodutch, H. Cable, T. Paterek, and V. Vedral, "The classical-quantum boundary for correlations: Discord and related measures," Rev. Mod. Phys. **84**, 1655–1707 (2012).

[75] B. P. Lanyon, P. Jurcevic, C. Hempel, M. Gessner, V. Vedral, R. Blatt, and C. F. Roos, "Experimental Generation of Quantum Discord via Noisy Processes," Phys. Rev. Lett. **111**, 100504 (2013).

[76] H. Hainzer, D. Kiesenhofer, T. Ollikainen, M. Bock, F. Kranzl, M. K. Joshi, G. Yoeli, R. Blatt, T. Gefen, and C. F. Roos, "Correlation Spectroscopy with Multiqubit-Enhanced Phase Estimation," Phys. Rev. X **14**, 011033 (2024).

[77] T. Monz, "Quantum information processing beyond ten ion-qubits," Ph.D. thesis, University of Innsbruck (2011).

[78] L. K. Grover, "A fast quantum mechanical algorithm for database search," Proceedings of the twenty-eighth annual ACM symposium on Theory of computing pp. 212–219 (1996).

[79] P. W. Shor, "Polynomial-time algorithms for prime factorization and discrete logarithms on a quantum computer," SIAM review **41**, 303–332 (1999).

[80] D. P. DiVincenzo, "The physical implementation of quantum computation," Fortschritte der Physik: Progress of Physics **48**, 771–783 (2000).

[81] C. Maier, "A quantum simulator with long strings of trapped ions," Ph.D. thesis, University of Innsbruck (2020).

[82] A. Y. Kitaev, "Quantum computations: algorithms and error correction," Russian Mathematical Surveys **52**, 1191 (1997).

[83] M. Hilbert and P. López, "The world's technological capacity to store, communicate, and compute information," Science **332**, 60–65 (2011).

[84] I. Buluta and F. Nori, "Quantum simulators," Science **326**, 108–111 (2009).

[85] E. Altman, K. R. Brown, G. Carleo, L. D. Carr, E. Demler, C. Chin, B. DeMarco, S. E. Economou, M. A. Eriksson, K.-M. C. Fu, M. Greiner, K. R. Hazzard, R. G.

Hulet, A. J. Kollár, B. L. Lev, M. D. Lukin, R. Ma, X. Mi, S. Misra, C. Monroe, K. Murch, Z. Nazario, K.-K. Ni, A. C. Potter, P. Roushan, M. Saffman, M. Schleier-Smith, I. Siddiqi, R. Simmonds, M. Singh, I. Spielman, K. Temme, D. S. Weiss, J. Vučković, V. Vuletić, J. Ye, and M. Zwierlein, "Quantum Simulators: Architectures and Opportunities," PRX Quantum **2**, 017003 (2021).

[86] C. Monroe, W. C. Campbell, L.-M. Duan, Z.-X. Gong, A. V. Gorshkov, P. W. Hess, R. Islam, K. Kim, N. M. Linke, G. Pagano, P. Richerme, C. Senko, and N. Y. Yao, "Programmable quantum simulations of spin systems with trapped ions," Rev. Mod. Phys. **93**, 025001 (2021).

[87] H. Bernien, S. Schwartz, A. Keesling, H. Levine, A. Omran, H. Pichler, S. Choi, A. S. Zibrov, M. Endres, M. Greiner *et al.*, "Probing many-body dynamics on a 51-atom quantum simulator," Nature **551**, 579–584 (2017).

[88] D. Bluvstein, A. Omran, H. Levine, A. Keesling, G. Semeghini, S. Ebadi, T. T. Wang, A. A. Michailidis, N. Maskara, W. W. Ho *et al.*, "Controlling quantum many-body dynamics in driven Rydberg atom arrays," Science **371**, 1355–1359 (2021).

[89] P. Scholl, M. Schuler, H. J. Williams, A. A. Eberharter, D. Barredo, K.-N. Schymik, V. Lienhard, L.-P. Henry, T. C. Lang, T. Lahaye *et al.*, "Quantum simulation of 2D antiferromagnets with hundreds of Rydberg atoms," Nature **595**, 233–238 (2021).

[90] F. Gyger, M. Ammenwerth, R. Tao, H. Timme, S. Snigirev, I. Bloch, and J. Zeiher, "Continuous operation of large-scale atom arrays in optical lattices," Phys. Rev. Res. **6**, 033104 (2024).

[91] M. Affolter, W. Ge, B. Bullock, S. C. Burd, K. A. Gilmore, J. F. Lilieholm, A. L. Carter, and J. J. Bollinger, "Toward improved quantum simulations and sensing with trapped two-dimensional ion crystals via parametric amplification," Phys. Rev. A **107**, 032425 (2023).

[92] J. Zhang, G. Pagano, P. W. Hess, A. Kyprianidis, P. Becker, H. Kaplan, A. V. Gorshkov, Z.-X. Gong, and C. Monroe, "Observation of a many-body dynamical phase transition with a 53-qubit quantum simulator," Nature **551**, 601–604 (2017).

[93] F. Kranzl, S. Birnkammer, M. K. Joshi, A. Bastianello, R. Blatt, M. Knap, and C. F. Roos, "Observation of Magnon Bound States in the Long-Range, Anisotropic Heisenberg Model," Phys. Rev. X **13**, 031017 (2023).

[94] A. Peruzzo, J. McClean, P. Shadbolt, M.-H. Yung, X.-Q. Zhou, P. J. Love, A. Aspuru-Guzik, and J. L. O'brien, "A variational eigenvalue solver on a photonic quantum processor," Nature Communications **5**, 4213 (2014).

[95] J. R. McClean, J. Romero, R. Babbush, and A. Aspuru-Guzik, "The theory of variational hybrid quantum-classical algorithms," New Journal of Physics **18**, 023023 (2016).

[96] R. M. Parrish, E. G. Hohenstein, P. L. McMahon, and T. J. Martínez, "Quantum Computation of Electronic Transitions Using a Variational Quantum Eigensolver," Phys. Rev. Lett. **122**, 230401 (2019).

[97] R. J. Glauber, "Coherent and incoherent states of the radiation field," Phys. Rev. **131**, 2766–2788 (1963).

[98] C. Hempel, B. Lanyon, P. Jurcevic, R. Gerritsma, R. Blatt, and C. Roos, "Entanglement-enhanced detection of single-photon scattering events," Nature Photonics **7**, 630–633 (2013).

[99] C. F. Roos, "Controlling the quantum state of trapped ions," Ph.D. thesis, University of Innsbruck (2000).

[100] C. Monroe, D. M. Meekhof, B. E. King, and D. J. Wineland, "A "Schrödinger cat" superposition state of an atom," Science **272**, 1131–1136 (1996).

[101] A. Sørensen and K. Mølmer, "Quantum Computation with Ions in Thermal Motion," Phys. Rev. Lett. **82**, 1971–1974 (1999).

[102] K. Mølmer and A. Sørensen, "Multiparticle Entanglement of Hot Trapped Ions," Phys. Rev. Lett. **82**, 1835–1838 (1999).

[103] A. Sørensen and K. Mølmer, "Entanglement and quantum computation with ions in thermal motion," Phys. Rev. A **62**, 022311 (2000).

[104] E. Solano, R. L. de Matos Filho, and N. Zagury, "Deterministic Bell states and measurement of the motional state of two trapped ions," Phys. Rev. A **59**, R2539–R2543 (1999).

[105] M. V. Berry, "Quantal phase factors accompanying adiabatic changes," Proceedings of the Royal Society of London. A. Mathematical and Physical Sciences **392**, 45–57 (1984).

[106] T. Monz, P. Schindler, J. T. Barreiro, M. Chwalla, D. Nigg, W. A. Coish, M. Harlander, W. Hänsel, M. Hennrich, and R. Blatt, "14-Qubit Entanglement: Creation and Coherence," Phys. Rev. Lett. **106**, 130506 (2011).

[107] D. Porras and J. I. Cirac, "Effective Quantum Spin Systems with Trapped Ions," Phys. Rev. Lett. **92**, 207901 (2004).

[108] P. Nevado and D. Porras, "Hidden frustrated interactions and quantum annealing in trapped-ion spin-phonon chains," Phys. Rev. A **93**, 013625 (2016).

[109] C. F. Roos, "Ion trap quantum gates with amplitude-modulated laser beams," New Journal of Physics **10**, 013002 (2008).

[110] K. Kim, M.-S. Chang, R. Islam, S. Korenblit, L.-M. Duan, and C. Monroe, "Entanglement and Tunable Spin-Spin Couplings between Trapped Ions Using Multiple Transverse Modes," Phys. Rev. Lett. **103**, 120502 (2009).

[111] M. Kitagawa and M. Ueda, "Squeezed spin states," Phys. Rev. A **47**, 5138–5143 (1993).

[112] L. Pezzé and A. Smerzi, "Entanglement, nonlinear dynamics, and the Heisenberg limit," Phys. Rev. Lett. **102**, 100401 (2009).

[113] D. T. C. Allcock, W. C. Campbell, J. Chiaverini, I. L. Chuang, E. R. Hudson, I. D. Moore, A. Ransford, C. Roman, J. M. Sage, and D. J. Wineland, "omg blueprint for trapped ion quantum computing with metastable states," Applied Physics Letters **119**, 214002 (2021).

[114] M. Hettrich, T. Ruster, H. Kaufmann, C. Roos, C. Schmiegelow, F. Schmidt-Kaler, and U. Poschinger, "Measurement of dipole matrix elements with a single trapped ion," Phys. Rev. Lett. **115**, 143003 (2015).

[115] P. A. Barton, C. J. S. Donald, D. M. Lucas, D. A. Stevens, A. M. Steane, and D. N. Stacey, "Measurement of the lifetime of the $3d^2D_{5/2}$ state in $^{40}Ca^+$," Phys. Rev. A **62**, 032503 (2000).

[116] L. Deslauriers, P. C. Haljan, P. J. Lee, K.-A. Brickman, B. B. Blinov, M. J. Madsen, and C. Monroe, "Zero-point cooling and low heating of trapped $^{111}Cd^+$ ions," Phys. Rev. A. **70**, 043408 (2004).

[117] P. Bado, C. R. Monroe, and W. C. Campbell, "Fused Silica Ion Trap Chip with Efficient Optical Collection System for Timekeeping, Sensing, and Emulation," URL: https://apps.dtic.mil/sti/citations/ADA567754 (2015).

[118] G. Araneda, G. Cerchiari, D. B. Higginbottom, P. C. Holz, K. Lakhmanskiy, P. Obšil, Y. Colombe, and R. Blatt, "The Panopticon device: An integrated Paul-trap–hemispherical mirror system for quantum optics," Rev. Sci. Instrum. **91**, 113201 (2020).

[119] M. Brownnutt, M. Kumph, P. Rabl, and R. Blatt, "Ion-trap measurements of electric-field noise near surfaces," Rev. Mod. Phys. **87**, 1419–1482 (2015).

[120] C. Noel, M. Berlin-Udi, C. Matthiesen, J. Yu, Y. Zhou, V. Lordi, and H. Häffner, "Electric-field noise from thermally activated fluctuators in a surface ion trap," Phys. Rev. A **99**, 063427 (2019).

[121] S. Ragg, C. Decaroli, T. Lutz, and J. P. Home, "Segmented ion-trap fabrication using high precision stacked wafers," Rev. Sci. Instrum. **90**, 103203 (2019).

[122] C. Decaroli, R. Matt, R. Oswald, C. Axline, M. Ernzer, J. Flannery, S. Ragg, and J. P. Home, "Design, fabrication and characterization of a micro-fabricated stacked-wafer segmented ion trap with two X-junctions," Quantum Sci. Technol. **6**, 044001 (2021).

[123] M. Brandl, M. Van Mourik, L. Postler, A. Nolf, K. Lakhmanskiy, R. Paiva, S. Möller, N. Daniilidis, H. Häffner, V. Kaushal *et al.*, "Cryogenic setup for trapped ion quantum computing," Rev. Sci. Instrum. **87** (2016).

[124] T. Leopold, S. A. King, P. Micke, A. Bautista-Salvador, J. C. Heip, C. Ospelkaus, J. R. Crespo López-Urrutia, and P. O. Schmidt, "A cryogenic radio-frequency ion trap for quantum logic spectroscopy of highly charged ions," Rev. Sci. Instrum. **90** (2019).

[125] J. A. Fedchak, J. K. Scherschligt, S. Avdiaj, D. S. Barker, S. P. Eckel, B. Bowers, S. O'Connell, and P. Henderson, "Outgassing rate comparison of seven geometrically similar vacuum chambers of different materials and heat treatments," Journal of Vacuum Science & Technology B **39**, 024201 (2021).

[126] J. Franke, "Magnetic field noise cancellation for quantum simulation experiment with trapped ions," Master's thesis, University of Innsbruck (2021).

[127] J. D. Siverns, L. R. Simkins, S. Weidt, and W. K. Hensinger, "On the application of radio frequency voltages to ion traps via helical resonators," Appl. Phys. B **107**, 921–934 (2012).

[128] D. Gandolfi, M. Niedermayr, M. Kumph, M. Brownnutt, and R. Blatt, "Compact radio-frequency resonator for cryogenic ion traps," Rev. Sci. Instrum. **83**, 084705 (2012).

[129] M. W. van Mourik, E. A. Martinez, L. Gerster, P. Hrmo, T. Monz, P. Schindler, and R. Blatt, "Coherent rotations of qubits within a surface ion-trap quantum computer," Phys. Rev. A **102**, 022611 (2020).

[130] K. Singer, U. Poschinger, M. Murphy, P. Ivanov, F. Ziesel, T. Calarco, and F. Schmidt-Kaler, "Colloquium: Trapped ions as quantum bits: Essential numerical tools," Rev. Mod. Phys. **82**, 2609 (2010).

[131] C. D. Bruzewicz, R. McConnell, J. Chiaverini, and J. M. Sage, "Scalable loading of a two-dimensional trapped-ion array," Nature Communications **7**, 13005 (2016).

[132] D. R. Leibrandt, R. J. Clark, J. Labaziewicz, P. Antohi, W. Bakr, K. R. Brown, and I. L. Chuang, "Laser ablation loading of a surface-electrode ion trap," Phys. Rev. A **76**, 055403 (2007).

[133] M. Guggemos, D. Heinrich, O. Herrera-Sancho, R. Blatt, and C. Roos, "Sympathetic cooling and detection of a hot trapped ion by a cold one," New Journal of Physics **17**, 103001 (2015).

[134] B. M. White, P. J. Low, Y. de Sereville, M. L. Day, N. Greenberg, R. Rademacher, and C. Senko, "Isotope-selective laser ablation ion-trap loading of $^{137}Ba^{+}$ using a $BaCl_2$ target," Phys. Rev. A **105**, 033102 (2022).

[135] R. Lechner, C. Maier, C. Hempel, P. Jurcevic, B. P. Lanyon, T. Monz, M. Brownnutt, R. Blatt, and C. F. Roos, "Electromagnetically-induced-transparency ground-state cooling of long ion strings," Phys. Rev. A **93**, 053401 (2016).

[136] A. Winkler, "Frequency Stabilization of a 729 nm Ti:Sa Laser for Qubit Manipulation in Trapped Calcium Ions," Master's thesis, University of Innsbruck (2023).

[137] L.-S. Ma, P. Jungner, J. Ye, and J. L. Hall, "Delivering the same optical frequency at two places: accurate cancellation of phase noise introduced by an optical fiber or other time-varying path," Optics letters **19**, 1777–1779 (1994).

[138] G. Kirchmair, "Frequency stabilization of a Titanium-Sapphire laser for precision spectroscopy on Calcium ions," Diploma thesis, University of Innsbruck (2006).

[139] P.-L. Liu, Y. Huang, W. Bian, H. Shao, H. Guan, Y.-B. Tang, C.-B. Li, J. Mitroy, and K.-L. Gao, "Measurement of Magic Wavelengths for the $^{40}Ca^{+}$ Clock Transition," Phys. Rev. Lett. **114**, 223001 (2015).

[140] J. Kaur, S. Singh, B. Arora, and B. K. Sahoo, "Magic wavelengths in the alkaline-earth-metal ions," Phys. Rev. A **92**, 031402 (2015).

[141] J. Benhelm, "Precision spectroscopy and quantum information processing with trapped Calcium ions," Ph.D. thesis, University of Innsbruck (2008).

[142] W. Nörtershäuser, N. Trautmann, K. Wendt, and B. A. Bushaw, "Isotope shifts and hyperfine structure in the $4s^2\ ^1S_0 \rightarrow 4s\ 4p^1P_1 \rightarrow 4s4d^1D_2$ transitions of stable calcium isotopes and calcium-41," Spectrochimica Acta Part B: Atomic Spectroscopy **53**, 709–721 (1998).

[143] S.-T. Wang, C. Shen, and L.-M. Duan, "Quantum computation under micromotion in a planar ion crystal," Scientific reports **5**, 8555 (2015).

[144] A. M. Hankin, E. R. Clements, Y. Huang, S. M. Brewer, J.-S. Chen, C. W. Chou, D. B. Hume, and D. R. Leibrandt, "Systematic uncertainty due to background-gas collisions in trapped-ion optical clocks," Phys. Rev. A **100**, 033419 (2019).

[145] M. W. van Mourik, P. Hrmo, L. Gerster, B. Wilhelm, R. Blatt, P. Schindler, and T. Monz, "rf-induced heating dynamics of noncrystallized trapped ions," Phys. Rev. A **105**, 033101 (2022).

[146] V. L. Ryjkov, X. Zhao, and H. A. Schuessler, "Simulations of the rf heating rates in a linear quadrupole ion trap," Phys. Rev. A **71**, 033414 (2005).

[147] T. Baba and I. Waki, "Spectral shape of in situ mass spectra of sympathetically cooled molecular ions," Journal of Applied Physics **92**, 4109–4116 (2002).

[148] M. Ester, H.-P. Kriegel, J. Sander, and X. Xu, "A Density-Based Algorithm for Discovering Clusters in Large Spatial Databases with Noise," Proceedings of the Second International Conference on Knowledge Discovery and Data Mining p. 226–231 (1996).

[149] L. Yan, W. Wan, L. Chen, F. Zhou, S. Gong, X. Tong, and M. Feng, "Exploring structural phase transitions of ion crystals," Scientific reports **6**, 21547 (2016).

[150] S. Kirkpatrick, C. D. Gelatt Jr, and M. P. Vecchi, "Optimization by simulated annealing," Science **220**, 671–680 (1983).

[151] R. Stricker, M. Meth, L. Postler, C. Edmunds, C. Ferrie, R. Blatt, P. Schindler, T. Monz, R. Kueng, and M. Ringbauer, "Experimental single-setting quantum state tomography," PRX Quantum **3**, 040310 (2022).

[152] G. Morigi, J. Eschner, and C. H. Keitel, "Ground state laser cooling using electromagnetically induced transparency," Phys. Rev. Lett. **85**, 4458 (2000).

[153] M. Joshi, A. Fabre, C. Maier, T. Brydges, D. Kiesenhofer, H. Hainzer, R. Blatt, and C. Roos, "Polarization-gradient cooling of 1D and 2D ion Coulomb crystals," New Journal of Physics **22**, 103013 (2020).

[154] E. Jordan, K. A. Gilmore, A. Shankar, A. Safavi-Naini, J. G. Bohnet, M. J. Holland, and J. J. Bollinger, "Near Ground-State Cooling of Two-Dimensional Trapped-Ion Crystals with More than 100 Ions," Phys. Rev. Lett. **122**, 053603 (2019).

[155] A. Hyvärinen and E. Oja, "Independent component analysis: algorithms and applications," Neural networks **13**, 411–430 (2000).

[156] F. Diedrich, J. C. Bergquist, W. M. Itano, and D. J. Wineland, "Laser cooling to the zero-point energy of motion," Phys. Rev. Lett. **62**, 403–406 (1989).

[157] C. Monroe, D. M. Meekhof, B. E. King, S. R. Jefferts, W. M. Itano, D. J. Wineland, and P. Gould, "Resolved-sideband Raman cooling of a bound atom to the 3D zero-point energy," Phys. Rev. Lett. **75**, 4011–4014 (1995).

[158] B. E. King, C. S. Wood, C. J. Myatt, Q. A. Turchette, D. Leibfried, W. M. Itano, C. Monroe, and D. J. Wineland, "Cooling the collective motion of trapped ions to initialize a quantum register," Phys. Rev. Lett. **81**, 1525–1528 (1998).

[159] J.-S. Chen, K. Wright, N. C. Pisenti, D. Murphy, K. M. Beck, K. Landsman, J. M. Amini, and Y. Nam, "Efficient-sideband-cooling protocol for long trapped-ion chains," Phys. Rev. A **102**, 043110 (2020).

[160] A. J. Rasmusson, M. D'Onofrio, Y. Xie, J. Cui, and P. Richerme, "Optimized pulsed sideband cooling and enhanced thermometry of trapped ions," Phys. Rev. A **104**, 043108 (2021).

[161] P. D. Lett, R. N. Watts, C. I. Westbrook, W. D. Phillips, P. L. Gould, and H. J. Metcalf, "Observation of atoms laser cooled below the Doppler limit," Phys. Rev. Lett. **61**, 169–172 (1988).

[162] J. Dalibard and C. Cohen-Tannoudji, "Laser cooling below the Doppler limit by polarization gradients: simple theoretical models," J. Opt. Soc. Am. B **6**, 2023–2045 (1989).

[163] G. Birkl, J. A. Yeazell, R. Rückerl, and H. Walther, "Polarization Gradient Cooling of Trapped Ions," Europhysics Letters **27**, 197 (1994).

[164] S. M. Yoo and J. Javanainen, "Polarization gradient cooling of a trapped ion," Phys. Rev. A **48**, R30–R33 (1993).

[165] C. F. Roos, D. Leibfried, A. Mundt, F. Schmidt-Kaler, J. Eschner, and R. Blatt, "Experimental demonstration of ground state laser cooling with electromagnetically induced transparency," Phys. Rev. Lett. **85**, 5547 (2000).

[166] Y. Lin, J. P. Gaebler, T. R. Tan, R. Bowler, J. D. Jost, D. Leibfried, and D. J. Wineland, "Sympathetic electromagnetically-induced-transparency laser cooling of motional modes in an ion chain," Phys. Rev. Lett. **110**, 153002 (2013).

[167] T. Kampschulte, W. Alt, S. Manz, M. Martinez-Dorantes, R. Reimann, S. Yoon, D. Meschede, M. Bienert, and G. Morigi, "Electromagnetically-induced-transparency control of single-atom motion in an optical cavity," Phys. Rev. A **89**, 033404 (2014).

[168] E. Haller, J. Hudson, A. Kelly, D. A. Cotta, B. Peaudecerf, G. D. Bruce, and S. Kuhr, "Single-atom imaging of fermions in a quantum-gas microscope," Nature Physics **11**, 738–742 (2015).

[169] N. Scharnhorst, J. Cerrillo, J. Kramer, I. D. Leroux, J. B. Wübbena, A. Retzker, and P. O. Schmidt, "Experimental and theoretical investigation of a multimode cooling scheme using multiple electromagnetically-induced-transparency resonances," Phys. Rev. A **98**, 023424 (2018).

[170] L. Feng, W. L. Tan, A. De, A. Menon, A. Chu, G. Pagano, and C. Monroe, "Efficient Ground-State Cooling of Large Trapped-Ion Chains with an Electromagnetically-Induced-Transparency Tripod Scheme," Phys. Rev. Lett. **125**, 053001 (2020).

[171] J. Evers and C. H. Keitel, "Double-EIT ground-state laser cooling without blue-sideband heating," Europhysics Letters **68**, 370 (2004).

[172] B. Lounis and C. Cohen-Tannoudji, "Coherent population trapping and Fano profiles," Journal de Physique II **2**, 579–592 (1992).

[173] R. Lechner, "Multi-mode cooling techniques for trapped ions," Ph.D. thesis, University of Innsbruck (2016).

[174] D. M. Meekhof, C. Monroe, B. E. King, W. M. Itano, and D. J. Wineland, "Generation of Nonclassical Motional States of a Trapped Atom," Phys. Rev. Lett. **76**, 1796–1799 (1996).

[175] M. Nötzold, S. Z. Hassan, J. Tauch, E. Endres, R. Wester, and M. Weidemüller, "Thermometry in a Multipole Ion Trap," Applied Sciences **10**, 5264 (2020).

[176] J. Roßnagel, K. N. Tolazzi, F. Schmidt-Kaler, and K. Singer, "Fast thermometry for trapped ions using dark resonances," New Journal of Physics **17**, 045004 (2015).

[177] C. B. Zhang, D. Offenberg, B. Roth, M. A. Wilson, and S. Schiller, "Molecular-dynamics simulations of cold single-species and multispecies ion ensembles in a linear Paul trap," Phys. Rev. A **76**, 012719 (2007).

[178] M. Herrmann, V. Batteiger, S. Knünz, G. Saathoff, T. Udem, and T. W. Hänsch, "Frequency Metrology on Single Trapped Ions in the Weak Binding Limit: The $3s_{1/2}$–$3p_{3/2}$ Transition in $^{24}Mg^{+}$," Phys. Rev. Lett. **102**, 013006 (2009).

[179] V. Rajagopal, J. P. Marler, M. G. Kokish, and B. C. Odom, "Trapped Ion Chain Thermometry and Mass Spectrometry through Imaging," European Journal of Mass Spectrometry **22**, 1–7 (2016).

[180] B. C. Sawyer, J. W. Britton, A. C. Keith, C.-C. J. Wang, J. K. Freericks, H. Uys, M. J. Biercuk, and J. J. Bollinger, "Spectroscopy and Thermometry of Drumhead Modes in a Mesoscopic Trapped-Ion Crystal Using Entanglement," Phys. Rev. Lett. **108**, 213003 (2012).

[181] D. Kalincev, L. S. Dreissen, A. P. Kulosa, C.-H. Yeh, H. A. Fürst, and T. E. Mehlstäubler, "Motional heating of spatially extended ion crystals," Quantum Science and Technology **6**, 034003 (2021).

[182] I. Vybornyi, L. S. Dreissen, D. Kiesenhofer, H. Hainzer, M. Bock, T. Ollikainen, D. Vadlejch, C. F. Roos, T. E. Mehlstäubler, and K. Hammerer, "Sideband Thermometry of Ion Crystals," PRX Quantum **4**, 040346 (2023).

[183] J.-S. Chen, S. M. Brewer, C. W. Chou, D. J. Wineland, D. R. Leibrandt, and D. B. Hume, "Sympathetic Ground State Cooling and Time-Dilation Shifts in an $^{27}Al^{+}$ Optical Clock," Phys. Rev. Lett. **118**, 053002 (2017).

[184] A. P. Kulosa, O. N. Prudnikov, D. Vadlejch, H. A. Fürst, A. A. Kirpichnikova, A. V. Taichenachev, V. I. Yudin, and T. E. Mehlstäubler, "Systematic study of tunable laser cooling for trapped-ion experiments," New Journal of Physics **25**, 053008 (2023).

[185] H. Landa, "Tuning nonthermal distributions to thermal ones in time-dependent Paul traps," Phys. Rev. A **100**, 013413 (2019).

[186] C. Wunderlich, T. Hannemann, T. Körber, H. Häffner, C. Roos, W. Hänsel, R. Blatt, and F. Schmidt-Kaler, "Robust state preparation of a single trapped ion by adiabatic passage," Journal of Modern Optics **54**, 1541–1549 (2007).

[187] K. Toyoda, T. Watanabe, T. Kimura, S. Nomura, S. Haze, and S. Urabe, "Generation of Dicke states using adiabatic passage," Phys. Rev. A **83**, 022315 (2011).

[188] S. An, J.-N. Zhang, M. Um, D. Lv, Y. Lu, J. Zhang, Z.-Q. Yin, H. Quan, and K. Kim, "Experimental test of the quantum Jarzynski equality with a trapped-ion system," Nature Physics **11**, 193–199 (2015).

[189] D. J. Wineland, W. M. Itano, J. C. Bergquist, and R. G. Hulet, "Laser-cooling limits and single-ion spectroscopy," Phys. Rev. A **36**, 2220–2232 (1987).

[190] M. S. Gulley, A. G. White, and D. F. James, "A Raman approach to quantum logic in Calcium-like ions," arXiv:quant-ph/0112117 (2001).

[191] R. Han, H. Khoon Ng, and B.-G. Englert, "Raman transitions without adiabatic elimination: A simple and accurate treatment," Journal of Modern Optics **60**, 255–265 (2013).

[192] D. James and J. Jerke, "Effective Hamiltonian theory and its applications in quantum information," Canadian Journal of Physics **85**, 625–632 (2007).

[193] D. J. Wineland, M. Barrett, J. Britton, J. Chiaverini, B. DeMarco, W. M. Itano, B. Jelenković, C. Langer, D. Leibfried, V. Meyer *et al.*, "Quantum information processing with trapped ions," Philosophical Transactions of the Royal Society of London. Series A: Mathematical, Physical and Engineering Sciences **361**, 1349–1361 (2003).

[194] R. Ozeri, W. M. Itano, R. Blakestad, J. Britton, J. Chiaverini, J. D. Jost, C. Langer, D. Leibfried, R. Reichle, S. Seidelin *et al.*, "Errors in trapped-ion quantum gates due to spontaneous photon scattering," Phys. Rev. A **75**, 042329 (2007).

[195] R. Gerritsma, G. Kirchmair, F. Zähringer, J. Benhelm, R. Blatt, and C. Roos, "Precision measurement of the branching fractions of the $4p^2P_{3/2}$ decay of Ca II," The European Physical Journal D **50**, 13–19 (2008).

[196] M. Ramm, T. Pruttivarasin, M. Kokish, I. Talukdar, and H. Häffner, "Precision Measurement Method for Branching Fractions of Excited $P_{1/2}$ States Applied to $^{40}Ca^+$," Phys. Rev. Lett. **111**, 023004 (2013).

[197] P. Richerme, Z.-X. Gong, A. Lee, C. Senko, J. Smith, M. Foss-Feig, S. Michalakis, A. V. Gorshkov, and C. Monroe, "Non-local propagation of correlations in quantum systems with long-range interactions," Nature **511**, 198–201 (2014).

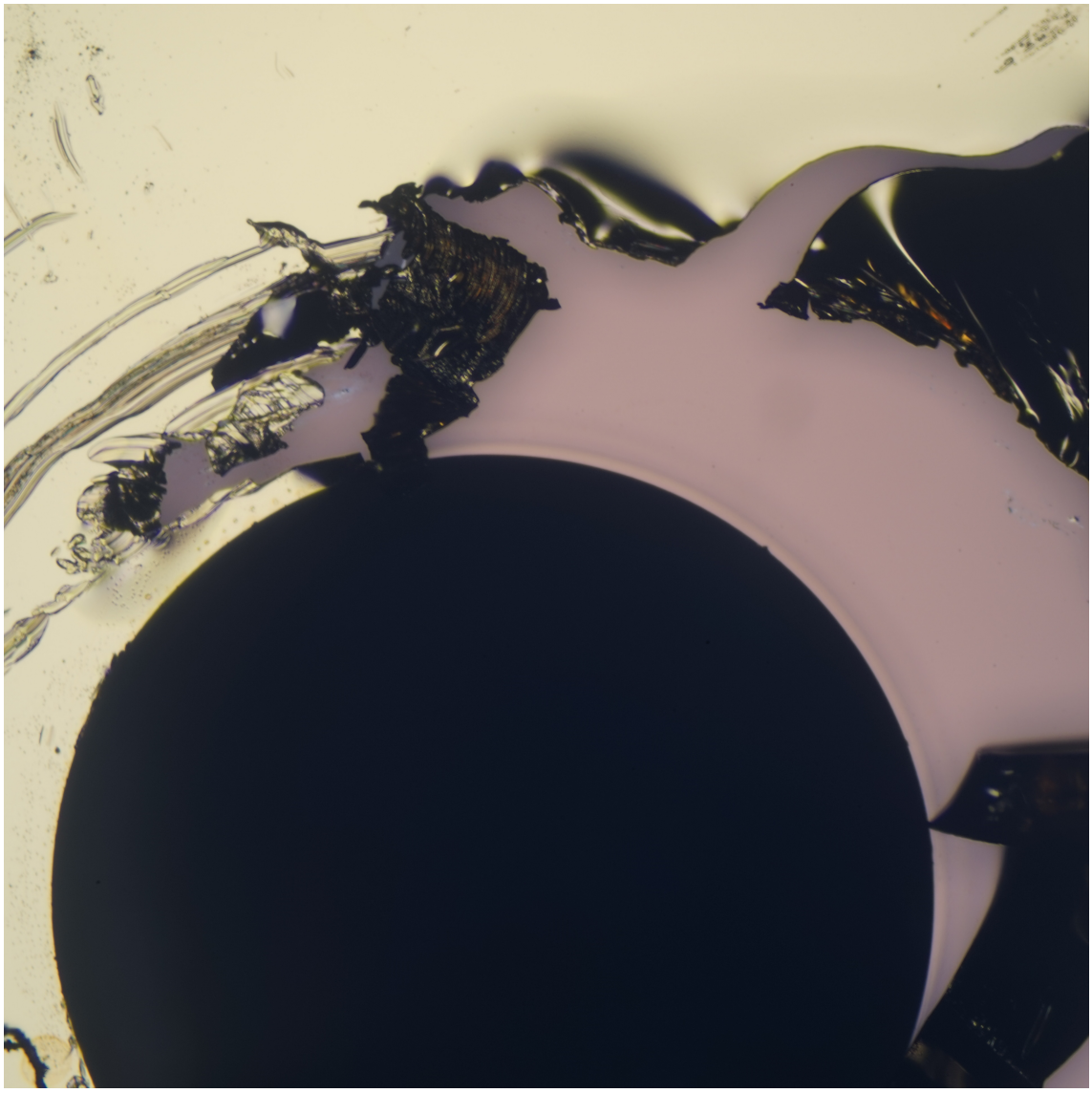

Acknowledgements

What a ride! Es gab Erfolge und viele schöne Seiten, aber daneben auch genügend Überraschungen und intensive Phasen des Zweifelns. Nach dem Glühen unserer Falle und dem versehentlichen Verheizen unseres Vakuum-Setups, fühlte sich das erste Mal die Abbildung eines zweidimensionalen Ionen-Kristall in unserem Setup zu sehen, fast so an, als hielte man die Ionen in eigenen Händen. Dieser PhD verlangte viel, gab aber auch viel zurück.
Da so ein Projekt aber alles andere als eine Solo-Tour ist, möchte ich hiermit allen meinen Dank aussprechen, die diese Arbeit in der einen oder anderen Form ermöglicht haben, auch wenn ein Dank in dieser schriftlichen Form nicht ausreichend sein kann. Ich hoffe die angesprochenen Menschen wissen auch tiefergehend, wie sehr ich sie und ihre Unterstützung schätze.
Ich möchte mit dem Menschen im Herzen des Projekts beginnen und somit meinem Betreuer, Christian Roos, danken. Seine Neugier und Leidenschaft sowie seine vielschichtige Art zu denken waren und sind inspirierend; sein Tempo, Datenanalysen und Simulationen in Matlab (beinahe in Echtzeit) zu erstellen, ist beeindruckend. Außerdem konnte ich auf seine menschliche und rücksichtsvolle Seite immer zählen. Ein herzliches Dankeschön dafür und für die offene und geduldige Weitergabe deines großen Wissens (inkl. Matlab-Code!). Ich hoffe du hast mir verziehen, dass ich in den ersten Monaten beinahe deinen Staubsauger entsorgt habe.
Ich möchte mich weiters bei der gesamten Blatt-Gruppe, und speziell beim Namensgeber der Gruppe und meinem zweiten Betreuer, Rainer Blatt, bedanken. Vielen Dank für deine Unterstützung und die Motivation, in der Physik etwas zu bewegen. Rainer hat eine Atmosphäre in der Gruppe geschaffen, in der man sich willkommen fühlt und in der es maßgeblich ist, das erlangte Wissen zu teilen und weiterzugeben, um so voneinander zu lernen, zu profitieren und gemeinsam weiterzukommen. Ohne die Hilfe und das Wissen von so vielen hilfsbereiten und offenen Menschen, würden derartige Projekte nicht auf diese Weise funktionieren. Ich bin froh, dass auch ich Teil dieser Gruppe sein durfte.
Als nächstes möchte ich unserem *GOAT*, Matthias Bock, ein großes Dankeschön aussprechen. Er kam zwei Jahre nach Beginn des Projekts hinzu und ohne ihn und seinen hochmotivierten und unermüdlichen Einsatz wäre das Experiment weit nicht da, wo es jetzt ist. Durch seinen Verdienst haben wir unseren Aufbau auch zu einem der modernsten und auch aufgeräumtesten(!) Setups gemacht, die es in Innsbruck und wohl weit darüber hinaus gibt. Durch diese Aufgeräumtheit hatte ich bei Labortouren immer das Bedürfnis, den Besucher:innen auch andere "spektakulärer" anzusehende Labore zu zeigen. Was *ground loops* betrifft, bin ich aber heilfroh, dass es bei uns nicht so aufregend ausgesehen hat. Zwei weiteren ebenso wichtigen Wegbegleitern im Team, nämlich Tuomas und Artem, möchte ich auch meinen Dank aussprechen. Der gemeinsame Arbeitsalltag mit Tuomas wurde durch COVID leider etwas verzögert. Es dauerte dann aber nicht allzu lange, dass er sich als unser OG Serles-Minister etablierte. Artem bildet derzeit den zweiten Teil des Dreamteams am Experiment. Er ist nicht nur ein würdiger Nachfolger, sondern bereits weit darüber hinausgewachsen. Matthias, Tuomas und Artem, ich danke euch für euren großen Einsatz, eure Hilfsbereitschaft und Offenheit, aber auch für die gemeinsame Zeit außerhalb des Labors, beim Aperitivo, im KI und für die vielen, manchmal auch leidenschaftlich, geführten Gespräche über Gott, Berge und die Welt.
Ein vorübergehendes Mitglied des 2d-Crystals-Teams war Philip Holz, der vom Wirebonden über das Testen der Falle bis hin zum ersten Fangen einen ganz wesentlichen Beitrag zum Experiment geleistet hat. Vielen Dank für dein Zutun und für deine Hilfe!
Als letzte, aber wesentlichste Gefährtin im urprünglichen 2d-Crystals-Team möchte ich Leni danken. Bis auf einige Monate haben wir die gesamte PhD-Zeit gemeinsam im Projekt verbracht. Ich könnte mir keine bessere Wegbegleiterin für die vergangenen Jahre vorstellen, und das obwohl wir so viel

Zeit auf so engem Raum verbracht haben. Leni hat nicht nur die beste Ionenfalle der Welt designt, sie hatte auch das Feingefühl, Gold-Pins händisch mit dem brüchigsten Alumina-PCB der Welt zu verpressen, ohne es zu zerstören - eine mir bis heute unvorstellbare Leistung! Leni, danke nicht nur für deinen Einsatz im Projekt, für deine Gewissenhaftigkeit, deine geduldige und rücksichtsvolle Art, danke auch für die gemeinsame Zeit - sei es im Büro, im Labor, auf der Dachterrasse, im Vakuumraum, beim Aperitivo oder bei mittäglichen Ausfahrten in die Stadt, um das Füllhorn an Möglichkeiten zum Essen auszukosten. Wir sehen uns in der großen Stadt!
Dank geht auch an Ben Lanyon und sein ganzes Team für die ausgesprochen gute Labor- und Büro-Nachbarschaft. Vielen Dank, Armin, dass du unser Büro mit abwechslungsreichen Themen und gemeinsamen Diskussionen aufgefrischt hast! Ich wünsche dir alles Gute für deinen weiteren PhD! Wir hören uns spätestens bei der nächsten Wahl.
Danke an Manoj, Florian und Jojo von QSIM, unserem Schwesternexperiment, für all die Hilfe, Diskussionen und das geteilte Laserlicht! Danke an alle Leute von AQT, speziell Georg, Max und Thomas F., die immer eine große Hilfe und für einen Austausch da waren. Danke an Thomas Monz, der diesen Austausch auch lebt und der einen immer über alles am Laufenden hielt.
Ich möchte weiters den Menschen danken, die durch ihre nicht-wissenschaftlichen Tätigkeiten Wissenschaft erst möglich machen. Herzlichsten Dank an Claudia und Patricia vom Institut für Experimentalphysik, an Leonarda vom projekt.service.büro und an Elisabeth, Klaus, Valentin, David und Herrn Knabl vom IQOQI Innsbruck. Großer Dank geht auch an Stefan, Andreas und Bernhard von der mechanischen Werkstatt am IQOQI und auch an Armin, Christoph und Toni an der Uni. Vielen Dank an Gerhard Hendl für die Unterstützung in elektronischen Angelegenheiten.
Spezieller Dank geht an jene Menschen, denen ich sowohl an der Uni aber auch außerhalb davon gute Erinnerungen und Gesellschaft zu verdanken habe, an die ich immer gerne denke. Danke insbesondere an Christine und Christian (Ro.), Milena, Martin, Manoj, Lata, Marco, Josef, Armin, Viktor, Mariano und einige mehr, die hoffentlich verzeihen, dass ich nicht alle namentlich aufzähle.
Danke, Klemens Schüppert, für die Untertützung in Server- und Website-Angelegenheiten. Danke, Manuel John, dass du diese nach mir übernommen hast.
Danke an alle Rauschbrunnen-Runners für die verschwitzten Mittagspausen mit herrlichem Ausblick!
Nicht zuletzt möchte ich auch den Menschen außerhalb des Innsbrucker Ionenfallen-Universums herzlich danken, die mich in den letzten Jahren in einer impliziten oder expliziteren Form unterstützt und begleitet haben! Besonderer Dank geht an meine Eltern für ihre auch sehr explizite Unterstützung während des gesamten Studiums und darüber hinaus. Danke an meine Geschwister und ihre Partner:innen fürs Dasein und auch Mitfiebern. Danke an meinen Innsbrucker "Verein", nicht nur, aber auch für die vielen gemeinsamen Abenteuer, Klettersessions und Essens-Exzesse. Danke an die "Wiener Physiker:innen" für die vielen schönen gemeinsamen Wochenenden in den letzten Jahren!
Und besonders dankbar bin ich auch meiner Partnerin Magdalena. Du warst und bist die wichtigste Stütze. Danke für deine Unterstützung in meiner Arbeit und abseits davon. Danke, dass ich mit dir auch oft den Weg in Abenteuer in den Bergen und anderswo gefunden habe. Ich freue mich auf die weiteren gemeinsamen Abenteuer, die auf uns warten!

Danke an alle, die ich hier vergessen oder nicht explizit erwähnt habe!

Danke, danke, danke!